FEMTOCHEMISTRY OF VIBRONICALLY COUPLED EXCITED ELECTRONIC STATES OF CARBONYL COMPOUNDS AND HIGHLY FLUORINATED BENZENE

OLE HÜTER

Dissertation zur Erlangung des Doktorgrades
der Mathematisch-Naturwissenschaftlichen Fakultät
der Christian-Albrechts-Universität zu Kiel
Kiel, April 2016

Christian-Albrechts-Universität zu Kiel

Mathematisch-Naturwissenschaftliche Fakultät
Institut für Physikalische Chemie

Dissertation

Femtochemistry of Vibronically Coupled Excited Electronic States of Carbonyl Compounds and Highly Fluorinated Benzene

Ole Hüter

Erster Gutachter Prof. Dr. Friedrich Temps
Institut für Physikalische Chemie
Christian-Albrechts-Universität zu Kiel

Zweiter Gutachter Prof. Dr. Jürgen Grotemeyer
Institut für Physikalische Chemie
Christian-Albrechts-Universität zu Kiel

Betreuer Prof. Dr. Friedrich Temps

4. April 2016

Ole Hüter
Femtochemistry of Vibronically Coupled Excited Electronic States of Carbonyl Compounds and Highly Fluorinated Benzene
Dissertation, 4. April 2016

Erster Gutachter: Prof. Dr. Friedrich Temps
Zweiter Gutachter: Prof. Dr. Jürgen Grotemeyer

Tag der mündlichen Prüfung: 14. Juni 2016
Zum Druck genehmigt: 14. Juni 2016

gez. Prof. Dr. Wolfgang J. Duschl, Dekan

Erklärung

Hiermit erkläre ich an Eides statt, dass die vorliegende Abhandlung – abgesehen von der Beratung durch meinen Betreuer Prof. Dr. Friedrich Temps – nach Inhalt und Form meine eigene Arbeit ist.

Diese Arbeit hat weder in Auszügen noch in ganzer Form einer anderen Stelle im Rahmen eines Prüfungsverfahrens vorgelegen. Sie wurde in ihrer Gesamtheit nicht veröffentlicht und auch nicht zur Veröffentlichung eingereicht.

Teile dieser Arbeit wurden zur Veröffentlichung in wissenschaftlichen Fachzeitschriften eingereicht. Dies bezieht sich auf die folgenden Kapitel:

KAPITEL 5
Ole Hüter, Matthieu Sala, Hendrikje Neumann, Song Zhang, Harald Studzinski, Dassia Egorova und Friedrich Temps, „Long-Lived Coherence in Pentafluorobenzene as a Probe of $\pi\pi^*-\pi\sigma^*$ Vibronic Coupling“, The Journal of Chemical Physics **145** (2016, AIP Publishing LLC).

Die Arbeit ist unter Einhaltung der Regeln guter wissenschaftlicher Praxis der Deutschen Forschungsgemeinschaft entstanden.

Kiel, 14. Juni 2016

Ole Hüter

For my family.

Abstract

In this Thesis, the femtochemistry of vibronically coupled excited electronic states of the carbonyl compounds acetone and cyclohexanone and the highly fluorinated benzene-derivative pentafluorobenzene is investigated after optical excitation under jet-cooled conditions using femtosecond time-resolved time-of-flight mass spectrometry and photoelectron imaging spectroscopy.

The simplest ketone acetone was photoexcited to the S_1 ($^1n\pi^*$) electronic state and to energetically high-lying Rydberg states. No sign for an α–CC bond cleavage on the $^1n\pi^*$ potential energy surface was observed for up to one nanosecond, thereby indicating a bond dissociation on the corresponding $^3n\pi^*$ surface, in accordance with the commonly accepted picture. After excitation to the $3d_{yz}$ Rydberg state, the CC bond was seen to break in 90 – 50 fs, very likely following a reaction pathway *via* the $^1\pi\pi^*$ potential energy surface. The high-lying Rydberg states of the cyclic ketone cyclohexanone were probed for a similar ultrafast electronic relaxation behavior. After femtosecond excitation of either the 3d or 3p Rydberg states, the electronic population is immediately transferred to the 3s Rydberg state in less than 35 fs. It then undergoes internal conversion to the $^1n\pi^*$ state, which in turn is found to be long-lived with a decay time of at least several hundred picoseconds.

After femtosecond excitation of pentafluorobenzene to the optically bright $\pi\pi^*$ excited electronic state, pronounced and long-lived transient oscillations of the parent ion yield were observed. The photoelectron spectra displayed the population of the $\pi\pi^*$ state only in the maxima of the oscillation, while the corresponding bands vanished in the minima. The results of *ab initio* calculations showed that the adiabatic excited state potential energy surface acquires a pronounced double-well character along specific vibrational out-of-plane modes due to vibronic interactions with the energetically close, optically dark $\pi\sigma^*$ state. Quantum dynamics simulations demonstrated that the excited wavepacket periodically oscillates in the anharmonic potential for several picoseconds. Near the outer turning points, the excited state acquires substantial $\pi\sigma^*$ character, thereby lowering the probability for ionization. The mixing of electronic characters is mirrored in the anisotropy of the corresponding photoelectron angular distribution. Thus, the ionizing probe laser pulse directly maps the wavepacket motion into the observed signal oscillations.

Zusammenfassung

In dieser Dissertation wird die Femtochemie vibronisch gekoppelter, angeregter Elektronenzustände der Carbonylverbindungen Aceton und Cyclohexanon sowie des Benzol-Derivats Pentafluorbenzol im Molekularstrahl mittels femtosekundenzeitaufgelöster Flugzeit-Massenspektrometrie und Photoelektronen-Geschwindigkeitskartographie untersucht.

Das einfachste Keton Aceton wurde in den elektronischen S_1-Zustand ($^1n\pi^*$) sowie hochenergetische Rydbergzustände angeregt. Es konnten keine Hinweise auf den Bruch der α–CC-Bindung auf der $^1n\pi^*$-Potentialfläche innerhalb einer Nanosekunde beobachtet werden, was auf einen Bindungsbruch nach dem allgemein anerkannten Reaktionsmechanismus auf der entsprechenden $^3n\pi^*$-Potentialfläche hindeutet. Nach Anregung des $3d_{yz}$-Rydbergzustands hingegen wird die CC-Bindung in 90 – 50 fs gebrochen, wobei der Reaktionsweg sehr wahrscheinlich über die $^1\pi\pi^*$-Potentialfläche verläuft. Die hochenergetischen Rydbergzustände des zyklischen Ketons Cyclohexanon wurden auf ein gleichartiges elektronisches Abklingverhalten hin untersucht. Nach Femtosekunden-Anregung sowohl der 3d- als auch der 3p-Rydbergzustände wurde der 3s-Rydbergzustand in weniger als 35 fs elektronisch besetzt. Die Lebensdauer des darauffolgend über interne Konversion erreichten $^1n\pi^*$-Zustands beträgt wenigstens einige hundert Picosekunden.

Nach Femtosekunden-Anregung des optisch hellen, elektronisch angeregten $\pi\pi^*$-Zustands von Pentafluorbenzol wurden ausgeprägte und langlebige Oszillationen der transienten Ionenausbeute des Stammmolekülions beobachtet. Die Photoelektronenspektren zeigten, dass der $\pi\pi^*$-Zustand nur in den Maxima der Oszillation besetzt ist, während die entsprechenden Banden in den Minima nicht auftreten. Die Ergebnisse von *ab initio*-Berechnungen zeigten, dass die adiabatische Potentialfläche des angeregten Zustands einen ausgeprägten Doppelminimum-Charakter entlang einiger bestimmter Schwingungsmoden annimmt, was auf die vibronische Wechselwirkung mit dem energetisch naheliegenden, optisch dunklen $\pi\sigma^*$-Zustands zurückgeführt werden konnte. Simulationen der Dynamik des quantenmechanischen Systems ergaben, dass das angeregte Wellenpaket in dem anharmonischen Potential für mehrere Picosekunden periodisch oszilliert. Nahe den äußeren Wendepunkten nimmt der angeregte Zustand ausgeprägten $\pi\sigma^*$-Charakter an, was die Ionisationswahrscheinlichkeit verringert. Das Vermischen der elektronischen Charaktere spiegelt sich in der Anisotropie der Photoelektronen-Winkelverteilung wider. Der ionisierende Laserpuls zeichnet daher die Bewegung des Wellenpakets in Form der beobachteten Signaloszillationen auf.

Contents

1 Introduction

In 1981, A. Zewail and coworkers conducted an experiment whose outcome has been considered a paradigm shift by many.[1] A selected vibronic state of anthracene in a molecular beam was excited with short picosecond laser pulses, and the anticipated outcome of the experiment was to see an exponentially decreasing population of this state due to the chaotic motion in the vibrational and rotational phase space of the system, caused by the random redistribution of the energy among the various degrees of freedom. Instead, the population was coherently oscillating between two vibrational states with a well-defined period and phase, causing pronounced and temporally long-lived oscillations of the emitted fluorescene at selected detection wavelengths.[2,3] The phase-coherent dynamics of anthracene illustrated the importance of the excitation of non-stationary states in molecules. The illumination with a coherent light source spanning multiple stationary (time-independent) states prepares a superposition of those states, forming a wavepacket that evolves with time. The experiment demonstrated that such a wavepacket can be prepared in-phase in an emsemble of molecules at the same time zero, and the subsequent coherent dynamics of the ensemble can be observed like the phase-space trajectory of a single molecule. This issue has become a fundamental concept for successive investigations of radiationless transitions involving multiple vibronic states and their interstate couplings.

The interstate coupling strengths between electronic states are determined by the nuclear motions accompanying the transition between them, often along a single molecular bond. Nuclear motion has velocities on the order of km/s.[1] Therefore, to record atomic-scale dynamics over the distance of an Ångström, a temporal resolution of less than 100 fs is required. The upcoming availability of laser light sources with femtosecond pulse duration later in the 1980s allowed researchers to study the fundamental dynamics of chemical bonds. The observation of reaction dynamics, i. e. the making and breaking of bonds, on their actual time scale constitutes the field of femtochemistry, which was largely established by the seminal work of Zewail and co-workers,[4–10] and honored with the Nobel prize in chemistry in 1999.[11]

Historically, the investigations on the alkali halides NaI and NaBr with femtosecond time resolution in 1988 lead to a new paradigm in the field of femtochemistry.[12–14] While the concept of ensemble coherence had been widely accepted at that time,

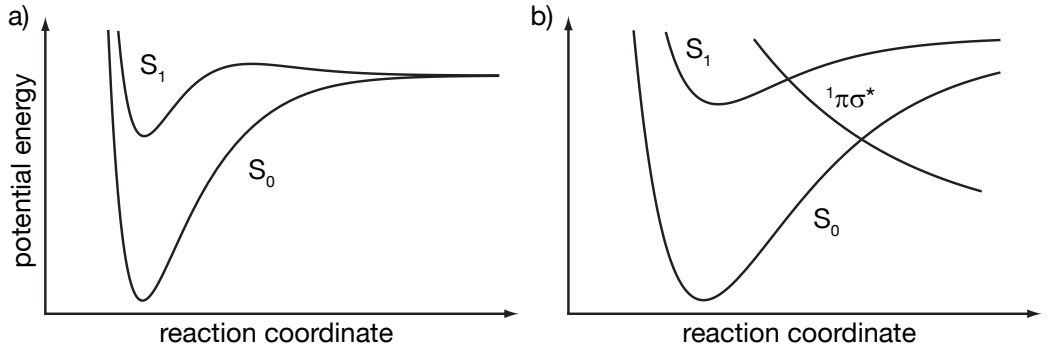

Figure 1.1. a) The vibronic interaction between the excited S_1 electronic state and the S_0 ground state induces an energy barrier for dissociation on the adiabatic potential energy curve of the S_1 state. b) Internal conversion from the excited S_1 state to a non-bonding $\pi\sigma^*$ electronic state can prompty dissociate a molecule. On the other hand, a further intersection of the $\pi\sigma^*$ state with the S_0 state can serve as a photochemical shortcut to the stable ground state.

the results showed that the excited wavepacket was also highly localized in space, hence establishing the concept of dynamics at atomic-scale resolution. The minimal spreading of the wavepacket over several picoseconds confirmed the view of the coherently excited ensemble as a single-molecule trajectory also on the time scale of nuclear motion. Furthermore, it was the first real-time observation of a chemical bond changing its character periodically between covalent and ionic. Today, a multitude of photophysical and photochemical reactions have successfully been researched employing various techniques of femtosecond time-resolved spectroscopy (see, e. g., the review by Hertel and Radloff[15] and references therein). Outstanding examples include the elucidation of the intramolecular mechanisms of vision,[16–18] photosynthesis[19–25] and the remarkable resistance of biologically relevant molecules against photolesion.[26–35]

This Thesis is concerned with the femtochemistry of vibronically strongly coupled electronic states after their optical excitation. Electronic states whose excitation will lead to dissociation of the molecule, or bound states that interact strongly with such non-bonding states are of particular interest. Unimolecular photodissociation reactions are among the most fundamental and therefore probably best studied photochemical proccesses.[15] In general, a molecule will dissociate if the deposited energy is larger than the binding energy of one of the molecular bonds. In practice, however, and especially for larger molecules, an energy significantly higher than the binding energy of the weakest bond has to be deposited, either because the energy is quickly redistributed among vibrational degrees of freedom, or an energetic barrier has to be surmounted before fragmentation can take place. Such barriers are often formed by vibronically induced avoided crossings between the adiabatic electronic potential energy surface of the initially excited state and the surface of another electronic state, on which the bond is subsequently broken. This situation is illustrated in Figure 1.1 a, where the vibronic interaction between the excited

S_1 state and the S_0 ground state induces a barrier in the adiabatic excited-state potential energy curve on the reaction pathway to dissociation. Of special interest are molecules in which a third electronic state has a repulsive potential enery curve with respect to the stretching of a certain bond. This situation is illustrated in Figure 1.1 b, showing the diabatic potential energy curve of a non-bonding $\pi\sigma^*$ state. In this case, after internal conversion from the optically excited S_1 state to the $\pi\sigma^*$ state, the bond is promptly broken due to the electronic repulsion in this state. The character of the initially excited state S_1 is then referred to as *predissociative*. If, however, the repulsive state also intersects with the S_0 ground state as shown in Figure 1.1 b, this originally dissociative reaction pathway may not dissociate the molecule at all, but serve as a photochemical shortcut to the stable ground state.[36] As will be seen later in this Thesis, in the special case of very large vibronic coupling strengths between the interacting electronic states, also energetically higher-lying $\pi\sigma^*$ states with non-intersecting potential energy curves can have pronounced influence on the excited-state dynamics of molecules.

In the anthracene experiment, the molecules were investigated in the gas phase in a seeded molecular beam, and the emitted fluorescence served as probe of the coherent nuclear dynamics. A supersonic molecular beam provides the ideal environment to observe coherent intramolecular phenomena, as the molecules are cooled close to their ground state and are isolated from each other under effectively collision-free conditions.[37,38] Intermolecular effects that contribute to the dephasing of the prepared wavepacket are avoided, and the intramolecular effects of interest are isolated. In the studies presented in this Thesis, the investigated molecules are prepared in a seeded molecular beam as well. A femtosecond laser pump pulse prepares an excited-state wavepacket, and the ensuing dynamics are interrogated by a second, time-delayed probing laser pulse that ionizes the molecules. Compared to laser-induced fluorescence, the resulting charged particles can be detected with much higher efficiency. The mass-, energy-, and angle-resolved spectra yield rich, highly multiplexed information on the ultrafast dynamics of the system. Furthermore, photoionization is a universal probing mechanism as no quantum-mechanical propensity rules have to be obeyed in the process.

The photoions are detected dispersed by mass by their time of flight in a linear flight tube of a mass spectrometer, enabling the selective measurement of parent molecule and photofragment ion yields. While this technique allows one to determine the lifetime of electronically excited states, it is particularly powerful for discerning the nuclear motions during a bond dissociation reaction, as the resulting fragments are readily distinguished by their respective time of flight. The complementary photoelectrons are detected using the energy- and angle-resolved photoelectron imaging technique.[39–48] This method allows one to follow radiationless electronic population transfer processes between excited states by monitoring the characteristic

kinetic energy of the electrons emitted from the respective states. Even if the resulting energy bands overlap, the recorded angular distribution delivers additional information on the emitting electronic states. Moreover, the temporal evolution of the molecular axis alignment is reflected in the angular emission pattern as well. With these two techniques, a range of problems in the excited-state dynamics of molecules can be elucidated, from a vibrational wavepacket on a single potential energy surface up to the disentanglement of intrinsically coupled electronic and nuclear motion, making it the ideal set of tools for studying photodissociation reactions. In Chapter 2 of this work, details will be given on how intramolecular photophysical processes are described in the quantum-mechanical picture of a molecular system, on how this picture translates into macroscopic observables, and on the practical experimental realization of the aforementioned techniques.

The α–CC Bond Cleavage in Acetone and Cyclohexanone

The first photochemical reaction under investigation in this Thesis is the photodissociation of the α–CC bond in acetone after irradiation with ultraviolet light. This reaction of the simplest aliphatic ketone is of great interest not only because of its fundamental nature,[49] but also its relevance to the photochemistry of the Earth's atmosphere,[50] in particular the production of ozone (O_3) in the upper troposphere. While ground-level ozone, being harmful to human health,[51] is considered a major air pollutant, ozone created in the upper troposphere replenishes the stratospheric ozone layer which is of fundamental importance for the life on Earth.[52]

The hydrogen radicals OH and HO_2 are of central relevance to the photochemistry of the whole troposphere,[53] and it was proposed that acetone could be a significant source in the upper troposphere.[54] One of the dominant mechanisms for the production of ozone (O_3) in the upper troposphere is initiated by the oxidation of carbon monoxide (CO) by the OH radical:[55]

$$\mathrm{OH} + \mathrm{CO} \xrightarrow{\mathrm{O_2}} \mathrm{HO_2} + \mathrm{CO_2} \tag{1.1a}$$

$$\mathrm{HO_2} + \mathrm{NO} \longrightarrow \mathrm{OH} + \mathrm{NO_2} \tag{1.1b}$$

$$\mathrm{NO_2} + h\nu \longrightarrow \mathrm{NO} + \mathrm{O} \tag{1.1c}$$

$$\mathrm{O} + \mathrm{O_2} \longrightarrow \mathrm{O_3}. \tag{1.1d}$$

On the other hand, the dominant mechanism for the production of OH radicals in the lower troposphere begins with the photolysis of an ozone molecule by solar ultraviolet radiation[56]

$$\mathrm{O_3} + h\nu \longrightarrow \mathrm{O}(^1\mathrm{D}) + \mathrm{O_2} \tag{1.2a}$$

$$\mathrm{O}(^1\mathrm{D}) + \mathrm{H_2O} \longrightarrow \mathrm{OH} + \mathrm{OH}, \tag{1.2b}$$

yielding an electronically excited O(^{1}D) atom that further reacts with water, which is abundant in the lower troposphere in the form of water vapour, to give two OH radicals. The upper troposphere is very arid, and therefore it has been thought that the low H_2O concentrations preclude a significant contribution of this OH formation pathway. This, however, stands in contradiction to measurements that showed high OH concentrations in the upper troposphere as well. It was suggested[57] that the photolysis of acetone

$$(CH_3)_2CO + h\nu \longrightarrow CH_3CO + CH_3 \tag{1.3a}$$
$$CH_3CO + O_2 \longrightarrow CH_3CO_3 \tag{1.3b}$$
$$CH_3 + O_2 \longrightarrow CH_3O_2, \tag{1.3c}$$

transported by convection from the lower troposphere, may provide a significant source of OH and HO_2 in the upper troposphere.[50,58] The subsequent reaction steps of CH_3CO_3 and CH_3O_2 then lead to the production of OH and HO_2,[59] as shown in the following scheme:

$$CH_3CO_3 + NO \xrightarrow{O_2} CH_3O_2 + CO_2 + NO_2 \tag{1.4a}$$
$$CH_3CO_3 + NO_2 \rightleftharpoons CH_3C(O)O_2NO_2 \tag{1.4b}$$
$$CH_3CO_3 + HO_2 \longrightarrow CH_3C(O)OOH + O_2 \tag{1.4c}$$
$$\longrightarrow CH_3COOH + O_3 \tag{1.4d}$$
$$CH_3O_2 + NO \xrightarrow{O_2} CH_2O + HO_2 + NO_2 \tag{1.4e}$$
$$CH_3O_2 + HO_2 \longrightarrow CH_3OOH + O_2 \tag{1.4f}$$
$$CH_3O_2 + CH_3O_2 \longrightarrow 2\,CH_3O + O_2 \tag{1.4g}$$
$$CH_3OOH + h\nu \xrightarrow{O_2} OH + HO_2 + CH_2O \tag{1.4h}$$
$$CH_3OOH + OH \longrightarrow OH + CH_2O + H_2O \tag{1.4i}$$
$$\longrightarrow CH_3O_2 + H_2O \tag{1.4j}$$
$$CH_2O + h\nu \xrightarrow{2\,O_2} 2\,HO_2 + CO \tag{1.4k}$$
$$\longrightarrow CO + H_2 \tag{1.4l}$$
$$CH_2O + OH \longrightarrow HO_2 + CO + H_2O. \tag{1.4m}$$

It was found that the production of OH and HO_2 from the photolysis of acetone in the upper troposphere can be many times larger than the contribution from the reaction O(^{1}D) + H_2O (Scheme 1.2).[55] The importance of this source of free radicals is underlined by the fact that acetone is globally distributed and has not only anthropogenic, but also biogenic sources. These sources include the emission from trees,[60] plant leaves, grass and clover,[61,62] as it is a by-product of the central plant metabolism.

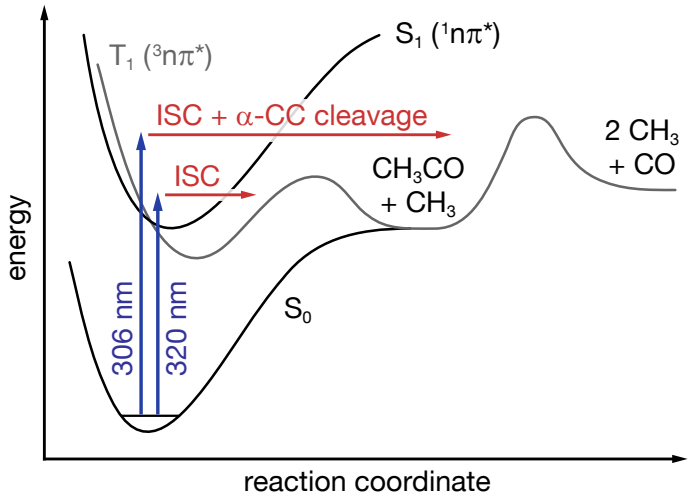

Figure 1.2. Schematic representation of the potential energy curves of acetone in the ground and the first excited singlet and triplet states along the α–CC bond dissociation coordinate. Intersystem crossing from S_1 to T_1 is observed at $\lambda \leq 320$ nm, eventually followed by α–CC bond cleavage on the triplet potential energy surface after excitation at $\lambda \leq 306$ nm. Excitation to higher energies leads to a further decomposition of the acetyl radical.

The first step (Reaction 1.3a) of the photolysis reaction of acetone is the cleavage of the α–CC bond in the Norrish type I reaction.[63] It is probably one of the most well-researched photochemical reactions and attracted wide interest not only for the relevance to atmospheric processes, but also for the fundamental nature of the C–C bond dissociation process. The commonly accepted photolysis mechanism is summarized in Figure 1.2. The photoexcitation of acetone with ultraviolet light at wavelengths of $\lambda < 320$ nm excites the transition to the energetically lowest, $^1n\pi^*$ electronic state, followed by intersystem crossing to the corresponding $^3n\pi^*$ state with a quantum yield close to one.[64] On the triplet potential energy surface, an energetic barrier is formed by an avoided crossing with the potential energy surface of the second excited triplet state. The surmounting of this barrier by an excitation with wavelengths of $\lambda < 306$ nm is promptly followed by the dissociation of the C–C bond.[65,66] The intersystem crossing rate has been deduced from fluorescence and phosphorescence lifetime measurements to be between $(2.4-1.6\ \text{ns})^{-1}$, depending on the excitation wavelength.[64,67–70] It has been commonly agreed upon that the intersystem crossing process is the rate-determining step in the photolysis reaction of acetone after photoexcitation.

On the other hand, results of femtosecond time-resolved investigations of the α–CC cleavage reaction suggested a C–C bond dissociation following femtosecond laser excitation in less than 200 femtoseconds.[71–87] More than five orders of magnitude lie in between these two experimentally determined reaction rates. The accessibility of an ultrafast pathway after photoexcitation from solar ultraviolet radiation would imply serious consequences on established models of atmospheric photochemistry involving acetone and similar precursors to OH and HO_2 radical formation pro-

cesses.[50,57,88–92] While ultrafast intersystem crossing processes have been observed in molecules containing heavy atoms,[93,94] the required very large spin-orbit coupling is not expected in acetone. As the intersystem crossing pathway has been confirmed by theoretical studies as well,[95–99] an experimental proof of the involvement of triplet states in the ultrafast α–CC cleavage reaction would lead to a paradigm shift on the importance of triplet states in ultrafast intramolecular processes. The goal of the work on the acetone molecule is to clarify, using the photoelectron imaging technique, which excited electronic states are involved in a photodissociation reaction pathway taking place on an ultrafast time scale. The results of our investigations are presented in Chapter 3. The weak absorption cross section of the $^1n\pi^*$ state makes it necessary to take electronic states excited by two-photon transitions into consideration, as will be seen in that Chapter. Spectral photoelectron bands from a population of energetically high-lying excited states are readily disclosed by their placement at higher kinetic energies than possible after one-photon excitation. The recorded spectra reveal a strong vibronic coupling between excited electronic Rydberg and valence states, enabling an hitherto unknown ultrafast pathway for fragmentation.

In the above context, the cyclic aliphatic ketone cyclohexanone has been investigated as well. The α–CC cleavage reaction after excitation to the lowest excited $^1n\pi^*$ state of cyclohexanone is expected to take place *via* the same reaction scheme as in acetone,[69,100,101] leading to an opening of the ring system. The vibronic coupling of the 3s Rydberg state with the $^1n\pi^*$ valence state has been subject of a series of theoretical and experimental investigations only recently,[102–104] but nothing is known on the couplings of energetically higher-lying Rydberg and valence states. Investigation on the ultrafast dynamics of the electronically excited states of cyclohexanone are presented in Chapter 4.

The Unusual Excited-State Dynamics of Pentafluorobenzene

In molecules that are of fundamental importance for life on Earth, such as the building blocks adenine, thymine, cytosine and guanine of all genomic material, photodissociation reactions after the absorption of ultraviolet light are generally undesirable. Genetic stability would be severely impaired, causing mutagenesis, carcinogenesis or apoptosis.[105] Although repair mechanisms in the form of photolyase enzymes exist,[106,107] many biologically relevant molecules prevent photolysis upfront by their inherent resistance against photolesion caused by ultraviolet radiation. It was first recognized in the seminal work of Sobolewski and Domcke[108–111] that the strongly absorbing $\pi\pi^*$ states of (hetero-)aromatic molecules often exhibit an easily accessible conical intersection mediating ultrafast internal conversion to a $\pi\sigma^*$ state, which in turn enables an highly efficient ultrafast electronic relaxation pathways through another conical intersection back to the ground state (as illustrated in Figure 1.1 b). The widespread relevance of this ultrafast electronic deactivation mecha-

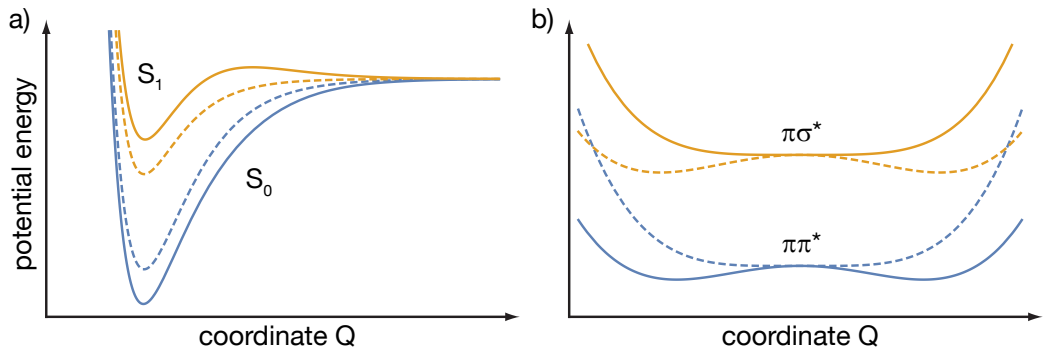

Figure 1.3. Examples of the diabatic (dashed lines) and adiabatic (solid lines) potential energy curves of two vibronically interacting electronic states. a) Morse potentials of a molecular ground state (S_0) and an excited state (S_1) along a bond stretching coordinate (cf. Figure 1.1 a). The coupling induces a barrier in the adiabatic S_1 potential energy curve. b) Potentials of an out-of-plane vibration in pentafluorobenzene. The unusually strong coupling between the energetically well-separated diabatic $\pi\pi^*$ and $\pi\sigma^*$ states induces a symmetric double-well shape of the adiabatic $\pi\pi^*$ potential energy curve.

nism has been theoretically and experimentally established for many systems such as the model chromophores pyrrole,[36,112–117] phenols,[118–124] imidazoles[125–127] and indoles,[128–130] individual nucleobases,[27,29,31,131–136] oligonucleotides,[26,28,30,32–35] and has been subject of several extensive reviews.[137–141]

In the investigation of the interplay between $\pi\pi^*$ and neighboring $\pi\sigma^*$ states, highly fluorinated benzenes are of special interest. In these molecules, the so-called perfluoro effect lowers the σ^* molecular orbitals in energy relative to the π^* molecular orbitals due to the strong electronegativity of the fluorine atoms.[142–144] These molecules are therefore well-suited for detailed investigations of the vibronic coupling mechanisms between energetically increasingly close $\pi\pi^*$ and $\pi\sigma^*$ states. In Chapter 5, the results of a joint experimental and theoretical study of the unusual excited-state dynamics of pentafluorobenzene after femtosecond laser excitation to the optically bright $\pi\pi^*$ electronic state are reported. The most prominent feature of the observed transient ion yield profiles is a long-lived, large-amplitude oscillation with a frequency of $\nu = 78-74$ cm^{-1}. Similar oscillations have been observed previously after $\pi\pi^*$ excitation in the femtosecond transient absorption spectra of 1,2,3,4-tetrafluorobenzene, pentafluorobenzene and hexafluorobenzene,[145] and in the femtosecond transient ion yield profiles of hexafluorobenzene.[146] The physical mechanism at the origin of the observed oscillations has so far remained unclear. In pentafluorobenzene, the lowest $\pi\sigma^*$ state, formed by promotion from the π system to a σ^* orbital on a C–F bond, was predicted to become nearly isoenergetic with the first $\pi\pi^*$ excited electronic state by *ab initio* electronic structure calculations.[144,146,147] In contrast, our electronic structure calculations showed that the energetic separation between the $\pi\sigma^*$ and $\pi\pi^*$ states is on the order of 1 eV, thus making a breakdown of the Born–Oppenheimer approximation in terms of a strong vibronic coupling unexpected at first.

The Born–Oppenheimer approximation is based on the fact that the energy separation of electronic eigenstates is generally much larger than typical separations of eigenstates associated with nuclear motion. When this condition is not fulfilled, transitions between adiabatic electronic states are caused by vibronic couplings between these states.[148–151] Often only two electronic states are close in energy in only a small region of nuclear coordinates. In this case, the framework around the Born–Oppenheimer approximation can be mostly preserved by the introduction of suitable *diabatic* electronic wavefunctions.[152–154] The electronic potential energy surfaces associated with diabatic wavefunctions are smooth and slowly varying functions of the nuclear coordinates,[155,156] may cross at avoided crossings of the adiabatic potential energy surfaces that are subject to noncrossing rule,[157,158] and can preserve the configurational character of the electronic states.[159] As an example, assume two vibronically interacting states denoted by Φ_1 and Φ_2. In the adiabatic picture, the matrix Hamiltonian $\boldsymbol{H}$ describing the nuclear motion in these two states reads

$$\boldsymbol{H} = \hat{T}_n \mathbf{1} + \boldsymbol{V} - \boldsymbol{\Lambda}, \tag{1.5}$$

with the kinetic energy operator for the nuclei $\hat{T}_n$, the identity matrix $\mathbf{1}$, the electronic potential energies $\boldsymbol{V}$, and the matrix $\boldsymbol{\Lambda}$ of the nonadiabatic coupling operators $\hat{\Lambda}_{nm}$.[151] Employing the orthogonal transformation

$$\widetilde{\boldsymbol{\Phi}} = \boldsymbol{S}\,\boldsymbol{\Phi} \tag{1.6}$$

of the adiabatic wavefunctions $\boldsymbol{\Phi} = (\Phi_1, \Phi_2)^T$ using a suitable unitary transformation matrix $\boldsymbol{S}$ yields diabatic electronic wavefunctions $\widetilde{\boldsymbol{\Phi}}$. $\boldsymbol{S}$ is chosen such that upon the transformation of $\boldsymbol{H}$ to the diabatic basis

$$\boldsymbol{H} = \hat{T}_n \mathbf{1} + \boldsymbol{W}(\boldsymbol{Q}), \tag{1.7}$$

the matrix $\boldsymbol{\Lambda}$ disappears and the coupling terms are contained in the diabatic potential energy matrix $\boldsymbol{W}(\boldsymbol{Q})$ in terms of dimensionless normal coordinates $\boldsymbol{Q}$. The elements of $\boldsymbol{W}(\boldsymbol{Q})$ can often be expressed as low-order Taylor expansion in $\boldsymbol{Q}$ as they are sufficiently smooth.[160] The diagonal terms W_{11} and W_{22} describe the diabatic potential energy surfaces, and the nondiagonal terms W_{12} and W_{21} contain the vibronic coupling terms between the diabatic states.

The implications of this transformation to the electronic potential energy surfaces are illustrated in Figure 1.3, where two different examples of adiabatic and diabatic potential energy curves of two vibronically interacting electronic states are depicted. In Figure 1.3 a, the adiabatic potential energy curves from Figure 1.1 a are shown again, together with the corresponding diabatic curves. The diabatic curves resemble the typical Morse potentials of molecular vibrations. The inclusion of the vibronic coupling terms introduces a repulsion between both potential energy curves, result-

ing in the energetic barrier in the S_1 state. The potential energy curves shown in Figure 1.3 b are typical for a molecular out-of-plane vibration of pentafluorobenzene, as will be seen in Chapter 5. The repulsion of the diabatic potential energy curves, induced by the unusually large vibronic couplings between the $\pi\pi^*$ and $\pi\sigma^*$ states, leads to a symmetric double-well shape of the adiabatic curves with minima at out-of-plane distorted molecular structures. To elucidate the physical mechanism at the origin of the experimentally observed transient ion yield oscillations, the adiabatic potential energy curves along all vibrational modes of b_1 symmetry were characterized using *ab initio* electronic structure calculations. From the results, a multi-dimensional vibronic coupling model Hamiltonian was parametrized.[151] Using this model Hamiltonian, simulations of the quantum dynamics in the diabatic representation were performed,[161] which provided detailed insight in the photophysics of pentafluorobenzene in the optically excited $\pi\pi^*$ state.

References

1. F. C. DeSchryver, S. De Feyter, and G. Schweitzer, eds., *Femtochemistry* (Wiley-VCH, Weinheim, 2001).
2. W. R. Lambert, P. M. Felker, and A. H. Zewail, "Quantum beats and dephasing in isolated large molecules cooled by supersonic jet expansion and excited by picosecond pulses: Anthracene," J. Chem. Phys. **75**, 5958–5960 (1981).
3. P. M. Felker and A. H. Zewail, "Direct Observation of Nonchaotic Multilevel Vibrational Energy Flow in Isolated Polyatomic Molecules," Phys. Rev. Lett. **53**, 501–504 (1984).
4. N. F. Scherer, J. L. Knee, D. D. Smith, and A. H. Zewail, "Femtosecond Photofragment Spectroscopy: The Reaction ICN $\rightarrow$ CN + I," J. Phys. Chem. **89**, 5141–5143 (1985).
5. M. Dantus, M. J. Rosker, and A. H. Zewail, "Real-time femtosecond probing of 'transition states' in chemical reactions," J. Chem. Phys. **87**, 2395–2397 (1987).
6. M. J. Rosker, M. Dantus, and A. H. Zewail, "Femtosecond real-time probing of reactions. I. The technique," J. Chem. Phys. **89**, 6113–6127 (1988).
7. M. Dantus, M. J. Rosker, and A. H. Zewail, "Femtosecond real-time probing of reactions. II. The dissociation reaction of ICN," J. Chem. Phys. **89**, 6128–6140 (1988).
8. R. B. Bernstein and A. H. Zewail, "Femtosecond real-time probing of reactions. III. Inversion to the potential from femtosecond transition-state spectroscopy experiments," J. Chem. Phys. **90**, 829–842 (1989).
9. T. S. Rose, M. J. Rosker, and A. H. Zewail, "Femtosecond real-time probing of reactions. IV. The reactions of alkali halides," J. Chem. Phys. **91**, 7415–7436

(1989).
10. A. Mokhtari, P. Cong, J. L. Herek, and A. H. Zewail, "Direct femtosecond mapping of trajectories in a chemical reaction," Nature **348**, 225–227 (1990).
11. A. H. Zewail, "Femtochemistry: Atomic-Scale Dynamics of the Chemical Bond Using Ultrafast Lasers (Nobel Lecture)," Angew. Chem. Int. Ed. **39**, 2586–2631 (2000).
12. T. S. Rose, M. J. Rosker, and A. H. Zewail, "Femtosecond real-time observation of wave packet oscillations (resonance) in dissociation reactions," J. Chem. Phys. **88**, 6672–6673 (1988).
13. M. J. Rosker, T. S. Rose, and A. H. Zewail, "Femtosecond real-time dynamics of photofragment-trapping resonances on dissociative potential energy surfaces," Chem. Phys. Lett. **146**, 175–179 (1988).
14. V. Engel, H. Metiu, R. Almeida, R. A. Marcus, and A. H. Zewail, "Molecular state evolution after excitation with an ultra-short laser pulse: A quantum analysis of NaI and NaBr dissociation," Chem. Phys. Lett. **152**, 1–7 (1988).
15. I. V. Hertel and W. Radloff, "Ultrafast dynamics in isolated molecules and molecular clusters," Rep. Prog. Phys. **69**, 1897 (2006).
16. R. W. Schoenlein, L. A. Peteanu, R. A. Mathies, and C. V. Shank, "The first step in vision: femtosecond isomerization of rhodopsin," Science **254**, 412–415 (1991).
17. P. Kukura, D. W. McCamant, S. Yoon, D. B. Wandschneider, and R. A. Mathies, "Structural Observation of the Primary Isomerization in Vision with Femtosecond-Stimulated Raman," Science **310**, 1006–1009 (2005).
18. D. Polli, P. Altoè, O. Weingart, K. M. Spillane, C. Manzoni, D. Brida, G. Tomasello, G. Orlandi, P. Kukura, R. A. Mathies, M. Garavelli, and G. Cerullo, "Conical intersection dynamics of the primary photoisomerization event in vision," Nature **467**, 440–443 (2010).
19. T. Brixner, J. Stenger, H. M. Vaswani, M. Cho, R. E. Blankenship, and G. R. Fleming, "Two-dimensional spectroscopy of electronic couplings in photosynthesis," Nature **434**, 625–628 (2005).
20. H. Lee, Y.-C. Cheng, and G. R. Fleming, "Coherence Dynamics in Photosynthesis: Protein Protection of Excitonic Coherence," Science **316**, 1462–1465 (2007).
21. L. Hammarström and S. Styring, "Coupled electron transfers in artificial photosynthesis," Philos. Trans. R. Soc. Lond. B Biol. Sci. **363**, 1283–1291 (2008).
22. S. Eberhard, G. Finazzi, and F.-A. Wollman, "The Dynamics of Photosynthesis," Annu. Rev. Genet. **42**, 463–515 (2008).
23. Y.-C. Cheng and G. R. Fleming, "Dynamics of Light Harvesting in Photosynthesis," Annu. Rev. Phys. Chem. **60**, 241–262 (2009).
24. E. Collini, C. Y. Wong, K. E. Wilk, P. M. G. Curmi, P. Brumer, and G. D. Scholes, "Coherently wired light-harvesting in photosynthetic marine algae at ambient temperature," Nature **463**, 644–647 (2010).

25. G. D. Scholes, G. R. Fleming, A. Olaya-Castro, and R. van Grondelle, "Lessons from nature about solar light harvesting," Nat. Chem. **3**, 763–774 (2011).
26. C. E. Crespo-Hernández, B. Cohen, P. M. Hare, and B. Kohler, "Ultrafast Excited-State Dynamics in Nucleic Acids," Chem. Rev. **104**, 1977–2020 (2004).
27. T. Pancur, N. K. Schwalb, F. Renth, and F. Temps, "Femtosecond fluorescence up-conversion spectroscopy of adenine and adenosine: experimental evidence for the $\pi\sigma^*$ state?" Chem. Phys. **313**, 199–212 (2005).
28. N. K. Schwalb and F. Temps, "Base Sequence and Higher-Order Structure Induce the Complex Excited-State Dynamics in DNA," Science **322**, 243–245 (2008).
29. N. K. Schwalb, T. Michalak, and F. Temps, "Ultrashort Fluorescence Lifetimes of Hydrogen-Bonded Base Pairs of Guanosine and Cytidine in Solution," J. Phys. Chem. B **113**, 16365–16376 (2009).
30. C. T. Middleton, K. d. L. Harpe, C. Su, Y. K. Law, C. E. Crespo-Hernández, and B. Kohler, "DNA Excited-State Dynamics: From Single Bases to the Double Helix," Annu. Rev. Phys. Chem. **60**, 217–239 (2009).
31. K. Röttger, R. Siewertsen, and F. Temps, "Ultrafast electronic deactivation dynamics of the rare natural nucleobase hypoxanthine," Chem. Phys. Lett. **536**, 140–146 (2012).
32. K. Röttger, F. D. Sönnichsen, and F. Temps, "Ultrafast electronic deactivation dynamics of the inosine dimer – a model case for H-bonded purine bases," Photochem. Photobiol. Sci. **12**, 1466–1473 (2013).
33. M. C. Stuhldreier and F. Temps, "Ultrafast photo-initiated molecular quantum dynamics in the DNA dinucleotide d(ApG) revealed by broadband transient absorption spectroscopy," Faraday Discuss. **163**, 173–188 (2013).
34. M. C. Stuhldreier, K. Röttger, and F. Temps, "Distinctive Spectral Features of Exciton and Excimer States in the Ultrafast Electronic Deactivation of the Adenine Dinucleotide," in *Ultrafast Phenomena XIX*, Springer Proceedings in Physics No. 162, edited by K. Yamanouchi, S. Cundiff, R. de Vivie-Riedle, M. Kuwata-Gonokami, and L. DiMauro (Springer International Publishing, 2015) pp. 452–454.
35. K. Röttger, H. J. B. Marroux, M. P. Grubb, P. M. Coulter, H. Böhnke, A. S. Henderson, M. C. Galan, F. Temps, A. J. Orr-Ewing, and G. M. Roberts, "Ultraviolet Absorption Induces Hydrogen-Atom Transfer in G·C Watson–Crick DNA Base Pairs in Solution," Angew. Chem. Int. Ed. **54**, 14719–14722 (2015).
36. A. L. Sobolewski and W. Domcke, "Conical intersections induced by repulsive $^1\pi\sigma^*$ states in planar organic molecules: malonaldehyde, pyrrole and chlorobenzene as photochemical model systems," Chem. Phys. **259**, 181–191 (2000).
37. G. Scoles, D. Bassi, U. Buck, and D. C. Laine, eds., *Atomic and Molecular Beam Methods: Volume 1* (Oxford University Press, New York, 1988).

38. G. Scoles, D. C. Laine, and U. Valbusa, eds., *Atomic and Molecular Beam Methods: Volume 2* (Oxford University Press, New York, 1992).
39. C.-Y. Ng, *Photoionization and Photodetachment* (World Scientific, 2000).
40. K. Takatsuka, Y. Arasaki, K. Wang, and V. McKoy, "Probing wavepacket dynamics with femtosecond energy- and angle-resolved photoelectron spectroscopy," Faraday Discuss. **115**, 1–15 (2000).
41. D. M. Neumark, "Time-Resolved Photoelectron Spectroscopy of Molecules and Clusters," Annu. Rev. Phys. Chem. **52**, 255–277 (2001).
42. T. Suzuki and B. J. Whitaker, "Non-adiabatic effects in chemistry revealed by time-resolved charged-particle imaging," Int. Rev. Phys. Chem. **20**, 313–356 (2001).
43. T. Seideman, "Time-Resolved Photoelectron Angular Distributions: Concepts, Applications, and Directions," Annu. Rev. Phys. Chem. **53**, 41–65 (2002).
44. K. L. Reid, "Photoelectron Angular Distributions," Annu. Rev. Phys. Chem. **54**, 397–424 (2003).
45. A. Stolow, "Femtosecond Time-Resolved Photoelectron Spectroscopy of Polyatomic Molecules," Annu. Rev. Phys. Chem. **54**, 89–119 (2003).
46. A. Stolow, A. E. Bragg, and D. M. Neumark, "Femtosecond Time-Resolved Photoelectron Spectroscopy," Chem. Rev. **104**, 1719–1758 (2004).
47. M. Wollenhaupt, V. Engel, and T. Baumert, "Femtosecond Laser Photoelectron Spectroscopy on Atoms and Small Molecules: Prototype Studies in Quantum Control," Annu. Rev. Phys. Chem. **56**, 25–56 (2005).
48. T. Suzuki, "Femtosecond time-resolved photoelectron imaging," Annu. Rev. Phys. Chem. **57**, 555–592 (2006).
49. H. Okabe, *Photochemistry of small molecules* (Wiley, 1978).
50. H. B. Singh, M. Kanakidou, P. J. Crutzen, and D. J. Jacob, "High concentrations and photochemical fate of oxygenated hydrocarbons in the global troposphere," Nature **378**, 50–54 (1995).
51. M. Lippmann, "Health Effects of Ozone: A Critical Review," J. Air Waste Manag. Assoc. **39**, 672–695 (1989).
52. P. Fabian and M. Dameris, *Ozone in the Atmosphere: Basic Principles, Natural and Human Impacts* (Springer, Berlin, 2014).
53. P. Warneck, *Chemistry of the Natural Atmosphere* (Academic Press, 1999).
54. B. J. Finlayson-Pitts and J. N. Pitts, Jr., *Chemistry of the Upper and Lower Atmosphere: Theory, Experiments, and Applications* (Academic Press, 1999).
55. P. O. Wennberg, T. F. Hanisco, L. Jaeglé, D. J. Jacob, E. J. Hintsa, E. J. Lanzendorf, J. G. Anderson, R.-S. Gao, E. R. Keim, S. G. Donnelly, L. A. D. Negro, D. W. Fahey, S. A. McKeen, R. J. Salawitch, C. R. Webster, R. D. May, R. L. Herman, M. H. Proffitt, J. J. Margitan, E. L. Atlas, S. M. Schauffler, F. Flocke, C. T. McElroy, and T. P. Bui, "Hydrogen Radicals, Nitrogen Radicals, and the Production of O_3 in the Upper Troposphere," Science **279**, 49–53 (1998).

56. D. Kley, "Tropospheric Chemistry and Transport," Science **276**, 1043–1044 (1997).
57. S. A. McKeen, T. Gierczak, J. B. Burkholder, P. O. Wennberg, T. F. Hanisco, E. R. Keim, R.-S. Gao, S. C. Liu, A. R. Ravishankara, and D. W. Fahey, "The photochemistry of acetone in the upper troposphere: A source of odd-hydrogen radicals," Geophys. Res. Lett. **24**, 3177–3180 (1997).
58. H. B. Singh, Y. Chen, A. Staudt, D. Jacob, D. Blake, B. Heikes, and J. Snow, "Evidence from the Pacific troposphere for large global sources of oxygenated organic compounds," Nature **410**, 1078–1081 (2001).
59. L. Jaeglé, D. J. Jacob, W. H. Brune, and P. O. Wennberg, "Chemistry of HO_x radicals in the upper troposphere," Atmos. Environ. **35**, 469–489 (2001).
60. R. Fall, "Biogenic emissions of volatile organic compounds from higher plants," in *Reactive Hydrocarbons in the Atmosphere*, edited by C. N. Hewitt (Academic Press, San Diego, 1998) pp. 41–96.
61. R. C. Macdonald and R. Fall, "Acetone emission from conifer buds," Phytochemistry **34**, 991–994 (1993).
62. W. Kirstine, I. Galbally, Y. Ye, and M. Hooper, "Emissions of volatile organic compounds (primarily oxygenated species) from pasture," J. Geophys. Res. **103**, 10605–10619 (1998).
63. R. G. W. Norrish, H. G. Crone, and O. D. Saltmarsh, "318. Primary photochemical reactions. Part V. The spectroscopy and photochemical decomposition of acetone," J. Chem. Soc., 1456–1464 (1934).
64. R. F. Borkman and D. R. Kearns, "Electronic-Relaxation Processes in Acetone," J. Chem. Phys. **44**, 945–949 (1966).
65. H. Zuckermann, B. Schmitz, and Y. Haas, "Dissociation energy of an isolated triplet acetone molecule," J. Phys. Chem. **92**, 4835–4837 (1988).
66. H. Zuckermann, B. Schmitz, and Y. Haas, "Acetone photophysics in seeded supersonic molecular beams," J. Phys. Chem. **93**, 4083–4091 (1989).
67. J. Heicklen, "The Fluorescence and Phosphorescence of Biacetyl Vapor and Acetone Vapor," J. Am. Chem. Soc. **81**, 3863–3866 (1959).
68. A. M. Halpern and W. R. Ware, "Excited Singlet State Radiative and Nonradiative Transition Probabilities for Acetone, Acetone-d_6, and Hexafluoroacetone in the Gas Phase, in Solution, and in the Neat Liquid," J. Chem. Phys. **54**, 1271–1276 (1971).
69. G. M. Breuer and E. K. C. Lee, "Fluorescence decay times of cyclic ketones, acetone, and butanal in the gas phase," J. Phys. Chem. **75**, 989–990 (1971).
70. J. C. Miller and R. F. Borkman, "Phosphorescence Lifetimes of Partially Deuterated Ketones," J. Chem. Phys. **56**, 3727–3729 (1972).
71. S. K. Kim, S. Pedersen, and A. H. Zewail, "Direct femtosecond observation of the transient intermediate in the α-cleavage reaction of $(CH_3)_2CO$ to $2CH_3+CO$: Resolving the issue of concertedness," J. Chem. Phys. **103**, 477–480 (1995).

72. S. A. Buzza, E. M. Snyder, and A. W. Castleman, Jr., "Further direct evidence for stepwise dissociation of acetone and acetone clusters," J. Chem. Phys. **104**, 5040–5047 (1996).
73. S. A. Buzza, E. M. Snyder, D. A. Card, D. E. Folmer, and A. W. Castleman, Jr., "Femtosecond excitation dynamics of acetone: Dissociation, ionization, and the evolution of multiply charged elemental species," J. Chem. Phys. **105**, 7425–7431 (1996).
74. T. Shibata and T. Suzuki, "Photofragment ion imaging with femtosecond laser pulses," Chem. Phys. Lett. **262**, 115–119 (1996).
75. J. C. Owrutsky and A. P. Baronavski, "Ultrafast studies of the photodissociation of the acetone 3s Rydberg state at 195 nm: Formation and unimolecular dissociation of the acetyl radical," J. Chem. Phys. **108**, 6652–6659 (1998).
76. J. C. Owrutsky and A. P. Baronavski, "Ultrafast photodissociation dynamics of the S_1 and S_2 states of acetone," J. Chem. Phys. **110**, 11206–11213 (1999).
77. Q. Zhong, L. Poth, and A. W. Castleman, Jr., "Ultrafast dissociation dynamics of acetone: A revisit to the S_1 state and 3s Rydberg state," J. Chem. Phys. **110**, 192–196 (1999).
78. P. Farmanara, V. Stert, and W. Radloff, "Ultrafast photodissociation dynamics of acetone excited by femtosecond 155 nm laser pulses," Chem. Phys. Lett. **320**, 697–702 (2000).
79. E. W.-G. Diau, C. Kötting, and A. H. Zewail, "Femtochemistry of Norrish Type-I Reactions: I. Experimental and Theoretical Studies of Acetone and Related Ketones on the S_1 Surface," ChemPhysChem **2**, 273–293 (2001).
80. E. W.-G. Diau, C. Kötting, and A. H. Zewail, "Femtochemistry of Norrish Type-I Reactions: II. The Anomalous Predissociation Dynamics of Cyclobutanone on the S_1 Surface," ChemPhysChem **2**, 294–309 (2001).
81. E. W.-G. Diau, C. Kötting, T. I. Sølling, and A. H. Zewail, "Femtochemistry of Norrish Type-I Reactions: III. Highly Excited Ketones—Theoretical," ChemPhysChem **3**, 57–78 (2002).
82. T. I. Sølling, E. W.-G. Diau, C. Kötting, S. De Feyter, and A. H. Zewail, "Femtochemistry of Norrish Type-I Reactions: IV. Highly Excited Ketones—Experimental," ChemPhysChem **3**, 79–97 (2002).
83. A. P. Baronavski and J. C. Owrutsky, "Ketone excited state lifetimes measured by deep UV ultrafast photoionization spectroscopy," Chem. Phys. Lett. **333**, 36–40 (2001).
84. W.-K. Chen, J.-W. Ho, and P.-Y. Cheng, "Ultrafast photodissociation dynamics of the acetone 3s Rydberg state at 195 nm: a new mechanism," Chem. Phys. Lett. **380**, 411–418 (2003).
85. W.-K. Chen, J.-W. Ho, and P.-Y. Cheng, "Ultrafast Photodissociation Dynamics of Acetone at 195 nm: I. Initial-state, Intermediate, and Product Temporal Evolutions by Femtosecond Mass-Selected Multiphoton Ionization Spectroscopy," J. Phys. Chem. A **109**, 6805–6817 (2005).

86. W.-K. Chen and P.-Y. Cheng, "Ultrafast Photodissociation Dynamics of Acetone at 195 nm: II. Unraveling Complex Three-Body Dissociation Dynamics by Femtosecond Time-Resolved Photofragment Translational Spectroscopy," J. Phys. Chem. A **109**, 6818–6829 (2005).
87. N. Rusteika, K. B. Møller, and T. I. Sølling, "New insights on the photodynamics of acetone excited with 253–288 nm femtosecond pulses," Chem. Phys. Lett. **461**, 193–197 (2008).
88. F. Arnold, V. Bürger, B. Droste-Fanke, F. Grimm, A. Krieger, J. Schneider, and T. Stilp, "Acetone in the upper troposphere and lower stratosphere: Impact on trace gases and aerosols," Geophys. Res. Lett. **24**, 3017–3020 (1997).
89. T. Gierczak, J. B. Burkholder, S. Bauerle, and A. R. Ravishankara, "Photochemistry of acetone under tropospheric conditions," Chem. Phys. **231**, 229–244 (1998).
90. S. Carr, D. E. Shallcross, C. E. Canosa-Mas, J. C. Wenger, H. W. Sidebottom, J. J. Treacy, and R. P. Wayne, "A kinetic and mechanistic study of the gas-phase reactions of OH radicals and Cl atoms with some halogenated acetones and their atmospheric implications," Phys. Chem. Chem. Phys. **5**, 3874–3883 (2003).
91. A. Maranzana, J. R. Barker, and G. Tonachini, "Master equation simulations of competing unimolecular and bimolecular reactions: application to OH production in the reaction of acetyl radical with O_2," Phys. Chem. Chem. Phys. **9**, 4129–4141 (2007).
92. R. Nádasdi, G. Kovács, I. Szilágyi, A. Demeter, S. Dóbé, T. Bérces, and F. Márta, "Exciplex laser photolysis study of acetone with relevance to tropospheric chemistry," Chem. Phys. Lett. **440**, 31–35 (2007).
93. N. H. Damrauer and J. K. McCusker, "Ultrafast Dynamics in the Metal-to-Ligand Charge Transfer Excited-State Evolution of [Ru(4,4'-diphenyl-2,2'-bipyridine)$_3$]$^{2+}$," J. Phys. Chem. A **103**, 8440–8446 (1999).
94. R. Morales-Cueto, M. Esquivelzeta-Rabell, J. Saucedo-Zugazagoitia, and J. Peon, "Singlet Excited-State Dynamics of Nitropolycyclic Aromatic Hydrocarbons: Direct Measurements by Femtosecond Fluorescence Up-Conversion," J. Phys. Chem. A **111**, 552–557 (2007).
95. H. Sakurai and S. Kato, "A theoretical study of the Norrish type I reaction of acetone," Journal of Molecular Structure: THEOCHEM **461–462**, 145–152 (1999).
96. D. Liu, W.-H. Fang, and X.-Y. Fu, "An ab initio study on photodissociation of acetone," Chem. Phys. Lett. **325**, 86–92 (2000).
97. S. Maeda, K. Ohno, and K. Morokuma, "A Theoretical Study on the Photodissociation of Acetone: Insight into the Slow Intersystem Crossing and Exploration of Nonadiabatic Pathways to the Ground State," J. Phys. Chem. Lett. **1**, 1841–1845 (2010).

98. S. Maeda, K. Ohno, and K. Morokuma, "Exploring Multiple Potential Energy Surfaces: Photochemistry of Small Carbonyl Compounds," Adv. Phys. Chem. **2012**, e268124 (2011).
99. L. Favero, G. Granucci, and M. Persico, "Dynamics of acetone photodissociation: a surface hopping study," Phys. Chem. Chem. Phys. **15**, 20651–20661 (2013).
100. E. W.-G. Diau, J. L. Herek, Z. H. Kim, and A. H. Zewail, "Femtosecond Activation of Reactions and the Concept of Nonergodic Molecules," Science **279**, 847–851 (1998).
101. S.-H. Xia, X.-Y. Liu, Q. Fang, and G. Cui, "Excited-State Ring-Opening Mechanism of Cyclic Ketones: A MS-CASPT2//CASSCF Study," J. Phys. Chem. A **119**, 3569–3576 (2015).
102. T. S. Kuhlman, S. P. A. Sauer, T. I. Sølling, and K. B. Møller, "Symmetry, vibrational energy redistribution and vibronic coupling: The internal conversion processes of cycloketones," J. Chem. Phys. **137**, 22A522 (2012).
103. T. S. Kuhlman, T. I. Sølling, and K. B. Møller, "Coherent Motion Reveals Non-Ergodic Nature of Internal Conversion between Excited States," ChemPhysChem **13**, 820–827 (2012).
104. T. S. Kuhlman, M. Pittelkow, T. I. Sølling, and K. B. Møller, "Pulling the Levers of Photophysics: How Structure Controls the Rate of Energy Dissipation," Angew. Chem. Int. Ed. **52**, 2247–2250 (2013).
105. G. P. Pfeifer, Y.-H. You, and A. Besaratinia, "Mutations induced by ultraviolet light," Mutat. Res. Fund. Mol. Mech. Mut. **571**, 19–31 (2005).
106. J. Li, Z. Liu, C. Tan, X. Guo, L. Wang, A. Sancar, and D. Zhong, "Dynamics and mechanism of repair of ultraviolet-induced (6-4) photoproduct by photolyase," Nature **466**, 887–890 (2010).
107. A. Dreuw and S. Faraji, "A quantum chemical perspective on (6-4) photolesion repair by photolyases," Phys. Chem. Chem. Phys. **15**, 19957–19969 (2013).
108. A. L. Sobolewski and W. Domcke, "On the mechanism of rapid non-radiative decay in intramolecularly hydrogen-bonded π systems," Chem. Phys. Lett. **300**, 533–539 (1999).
109. A. L. Sobolewski and W. Domcke, "Ab initio investigations on the photophysics of indole," Chem. Phys. Lett. **315**, 293–298 (1999).
110. A. L. Sobolewski, W. Domcke, C. Dedonder-Lardeux, and C. Jouvet, "Excited-state hydrogen detachment and hydrogen transfer driven by repulsive $^1\pi\sigma^*$ states: A new paradigm for nonradiative decay in aromatic biomolecules," Phys. Chem. Chem. Phys. **4**, 1093–1100 (2002).
111. A. L. Sobolewski and W. Domcke, "On the mechanism of nonradiative decay of DNA bases: ab initio and TDDFT results for the excited states of 9H-adenine," Eur. Phys. J. D **20**, 369–374 (2002).
112. J. Wei, A. Kuczmann, J. Riedel, F. Renth, and F. Temps, "Photofragment velocity map imaging of H atom elimination in the first excited state of pyrrole," Phys. Chem. Chem. Phys. **5**, 315–320 (2003).

113. B. Cronin, M. G. D. Nix, R. H. Qadiri, and M. N. R. Ashfold, "High resolution photofragment translational spectroscopy studies of the near ultraviolet photolysis of pyrrole," Phys. Chem. Chem. Phys. **6**, 5031–5041 (2004).
114. H. Lippert, H.-H. Ritze, I. V. Hertel, and W. Radloff, "Femtosecond Time-Resolved Hydrogen-Atom Elimination from Photoexcited Pyrrole Molecules," ChemPhysChem **5**, 1423–1427 (2004).
115. V. Vallet, Z. Lan, S. Mahapatra, A. L. Sobolewski, and W. Domcke, "Photochemistry of pyrrole: Time-dependent quantum wave-packet description of the dynamics at the $^1\pi\sigma^*$-S_0 conical intersections," J. Chem. Phys. **123**, 144307 (2005).
116. R. Montero, Á. Peralta Conde, V. Ovejas, M. Fernández-Fernández, F. Castaño, J. R. Vázquez de Aldana, and A. Longarte, "Femtosecond evolution of the pyrrole molecule excited in the near part of its UV spectrum," J. Chem. Phys. **137**, 064317 (2012).
117. G. Wu, S. P. Neville, O. Schalk, T. Sekikawa, M. N. R. Ashfold, G. A. Worth, and A. Stolow, "Excited state non-adiabatic dynamics of pyrrole: A time-resolved photoelectron spectroscopy and quantum dynamics study," J. Chem. Phys. **142**, 074302 (2015).
118. A. L. Sobolewski and W. Domcke, "Photoinduced Electron and Proton Transfer in Phenol and Its Clusters with Water and Ammonia," J. Phys. Chem. A **105**, 9275–9283 (2001).
119. Z. Lan, W. Domcke, V. Vallet, A. L. Sobolewski, and S. Mahapatra, "Time-dependent quantum wave-packet description of the $^1\pi\sigma^*$ photochemistry of phenol," J. Chem. Phys. **122**, 224315 (2005).
120. M. G. D. Nix, A. L. Devine, B. Cronin, R. N. Dixon, and M. N. R. Ashfold, "High resolution photofragment translational spectroscopy studies of the near ultraviolet photolysis of phenol," J. Chem. Phys. **125**, 133318 (2006).
121. A. Iqbal, M. S. Y. Cheung, M. G. D. Nix, and V. G. Stavros, "Exploring the Time-Scales of H-Atom Detachment from Photoexcited Phenol-h_6 and Phenol-d_5: Statistical vs Nonstatistical Decay," J. Phys. Chem. A **113**, 8157–8163 (2009).
122. R. N. Dixon, T. A. A. Oliver, and M. N. R. Ashfold, "Tunnelling under a conical intersection: Application to the product vibrational state distributions in the UV photodissociation of phenols," J. Chem. Phys. **134**, 194303 (2011).
123. G. M. Roberts, A. S. Chatterley, J. D. Young, and V. G. Stavros, "Direct Observation of Hydrogen Tunneling Dynamics in Photoexcited Phenol," J. Phys. Chem. Lett. **3**, 348–352 (2012).
124. A. S. Chatterley, J. D. Young, D. Townsend, J. M. Żurek, M. J. Paterson, G. M. Roberts, and V. G. Stavros, "Manipulating dynamics with chemical structure: probing vibrationally-enhanced tunnelling in photoexcited catechol," Phys. Chem. Chem. Phys. **15**, 6879–6892 (2013).
125. D. J. Hadden, K. L. Wells, G. M. Roberts, L. T. Bergendahl, M. J. Paterson, and V. G. Stavros, "Time resolved velocity map imaging of H-atom elimination from

photoexcited imidazole and its methyl substituted derivatives," Phys. Chem. Chem. Phys. **13**, 10342–10349 (2011).

126. R. Crespo-Otero, M. Barbatti, H. Yu, N. L. Evans, and S. Ullrich, "Ultrafast Dynamics of UV-Excited Imidazole," ChemPhysChem **12**, 3365–3375 (2011).
127. R. Montero, Á. P. Conde, V. Ovejas, M. Fernández-Fernández, F. Castaño, and A. Longarte, "Ultrafast Evolution of Imidazole after Electronic Excitation," J. Phys. Chem. A **116**, 10752–10758 (2012).
128. H. Lippert, H. H. Ritze, I. V. Hertel, and W. Radloff, "Femtosecond time-resolved analysis of the photophysics of the indole molecule," Chem. Phys. Lett. **398**, 526–531 (2004).
129. R. Livingstone, O. Schalk, A. E. Boguslavskiy, G. Wu, L. Therese Bergendahl, A. Stolow, M. J. Paterson, and D. Townsend, "Following the excited state relaxation dynamics of indole and 5-hydroxyindole using time-resolved photoelectron spectroscopy," J. Chem. Phys. **135**, 194307 (2011).
130. T. A. A. Oliver, G. A. King, and M. N. R. Ashfold, "Position matters: competing O–H and N–H photodissociation pathways in hydroxy- and methoxy-substituted indoles," Phys. Chem. Chem. Phys. **13**, 14646–14662 (2011).
131. S. Perun, A. L. Sobolewski, and W. Domcke, "Ab Initio Studies on the Radiationless Decay Mechanisms of the Lowest Excited Singlet States of 9H-Adenine," J. Am. Chem. Soc. **127**, 6257–6265 (2005).
132. S. Perun, A. L. Sobolewski, and W. Domcke, "Photostability of 9H-adenine: mechanisms of the radiationless deactivation of the lowest excited singlet states," Chem. Phys. **313**, 107–112 (2005).
133. M. G. D. Nix, A. L. Devine, B. Cronin, and M. N. R. Ashfold, "Ultraviolet photolysis of adenine: Dissociation via the $^1\pi\sigma^*$ state," J. Chem. Phys. **126**, 124312 (2007).
134. W. C. Chung, Z. Lan, Y. Ohtsuki, N. Shimakura, W. Domcke, and Y. Fujimura, "Conical intersections involving the dissociative $^1\pi\sigma^*$ state in 9H-adenine: a quantum chemical ab initio study," Phys. Chem. Chem. Phys. **9**, 2075–2084 (2007).
135. A. Iqbal and V. G. Stavros, "Active Participation of $^1\pi\sigma^*$ States in the Photodissociation of Tyrosine and Its Subunits," J. Phys. Chem. Lett. **1**, 2274–2278 (2010).
136. K. L. Wells, D. J. Hadden, M. G. D. Nix, and V. G. Stavros, "Competing $\pi\sigma^*$ States in the Photodissociation of Adenine," J. Phys. Chem. Lett. **1**, 993–996 (2010).
137. W. Domcke and A. L. Sobolewski, "Unraveling the Molecular Mechanisms of Photoacidity," Science **302**, 1693–1694 (2003).
138. M. N. R. Ashfold, B. Cronin, A. L. Devine, R. N. Dixon, and M. G. D. Nix, "The Role of $\pi\sigma^*$ Excited States in the Photodissociation of Heteroaromatic Molecules," Science **312**, 1637–1640 (2006).

139. M. N. R. Ashfold, G. A. King, D. Murdock, M. G. D. Nix, T. A. A. Oliver, and A. G. Sage, "$\pi\sigma^*$ excited states in molecular photochemistry," Phys. Chem. Chem. Phys. **12**, 1218–1238 (2010).
140. M. Z. Zgierski, T. Fujiwara, and E. C. Lim, "Role of the $\pi\sigma^*$ State in Molecular Photophysics," Acc Chem Res **43**, 506–517 (2010).
141. G. M. Roberts and V. G. Stavros, "The role of $\pi\sigma^*$ states in the photochemistry of heteroaromatic biomolecules and their subunits: insights from gas-phase femtosecond spectroscopy," Chem. Sci. **5**, 1698–1722 (2014).
142. C. R. Brundle, M. B. Robin, N. A. Kuebler, and H. Basch, "Perfluoro effect in photoelectron spectroscopy. I. Nonaromatic molecules," J. Am. Chem. Soc. **94**, 1451–1465 (1972).
143. C. R. Brundle, M. B. Robin, and N. A. Kuebler, "Perfluoro effect in photoelectron spectroscopy. II. Aromatic molecules," J. Am. Chem. Soc. **94**, 1466–1475 (1972).
144. A. P. Hitchcock, P. Fischer, A. Gedanken, and M. B. Robin, "Antibonding σ^* valence MOs in the inner-shell and outer-shell spectra of the fluorobenzenes," J. Phys. Chem. **91**, 531–540 (1987).
145. S. A. Kovalenko, A. L. Dobryakov, and V. Farztdinov, "Detecting Electronic Coherence in Excited-State Electron Transfer in Fluorinated Benzenes," Phys. Rev. Lett. **96**, 068301 (2006).
146. H. Studzinski, S. Zhang, Y. Wang, and F. Temps, "Ultrafast nonradiative dynamics in electronically excited hexafluorobenzene by femtosecond time-resolved mass spectrometry," J. Chem. Phys. **128**, 164314 (2008).
147. M. Z. Zgierski, T. Fujiwara, and E. C. Lim, "Photophysics of aromatic molecules with low-lying $\pi\sigma^*$ states: Fluorinated benzenes," J. Chem. Phys. **122**, 144312–144312–6 (2005).
148. M. Born and R. Oppenheimer, "Zur Quantentheorie der Molekeln," Ann. Phys. **389**, 457–484 (1927).
149. M. Born and K. Huang, *Dynamical Theory of Crystal Lattices* (Oxford University Press, New York, 1954).
150. C. J. Ballhausen and A. E. Hansen, "Electronic Spectra," Ann. Rev. Phys. Chem. **23**, 15–38 (1972).
151. H. Köppel, W. Domcke, and L. S. Cederbaum, "Multimode Molecular Dynamics Beyond the Born-Oppenheimer Approximation," in *Advances in Chemical Physics*, Vol. 57, edited by I. Prigogine and S. A. Rice (John Wiley & Sons, Inc., 1984) pp. 59–246.
152. M. Baer, "Adiabatic and diabatic representations for atom-molecule collisions: Treatment of the collinear arrangement," Chem. Phys. Lett. **35**, 112–118 (1975).
153. V. Sidis, "Diabatic Potential Energy Surfaces For Charge-Transfer Processes," in *Advances in Chemical Physics*, Vol. 82, edited by M. Baer and C.-Y. Ng (John Wiley & Sons, Inc., 1992).

154. T. Pacher, L. S. Cederbaum, and H. Köppel, "Adiabatic and Quasidiabatic States in a Gauge Theoretical Framework," in *Advances in Chemical Physics*, Vol. 84, edited by I. Prigogine and Rice, S. A. (John Wiley & Sons, Inc., 1993).
155. F. T. Smith, "Diabatic and Adiabatic Representations for Atomic Collision Problems," Phys. Rev. **179**, 111–123 (1969).
156. R. D. Levine, B. R. Johnson, and R. B. Bernstein, "Role of Potential Curve Crossing in Subexcitation Molecular Collisions: Exact (Two-State) Computations vs Decoupling Approximations for Resonance Positions," J. Chem. Phys. **50**, 1694–1701 (1969).
157. H. C. Longuet-Higgins, "Some Recent Developments in the Theory of Molecular Energy Levels," in *Advances in Spectroscopy*, Vol. II, edited by H. W. Thompson (Interscience Publishers, New York, 1961).
158. T. F. O'Malley, "Slow Heavy-Particle Collision Theory Based on a Quasiadiabatic Representation of the Electronic States of Molecules," Phys. Rev. **162**, 98–104 (1967).
159. H. Nakamura and D. G. Truhlar, "The direct calculation of diabatic states based on configurational uniformity," J. Chem. Phys. **115**, 10353–10372 (2001).
160. C. A. Mead and D. G. Truhlar, "Conditions for the definition of a strictly diabatic electronic basis for molecular systems," J. Chem. Phys. **77**, 6090–6098 (1982).
161. G. A. Worth, H.-D. Meyer, H. Köppel, L. S. Cederbaum, and I. Burghardt, "Using the MCTDH wavepacket propagation method to describe multimode non-adiabatic dynamics," Int. Rev. Phys. Chem. **27**, 569–606 (2008).

2

Femtosecond Time-Resolved Molecular Spectroscopy in a Seeded Molecular Beam

The photophysical molecular processes and photochemical reactions under investigation in this work can only be temporally resolved with an experimental time resolution on the order of femtoseconds. The intramolecular dynamics induce changes in macroscopic, and therefore experimentally accessible, observables on a similar time scale, for example in the absorbance or emittance of the molecules. It is technically unfeasible, however, to monitor these changes by conventional spectroscopic techniques. Commonly employed electronic detection devices such as semiconductor photodiodes intrinsically have a response time orders of magnitude too slow to detect changes in the available observables on the required ultrafast time scale. The laser-spectroscopic pump and probe technique in combination with femtosecond laser pulses isolates a slice of the temporal information from the molecular response optically, before the electronic detection takes place. By selecting slices at gradually incrementing positions in time, the observable can be temporally resolved.

In a femtosecond pump and probe experiment, an ultrashort pump laser pulse excites the molecule to a non-stationary superposition of vibronic eigenstates, which will consequently evolve in time. The probe laser pulse subsequently interacts with the molecule after a well-defined time delay. This interaction ends the temporal evolution and results in a time-independent macroscopic response, which only depends on the quantum state of the molecule in the moment of interaction. The state of the system as a function of the time delay between the pump and the probe pulses can thus be recorded with conventional, slow detectors. More elaborate femtosecond time-resolved spectroscopic methods employ more than two laser pulses, such as pump–repump–probe schemes[1–3] and the wide field of coherent two-dimensional nonlinear spectroscopy.[4–6] Different types of transient spectroscopies are distinguished by the observable chosen to monitor the molecular response. Common methods include transient absorption and fluorescence spectroscopy, time-resolved mass spectrometry, and photoelectron or photofragment imaging spectroscopy.

In the present work, femtosecond time-resolved mass spectrometry and photoelectron imaging spectroscopy have been performed on jet-cooled molecules in a seeded molecular beam. In these methods, the interaction of the molecule with the probe pulse leads to an ionization of the molecule and the superposition of states created by the pump pulse is projected onto the ionization continua of cationic and photoelectron states. The photoelectron imaging method measures the kinetic energies and angular distributions of the ejected photoelectrons and is thus a frequency-dispersed technique. The mass spectrometry method measures the yield of the complementary cationic fragments, making it a frequency-integrated, but mass-dispersed technique. The evaluation and interpretation of the resulting photoelectron kinetic energy spectra is only possible when the photon energy that is deposited in a molecule is conserved, i. e. the molecule must not transfer energy to its environment. A molecular beam in vacuum is a practical realization of this idealized environment, as it provides a directed and spatially confined flux of molecules under effectively collision-free conditions.[7] Furthermore, during the adiabatic expansion into the vacuum, the molecules are cooled to rotational and vibrational temperatures close to absolute zero. They are therefore assumed to be in their ground state,[8,9] which simplifies the resulting photoelectron spectra. In the following Section 2.1, the quantum-mechanical description of the molecular eigenstates is briefly reiterated and applied to the excitation and ionization processes in the pump and probe spectroscopic experiment. Beginning with the molecular wavefunctions, the constitution of the measured photoion and photoelectron signals is explained, and which information can be gained from them. The experimental realization of the applied spectroscopic techniques follows in Section 2.2 thereafter.

2.1 Physical Background

For any given molecule, the molecular Hamiltonian for nuclei and electrons reads

$$\hat{H} = \hat{T}_n + \hat{T}_e + \hat{V} \tag{2.1}$$

with the kinetic energy operators for the nuclei and electrons $\hat{T}_n$ and $\hat{T}_e$, and the potential energy operator $\hat{V}$ for both nuclei and electrons.[10] To keep the quantum mechanical picture simple, the validity of the Born–Oppenheimer approximation[11] is assumed in the following derivations. It allows for a simplification of the molecular Schrödinger equation by separation of nuclear and electronic motion as a consequence of the large difference in their masses. A product ansatz for the total molecular wavefunction $|\psi\rangle$ in the adiabatic approximation can be made by

$$|\psi\rangle = \left|\psi_n^{(\alpha)}\right\rangle \left|\psi_e^{(\alpha)}\right\rangle, \tag{2.2}$$

where α is the (excited) electronic state, and $|\psi_n^{(\alpha)}\rangle$ and $|\psi_e^{(\alpha)}\rangle$ are the nuclear and electronic wavefunctions, respectively.

Under the clamped nuclei approximation, $|\psi_e^{(\alpha)}\rangle$ fulfills the electronic Schrödinger equation

$$\left(\hat{T}_e + \hat{V}\right) \left|\psi_e^{(\alpha)}\right\rangle = V_e^{(\alpha)} \left|\psi_e^{(\alpha)}\right\rangle , \tag{2.3}$$

thus providing the potential energy eigenvalue $V_e^{(\alpha)}$ of the electronic state α. Each $V_e^{(\alpha)}$ represents a s-dimensional hypersurface (with $s = 3N - 6$ being the number of internal nuclear degrees of freedom of a polyatomic molecule with N atoms) of the potential electronic energy, which defines the movement of the nuclei. It is thus a central concept for the understanding of molecular dynamics from a mechanistic point of view. The nuclear wavefunctions, and therefore the motion of the nuclei on the s-dimensional potential energy surface $V_e^{(\alpha)}$, are then given by the Born–Oppenheimer equation

$$\left(\hat{T}_n + V_e^{(\alpha)}\right) \left|\psi_n^{(\alpha)}\right\rangle = E \left|\psi_n^{(\alpha)}\right\rangle . \tag{2.4}$$

The Born–Oppenheimer approximation does not hold true in all cases. Sometimes electronic and nuclear motion are strongly coupled and show a pronounced influence on the molecular dynamics, as will be seen in the following chapters of this work. This is true in particular in the region near intersections between different potential energy surfaces. It nevertheless provides an instructive starting point for the general understanding of photoelectron spectra. For this purpose, we next determine the ionization probability in terms of the transition strength from an electronic state α into the ionization continuum.

2.1.1 Derivation of the Photoionization Transition Strength

The nuclear wavefunction $|\psi_n\rangle$, as defined in Eq. 2.2, is further factorized and only the vibrational part $|\psi_v\rangle$ is considered. It is not neccessary to include a rotational part of the wavefunction in this treatise, because it is usually not even possible to resolve most vibrational transitions in the recorded photoelectron spectra due to the broad spectral width of femtosecond laser pulses, let alone rotational transitions. The total molecular wavefunction $|\psi\rangle$ for a single electronic state is then written as the vibronic product wavefunction

$$|\psi\rangle = |\psi_e\rangle \, |\psi_v\rangle , \tag{2.5}$$

omitting the index α in the following. The probability for a photoionization transition depends on the vibronic wavefunctions of the initial and final state and can be given similar to a bound–bound transition, but with a continuum electronic wavefunction

replacing the bound final state. For optical electric dipole transitions between different electronic states, only the electronic part $\hat{\boldsymbol{\mu}}^e$ of the electric dipole operator $\hat{\boldsymbol{\mu}}$ needs to be considered, while the nuclear part $\hat{\boldsymbol{\mu}}^n$ does not contribute.[12] The transition strength S^{ev} generally reads

$$S^{\mathrm{ev}} = \left|\langle\psi'_v|\,\langle\psi'_e|\,\hat{\boldsymbol{\mu}}^{\boldsymbol{e}}\,|\psi''_e\rangle\,|\psi''_v\rangle\right|^2 = \left|\langle\psi'_v|\,D_{\mathrm{e}',\mathrm{e}''}\,|\psi''_v\rangle\right|^2, \tag{2.6}$$

with the matrix element of the electronic transition dipole moment

$$D_{\mathrm{e}',\mathrm{e}''} = \langle\psi'_e|\,\hat{\boldsymbol{\mu}}^{\boldsymbol{e}}\,|\psi''_e\rangle\,. \tag{2.7}$$

The wavefunction of the final electronic state is written as the product

$$|\psi'_e\rangle = |\phi_k\rangle\;|\psi^+_{e,k}\rangle \tag{2.8}$$

of the electronic wavefunction $|\psi^+_{e,k}\rangle$ of the cation and the wavefunction $|\phi_k\rangle$ of the photoelectron with linear momentum k.[13] The angular momentum of the photoelectron is expressed as a partial wave expansion in the quantum number l

$$|\phi_k\rangle = \sum_{l,m_l} c_l\; R_l(r)\; Y_{lm_l}(\theta,\phi), \tag{2.9}$$

where $R_l(r)$ denotes the radial part and $Y_{lm_l}(\theta,\phi)$ are the spherical harmonics.[14]

In the evaluation of Eq. 2.6 it is usually argued that the electronic transition moment is independent of the atomic coordinates and hence can be factored out of the integral, resulting in the well-known Condon approximation

$$S^{\mathrm{ev}} = \left|D_{\mathrm{e}',\mathrm{e}''}\right|^2\,\left|\langle\psi'_v|\psi''_v\rangle\right|^2 = \left|D_{\mathrm{e}',\mathrm{e}''}\right|^2\,\prod_j\,\left|\left\langle\psi''_{\nu_j}(Q_j)\middle|\psi''_{\nu_j}(Q_j)\right\rangle\right|^2, \tag{2.10}$$

where the squared vibrational overlap integral is called the Franck–Condon factor for the vibrational normal mode j.[12] This expression determines the structure of the photoelectron kinetic energy spectrum as follows:

- The factor $\left|D_{\mathrm{e}',\mathrm{e}''}\right|^2$ determines the electronic transition strength and can be evaluated in terms of molecular symmetry arguments. In order for the ionization transition to be allowed, i. e. $\left|D_{\mathrm{e}',\mathrm{e}''}\right|^2 > 0$,

  $$\Gamma_{\psi''_e} \otimes \Gamma_{\mu^e} \otimes \Gamma_{\psi^+_e} \otimes \Gamma_{\phi_k} \supseteq \Gamma_{\mathrm{TS}} \tag{2.11}$$

  must hold. The vibronic symmetry of the neutral state, the ionic state and the ejected photoelectron is denoted by their respective irreducable representation Γ. The product of all representations must contain the totally symmetric irreducable representation Γ_{TS} of the respective molecular symmetry group.[15]

Formally, ionization is always allowed, because the symmetry species of the photoelectron Γ_{ϕ_k} is not subject to any restrictions and can freely adapt to the species of the other factors. The symmetry of the photoelectron wavefunction determines the composition of the partial wave expansion in Eq. 2.9, that can be measured with the photoelectron imaging method as will be discussed in the Sections 2.1.3 and 2.1.4.

- The Franck–Condon factor determines the shape of the resulting spectral band. When the nuclear equilibrium structure in both states is very similar, there will be a maximal overlap of vibrational wavefunctions of the same vibrational quantum number. Therefore, transitions without a change of that quantum number are favored, and the resulting spectral band will be rather narrow. In the case of very different equilibrium structures in the neutral and cationic state, the Franck–Condon factor will be large for a range of different vibrational quantum numbers, resulting in a broad spectral band. Therefore, from the spectroscopists point of view, the shape of the spectral photoelectron bands allows one to draw conclusions on the nuclear equilibrium structures of the involved electronic states.

The separation of the integrals in Eq. 2.10 (the Condon approximation) will not be valid if the electronic transition dipole matrix element depends strongly on the nuclear coordinates. Such a dependence may be created by vibronic coupling effects, which change the electronic character of the initial (or final) state with nuclear motion. Such a behavior was observed in the first excited electronic state of the pentafluorobenzene molecule (see Chapter 5), where the influence of the nuclear coordinates on $D_{\mathrm{e}',\mathrm{e}''}$ during a molecular vibration periodically modulated the ionization transition strength S^{ev}. Well-known mechanisms of vibronic coupling are, for example, the Renner-Teller effect,[16] the Jahn–Teller effect[17] and the pseudo-Jahn–Teller effect.[18]

So far, only stationary eigenstates of the molecular Hamiltonian have been considered. Because of its broad spectral width, the femtosecond pump pulse does not prepare a single stationary vibronic state, but a superposition of vibrational eigenstates

$$|\psi(t)\rangle = \sum_i c_i(t)\, e^{-i\omega_i t} \left|\psi''_{\nu_i}\right\rangle \tag{2.12}$$

in the excited electronic state, called a vibrational wavepacket. Due to the individual phase factors of the different vibrational eigenstates, the wavepacket does not form a stationary state, but consequently evolves in time. Moreover, the electronic wavefunction can be superposition of several electronic states as well, adding additional complexity to the temporal evolution of the molecular system. In comparison to

Eq. 2.2, the total molecular wavefunction now is a function of time $|\psi\rangle \equiv |\psi(t)\rangle$, and its temporal evolution is determined by the time-dependent Schrödinger equation

$$i\frac{\partial}{\partial t}\,|\psi(t)\rangle = \hat{H}(t)\,|\psi(t)\rangle\,. \tag{2.13}$$

The introduction of this time dependence leads to various transient intramolecular photophysical phenomena taking place on an often ultrafast time scale. Commonly distinguished phenomena are, for example, electronic population transfer processes between excited electronic states *via* internal conversion or intersystem crossing, or nuclear dynamics such as vibrational energy redistribution and bond dissociation reactions. The experimental methods applied in this work allow us to monitor those processes in form of the temporal evolution of the wavefunction $|\psi(t)\rangle$.

2.1.2 Probing Intramolecular Dynamics through Photoionization

The time dependence of the wavefunction $|\psi(t)\rangle$ influences the electronic transition moment $D_{\mathrm{e}',\mathrm{e}''}$ and the Franck–Condon factors, so that the ionization transition strength consequently becomes a function of time $S^{\mathrm{ev}} \equiv S^{\mathrm{ev}}(t)$ as well. The corresponding macroscopic, experimentally detectable observable is the photoionization cross section $\sigma(t) \propto S^{\mathrm{ev}}(t)$. For an isotropic gas and a non-degenerate initial state, the conversion between both quantities reads

$$\sigma(t) = \frac{4\pi^2\nu}{3c\epsilon_0 h}\; S^{\mathrm{ev}}(t), \tag{2.14}$$

with the energy difference $E = h\nu$ between initial and final state.[19] This expression defines the transient ion yield measured in the time-resolved mass spectrometry experiment, and the equivalent frequency-integrated total photoelectron yield in the photoelectron imaging experiment.

For an interpretation of the frequency-dispersed photoelectron spectra, the actual initial and final electronic states have to be known, which might pose a challenging premise. On the one hand, the initial electronic state can usually be well characterized by the common variety of static absorption and emission (laser) spectroscopic techniques, and a wavepacket on its potential energy hypersurface can be selectively excited by the pump laser pulse. Information on the possible cationic final states, on the other hand, is much less frequently found in the literature and often limited to the first ionization energy. The interpretation of the photoelectron spectra is nonetheless often facilitated by the evaluation of the energy balance of the photoionization process. In order for photoionization to take place at all, the total photonic energy supplied by the pump and probe laser pulses has to exceed the lowest adi-

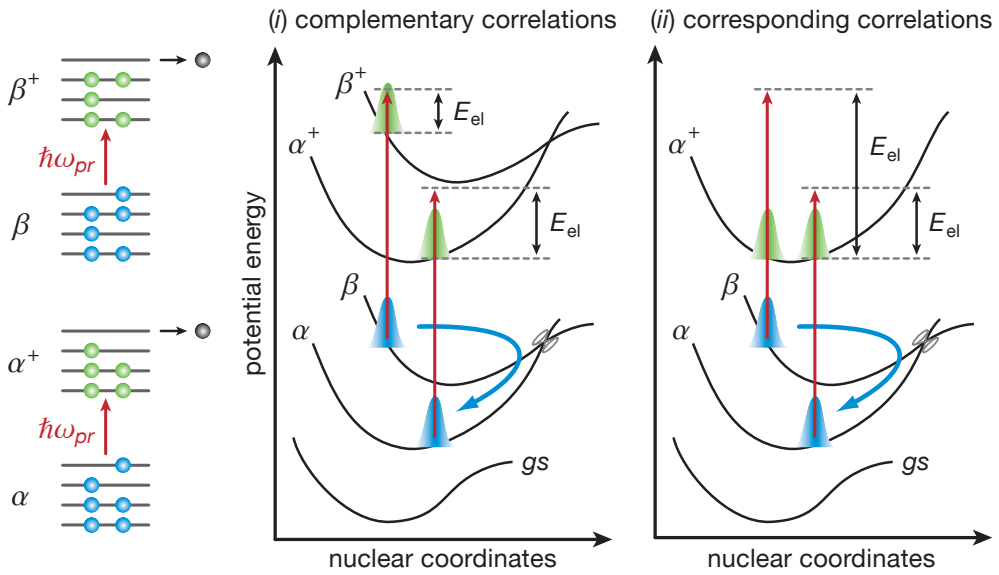

Figure 2.1. The excited electronic states α and β are distinguished by their their electronic configuration, as shown on the left. They can be ionized (*i*) into the different cationic states α^+ and β^+ (complementary ionization correlations), or (*ii*) into the same cationic state α^+ (corresponding ionization correlations). A transfer of the excited wavepacket from one state to another is often accompanied by a spectral shift of the resulting photoelectron band as indicated.

abatic ionization energy (IE_1) of the molecule. The energy balance of a $(n + m')$ photoionization process with n pump and m probe photons can be expressed as

$$E_{\mathrm{el}} = \hbar\,(n \times \omega_{\mathrm{pump}} + m \times \omega_{\mathrm{probe}}) - IE_1 - E^+_{\mathrm{int}}, \tag{2.15}$$

where E_{el} is the photoelectron kinetic energy and E^+_{int} the internal energy remaining in the cation. If a different cationic state is accessed, its ionization energy IE_i has to be substituted for IE_1. The maximum available kinetic energy E_{avl} that a photoelectron can have when no internal energy is left remaining in the cation is then given by

$$E_{\mathrm{avl}} \equiv E_{\mathrm{el}} \quad \text{for} \quad E^+_{\mathrm{int}} = 0, \tag{2.16}$$

which defines an upper energetic bound in the photoelectron spectra for given numbers of pump and probe photons. If spectral bands above this bound are observed, possibly unwanted processes involving more photons have to be considered.

The distribution of the internal energy E^+_{int} to (*i*) nuclear (vibrational) degrees of freedom of the cation is determined by the corresponding Franck–Condon factors between the initial and final electronic states, as was discussed in the previous section; and to (*ii*) electronic degrees of freedom of the cation is determined by the matrix elements of the electronic transition dipole moment $D_{\mathrm{e}',\mathrm{e}''}$ for the different cationic final states. These matrix elements are often discussed in terms of Koopmans' picture.[20] Originally, Koopmans' theorem states that the ionization energy of a molecule is equal to the relative energy of the highest occupied molecular orbital.[20]

This has often been rephrased in a way that the ionization of an electron happens without a simultaneous reorganization of the electronic core. Although just a (rather crude) approximation,[21] the theorem creates a connection between the neutral and ionic electronic states that allows for an interpretation of the photoelectron spectra even with little knowledge about the electronic structure of the molecular cation.

In Koopmans' picture, two distinct cases are distinguished: (*i*) complementary[22] (type I) and (*ii*) corresponding[23] (type II) ionization correlations. Both cases are illustrated in Figure 2.1. In the case of complementary correlations, different neutral excited states are favorably ionized into different cationic states. Pairs of electronic states state that correlate with each other have a large magnitude of the electronic transition dipole moment, and vice versa. In the case of corresponding ionization correlations, different neutral excited states correlate with the same cationic state. In both cases, transient electronic population dynamics can be monitored in the resulting photoelectron spectra. When a vibrational wavepacket $|\psi'_e(t)\rangle$ in an excited neutral state α is transferred to another electronic state β as indicated in Figure 2.1, the cationic vibronic state into which ionization occurs will change as well. The population transfer is reflected by a decrease in spectral intensity of photoelectron bands from state α, and the appearance of new bands of different spectral position and intensity from state β. While the spectral bands are often well separated in the case of complementary ionization correlations, this might not neccessarily be true in the case of corresponding correlations. Depending on the respective Franck–Condon factors involved, the bands may overlap strongly and the occuring dynamics are not easily discerned by the energy spectrum alone. If the neutral excited electronic states belong to different symmetry species, the analysis of the photoelectron angular distribution can provide complementary information on the molecular dynamics, as will be discussed in the next section.

2.1.3 The Photoelectron Angular Distribution

The angular part of the wavefunction of the ejected photoelectron is given by the partial wave expansion from Eq. 2.9. Inserting into the equations for the ionization transition strength S^{ev} (Eq. 2.6) and the photoionization cross section σ (Eq. 2.14) readily results in an expression for the differential ionization cross section σ_Ω for the ejection of an electron into the element of solid angle $\mathrm{d}\Omega$. In a general form for a $(n + m')$ photonionization of an unaligned sample, the resulting expression reads

$$\sigma_\Omega(t) = \frac{\sigma(t)}{4\pi} \sum_{L=0}^{N} \sum_{M} \beta_{LM}(t)\, Y_{LM}(\theta, \phi), \tag{2.17}$$

where L must be even,[13] and $N \leq 2n + 2m$ because the angular momentum of each photon can add anisotropy to the distribution.[24] The expansion coefficients have been renamed to β_{LM} to meet the usual conventions of the common literature on this topic,[25–27] and contain the temporal evolution of the system's angular momentum. In the common case of linearly polarization of the laser pulses, where the polarizations of pump and probe beams are parallel with each other, a unique axis of symmetry is introduced (usually the z axis is chosen) and the angular distribution has axial symmetry in respect to that axis. In spherical coordinates, θ is then the angle between the laser polarization and the direction of the ejected electron, and $\phi = 0$ due to the axial symmetry. This translates to $M = 0$ in Eq. 2.17, which becomes

$$\sigma_\Omega(t) = \frac{\sigma(t)}{4\pi} \sum_{L=0}^{N} \beta_{L0}(t)\ Y_{L0}(\theta, \phi). \tag{2.18}$$

This equation can be further simplified by replacing the spherical harmonics with the corresponding Legendre polynomials reading

$$P_L(\cos\theta) = \sqrt{4\pi/(2L+1)}\ Y_{L0}(\theta, \phi). \tag{2.19}$$

Finally, the time-dependent photoelectron angular distribution for a multi-photon ionization process using linear polarizations

$$\sigma_\Omega(t) = \frac{\sigma(t)}{4\pi} \left(1 + \sum_{L=2}^{N} \beta_L(t)\ P_L(\cos\theta)\right) \tag{2.20}$$

in a general form is received. The expansion coefficients β_L are usually denoted as the anisotropy parameters of L-th order. In particular, the second-order parameter β_2 takes the limiting values $+2$ for a $\cos^2(\theta)$ distribution and -1 for a $\sin^2(\theta)$ distribution.[28] For $\beta_2 = 0$, the angular distribution is isotropic. Bounds for higher-order anisotropy parameters are not easily derived.

Two different types of phenomena are known to be mirrored by the time-resolved photoelectron angular distribution:[25]

1. *The symmetry species of the emitting electronic state.*
   For the transition dipole matrix element of the emitting state and the cationic state to be non-zero, their respective symmetry representations have to fulfill Eq. 2.11. When the electronic symmetry $\Gamma_{\psi_e''}$ of the excited states changes, the symmetry species of the final cationic state $\Gamma_{\psi_e^+}$ and/or of the emitted photoelectron Γ_{ϕ_k} have to change accordingly in order that photoionization remains allowed. In the case of corresponding ionization correlations, the final state is the same for the neutral excited states, and the cationic state symmetry $\Gamma_{\psi_e^+}$ does not change. Consequently, the symmetry Γ_{ϕ_k} of the photoelectron

and therefore the composition of the partial wave expansion in Eq. 2.9 have to change. Transitions between electronic states thus affect the temporal evolution of the photoelectron angular distribution.

2. *The alignment of the moleculer axis with respect to the laser polarization.* During the interaction with the pump laser pulse, only those ground state molecules with a non-zero projection of the transition dipole moment vector on the electric field vector of the laser pulse are photoexcited.[28] The interaction induces an alignment of the transition dipole moment, hence spatially aligning the molecules. After a one-photon excitation with linearly polarized light, the molecular axis alignment is completely described by second-order anisotropy in terms of β_2.[28] As the pump laser pulse creates a non-stationary superposition of rotational eigenstates, the molecular axis distribution of the sample molecules evolves in time. Upon photoionization, this temporal evolution is mirrored in the photoelectron angular distribution by the time-dependent anisotropy parameters.

These electronic and rotational dynamics take place simultaneously, but can often be distinguished by the time scales on which they occur. While electronic transitions between states of the same multiplicity happen within tens or hundreds of femtoseconds, molecular alignment effects manifest themselves within rotational periods on the order of picoseconds. In this Thesis, an example of the time-resolved observation of electronic dynamics through the time-dependent photoelectron angular distribution is observed in the pentafluorobenzene molecule (Chapter 5). The electronic character of the excited state changes from $\pi\pi^*$ to $\pi\sigma^*$, with β_2 changing accordingly on a time scale of about 200 fs. A classical example of rotational wavepacket dynamics is pyrazine, where such effects were observed with femtosecond temporal resolution for the first time.[29] Coherent revivals of the photoelectron yield and the anisotropy parameters after characteristic times of $1/2X$ (where X is one of the rotational constants A, B, C) clearly showed the rotational origin of the phenomenon.

The limiting values of $\beta_2 = +2$ or -1 can only be observed in photoelectron angular distributions from the one-photon ionization of atoms under very specific requirements to the angular momenta of the initial and final states.[30–32] These values are very likely to be not observed in distributions following (multi-photon) ionization of a polyatomic molecule with femtosecond laser pulses. In molecular systems, the electronic angular momentum l is no longer a good quantum number and the initial excited state cannot be expressed in terms of a single value of l. Furthermore, the centro-symmetry of the Coulombic potential as a prerequisite for the validity of the partial wave expansion is only met approximately at a larger distance (the "far field") to the molecular ion core. A photoelectron partial wave that is generated

with a given value of l can be scattered by the anisotropy of the molecular potential in the "near field", thus changing its l value.[26] The recovery of the original partial wave composition is not readily possible, because the phase shifts between the individual partial waves are lost in the measurement process. The pre-alignment of the molecular axis by the pump pulse and the temporal evolution of the excited rovibronic wavepacket further complicate the situation, and make the interpretation of absolute β_2 values very challenging.[33]

2.1.4 Photoelectron Imaging Spectroscopy

The general idea of the photoelectron imaging spectrometer is that photoelectrons produced at the same time in the same place with a given kinetic energy $E_{\mathrm{kin}}(k) = (\hbar\mathbf{k})^2/2m$ are later found on the surface of a sphere with radius r_k, expanding with time according to

$$r_k(t) = \sqrt{2E_{\mathrm{kin}}(k)/m_e}\, t. \tag{2.21}$$

This three-dimensional distribution of charged particles, often called Newton sphere, is projected onto a two-dimensional position-sensitive detector by a suitable configuration of accelerating electric fields. The photoelectron kinetic energy distribution is determined by the spectral width and shape of the laser pulses. For an $(n + m')$ ionization process, the spectral width $\Delta\omega$ is given by

$$\Delta\omega^2 = \sum_n \Delta\omega^2_{\mathrm{pump}} + \sum_m \Delta\omega^2_{\mathrm{probe}}, \tag{2.22}$$

while the shape is determined by the spectral pulse shape, which is usually assumed to be Gaussian. Multiplication with the differential ionization cross section $\sigma_\Omega(\Delta t)$ (where Δt denotes the delay time between pump and probe pulses) and summation over all possible k values, evaluated at the time of detection t', gives the three-dimensional intensity distribution

$$I(x, y, z) = \sum_k \sigma_\Omega(\Delta t) \times G(r, r_k(t), \sigma_{\Delta\omega}) \Big|_{t=t'}, \tag{2.23}$$

where $G(r, r_k(t), \sigma_{\Delta\omega})$ denotes a Gaussian distribution centered at $r_k(t)$ with standard deviance $\sigma_{\Delta\omega}$. The two-dimensional projection of $I(x, y, z)$ along the direction of the accelerating electric fields (here the y axis was chosen) is the measured quantity in the photoelectron imaging experiment. Because of the unique axis of cylindrical symmetry along the z axis (*vide supra*), the original and the projected distributions are connected through the Abel transform

$$P(x, z) = \int_{-\infty}^{\infty} I(x, y, z)\, \mathrm{d}y = 2\int_x^{\infty} \frac{r\, I(r, z)}{\sqrt{r^2 - x^2}}\, \mathrm{d}r \tag{2.24}$$

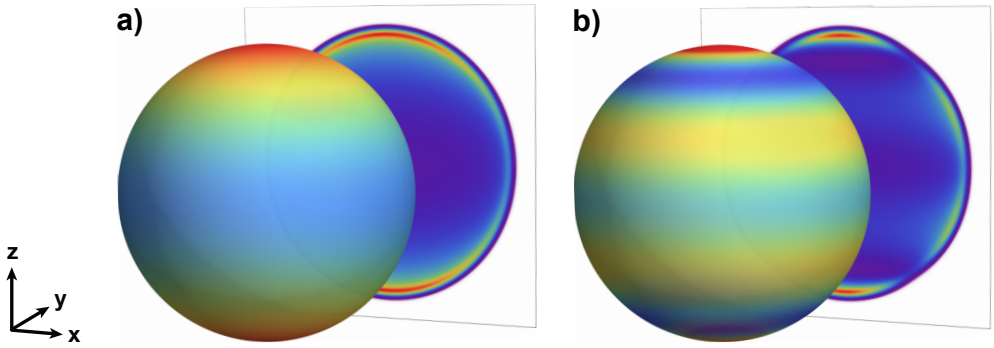

Figure 2.2. Two examples of Newton spheres with different angular distributions projected onto their surface, and the resulting two-dimensional projection onto the detector surface. a) PAD with $\beta_2 = 1$ and $\beta_4 = \beta_6 = 0$. b) PAD with $\beta_2 = 0$, $\beta_4 = 0.5$ and $\beta_6 = 1.5$. The coordinate system is indicated on the left.

where the second integral is transformed to cylindrical coordinates according to the symmetry of the problem.[34] Two exemplary photoelectron distributions $I(x, y, z)$ and their corresponding projection $P(x, z)$ have been visualized in Figure 2.2. The angular distribution is color-coded onto the surface of a unit Newton sphere, illustrating their axial symmetry along the z axis. In the experimental reality, usually several spheres of different radii and intensities are superimposed according to the vibronic structure of the emitting molecule. The photoelectron imaging method is able to simultaneously capture the angle-resolved partial ionization cross section over 4π full solid angle, making it stand out from other angle-resolved methods, where usually an energy analyzer is mechanically scanned around the photoelectron source, leading to long measurement times and only 2π resolved solid angle.[35] To obtain the information on the photoelectron kinetic energy and angular distribution after the measurement, the initial three-dimensional distribution has to be recovered. A direct application of the inverse Abel transformation

$$I(r, z) = -\frac{1}{\pi} \int_r^\infty \frac{\partial P(x, z)/\partial x}{\sqrt{x^2 - r^2}} \, \mathrm{d}x \tag{2.25}$$

magnifies the overall noise of the image (because the derivate of $P(x, z)$ is taken of data sets containing high noise levels) and introduces artificially amplified artifacts at the lower integration bound (singularity in denominator) termed center-line noise.[28] A number of inversion methods circumventing these problems have been developed, which will be described in Section 2.2.5.

2.2 Experimental Setup

The experiments described in the following Chapters of this Thesis have been carried out using a regeneratively amplified Ti:Sa femtosecond pulsed laser together with a combined time-of-flight mass spectrometer and photoelectron imaging spectrometer.

The generation of the pump and probe laser pulses at selected wavelengths from the laser fundamental output beam is based on several nonlinear optical frequency conversion processes, described in detail in several earler PhD theses written in the group[36–39] and in a number of textbooks.[40–42] The design and setup of the vacuum system containing the spectrometers has been elaborately explained in the thesis of H. Studzinski.[43] Many parts of the optical setup, and most of the data acquisition and processing system have undergone further development during the work on this Thesis. The overall data acquisition rate has been increased fourfold, and the handling of the complete experiment is more automated and therefore less susceptible to human error. The controlling computer programs automatically save the obtained data and complement them with all electronically available experimental parameters to make the performed measurements well documented and the subsequent data processing steps reproducible.

2.2.1 Pump and Probe Laser Pulse Generation

A commercial pulsed laser system (Coherent Libra-HE) was used in this work, emitting Gaussian-shaped laser pulses with a duration of 90 fs full width half maximum (FWHM) and a pulse energy of typically 3.6 mJ, centered at 804 nm wavelength at a repetition rate of 1 kHz. The fundamental laser beam is divided by several beam splitters to allow for the simultaneous execution of multiple experiments. Laser pulses with an energy of 1.8 mJ are used for the generation of the pump and probe pulses required for the mass spectrometry and photoelectron imaging experiments. A schematic overview of the complete optical setup in its current status is depicted in Figure 2.3.

Wavelength-tuneable pulses in the range from $480 \leq \lambda \leq 700$ nm were generated by a (two-stage) non-collinear optical parametric amplifier (NOPA)[44–46] pumped, in double-stage operation, with 300 µJ laser fundamental pulses each, or 600 µJ pulses in single-stage operation. In the NOPA, a strongly chirped white-light continuum seed pulse is generated in a sapphire crystal by supercontinuum generation.[47] It is temporally and spatially overlapped in a β-bariumborate (BBO) crystal with the pump pulse of 402 nm wavelength, provided by the frequency-doubled laser fundamental. By choosing different delay times between both pulses, only a certain part of the white light spectrum is selectively amplified. The obtained NOPA pulses had typical energies of 2 – 8 µJ (300 µJ pump pulse energy) or 5 – 25 µJ (600 µJ pump pulse energy), depending on their wavelength, and a duration of ∼200 femtoseconds. A second NOPA amplification stage was set up during this work and could be used as neccessary. The second stage was pumped with the remaining 300 µJ from the laser fundamental, resulting in final pulse energies of 10 – 20 microjoules. The second NOPA stage was mostly used in the very red wavelength range > 600

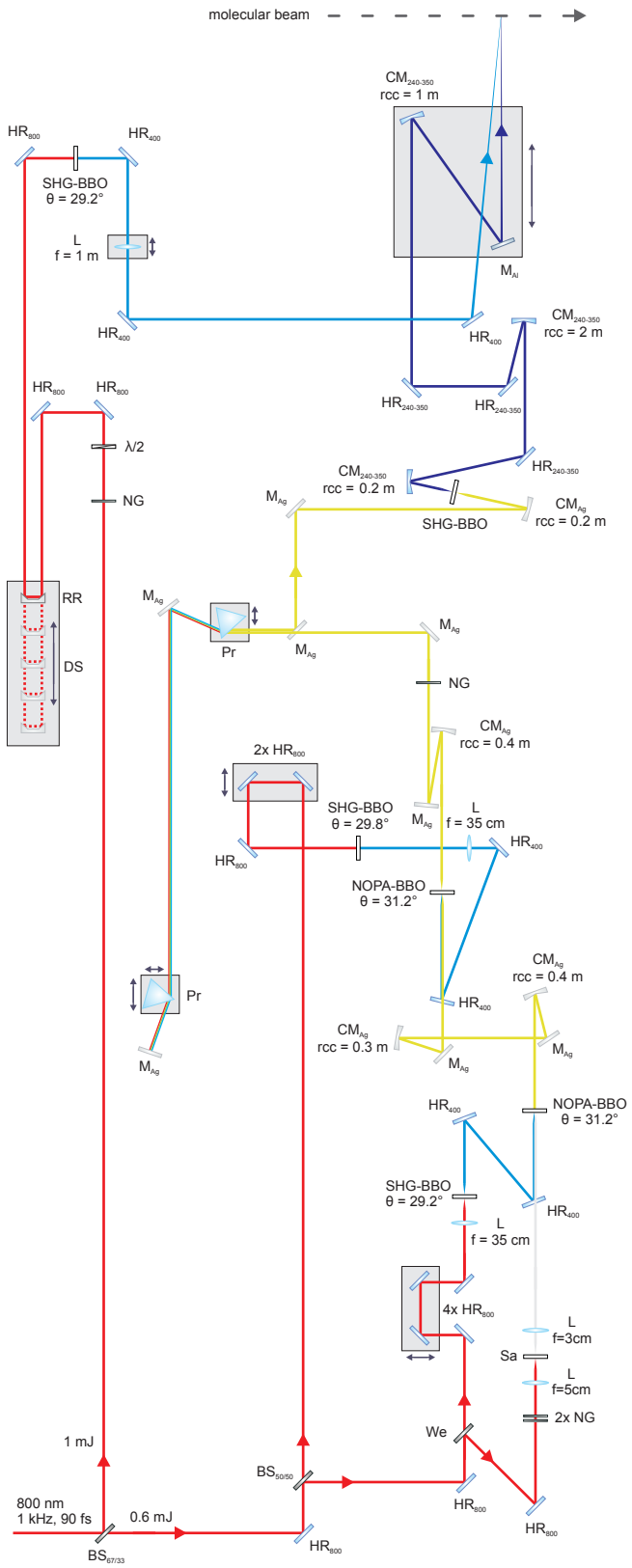

HR_{800}	high-reflective mirror, 800 nm
HR_{400}	high-reflective mirror, 400 nm
$HR_{240–350}$	high-reflective mirror, 240 – 350 nm
M_{Ag}	planar mirror, Ag-coated
M_{Al}	planar mirror, Al-coated
CM_{Ag}	concave mirror, Ag-coated
$CM_{240–350}$	concave mirror, HR-coated
$BS_{67/33}$	beamsplitter, R=67%
$BS_{50/50}$	beamsplitter, R=50%
We	wedge
NG	neutral density gradient filter
L	lens
Sa	sapphire plate
SHG	second harmonic generation
BBO	β-BaB_2O_4 crystal
Pr	fused silica prism
DS	delay stage
RR	retroreflector, Ag-coated
$\lambda/2$	half-wave plate

Figure 2.3. Scheme of the optical setup of the pump- and probe-pulse generation for the femtosecond time-of-flight mass spectrometry and photoelectron imaging experiment. The colors of the beams are chosen for illustration and do not necessarily reflect the real wavelengths.

nm, where the pulse energy achieved with a single stage was not sufficient for the subsequent compression and frequency-doubling steps. The NOPA pulses were compressed to typically 20 – 30 fs FWHM with a prism compressor, and subsequently frequency-doubled in a suitable BBO crystal yielding the final pump pulses in the $240 \leq \lambda \leq 350$ nm wavelength range with pulse energies of 0.5 – 1 microjoules. The polarization of the pump pulses already had the correct orientation from the non-linear optical processes and was always verified to be purely vertical, i. e. parallel to the photoelectron imaging detector surface. The pump pulses were focused into the vacuum chamber with a curved mirror of 50 cm focal length.

The laser fundamental pulses at 804 nm were used as probe pulses in most of the time-of-flight mass spectrometry measurements presented in this work (unless noted otherwise in the corresponding chapter). As the fundamental beam polarization is oriented horizontally, it was rotated using a $\lambda/2$ wave plate. For the laser pulses used as probe in photoelectron imaging measurements, the fundamental beam was frequency-doubled in a BBO crystal, resulting in pulses centered at 402 nm with the required vertical polarization. The probe pulses were focused into the vacuum chamber with a lens of 100 cm nominal focal length. The probe pulse could be delayed or advanced with respect to the pump pulse using a computer-controlled linear translation stage (Physik Instrumente M-521.DG) covering a delay time of up to 1.38 ns.

2.2.2 Time-of-Flight and Photoelectron Imaging Spectrometer Setup

The home-built linear time-of-flight mass spectrometer and photoelectron imaging apparatus consists of two differentially pumped, electropolished stainless steel high vacuum chambers used for the ultrasonic expansion of the sample and the generation and detection of ions and electrons. The expansion and ion source parts of the setup are depicted in Figure 2.4. Under operating conditions, the turbomolecular pumps evacuated the chambers to typical pressures of 1×10^{-5} mbar in the entrance and 3×10^{-7} mbar in the detection compartment. The liquid samples to be investigated were kept in a glass reservoir outside the vacuum tank. A gas mixture was prepared by flowing Helium carrier gas at 2 bar pressure over the liquid. The resulting seeded gas was expanded into the vacuum chamber through a solenoid-actuated pulsed valve (Parker General Valve series 9, 0.5 mm orifice diameter) operated at 100 Hz repetition rate with 65 µs opening time, driven by a home-built power supply. If the vapor pressure of the sample was found to be too low for a sufficient seeding of the carrier gas (as for the cyclohexanone molecule, Chapter 4), the reservoir and all further parts in contact with the gas mixture, including the pulsed valve, could be heated up to 130°C. The orifice of the valve in its closed state is sealed from the vacuum by a gasket in the shape of a pointed

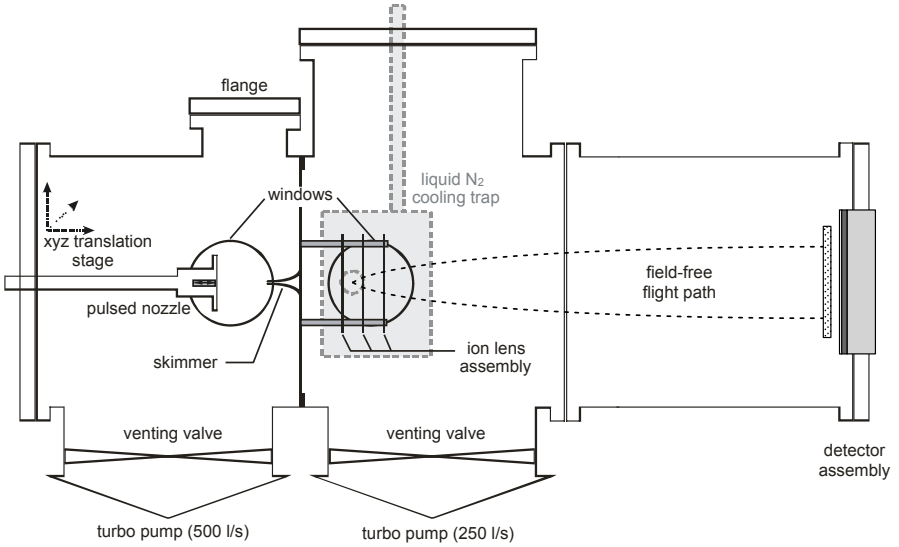

Figure 2.4. Illustration of the vacuum chamber from the time-of-flight mass spectrometry and photoelectron imaging experimental setup. In the left chamber (entrance compartment), the pulsed nozzle is mounted on an adjustable (x, y, z)-translation stage. The molecular beam formed by the skimmer passes through the ion lens assembly (detection compartment), where the molecules are excited and ionized by the laser pulses and accelerated by electric fields. After traversing the field-free flight zone, the charged particles impact onto the detector assembly. Modified graphic, original adapted from H. Studzinski.[43]

cylinder called poppet. While a poppet made from Teflon is supplied with the valve, in this work a poppet made from a polyimide-based plastic (DuPont Vespel) was used. Vespel posseses a very high mechanical and chemical resistance that is also retained at high temperatures, and produces very low outgassing under vacuum. The Vespel poppet showed a by far superior performance compared to Teflon, with nearly no signs of wear after several weeks of use even at the employed high temperature and repetition rate. During the expansion of the seeded gas through the nozzle orifice, the sample molecules transfer internal energy to the carrier gas molecules by two-body interactions, thereby lowering the energy located in rotational and vibrational degrees of freedom and cooling the molecules.[8,9] A rotational temperature of only a few Kelvin is typically achieved in this process,[48,49] and a vibrational temperature of around 50 K was reported previously for the setup used in this work.[43] A molecular beam was formed by a 0.5 mm orifice diameter conical skimmer (Beam Dynamics Model I), through which the beam entered the ion source in the detection chamber without the introduction of turbulences. The velocity distribution inside the molecular beam is very narrow in the flight direction, and has nearly vanishing components perpendicular to that direction, effectively eliminating collisions between the particles. Thus, an ensemble of effecively ground-state, non-interacting molecules is created.[50]

The ion source is similar to the design introduced by Wiley and McLaren,[51] with the modification of gridless electrodes as proposed by Eppink and Parker.[52] Between the

repeller and extractor plates, the molecular beam is crossed perpendicularly by the laser beams. In the time-of-flight mass spectrometer operation, high positive voltages of 2000 V and 1820 V were applied to the repeller and extractor electrodes. The resulting uniform electrical field extracts the generated cations from the interaction region. The field between the extractor plate and the grounded third plate further accelerates the cations into the field-free flight tube towards the detector assembly. The time of flight of the cations

$$t_{\mathrm{F}} \propto \sqrt{m/z} \tag{2.26}$$

can be shown to depend only on the mass to charge ratio of the particles.[53] The proportionality factor depends on the geometry of the ion source, the location of ion formation, the chosen voltages and the lengths of the field-free flight zone. Under the assumption of only singly charged species, the cations are separated into bunches, reaching the detector with the lightest species first, successively followed by heavier masses. The calibration of the time-of-flight mass spectrometer was performed with substances of known mass that showed no fragmentation upon multi-photon ionization, usually benzene or toluene. In the photoelectron imaging spectrometer operation, a magnetically shielding metal tube (Goodfellow Mumetal) was installed in the field-free flight zone as a protection from stray magnetic fields. The gridless electrode design from Eppink and Parker[52] makes "velocity map imaging" possible, i. e. all particles with the same initial velocity are mapped onto a radially symmetric ring on the detector (cf. Section 2.1.4). High negative voltages of -4000 V and -2990 V were applied to the repeller and extractor plates for that purpose. During all measurements, the ion source assembly was surrounded by a liquid N_2-filled cold trap to lower the pressure in the detector chamber by one order of magnitude and thereby reducing the background ion and photoelectron signal.

2.2.3 Temporally and Spatially Resolved Charged Particle Detection

The charged particles generated in the ion source are detected using a stack of two microchannel plate (MCP) secondary electron multipliers. A microchannel plate is a thin lead glass plate consisting of several million bonded capillaries oriented parallel to each other, treated to be semiconducting.[54] Each channel performs similar to a miniaturized channel electron multiplier,[55] and can be considered as a continuous dynode which acts as its own dynode resistor chain. A metallic coating is deposited on the plates that serves as electrical contact. The MCPs used in this work have a channel diameter of 10 µm and an interchannel spacing of 12 µm, biased at an angle of 8° to the input surface. Upon impact of a single charged particle on the face of the MCP, a cascade of electrons is generated which can be detected after their exit from the other side. Typical electron multiplication factors for a pair of MCPs are on

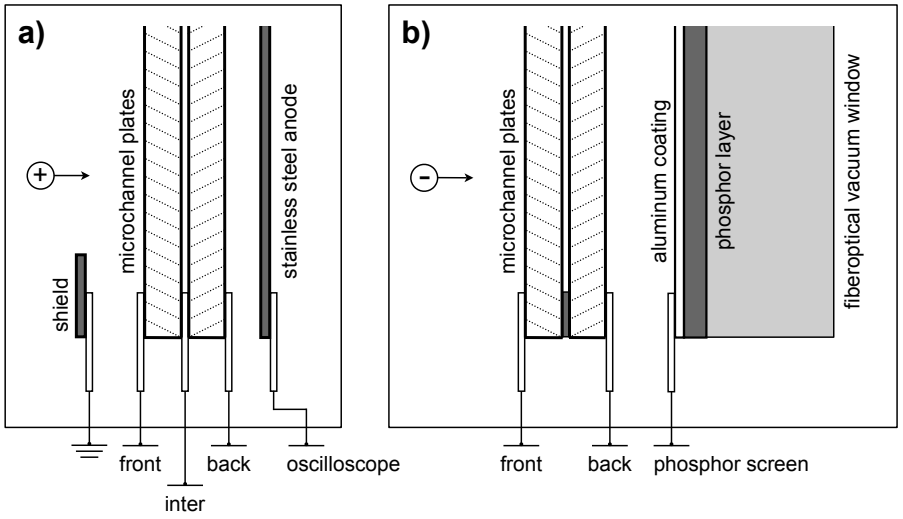

Figure 2.5. Electrical connections of the a) time-of-flight and b) photoelectron imaging microchannel plate detector assemblies. Both detectors consist of an MCP pair in Chevron configuration. The time-of-flight detector has an additional interplate voltage connector, while the photoelectron imaging detector has none. Modified graphic, original adapted from H. Studzinski.[43]

the order of 10^9, coupled with a high detection efficiency of >0.5 and a very high temporal resolution below 100 picoseconds.[54]

Schematic drawings of the detector assemblies for the mass spectrometry and photoelectron imaging measurements are depicted in Figure 2.5 a and b, respectively. The two microchannel plates are mounted in Chevron configuration[56] in the detector assembly, as indicated by the dotted lines. They are oriented so that the channel bias angles provide a large directional change to prohibit ion feedback effects, where positive ions are produced in the high charge density region at the output side by collisions with electrons, drift backwards through the channel and cause undesirable afterpulses. The MCPs of both assemblies are electrically contacted on the front and the back of the stack. A potential difference of typically 1600 – 1700 V is specified by manufactures to be applied between both sides. The time-of-flight detector has an additional electrode between the plates through which an interplate voltage can be applied, by which the efficiency of the electron multiplication process is increased: when an accelerating potential is applied between the plates, there is less time for the charge cloud exiting from the first plate to spread radially. This leads to fewer excited channels in the second plate, but each is driven more efficiently.[54] The required high voltages are generated from a single power supply by a voltage divider. The voltage divider circuits and the specific voltages used for the detector assemblies are discussed below.

For time-of-flight measurements, the detector depicted in Figure 2.5 a is used. As a negative voltage is applied to the front surface of the first MCP, a grounded shielding

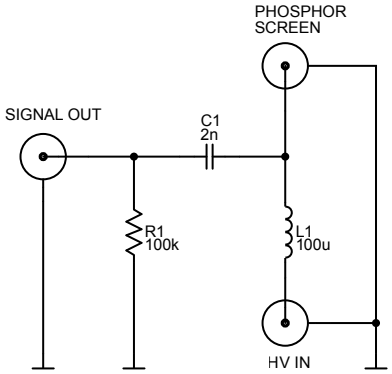

Figure 2.6. Schematic of the high voltage bias tee. The capacitor C1 decouples the high-frequency AC signal from the DC voltage. The inductance L1 prevents it from being strongly damped by the small internal resistance of the high-voltage power supply.

electrode is placed in front of it to maintain a field-free flight path. The MCPs are backed by a steel anode to capture the exiting electron cloud and measure the voltage change induced by the electron current. The photoelectron imaging detector is depicted in Figure 2.5 b. Here, the MCPs are backed by a fiber-optical vacuum window coated with a P43 phosphorescence layer and thin aluminum layer on top. A high positive voltage is applied to the aluminum coating that serves as electrode, accelerating the electrons into the phosphorescence layer and, by the following collisions, exciting it to luminescence. The emitted light is directionally transferred through the fiber-optical window and can be captured by a suitable camera. In this way, the impact location of the electron on the first MCP is transferred to the outer side of the vacuum window with minimal radial displacement and blurring.

Time-of-Flight Mass Spectrometry Detector

In the home built detector assembly,[43] a pair of Hamamatsu MCPs (F4294-07) is used. A voltage of -2000 V is applied to the voltage divider made from three resistors, resulting in voltages of -1900 V at the front electrode, -1000 V at the interplate electrode and -180 V at the back electrode. The shape of the steel anode is not flat as indicated in Figure 2.5 a, but was machined to a conical form. The conical shape was chosen to match its electrical impedence to that of the 50 Ω connectors and coaxial transmission lines used, to prevent the broadening and reflection of the high-frequency electrical signal.[57] The signal was amplified by a factor of 5 or 25 with a fast, high-bandwidth amplifier (Stanford Research SR445). The output of the amplifier was connected to a digital storage oscilloscope (LeCroy LT264) with 350 MHz bandwidth and 1 GSa/s sampling rate.

Photoelectron Imaging Detector

The photoelectron imaging detector was assembled by Burle Electro-Optics (Model 3025FM). The originally equipped MCPs were replaced by MCPs manufactured by Photonis (MCP 40/12/10/8 I 60:1 MP, MS). The condition of a field-free flight path has to be exactly met in the imaging application to not distort the original distribution of the photoelectrons. Therefore, the MCP front electrode was connected to ground, and a positive voltage of 1700 V was applied to the back electrode. To avoid recording emissions from unwanted stray electrons or high-energy atmospheric particles, the high voltage was gated by a fast transistor switch (Behlke HTS 31-03-GSM, 6 ns rise time). A positive voltage of 4500 V was applied to the aluminum coating electrode. The emittance from the phosphorescence screen was recorded by a CCD camera (pco.1600, 1600×1200 pixel, 14-bit digitization) with the image sensor thermoelectrically cooled to −20°C.

The phosphorescence detector can not only be used for the position-sensitive acquisiton of photoelectron images, but also for time-of-flight measurements of ions. The thin aluminum coating serves as anode for the electron emission of the MCP, and the ion mass signals are acquired and processed as explained above. It was found that supplying an attractive potential on the anode, i. e. a positive high voltage, improves its collection efficiency. The ion time-of-flight AC signal then has to be isolated from the high DC voltage. For that purpose, a high-voltage bias tee was designed to supply a high voltage *to* the anode, but simultaneously measure the voltage spike coming *from* the anode. The corresponding schematic is depicted in Figure 2.6. The high-voltage capacitor C1 decouples the AC signal from the DC voltage. The resistance R1 limits the charging current of C1 and thereby prevents damage in the amplifier connected to the signal output. The inductance L1 acts as a resistor for high frequency signals, and therefore prevents the AC signal from being damped to zero by the low output resistance of the high-voltage supply connected to HV IN.

The mass signals in the ion time-of-flight spectra acquired in that way were broad and of small amplitude in comparison with the steel-anode time-of-flight detector, and showed pronounced reflections of the electrical signal (“ringing”). While the electrical impendance of the steel anode was matched to the 50 Ω impedance of the following transmission line (see above), the flat aluminum coating has an unknown, different impedance causing problems in the electrical transmission of the mass signals. Therefore, a transimpedance amplifier[58] based on a low distortion, wideband operational amplifier (Texas Instruments LMH6702) was devised to be inserted between the bias tee and the actual amplifier. The schematics are depicted in Figure 2.7. The input impedance can be varied between 50 Ω and 10 kΩ using the variable resistance R2. The gain factor is set by the fraction R3/R4 = 1, a choice that

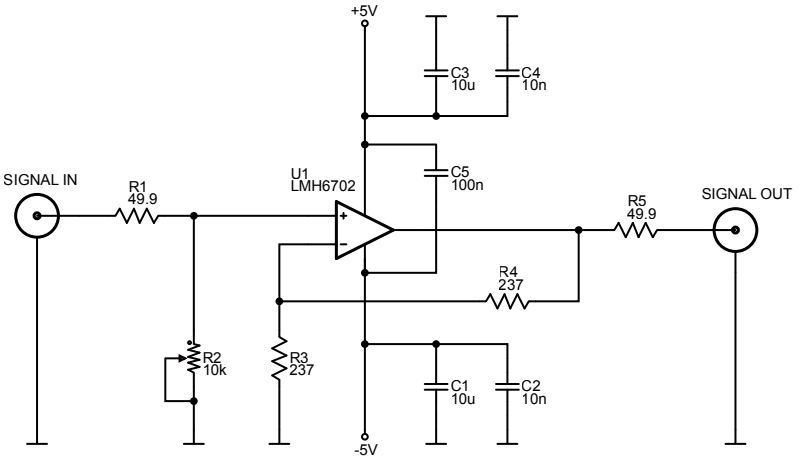

Figure 2.7. Schematic of the transimpedance amplifier. The input impedance is definied by R1 and R2 and can be set to any value between 50 Ω and 10 kΩ. The amplifier gain is set by the ratio R3/R4, where a ratio of 1 gave the best results. The output impedance is 50 Ω.

enables the full bandwidth and least noise. The impedance of the signal output is set to 50 Ω. Time-of-flight mass spectra recorded using the transimpedance amplifier show the same electrical signal quality as spectra recorded with the steel-anode detector.

A further increase in the mass signal amplitude could be observed when using a voltage divider for the MCPs front and back electrodes, although no interplate voltage could be applied with the given detector assembly. The schematic of the voltage divider is depicted in Figure 2.8. The increase in the mass signal amplitude is probably due to the higher acceleration of the ions towards the MCP front surface. A voltage of −2500 V was applied to the input, resulting in voltages of −1950 V at the front electrode, and −180 V at the back electrode. The voltage output for each MCP side is combined with a bias tee of identical design as presented in Figure 2.6. The corresponding outputs can be used to pick up the ion mass signal directly from the MCPs. They were used during the development of the electronic circuits presented in this section, but not for any actual measurements.

2.2.4 Acquisition and Analysis of Time-of-Flight Mass Spectra and Transient Ion Yield Curves

At a fixed pump–probe delay time, time-of-flight mass spectra were accumulated and averaged over typically 500 laser shots. The mass spectra were gated over individual time-of-flight mass peaks, integrated and stored on a computer. A program written in LabView 2013 (National Instruments) controlled the experiment and the storage of the mass spectra. It is based on the software written by H. Studzinski[43] and has been modified in a large extent to allow for faster data acquisition in a more user-friendly

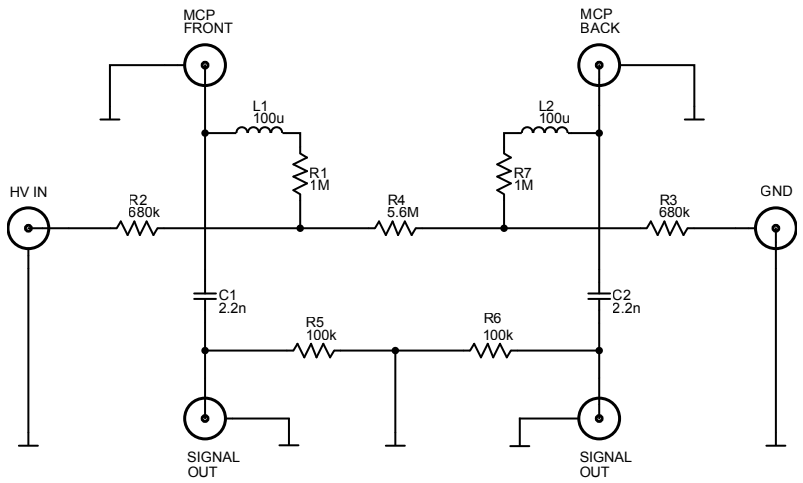

Figure 2.8. Schematic of the combined high voltage divider and bias tee for the MCPs of the photoelectron imaging detector, when used to record time-of-flight mass spectra. The bias tees are set up identically with Figure 2.6. Their outputs can be used to pick up the ion mass signal directly from the MCPs.

way. A detailed description is given in the appendix of this work. The measured transient ion yields are fitted with a kinetic model consisting of exponential decay components of the type

$$M_i(t) = a_i \; e^{-t/\tau_i}, \tag{2.27}$$

with τ_i being the respective decay time constant and a_i its amplitude. A delayed rising signal, as was observed in the acetyl fragments of the acetone molecule (see Chapter 3) was modeled using terms of the form

$$R_i(t) = a_i \left(e^{-t/\tau_i} - e^{-t/\tau_{\mathrm{rise}}} \right) \tag{2.28}$$

with the exponential rise time τ_{rise}. The coherent oscillation observed in the pentafluorobenzene molecule (see Chapter 5) was fitted with exponentially damped cosine terms of the form

$$C_i(t) = a_i \; \cos(\omega_i t + \varphi_i) \; e^{-t/\tau_D}, \tag{2.29}$$

with frequency ω_i, phase φ_i and damping time constant τ_D. A sum of these expressions was composed as required in the particularly analysed data set. Here, a generalized expression is given. It was convoluted with a Gaussian function

$$G(t) = \frac{1}{\sqrt{2\pi}\sigma_{\mathrm{IRF}}} \; \exp\left(-\frac{t - t_0}{2\sigma_{\mathrm{IRF}}} \right)^2 \tag{2.30}$$

describing the instrument response function, giving the experimentally acquired signal

$$S(t) = G(t) \; \otimes \; \left(\sum_i \; M_i(t) + \sum_j \; R_j(t) + \sum_k \; C_k(t) \right), \tag{2.31}$$

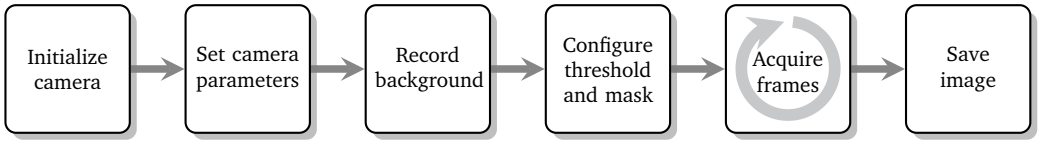

Figure 2.9. Schematic illustration of the photoelectron imaging program sequence. After initializing the camera and, if neccessary, setting the camera parameters, the acquisiton loop for a photoelectron image can be started.

where the t_0 parameter determines the point of zero temporal delay between pump and probe pulse, and the standard deviation σ_{IRF} of the Gaussian instrument function is a direct measure for the experimental time resolution. With a well-compressed pump pulse, values of $\sigma_{\mathrm{IRF}} = 30-35$ fs were achieved. The model function $S(t)$ was fitted to the experimental data points using the Levenberg-Marquard algorithm implemented in Wolfram Mathematica 10.[59]

2.2.5 Acquisition and Analysis of Photoelectron Images

The photoelectron images in this work were acquired over typically 50,000 laser shots at a fixed pump–probe delay time. The LabView program controlling the photoelectron imaging experiment has been written from scratch in this work. It allows for the acquisiton and subsequent processing of photoelectron images with the highest possible frame rate, only restricted by the readout time of the CCD imaging sensor of the camera. After a short introduction to the program, the configurations of the camera hardware and the interface with the computer for maximum image data transfer speed are described. The image processing steps leading to the final photoelectron image as well as the image inversion procedure are explained thereafter.

The sequence of the photoelectron imaging program is shown schematically in Figure 2.9. A more detailed description is given in the appendix of this work. After the initialization of the camera driver, the acquisition parameters like the exposure time have to be defined. A background image of the thermal and electrical sensor noise has to be recorded, which is subtracted from every single acquired frame. A threshold value is set that determines which intensity value a pixel must exceed in order to be recognized as a photoelectron. A mask of arbitrary geometric shape, whose contents will be deleted from every acquired frame, can be defined as well. Default values for all these parameters are pre-defined, which usually do not have to be changed. Next, the measurement of a single photoelectron image or of an image series at several defined pump–probe delay times can the initiated. The series measurement is started from the TOF-MS software, which controls the movement of the delay stage. In this mode of operation, the recorded images are automatically saved after their acquisition.

Camera Configuration and Data Transfer

The camera driver allows to set various internal parameters of the camera that affect the readout time of the CCD image sensor. The pixel clock determines the rate at which the horizontal pixel rows are digitized and was set to 40 MHz. The digitization of the pixel rows is done by analog-to-digital converters (ADCs). One row can be digitized by two separate ADCs, each processing one half of the row, thus doubling the acquisition rate. The readout time of the CCD sensor is limited by the number of horizontal rows, i. e. the vertical sensor resolution. A readout time of 30 ms for the full sensor resolution of 1600×1200 pixel (horizontal $\times$ vertical) is specified in the data sheet and was experimentally confirmed, corresponding to a frame rate of 33 frames/s.

In the experimental setup, not the full sensor resolution but a region of interest (ROI) of 1000×1000 pixels was used, set according to the size and position of the phosphor screen in the image. For a further increase in the acquisiton rate, a vertical binning factor of 2 was selected. Binning allows charges from adjacent pixels to be combined, resulting in faster readout speeds at the expense of spatial resolution. Horizontal binning was not used, as it was found to not substantially affect the readout time. Therefore, the images acquired from the camera had an effective resolution of 1000×500 pixels. As described later in this section, in the image processing procedure the images are "un-binned" again to the full 1000×1000 pixels. In this way, the CCD readout time was decreased to about 12 ms per image, resulting in an effective image acquisition rate of 50 Hz (one image every 20 ms) because the pulsed valve running at 100 Hz only delivers a molecular sample pulse every 10 ms. Therefore, 8 ms are available for the image transfer and processing, and data storage. If more than 8 ms per image are needed, the images accumulate and would quickly fill up the computer memory due to their large size (the overall data throughput is $1000 \times 500 \times 14$ bit $\times$ 50 Hz = 42 MByte/s).

The camera was connected to a framegrabber card in the computer (Matrox Solios eCL) *via* a single-tap Camera Link interface allowing for up to 255 MByte/s data transfer rate. The photoelectron imaging program allocates two buffers in the memory of the framegrabber card into which the images are transferred from the camera on-board memory. The two buffers are used alternatingly: while the content of one buffer is read by the imaging program, the other buffer is ready to accept a new image from the camera. During the actual photoelectron image measurement loop, the image acquisition is running in one CPU thread and stores the raw images in the computer memory using the LabView Queue datatype, which is similar to the common "linked list" data structure. In a concurrently running second thread, the last image from the list is de-queued and subsequently processed. The execution speeds of both threads are independent from each other. If the image processing

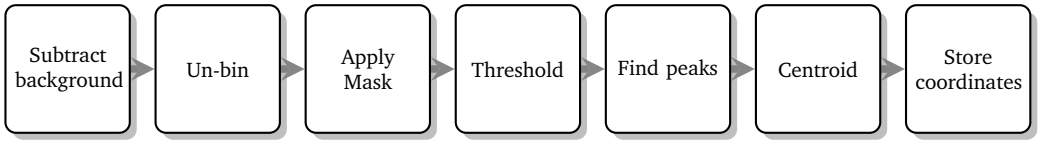

Figure 2.10. Processing steps applied to every single frame acquired from the camera. After the background subtraction and resampling to the desired size, the pixel coordinates of every captured electron impact are determined using a peak-finding routine, and subsequently saved to memory.

takes more than the available 8 ms for any reason, no acquired images are lost. In this way, the maximum possible image transfer rate is achieved, without loosing images to timing issues and intermediate storage memory filling up.

Processing of the Acquired Single Images

The image processing steps performed on every acquired single image are schematically presented in Figure 2.10. First, the initially recorded background image is subtracted. The image is then un-binned from 1000×500 to 1000×1000 pixel with a bilinear resampling routine. If a mask was defined, the corresponding regions are removed from the image. This function has not been used in the experiments performed in this Thesis. It severly increases the image processing time and should be avoided unless absolutely neccessary. Next, the image is thresholded, which means that every pixel with an intensity value lower than the threshold value is set to zero. The image now only contains the phosphor emmitance peaks corresponding to detected photoelectrons. A centroiding algorithm determines the center of mass of the intensity distribution for each peak, and returns a list of floating-point x and y coordinates. Only these coordinates are saved and the image is discarded. This technique has been described in several publications and can be used to artificially create velocity-map images of a very high resolution ("super-resolution imaging").[60–62] From the stored pixel coordinates, the final photoelectron image is "synthesized" in the desired size and saved for the next processing steps. The list of coordinates is saved as well, so that images at different sizes can be generated at later times if desired.

In the photoelectron spectra recorded with femtosecond laser pulses, the energy resolution is limited by the spectral width of the laser pulses, and an increase in the photoelectron image resolution would not result in an increased energy resolution. For the pump-and-probe scheme with one pump and two probe photons typically employed in this work, an energy resolution of about 70 meV is achieved. It was thoroughly tested and verified that the vertical binning and unbinning procedure does not reduce the energy resolution. The recorded images have most of their intensity parallel to the laser polarization axis, that is the vertical axis in the laboratory frame. To avoid even the possibility of an inherent resolution decrease, the camera

was rotated by 90°, so that the vertical binning axis of the CCD sensor corresponds to the horizontal axis of the laboratory frame.

Photoelectron Image Post-Processing and Inversion

A further LabView program has been written for manually post-processing the acquired photoelectron images in a reproducable way. A second photoelectron image can be selected for subtraction, for example from the separate measurement of a background signal. The center of the photoelectron image is determined using a center-of-mass algorithm, and the resulting center coordinate is refined using a method described by Bordas *et al.* [63] A numerical routine was written that finds the maximum of the function

$$\sum_p T\left(x_p, y_p\right)\ T\left(2x_0 - x_p, 2y_0 - y_p\right), \tag{2.32}$$

where $T(x, y)$ refers to the image intensity at the pixel position specified by $p = (x_p, y_p)$. The T on the right of the equation corresponds to an image obtained by mirroring the original image at the trial center position (x_0, y_0). The center position yielding the maximum value of the sum is used in the following steps. The image is cropped to the desired final size around the center position, and its four quadrants are averaged, symmetrizing the images about the vertical laser polarization and horizontal axes. A detailed description of the image post-processing program is given in Appendix A. The processed images are then subjected to the inversion procedure. As the direct application of the inverse Abel transform (Eq. 2.25) artifically introduces or enhances different image artifacts (cf. Section 2.1.4), a number of inversion methods avoiding the connected problems have been developed. Among those are the Fourier-Hankel method,[64–66] the "onion-peeling" method,[67] the BASEX (basis set expansion) method,[68] the pBASEX (polar basis set expansion method) method[69] and an iterative Landweber-algorithm[70] based regularization and cross validation method.[71] In this work, the pBASEX method developed by Garcia *et al.*[69] is employed for the image inversion. In this method, a set of polar basis functions with analytical inverse Abel transforms is fitted to the image. It is based on the three-dimensional photoelectron distribution $I(x, y, z)$ from Eq. 2.23, transformed to polar coordinates and written in the more general form

$$I(r, \theta) = \sum_{k=0}^{k_{\max}} \sum_{L=0}^{L_{\max}} c_{kL}\ f_{kL}(r, \theta) \tag{2.33}$$

with the forward basis functions

$$f_{kL}(r, \theta) = e^{-(r-r_k)^2/\sigma}\ P_L(\cos\theta) \tag{2.34}$$

containing a Gaussian radial part and the angular part in terms of the Legendre polynomials. In the following, the coordinates of the original three-dimensional distribution are denoted by (r, θ), and coordinates of its two-dimensional projection by (R, Θ). The forward basis functions are then Abel-transformed into the projected basis functions

$$g_{kL}(R,\Theta) = 2\int_x^\infty \frac{r'\, f_{kL}(r,\theta)}{\sqrt{r'^2 - x^2}}\,\mathrm{d}r' \tag{2.35}$$

$$\text{with} \quad x = R\sin\Theta \quad \text{and} \quad r' = r\sin\theta \tag{2.36}$$

used to model the projected, two-dimensional distribution $P(R, \Theta)$ on the detector (cf. Eq. 2.24). This distribution is then expressed as a linear expansion of the above basis functions

$$P(R,\Theta) = \sum_{k,L} c_{kL}\; g_{kL}(R,\Theta), \tag{2.37}$$

and is fitted to the experimentally acquired image using a computationally very efficient singular value decomposition (SVD) matrix method, resulting in the expansion factors c_{kL}. These factors are substituted into Eq. 2.33 to reconstruct the original three-dimensional distribution.[69] In this way, photoelectron spectra as well as anisotropy parameters describing the photoelectron angular distribution are gained. The photoelectron spectrum recorded at zero delay time has usually been normalized to unity. All subsequently recorded spectra at larger delay times were scaled relative to that by setting the number of counted electrons and the area under the curve in relation, resulting in the normalization factor

$$N_{\Delta t} = \frac{n_{\mathrm{el}}(\Delta t)}{n_{\mathrm{el}}(t_0)} \times \int \sigma(t_0)\,\mathrm{d}E \Big/ \int \sigma(\Delta t)\,\mathrm{d}E \tag{2.38}$$

where n_{el} denotes the total number of recorded electron impacts. The delay times Δt noted in the plotted spectra in this work are always given in respect to the t_0 value gained from the fit of the transient mass spectra.

2.2.6 Energy Calibration of the Imaging Detector

For the energy calibration of imaging detector, multi-photon above-threshold ionization[72] (ATI) measurements of Xenon were used. Xenon was chosen because it is chemically inert, has the lowest ionization energy of all noble gases and, most importantly, as an atom does not have any vibrational or rotational degrees of freedom that could introduce ambiguities to the resulting photoelectron spectrum. In the very high peak intensity present during a femtosecond laser pulse, the atoms are easily ionized and the ejected electron can absorb additional photons, thereby gaining kinetic energy equivalent to the photonic energy $h\nu$. ATI spectra are hence very useful for calibration purposes, as they show photoelectron peaks separated by

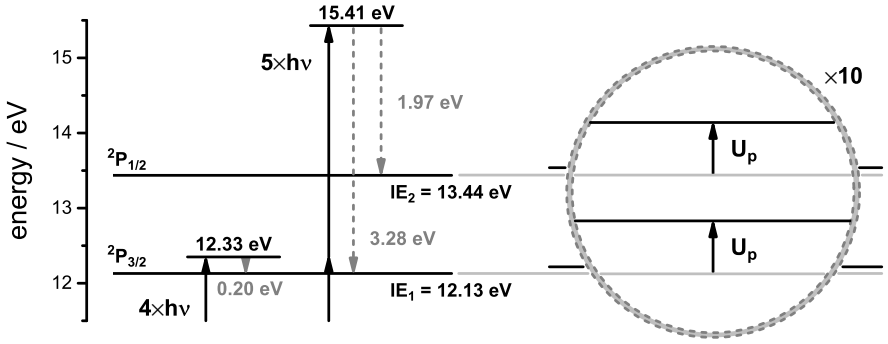

Figure 2.11. Ionization energies of the $^2P_{3/2}$ cationic ground state (IE_1 = 12.13 eV) and the first $^2P_{1/2}$ excited state (IE_2 = 13.44 eV) of Xenon. The photoelectron energies after multiphoton ionization are given next to the dashed arrows. On the right side, the ponderomotive shift of the energy levels by U_p is indicated, resulting in a reduction of the measured photoelectron energies.

the photon energy. To record a Xenon photoelectron calibration spectrum, a 10% Xenon in Helium gas mixture was expanded into the vacuum chamber and ionized with four or five photons from the probe laser pulse centered at 402 nm (3.08 eV). The excitation scheme is depicted on the left in Figure 2.11. In the four-photon process, transitions to the $^2P_{3/2}$ cationic ground state of Xenon at 12.13 eV[73] could be observed as photoelectron bands at 0.20 eV. After absorption of an additional fifth photon, also transitions to the $^2P_{1/2}$ excited state at 13.44 eV were energetically possible, resulting in a band at 1.97 eV. The $^2P_{3/2}$ band after five-photon absorption is expected at (0.2 eV + $h\nu$) = 3.28 eV. The resulting photoelectron spectrum with these assignments, measured as a function of the detector pixel units, is depicted in Figure 2.12 a (open circles). For the determination of the exact ring radii of the observed photoelectron bands, the spectrum was fitted with a sum of Gaussian line profiles $G_i(r, r_0^i, \sigma_i)$ centered at r_0^i. The complete fitting model $S(r)$ reads

$$S(r) = \Theta\left(r - r_0^{i=1}\right) p(r) + \sum_i G_i(r, r_0^i, \sigma_i), \tag{2.39}$$

where $\Theta\left(r - r_0^{i=1}\right)$ is the Heaviside step function and $p(r)$ is a power series usually cut off after the second-order term to model the background signal. The fitted model is plotted in the spectrum in Figure 2.12 a as the black line, giving three ring radii r_0^i corresponding to the known photoelectron energies listed above. As the ring radius on the detector is directly proportional to the velocity v of the electrons (cf. Eq. 2.21), and the photoelectron kinetic energy is given by $E_\mathrm{kin} = 1/2 m_e v^2$, a suitable energy calibration curve of the detector reads

$$E(r) = kr^2, \tag{2.40}$$

with the calibration factor k. The curve is fitted to the determined ring radii of the photoelectron bands, resulting in the calibration curve depicted in Figure 2.12 b. The

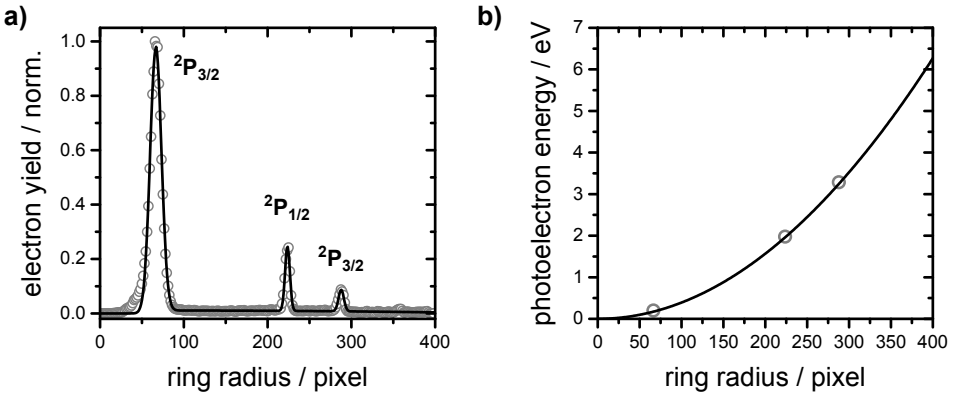

Figure 2.12. a) Photoelectron spectrum of the multiphoton ionization of Xenon with 41 µJ laser pulses centered at 402 nm. The bands are fitted with Gaussian profiles to determine their ring radius in pixel units. b) The known photoelectron energies are plotted over the radii in pixel units. A quadratic fit of the data points is performed, resulting in the detector energy calibration curve.

energy calibration gained this way does not, however, give entirely correct results for the photoelectron kinetic energies, because the ionic energy levels of Xenon are shifted to higher energies due to the high intensity of the femtosecond laser pulse, which has to be accounted for.

Ponderomotive Shift of the Ionization Energies

The oscillating electric and magnetic fields of an optical wave excert a force on a free electron, causing it to perform a "wiggling" motion.[74] The wiggle, or ponderomotive, energy U_p in an optical field with the peak value E_0 is given by[75]

$$U_\mathrm{p} = \frac{e^2 E_0^2}{4 m_e \omega^2}, \tag{2.41}$$

or in terms of the intensity I of the laser pulse,

$$U_\mathrm{p} = \frac{e^2 I}{2 c \epsilon_0 m_e \omega^2}. \tag{2.42}$$

Due to the very high intensity of the femtosecond laser pulse, there is also an effect on the bound electrons of the Xenon atom. While the ground state is strongly bound and its energy is nearly not shifted at all, loosely bound high-lying Rydberg states are subject to the same wiggling motion as free electrons. Thus, the total energy of Rydberg states is increased by nearly U_p.[76] Since all levels near the ionization limit, both bound and unbound, are shifted by the same amount, the ionization limit of Xenon is necessarily shifted to higher energy,[77] and the measured photoelectron energies are therefore shifted to smaller values as indicated on the right in Figure 2.11. For a correct energy calibration of the imaging detector, the photoelectron energies corresponding to the true ionization energies of Xenon

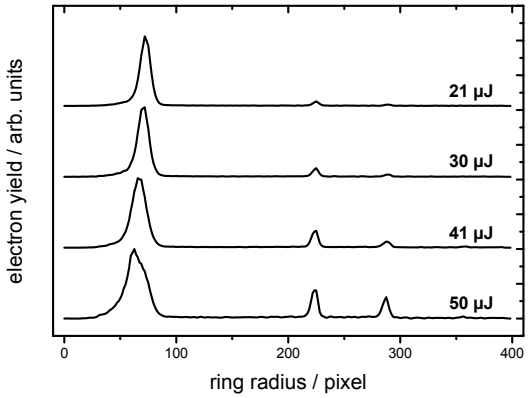

Figure 2.13. Photoelectron spectra of the multiphoton ionization of Xenon with different laser pulse intensities as indicated in the graph. With increasing intensity, the cationic energy levels are shifted to higher energies. The photoelectron bands are therefore shifted to smaller kinetic energies, corresponding to smaller ring radii.

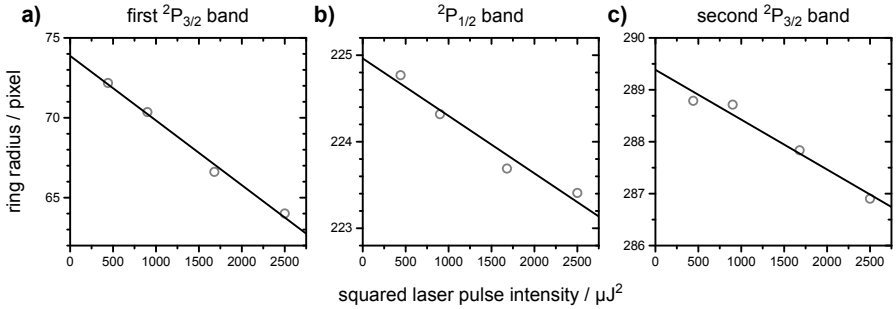

Figure 2.14. a) – c) Plots of the linear relationship of the photoelectron ring radii of the three recorded bands with the squared laser pulse intensity. The ordinate intercept of the fitted lines give the "true" ring radii with $U_\mathrm{p} = 0$, used for the final energy calibration curve.

with $U_\mathrm{p} = 0$ have to be obtained. To achieve this, an ATI measurement series of Xenon with four different laser pulse intensities was performed. The obtained photoelectron kinetic energy spectra are depicted in Figure 2.13. The shift of the bands to smaller radii, corresponding to less kinetic energy, with increasing pulse energy is clearly visible. The pixel position of each photoelectron band was plotted over the corresponding squared pulse energy to obtain a linear relationship between r and I, as shown in Figure 2.14 a – c. To determine the "true" pixel position corresponding to an ionization without a ponderomotive shift of the ionization energies, i. e. for $U_\mathrm{p} = 0$, a linear fit of the data points was performed. The "true" pixel position can then directly be found from the ordinate intercept.

The energy calibration curve was fitted to the "true" pixel position as described above. In comparison with the calibration curve using the uncorrected band positions, the calibration factor k differs by about 2%. The correction for the ponderomotive shift of the ionization energies turned out to be very important when evaluating the obtained photoelectron spectra of the investigated molecules. Without the correction, in some spectra photoelectron bands were observed at unphysically large

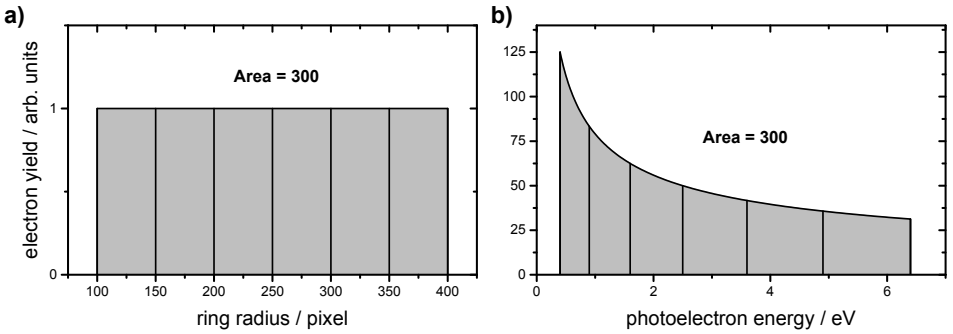

Figure 2.15. Evenly spaced intervals in pixel units are unevenly spaced in energy due to their quadratic relationship. a) A constant signal in evenly spaced pixel units with an area of 300 (shaded in gray in the illustration). b) The area under the curve in energy units must be the same after application of the Jacobian transformation, because the number of measured electrons is preserved.

energies, whose appearance could not be explained in spite of good knowledge of the electronic structure of the molecule and the number of photons involved in the ionization process. The measurement series for the correction of the ponderomotive shift was performed once for a fixed ionization geometry in terms of pump and probe laser beam positions. The energy calibration was repeated every day before or after photoelectron images were recorded.

The Jacobian Transformation

When transforming photoelectron spectra from the pixel (i. e. velocity) units of the detector to kinetic energy units, an appropiate Jacobian transformation of the ordinate has to be applied. Denoting the recorded pixel-unit spectrum as the function $f(r)$, the relation

$$f(r)\mathrm{d}E = f(E)\mathrm{d}E, \tag{2.43}$$

must hold, where $f(E)$ corresponds to the spectrum in energy units. In other words, the area under the curve must be the same in both spectra, because the number of measured electrons is conserved. As the conversion factor is not equal to 1 due to the quadratic relationship between energy and radius $E \propto r^2$, the intervals $\mathrm{d}r$ in the pixel-unit spectrum are not evenly sized across the energy spectrum. The conversion factor can be determined by inserting Eq. 2.40 into Eq. 2.43, yielding

$$f(E) = \frac{1}{2\sqrt{kE}}\, f(r) \quad (\forall k > 0)\,, \tag{2.44}$$

where $(2\sqrt{kE})^{-1}$ is the Jacobian transformation factor. In Figure 2.15, the transformation of an exemplary pixel spectrum with $\mathrm{d}r = 100$ pixel (Figure 2.15 a) to energy units (Figure 2.15 b) is shown to illustrate the situation. The application of the Jacobian transformation to real photoelectron spectra gives unphysically large ordinate values at small energies, because E stands in the denominator of the

fraction, as can also be seen in Figure 2.15 b. Therefore, data of the first 0.02 eV are omitted in photoelectron kinetic energy spectra in this work.

References

1. W. Wohlleben, T. Buckup, H. Hashimoto, R. J. Cogdell, J. L. Herek, and M. Motzkus, "Pump-Deplete-Probe Spectroscopy and the Puzzle of Carotenoid Dark States," J. Phys. Chem. B **108**, 3320–3325 (2004).
2. E. Papagiannakis, M. Vengris, D. S. Larsen, I. H. M. van Stokkum, R. G. Hiller, and R. van Grondelle, "Use of Ultrafast Dispersed Pump-Dump-Probe and Pump-Repump-Probe Spectroscopies to Explore the Light-Induced Dynamics of Peridinin in Solution," J. Phys. Chem. B **110**, 512–521 (2006).
3. S. Draxler, T. Brust, S. Malkmus, J. A. DiGirolamo, W. J. Lees, W. Zinth, and M. Braun, "Ring-opening reaction of a trifluorinated indolylfulgide: mode-specific photochemistry after pre-excitation," Phys. Chem. Chem. Phys. **11**, 5019–5027 (2009).
4. D. M. Jonas, "Two-Dimensional Femtosecond Spectroscopy," Annu. Rev. Phys. Chem. **54**, 425–463 (2003).
5. M. Cho, "Coherent Two-Dimensional Optical Spectroscopy," Chem. Rev. **108**, 1331–1418 (2008).
6. P. Nürnberger, S. Rützel, and T. Brixner, "Multidimensional Electronic Spectroscopy of Photochemical Reactions," Angew. Chem. Int. Ed. **54**, 11368–11386 (2015).
7. D. M. Lubman, C. T. Rettner, and R. N. Zare, "How isolated are molecules in a molecular beam?" J. Phys. Chem. **86**, 1129–1135 (1982).
8. G. Scoles, D. Bassi, U. Buck, and D. C. Laine, eds., *Atomic and Molecular Beam Methods: Volume 1* (Oxford University Press, New York, 1988).
9. G. Scoles, D. C. Laine, and U. Valbusa, eds., *Atomic and Molecular Beam Methods: Volume 2* (Oxford University Press, New York, 1992).
10. G. Herzberg, *Electronic Spectra and Electronic Structure of Polyatomic Molecules*, Molecular Spectra and Molecular Structure, Vol. III (Krieger Publishing Company, 1991).
11. M. Born and R. Oppenheimer, "Zur Quantentheorie der Molekeln," Ann. Phys. **389**, 457–484 (1927).
12. R. Zare, *Angular Momentum* (John Wiley & Sons Inc, New York, 1988).
13. S. T. Pratt, "Excited-state molecular photoionization dynamics," Rep. Prog. Phys. **58**, 821–883 (1995).
14. R. Signorell and F. Merkt, "General symmetry selection rules for the photoionization of polyatomic molecules," Mol. Phys. **92**, 793–804 (1997).

15. P. R. Bunker and P. Jensen, *Molecular Symmetry and Spectroscopy* (NRC Press, Ottawa, 2008).
16. R. Renner, "Zur Theorie der Wechselwirkung zwischen Elektronen- und Kernbewegung bei dreiatomigen, stabförmigen Molekülen," Z. Physik **92**, 172–193 (1934).
17. H. A. Jahn and E. Teller, "Stability of Polyatomic Molecules in Degenerate Electronic States. I. Orbital Degeneracy," Proc. R. Soc. Lond. Math. Phys. Eng. Sci. **161**, 220–235 (1937).
18. I. B. Bersuker, "Pseudo-Jahn–Teller Effect—A Two-State Paradigm in Formation, Deformation, and Transformation of Molecular Systems and Solids," Chem. Rev. **113**, 1351–1390 (2013).
19. H. A. Bethe and E. E. Salpeter, *Quantum Mechanics of One- and Two-Electron Atoms* (Springer, Berlin, 1957).
20. T. Koopmans, "Über die Zuordnung von Wellenfunktionen und Eigenwerten zu den einzelnen Elektronen eines Atoms," Physica **1**, 104–113 (1934).
21. W. J. Hehre, L. Radom, P. V. R. Schleyer, and J. A. Pople, *Ab Initio Molecular Orbital Theory*, 2nd ed. (John Wiley & Sons Inc, New York, 1986).
22. V. Blanchet, M. Z. Zgierski, and A. Stolow, "Electronic continua in time-resolved photoelectron spectroscopy. I. Complementary ionization correlations," J. Chem. Phys. **114**, 1194–1205 (2001).
23. M. Schmitt, S. Lochbrunner, J. P. Shaffer, J. J. Larsen, M. Z. Zgierski, and A. Stolow, "Electronic continua in time-resolved photoelectron spectroscopy. II. Corresponding ionization correlations," J. Chem. Phys. **114**, 1206–1213 (2001).
24. D. Dill, "Fixed-molecule photoelectron angular distributions," J. Chem. Phys. **65**, 1130–1133 (1976).
25. T. Seideman, "Time-Resolved Photoelectron Angular Distributions: Concepts, Applications, and Directions," Annu. Rev. Phys. Chem. **53**, 41–65 (2002).
26. K. L. Reid, "Photoelectron Angular Distributions," Annu. Rev. Phys. Chem. **54**, 397–424 (2003).
27. T. Suzuki, "Femtosecond time-resolved photoelectron imaging," Annu. Rev. Phys. Chem. **57**, 555–592 (2006).
28. B. J. Whitaker, ed., *Imaging in Molecular Dynamics: Technology and Applications* (Cambridge University Press, Cambridge, 2003).
29. M. Tsubouchi, B. J. Whitaker, L. Wang, H. Kohguchi, and T. Suzuki, "Photoelectron Imaging on Time-Dependent Molecular Alignment Created by a Femtosecond Laser Pulse," Phys. Rev. Lett. **86**, 4500–4503 (2001).
30. S. T. Manson, "Dependence of the angular distribution of atomic photoelectrons on energy and Z: I. p-Subshells," J. Electron. Spectrosc. Relat. Phenom. **1**, 413–438 (1972).
31. S. T. Manson, "Dependence of the angular distribution of atomic photoelectrons on energy and Z. II. d- and f-subshells," J. Electron. Spectrosc. Relat. Phenom. **37**, 37–56 (1985).

32. S. T. Manson and A. F. Starace, "Photoelectron angular distributions: energy dependence for s subshells," Rev. Mod. Phys. **54**, 389–405 (1982).
33. G. Wu, P. Hockett, and A. Stolow, "Time-resolved photoelectron spectroscopy: from wavepackets to observables," Phys. Chem. Chem. Phys. **13**, 18447–18467 (2011).
34. N. H. Abel, "Auflösung einer mechanischen Aufgabe." J. Reine Angew. Math. **1**, 153–157 (1826).
35. A. Damascelli, "Probing the Electronic Structure of Complex Systems by ARPES," Phys. Scr. **T109**, 61 (2004).
36. T. Pancur, N. K. Schwalb, F. Renth, and F. Temps, "Femtosecond fluorescence up-conversion spectroscopy of adenine and adenosine: experimental evidence for the $\pi\sigma^*$ state?" Chem. Phys. **313**, 199–212 (2005).
37. M. Foca, *Investigations of ultrafast photoisomerization of photochromic molecular switches by fs-time resolved transient absorption spectroscopy*, Dissertation, Universität Kiel, Kiel (2005).
38. N. K. Schwalb, *Ultrafast electronic deactivation dynamics in DNA model systems by femtosecond UV fluorescence spectroscopy*, Dissertation, Universität Kiel, Kiel (2009).
39. R. Siewertsen, *Ultrafast photochromic reactions of structurally modified furylfulgides and a bridged azobenzene*, Dissertation, Universität Kiel, Kiel (2011).
40. S. Mukamel, *Principles of Nonlinear Optical Spectroscopy* (Oxford University Press, 1999).
41. R. W. Boyd, *Nonlinear Optics* (Academic Press, 2013).
42. A. M. Weiner, *Ultrafast Optics* (Wiley, Oxford, 2009).
43. H. Studzinski, *Ultrafast Radiationless Dynamics of Selected Electronically Excited Aromatic Molecules by Femtosecond Time-Resolved Mass Spectrometry and Photoelectron Imaging*, Dissertation, Universität Kiel (2007).
44. T. Wilhelm, J. Piel, and E. Riedle, "Sub-20-fs pulses tunable across the visible from a blue-pumped single-pass noncollinear parametric converter," Opt. Lett. **22**, 1494–1496 (1997).
45. E. Riedle, M. Beutter, S. Lochbrunner, J. Piel, S. Schenkl, S. Spörlein, and W. Zinth, "Generation of 10 to 50 fs pulses tunable through all of the visible and the NIR," Appl. Phys. B **71**, 457–465 (2000).
46. G. Cerullo and S. D. Silvestri, "Ultrafast optical parametric amplifiers," Rev. Sci. Instrum. **74**, 1–18 (2003).
47. S. L. Chin, A. Brodeur, S. Petit, O. G. Kosareva, and V. P. Kandidov, "Filamentation and supercontinuum generation during the propagation of powerful ultrashort laser pulses in optical media (white light laser)," J. Nonlinear Optic. Phys. Mat. **08**, 121–146 (1999).
48. U. Even, J. Jortner, D. Noy, N. Lavie, and C. Cossart-Magos, "Cooling of large molecules below 1 K and He clusters formation," J. Chem. Phys. **112**, 8068–8071 (2000).

49. M. Hillenkamp, S. Keinan, and U. Even, "Condensation limited cooling in supersonic expansions," J. Chem. Phys. **118**, 8699–8705 (2003).
50. V. Vaida, "Electronic absorption spectroscopy of jet-cooled molecules," Acc. Chem. Res. **19**, 114–120 (1986).
51. W. C. Wiley and I. H. McLaren, "Time-of-Flight Mass Spectrometer with Improved Resolution," Rev. Sci. Instrum. **26**, 1150 (1955).
52. A. T. J. B. Eppink and D. H. Parker, "Velocity map imaging of ions and electrons using electrostatic lenses: Application in photoelectron and photofragment ion imaging of molecular oxygen," Rev. Sci. Instrum. **68**, 3477 (1997).
53. F. Chandezon, B. Huber, and C. Ristori, "A new-regime Wiley–McLaren time-of-flight mass spectrometer," Rev. Sci. Instrum. **65**, 3344–3353 (1994).
54. J. L. Wiza, "Microchannel plate detectors," Nucl. Instrum. Methods **162**, 587–601 (1979).
55. J. Adams and B. W. Manley, "The Mechanism of Channel Electron Multiplication," IEEE Trans. Nucl. Sci. **13**, 88–99 (1966).
56. W. B. Colson, J. McPherson, and F. T. King, "High-gain imaging electron multiplier," Rev. Sci. Instrum. **44**, 1694–1696 (1973).
57. P. Wurz and L. Gubler, "Impedance-matching anode for fast timing signals," Rev. Sci. Instrum. **65**, 871–876 (1994).
58. P. Schwartze, H. Baumgärtel, and C. G. Eisenhardt, "A simple and fast transimpedance amplifier for microchannel plate detectors," Rev. Sci. Instrum. **72**, 3125–3126 (2001).
59. Wolfram Research, Inc., Mathematica, Version 10.0, Champaign, IL (2014).
60. B.-Y. Chang, R. C. Hoetzlein, J. A. Mueller, J. D. Geiser, and P. L. Houston, "Improved two-dimensional product imaging: The real-time ion-counting method," Rev. Sci. Instrum. **69**, 1665–1670 (1998).
61. N. Yonekura, C. Gebauer, H. Kohguchi, and T. Suzuki, "A crossed molecular beam apparatus using high-resolution ion imaging," Rev. Sci. Instrum. **70**, 3265–3270 (1999).
62. W. Li, S. D. Chambreau, S. A. Lahankar, and A. G. Suits, "Megapixel ion imaging with standard video," Rev. Sci. Instrum. **76**, 063106 (2005).
63. C. Bordas, F. Paulig, H. Helm, and D. L. Huestis, "Photoelectron imaging spectrometry: Principle and inversion method," Rev. Sci. Instrum. **67**, 2257–2268 (1996).
64. L. Montgomery Smith, D. R. Keefer, and S. I. Sudharsanan, "Abel inversion using transform techniques," J. Quant. Spectrosc. Radiat. Transfer **39**, 367–373 (1988).
65. K. R. Castleman, *Digital Image Processing* (Prentice Hall, 1996).
66. S. M. Candel, "An algorithm for the Fourier-Bessel transform," Comput. Phys. Commun. **23**, 343–353 (1981).
67. S. Manzhos and H.-P. Loock, "Photofragment image analysis using the Onion-Peeling Algorithm," Comput. Phys. Commun. **154**, 76–87 (2003).

68. V. Dribinski, A. Ossadtchi, V. A. Mandelshtam, and H. Reisler, "Reconstruction of Abel-transformable images: The Gaussian basis-set expansion Abel transform method," Rev. Sci. Instrum. **73**, 2634–2642 (2002).
69. G. A. Garcia, L. Nahon, and I. Powis, "Two-dimensional charged particle image inversion using a polar basis function expansion," Rev. Sci. Instrum. **75**, 4989–4996 (2004).
70. L. Landweber, "An Iteration Formula for Fredholm Integral Equations of the First Kind," Amer. J. Math. **73**, 615–624 (1951).
71. F. Renth, J. Riedel, and F. Temps, "Inversion of velocity map ion images using iterative regularization and cross validation," Rev. Sci. Instrum. **77**, 033103–033103–12 (2006).
72. P. Agostini, F. Fabre, G. Mainfray, G. Petite, and N. K. Rahman, "Free-Free Transitions Following Six-Photon Ionization of Xenon Atoms," Phys. Rev. Lett. **42**, 1127–1130 (1979).
73. J. E. Hansen and W. Persson, "Revised analysis of singly ionized xenon, Xe II," Phys. Scr. **36**, 602 (1987).
74. T. W. B. Kibble, "Refraction of Electron Beams by Intense Electromagnetic Waves," Phys. Rev. Lett. **16**, 1054–1056 (1966).
75. P. H. Bucksbaum, M. Bashkansky, and T. J. McIlrath, "Scattering of electrons by intense coherent light," Phys. Rev. Lett. **58**, 349–352 (1987).
76. R. R. Freeman and P. H. Bucksbaum, "Investigations of above-threshold ionization using subpicosecond laser pulses," J. Phys. B At. Mol. Opt. Phys. **24**, 325 (1991).
77. P. Kruit, J. Kimman, and M. J. V. der Wiel, "Absorption of additional photons in the multiphoton ionisation continuum of xenon at 1064, 532 and 440 nm," J. Phys. B: At. Mol. Phys. **14**, L597 (1981).

3

Ultrafast α–CC Bond Cleavage of Acetone upon Excitation to the $3d_{yz}$ Rydberg State by Femtosecond Time-Resolved Photoelectron Imaging

Ole Hüter and Friedrich Temps

Institute of Physical Chemistry, Christian-Albrechts-University Kiel, Olshausenstr. 40, D-24098 Kiel, Germany

Manuscript in preparation.

Abstract

The radiationless electronic decay and α–CC bond cleavage dynamics of jet-cooled acetone in the S_1 ($n\pi^*$) state and in high-lying 3p and 3d Rydberg states were investigated by femtosecond time-resolved mass spectrometry and photoelectron imaging. The S_1 state was reached by absorption of a UV pump photon at wavelengths between λ = 320 and 250 nm. Time-resolved photoelectron imaging after two-photon ionization at λ = 402 nm eliminated a CC bond cleavage on the S_1 potential energy hypersurface on time scales up to one nanosecond, in accordance with the commonly accepted picture. However, absorption of a second UV pump photon by the S_1 ($n\pi^*$) state was found to populate a series of high-lying states belonging to the n = 3 Rydberg manifold. The distinct energies revealed by the photoelectron images allowed for assignments to the 3p and $3d_{yz}$ states. At excitation energies higher than 8.1 eV, an ultrafast reaction pathway for breaking the α–CC bond in 50 – 90 fs *via* the $3d_{yz}$ Rydberg state and the elusive $\pi\pi^*$ state was observed.

3.1 Introduction

The electronic excitation of aliphatic ketones with ultraviolet (UV) light leads to the cleavage of one of the α–CC bonds in the well-known Norrish type I reaction resulting in an acyl radical and an alkyl radical.[1–3] Acetone as the simplest aliphatic ketone, which gives acetyl and methyl as products, is the prototypical example. The acetone molecule has thus been the subject of intense investigations for years, which showcase not only its basic photophysical behavior on the nanosecond to microsecond time scales,[4–14] but also its primary and secondary photochemistry with respect to its enormous atmospheric importance.[15–31]

The gas phase UV absorption spectrum of acetone from its S_0 ($^1A_1$) electronic ground state is depicted in Figure 3.1 b. The S_1 first excited state ($^1A_2$) is reached through the $n\pi^*$ transition, which is forbidden in C_{2v} symmetry, but arises weakly through intensity borrowing by vibronic coupling.[32,33] The absorption maximum lies at 275 nm (4.5 eV). A further singlet valence state is expected by the $\pi\pi^*$ ($^1A_1$) transition, but has not been directly observed in experiments. The $\pi\pi^*$ state has been assigned to a diffuse broad band in the VUV absorption spectrum[34] and is suspected to strongly couple to the $3p_y$ ($^1A_1$) and $3d_{yz}$ ($^1A_1$) Rydberg states, causing anomalies in their intensities and vibrational structures.[35–39] The cited studies locate the vertical excitation energy of the $\pi\pi^*$ state between 7.5 and 8.0 eV. The intense band in the UV absorption spectrum peaking at 194 nm marks the onset of transitions to Rydberg states belonging to the n s,[40–44] n p[35–39,45–47] and n d[34,36,38,48] series, which converge to the first ionization energy (9.708 eV).[47] The C_{2v} symmetry is

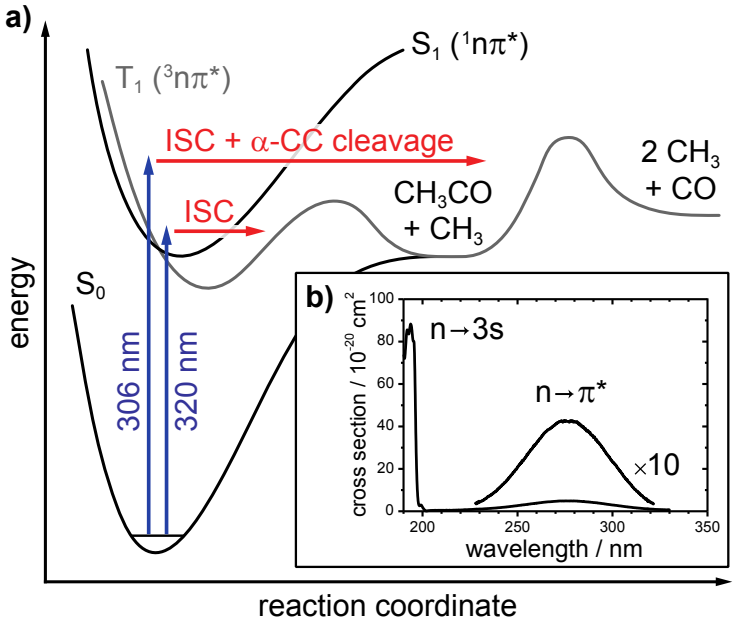

Figure 3.1. a) Schematic representation of the potential energy surfaces of acetone in the ground and the first excited singlet and triplet states. Intersystem crossing from S_1 to T_1 is observed at $\lambda \leq 320$ nm, followed by α–CC bond cleavage on the triplet PES after excitation at $\lambda \leq 306$ nm. Excitation to higher energies leads to a further decomposition of the acetyl radical. b) UV absorption spectrum of acetone vapor ($p = 18$ mbar). The S_1 (n$\rightarrow \pi^*$) absorption band is amplified by a factor of 10 for clarity. The (n$\rightarrow$3s) transition begins at $\lambda < 200$ nm.

retained in the cationic ground state and therefore in the Rydberg states as well,[49] although this may not hold for states perturbed by the $\pi\pi^*$ valence state. CC bond cleavage is observed after excitation to any of the aforementioned states, but the exact reaction pathways are not well known.

The commonly accepted acetone photolysis mechanism *via* the S_1 ($n\pi^*$) state is summarized in Figure 3.1 a. After excitation of the 0–0 vibrational transition (3.774 eV,[13] corresponding to $\lambda = 328.5$ nm), weak long-lived fluorescence with a lifetime of $\tau = 1.0$ µs was observed.[9] On excitation with an additional 800 cm^{-1} of energy ($\lambda \leq 320$ nm), intersystem crossing (ISC) to the T_1 ($^3A_2$) state takes place with a quantum yield (in the absence of prior quenching) near unity.[4] Following excitation at 313 nm, the fluorescence lifetime reduces to 2.4 ns and its quantum yield to $\Phi_F = 0.0012$.[6] The presence of an energy barrier on the triplet potential energy surface (PES) requires a threshold excitation wavelength of $\lambda = 305.8$ nm for the dissociation to acetyl and methyl.[11,12] At higher excitation energies, the fluorescence lifetime decreases from 2.1 ns at 295 nm to 1.6 ns at 260 nm.[5] The ISC process thus appears to remain the rate-determining step in the overall photodissociation mechanism at these wavelengths.

In apparent contrast, results of time-resolved investigations of acetone after femtosecond laser excitation to S_1 and to higher-lying Rydberg states suggested dissociation

on an ultrafast time scale.[50–62] The majority of studies employed time-of-flight mass spectrometry (TOF-MS) with femtosecond pump and probe laser pulses involving multi-photon ionization. Transient signals of the acetone parent ion were observed to decay in a few picoseconds or faster after Rydberg excitation[51,52,54–56,58–61] and in less than 200 fs after S_1 excitation,[50,51,53–55] while acetyl fragment signals arose on similar time scales. Recently, the ultrafast decay time of the ion signal from the S_1 ($n\pi^*$) state has been ascribed to structural changes (out-of-plane pyramidalization)[8,13] and an accompanying departure of the excited wavepacket from the Franck–Condon (FC) probe window.[62,63] In this light, the origin of the rising complementary acetyl signal has remained unknown, although it has sometimes been attributed to the decomposition of the acetone cation to an acetyl ion and a neutral methyl radical after photoionization with more than 0.8 eV excess energy above the ionization threshold.[64–66] It is inherent to the TOF-MS method, however, that it is difficult to assess which electronic states are actually excited by the pump and probe laser pulses, because the occurrence of multi-photon excitations can only be indirectly inferred. In acetone, in particular, transitions to the higher-lying valence and Rydberg states have roughly three orders-of-magnitude higher absorption cross sections than to the S_1 ($n\pi^*$) state,[34] making two-photon transitions quite likely especially in view of the high peak intensities of femtosecond laser pulses. Furthermore, as a frequency-integrated technique, TOF-MS does not allow one to determine how the available total excess energy after multi-photon photoionization is partitioned between the parent ion and the ejected photoelectron, when resonant intermediate states can accommodate substantial amounts of vibrational excitation.

In the present publication, we report a time-resolved study of acetone in a supersonic molecular beam by femtosecond mass spectrometry and femtosecond photoelectron imaging spectroscopy designed to resolve the above questions and develop a consistent picture of the ultrafast photochemistry of acetone in the S_1 state and in higher-lying (Rydberg) electronic states reached through multiphoton excitations. The energy-dispersed, time- and angle-resolved detection of the ejected electrons with the photoelectron imaging method is a powerful complementary technique that allows for real-time observation of the non-adiabatic excited-state dynamics and radiationless transitions with full electronic state specificity.[67–70] Multi-photon processes are readily revealed by the appearance of photoelectron (PE) bands in energy regimes that are inaccessible after single-photon excitation. The major aims of this work have thus been to clarify, which electronic states can lead to dissociation of the photo-excited acetone molecules on an ultrafast time scale, and to elucidate the role of the acetone cation in the observed dissociation processes. Towards these ends, we selected excitation (pump) wavelengths between $\lambda_{\mathrm{pump}} = 320$ and 250 nm distributed over the S_1 ($n\pi^*$) absorption band and detection (probe) wavelengths for multi-photon ionization of $\lambda_{\mathrm{probe}} = 804$ nm or 402 nm, respectively.

3.2 Experimental Methods

The experiments employed a home-built linear time-of-flight mass spectrometer (TOF-MS) and photoelectron imaging (PEI) machine. The setup consisted of two differentially pumped, electropolished stainless steel high vacuum chambers for the supersonic molecular expansion of the molecules and their subsequent ionization and detection. Acetone was used as supplied by Merck (Uvasol spectroscopic grade, 99.9% purity). A gas mixture was prepared by flowing helium carrier gas at 2 bar pressure over the liquid in a glass reservoir at room temperature. The seeded gas expanded into the entrance vacuum chamber through a solenoid-actuated pulsed valve (Parker series 9, 0.5 mm orifice diameter) driven by a home-built power supply at 100 Hz repetition rate with 65 μs opening time. A molecular beam was formed by a 0.5 mm skimmer (Beam Dynamics) at the entrance to the second vacuum chamber, which contained the ion source surrounded by a LN_2 cold trap. The co-propagating pump and probe laser beams crossed the molecular beam perpendicularly between the repeller and extractor plates. The following field-free flight zone was shielded from stray magnetic fields by a μ-metal tube and terminated by a microchannel plate (MCP) detector backed by a steel anode connected to a 1 GSa/s digital storage oscilloscope (LeCroy LT264) for ion time-of-flight measurements or by a phosphorescence screen for photoelectron imaging on a Peltier-cooled, 1600×1200 pixel CCD camera (pco.1600, 14-bit digitization). The high voltage applied to the MCPs for photoelectron imaging was gated by a fast transistor switch (Behlke HTS 31-03-GSM, 6 ns rise time). The timing of all components was controlled by a digital delay generator (Stanford Research DG645).

All laser pulses were derived from an 804 nm, 1 kHz regeneratively amplified Ti:Sa laser system (Coherent Libra-HE) producing 3.7 mJ pulses of 90 fs full-width at half-maximum (FWHM) duration. The required tunable UV pump pulses were generated in a home-built, two-stage noncollinear optical parametric amplifier (NOPA) equipped with a prism pulse compressor and a BBO doubling crystal and focused into the molecular beam in the ion source with a 50 cm focal length concave mirror. The probe pulses for multi-photon ionization came from the Ti:Sa laser fundamental (804 nm) for TOF-MS or its second harmonic (402 nm) for PEI and focused into the molecular beam with a 100 cm focal length lens. The pump and probe polarizations were both oriented parallel to the detector surface. Temporal profiles as function of pump–probe time delay were recorded using a linear translation stage (PI M-521.DG) allowing for a maximum displacement up to 1.38 ns. At a fixed pump–probe delay time, ion mass spectra were typically accumulated over 1,000 laser shots, photoelectron images over typically 200,000 laser shots. The

mass spectra were gated over individual time-of-flight mass peaks, integrated and stored on a desktop computer.

The acetone ion time profiles were modeled using a sum of exponentials with decay time constants τ_i and amplitudes a_i, convoluted with a Gaussian with parameters t_0 for the time zero of the pump–probe delay and σ for the experimental time resolution limited by the instrument response function (IRF). The acetyl fragment ions, which were measured as well, may appear either after ionization of the neutral CH_3CO radicals from the acetone photodissociation, or through decomposition of the acetone cation after the pump-and-probe steps. In the first case, the acetyl signal exhibits a delayed rise prior to its subsequent decay, which is accounted for by the difference of two exponentials. In the second case, the temporal evolution of the acetyl ion cannot be experimentally followed, as the acetone and acetyl ion signals appear at the same pump–probe delay time and exhibit the same rise time. Suitable kinetic model curves were fitted to the recorded acetone and acetyl ion time profiles simultaneously using the Levenberg-Marquard algorithm as implemented in Mathematica.[71]

The acquired photoelectron images were background-subtracted and thresholded, followed by a peak finding and centroiding algorithm implemented in the LabView control software,[72–75] and inverted to determine meridional slices through the original three-dimensional PE distributions using the pBASEX program.[76] Calibrations were performed by measurements of the $^2P_{3/2}$ and $^2P_{1/2}$ lines[77] from ionization of xenon in a multi-photon above-threshold ionization (ATI) process, which were corrected for the ponderomotive shift of the ionization energies caused by the intense electric field. The energy resolution of the photoelectron spectra is limited to typically 70 meV (FWHM) by the spectral widths of the pump and probe laser pulses, the temporal resolution was of the order of 35 fs under optimal conditions. The photoelectron angular distributions (PADs) as function of the angle θ between the laser polarization and the direction of the ejected electrons were described as usual for a three-photon ionization scheme by Legendre polynomials $P_L(\cos\theta)$ up to the third order ($L = 6$).[78]

3.3 Experimental Results

3.3.1 Energy Diagram and Pump–Probe Schemes

Figure 3.2 shows an energy diagram of the acetone molecule giving an overview of the pump and probe transitions of importance in this work with 402 nm probe. The S_1 ($n\pi^*$) state was accessed at ten selected wavelengths from $\lambda_{\mathrm{pump}} = 320$ to

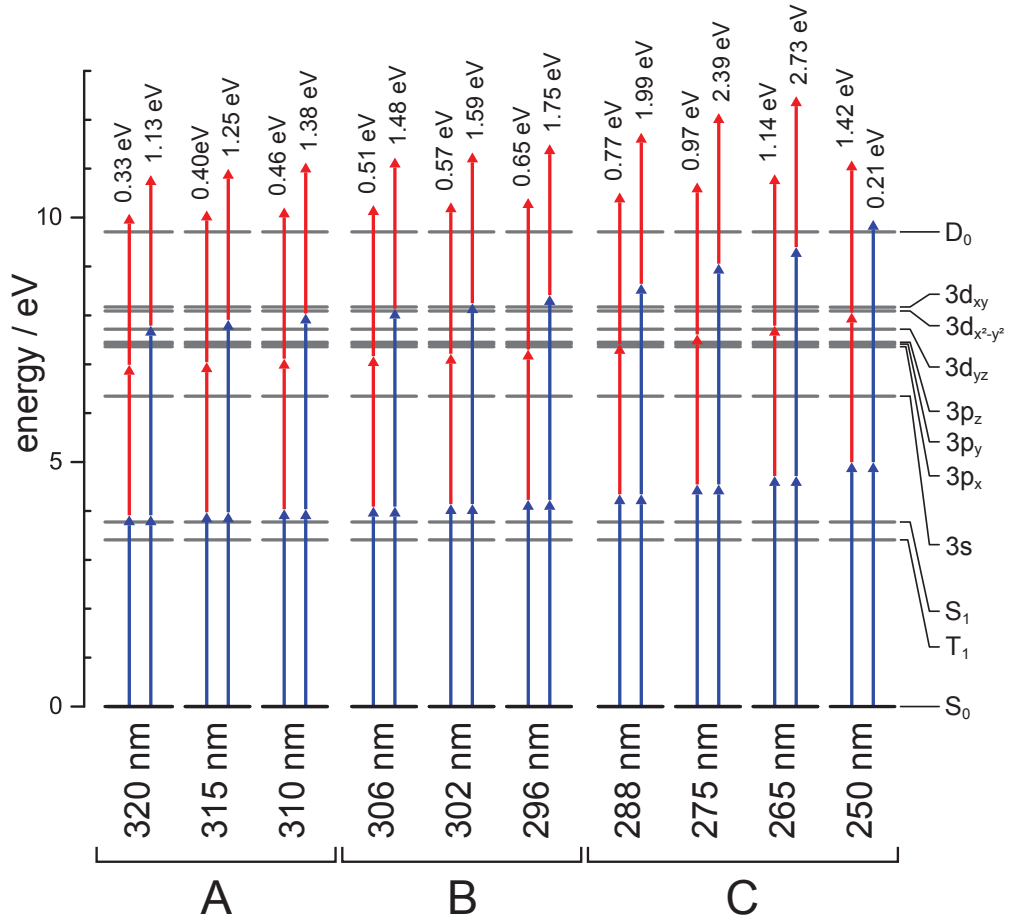

Figure 3.2. Pump–probe schemes in the photoelectron imaging experiment showing the excitation of the acetone molecules with one or two pump photons (blue arrows) at wavelengths of (A) λ_{pump} = 320 – 310 nm, (B) λ_{pump} = 306 – 296 nm and (C) λ_{pump} = 288 – 250 nm as indicated below the arrows, and the subsequent ionization at λ_{probe} = 402 nm (red arrows). Transient mass signals were recorded using λ_{probe} = 804 nm, doubling the number of required probe photons in most cases. The maximal available photoelectron kinetic energies $E_{\mathrm{avl}}^{1+2'}$ and $E_{\mathrm{avl}}^{2+1'}$ are given vertically above the arrows. The division into schemes A – C is made to distinguish the observed three different dynamics regimes (cf. Figs. 3.3 – 3.5).

250 nm. Closely spaced steps were taken around the CC bond dissociation barrier near 306 nm. By the absorption of a second pump photon, transitions are excited to the 3p and 3d Rydberg states. Two 250 nm pump photons are sufficient for a direct ionization of the molecule, so that a transition to Rydberg states by excitation at this wavelength is not expected. The 0–0 transition energies of all valence, Rydberg and ionic states of interest known from previous spectroscopic reports are compiled in Table 3.I. Based on the energy diagram, TOF-MS experiments involving single UV pump photon absorption were performed with four-photon ionization at 804 nm and photoelectron imaging measurements with two-photon ionization at 402 nm. After excitation by two UV pump photons, one to two 804 nm photons or one 402 nm photon were needed for ionization, respectively. The division into the excitation wavelength regions A – C is made to distinguish the observed three different dynamics regimes.

Table 3.I. Compilation of the excitation energies of the vibrationless transitions to relevant electronic valence and Rydberg states of acetone and the symmetry of the excited state. All values given were experimentally determined in the referenced studies.

electronic state	symmetry	transition energy / eV	reference
Valence states:			
S_0	$1\ ^1A_1$	0.000	
S_1 ($n \rightarrow \pi^*$)	$1\ ^1A_2$	3.774	13
T_1 ($n \rightarrow \pi^*$)	$1\ ^3A_2$	3.469	14
$\pi \rightarrow \pi^*$	$4\ ^1A_1$	~ 7.6 [a]	34
Rydberg states:			
$n \rightarrow 3s$	$1\ ^1B_2$	6.348	45
$n \rightarrow 3p_x$	$1\ ^1B_2$	7.360	38
$n \rightarrow 3p_y$	$2\ ^1A_2$	7.411	38
$n \rightarrow 3p_z$	$2\ ^1A_1$	7.451	38
$n \rightarrow 3d_{yz}$	$3\ ^1A_1$	7.715	34
$n \rightarrow 3d_{x^2-y^2}$	$3\ ^1B_2$	8.090	38
$n \rightarrow 3d_{xy}$	$1\ ^1B_1$	8.172	38
Ionic states:			
D_0 (n^{-1})	$1\ ^2B_2$	9.70804	47
D_1 (π_{CO}^{-1})	$1\ ^2B_1$	12.45	79

[a] Estimated vertical excitation energy.

The corresponding energy balance for the $(n + m)$ photoionization schemes with n pump and m probe photons dictates that the photoelectron kinetic energy E_{el} is determined by

$$E_{\mathrm{el}} = \hbar(n \times \omega_{\mathrm{pump}} + m \times \omega_{\mathrm{probe}}) - IE - E_{\mathrm{int}}^{+},$$

where IE is the adiabatic ionization energy and E_{int}^{+} is the internal energy in the cation. The PE kinetic energy reaches the available maximal value $E_{\mathrm{el}} = E_{\mathrm{avl}}$ in the case that $E_{\mathrm{int}}^{+} = 0$. Since the available energies in our experiments all remain below the first excited cationic state (IE_2 = 12.45 eV from Ref. 79), only the acetone cation in its ground electronic state (D_0) needs to be taken into account.

3.3.2 Time-Resolved Time-of-Flight Mass Spectrometry

The measured time profiles for acetone and the acetyl fragment by the TOF-MS experiment are displayed in Figs. 3.3 – 3.5. Based on the ensuing molecular processes at the different pump wavelengths, the results are divided into three groups, which include pump wavelengths from (A) λ_{pump} = 320 – 310 nm (Figure 3.3), (B) λ_{pump} = 306 – 296 nm (Figure 3.4) and (C) λ_{pump} = 288 – 250 nm (Figure 3.5). The

Table 3.II. Fit results for the measured excited state decay dynamics of acetone and the acetyl fragment. The experimental time resolution is given by the σ parameter of the gaussian instrument function. The first decay component τ_1 of the acetyl fitting model (where present) is always unaffected by a possibly listed rise time τ^{rise}. The second and third decay components (τ_2 and τ_3) are modeled with a rising component only if τ^{rise} is given, else likewise to τ_1. The standard deviation obtained from the nonlinear least squares fit is given in parentheses.

		acetone				acetyl						
λ_{pump} / nm	σ / fs	A_1 / %	τ_1 / fs	A_2 / %	τ_2 / ps	A_1 / %	τ_1 / fs	A_2 / %	τ^{rise} / fs	τ_2 / ps	A_3 / %	τ_3 / ns
320	35(1)	0.66	80(5)	0.34	0.71(4)	0.25	190(30)	0.74	—	0.96(5)	0.01	const.
315	33(1)	0.93	$<\sigma$	0.07	0.43(8)	0.56	45(5)	0.43	—	0.67(3)	0.01	const.
310	31(1)	0.91	$<\sigma$	0.09	0.28(4)	0.25	$<\sigma$	0.74	—	0.52(1)	0.01	const.
306	34(2)	0.65	60(10)	0.35	0.31(4)	—	—	0.99	90(5)	0.36(1)	0.01	const.
302	34(2)	0.97	50(5)	0.03	0.4(4)	—	—	0.99	50(5)	0.37(1)	0.01	const.
296	35(1)	0.97	40(5)	0.03	0.2(2)	—	—	0.99	50(5)	0.31(1)	0.01	const.
288	64(2)	0.97	$<\sigma$	0.03	0.4(3)	0.25	$<\sigma$	0.50	60(10)	0.21(2)	0.25	1.3(2)
275	45(1)	0.94	$<\sigma$	0.60	0.42(7)	0.49	$<\sigma$	0.29	60(10)	0.21(3)	0.22	1.4(2)
265	50(1)	0.93	$<\sigma$	0.07	0.38(7)	0.44	$<\sigma$	0.37	—	0.32(2)	0.19	1.3(1)
250	48(1)	0.91	$<\sigma$	0.09	0.13(3)	0.96	$<\sigma$	0.04	—	0.13(3)	—	—

acetone ion signals in each time profile are normalized to unity, while the respective acetyl fragment signals are scaled according to the relative count rates. The different time constants extracted by nonlinear least squares fitting to the experimental data are summarized in Table 3.II. As can be seen, the acetone transients always exhibit two exponential decay components. The determination of the fast time constant (τ_1) was limited in most cases by the experimental time resolution and reached its longest value of 80 fs on excitation at λ_{pump} = 320 nm, close to the electronic origin. The second time constant (τ_2) was between 700 and 110 fs, depending on the excitation wavelength.

Acetyl fragment ions were observed in the mass spectra with all pump wavelengths. After excitation in region A, between λ_{pump} = 320 and 310 nm, the fragment ion appeared promptly together with the acetone ion, and an acetyl/acetone ion signal ratio of ∼20% was measured. This would be in agreement with a dissociation of acetone ions after the multiphoton ionization. The decay dynamics could be fitted using one fast and one slow exponential as well as a constant offset of very small amplitude (∼1%). Following excitation in region B, between 306 and 296 nm, the acetyl/acetone ratio increased strongly and showed a delayed rise, with associated time constants of τ^{rise} = 90 – 50 femtoseconds. This was observed especially at 306 nm, where the ion signal ratio reached nearly unity. No prompt component was observed in this wavelength range, indicating the onset of CC bond dissociation from excited neutral acetone molecules. The prompt acetyl ion signal started to show up again, however, next to the delayed acetyl signal, in the transients after excitation in

region C, between 288 and 275 nm, although great experimental care was taken to use the lowest possible probe pulse intensities. Here, time constants were fitted for both channels. After 265 nm excitation, the two channels were no longer separated, and the acetyl signal was modeled using three exponential decay terms, without a rising component. Following excitation at 250 nm, eventually, the acetone and acetyl ion transients were nearly completely reduced to the cross-correlation of the pump and probe laser pulses, as their buildup and decay became too fast for our experimental time resolution. A slow rise of the acetyl ion on a time scale of several tens or hundreds of picoseconds, as was reported by Diau *et al.*,[57] was not observed in our data.

3.3.3 Time-Resolved Photoelectron Imaging

Photoelectron images were taken at a number of fixed delay times using the same pump wavelengths as for the MS data above, but with $\lambda_{\mathrm{probe}} = 402$ nm. The resulting photoelectron spectra are plotted in Figs. 3.3 – 3.5 on the right, next to the respective acetone and acetyl ion time profiles by MS on the left. All spectra exhibit signals in two distinct energy regimes which are defined by the respective maximal available photoelectron kinetic energies $E_{\mathrm{avl}}^{1+2'}$ and $E_{\mathrm{avl}}^{2+1'}$ originating from the two possible pump–probe multi-photon ionization schemes. Photoelectrons in a lower energy region up to $E_{\mathrm{avl}}^{1+2'}$ arise by absorption of one UV pump photon and ionization with two 402 nm probe photons. Photoelectrons with higher energy up to $E_{\mathrm{avl}}^{2+1'}$ require absorption of two UV pump photon followed by one-photon (402 nm) ionization. The respective values of $E_{\mathrm{avl}}^{1+2'}$ and $E_{\mathrm{avl}}^{2+1'}$ depend on the pump wavelength and are marked in the PE spectra by dashed vertical lines. Photoelectrons directly at $E_{\mathrm{el}} = E_{\mathrm{avl}}^{2+1'}$ can be caused by a sequence of pump + pump + probe or pump + probe + pump absorption at zero time delay and are therefore not unambiguously assignable. The broad PE background reaching from 0 eV up to 2.6 eV in the spectrum with 250 nm excitation, where the signal-to-noise ratio by the 1+2' ionization mechanism was very low, stems from single-color four-photon ionization at $\lambda_{\mathrm{probe}} = 402$ nm.

The anisotropy parameters of the photoelectron angular distributions were only evaluated at the shortest time delays. Anisotropy parameters at larger time delays showed a large uncertainty and were thus omitted. During the temporal overlap of the pump and probe laser pulses, the anisotropy of the PAD is primarily determined by the alignment of the transition dipole moment to the laser polarization with a $\cos^2(\theta)$ distribution. This is mirrored by the values of $\beta_2 \approx 0.9$ and $\beta_4 \approx 0$ for photoelectrons assigned to the S_1 ($n\pi^*$) state. In comparison, β_2 values for photoelectrons emitted from the 3p and $3d_{yz}$ Rydberg states were found to be slightly reduced to $\beta_2 \approx 0.6$. This may be caused by the vibronic interaction of the A_1 Rydberg states with the $\pi\pi^*$ (A_1) valence state that will be discussed below.

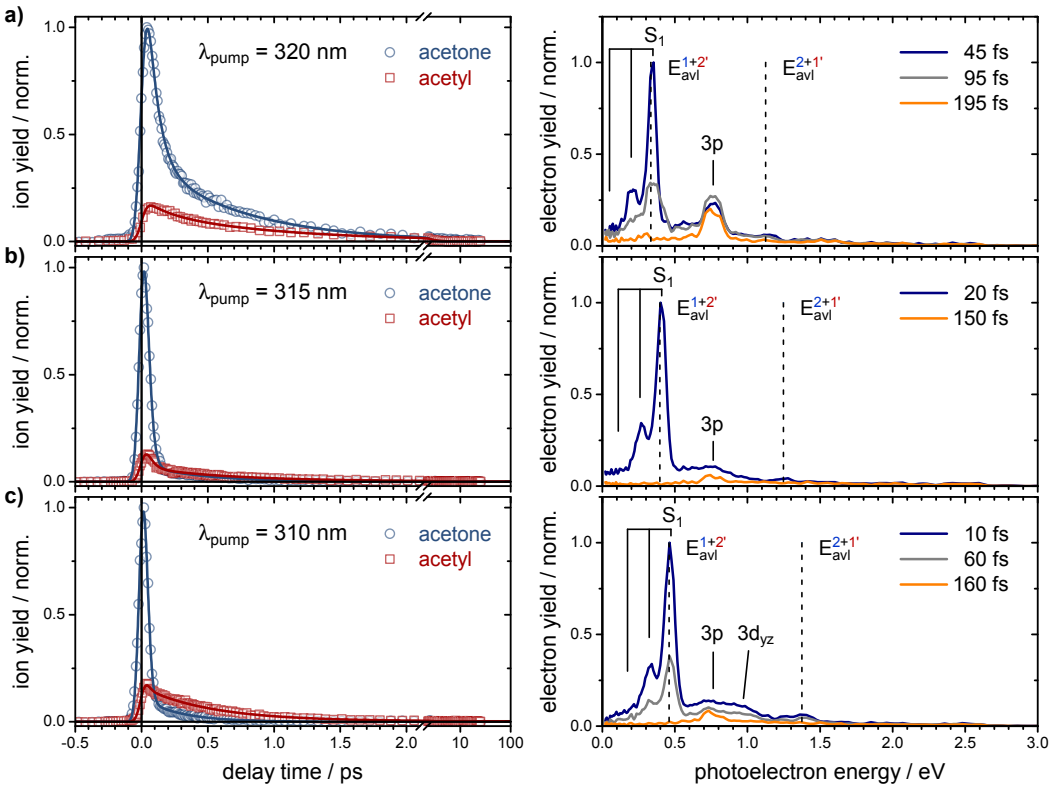

Figure 3.3. Recorded transient ion signals together with the fitted time profiles (left; acetone in blue, acetyl in red) and photoelectron spectra (right) after excitation at a) λ_{pump} = 320 nm, b) 315 nm and c) 310 nm. The maximal available energies in the photoelectron spectra by (1+2') and (2+1') ionization are indicated by the dashed vertical lines. The S_1 state photoelectron band shows the indicated CO stretch (1211 cm^{-1}) vibrational progression. The photoelectron spectra at zero time delay were normalized to unity, and all other spectra were scaled according to the number of recorded photoelectrons. The maximal available photoelectron kinetic energies by (1+2') and (2+1') ionization are indicated by the dashed vertical lines.

3.4 Discussion

3.4.1 Region A: Excitation Below the CC Dissociation Barrier (320 nm $\geq \lambda_{\mathrm{pump}} \geq$ 310 nm)

Upon excitation of the acetone molecule to the S_1 electronic state at λ_{pump} = 320, 315 or 310 nm, the PE spectra, depicted in Figure 3.3 a – c on the right, show the most intense signal from the S_1 transition directly at $E_{\mathrm{el}} = E_{\mathrm{avl}}^{1+2'}$. The respective peaks are accompanied by a vibrational progression with up to two quanta of excitation. The spacing of 0.15 eV corresponds to the known CO stretch frequency in the S_1 state (ν = 1211 cm^{-1}, Ref. 8). The virtually complete disappearance of the S_1 PE band in less than 150 fs is in excellent agreement with the observed fast (τ_1 = 80 – 35 fs) decay of the acetone ion mass signal. Both findings contrast with the established picture that the S_1 state is long-lived, with a lifetime extending even

into the microsecond range.[5,6,8–10,12,14,80] However, Brogaard *et al.*[63] proposed an explanation based on ab initio quantum dynamics simulations which showed that the initially prepared wavepacket on the S_1 PES actually leaves the Franck–Condon probing window for ionization in less than 30 fs towards the S_1 potential energy minimum, where the molecular structure is deplanarized around the central carbon atom (the aforementioned C–CO–C pyramidalization). Thus, the observed ultrafast decay of the acetone signal is not due to dissociation, but to a relaxation to the excited state minimum.

Surprisingly, acetyl mass signals appearing with the acetone mass signals are observed, as can be seen in Figure 3.3 a – c on the left. For their explanation, we turn to the energy range up to $E_{\mathrm{avl}}^{2+1'}$ in the PE spectra. The absorption of two pump photons in this pump wavelength region is seen to drive transitions to the 3p Rydberg states. The 3p PE band at 0.77 eV after 320 nm excitation is pronounced, but rather broad, as it likely arises by a superposition from more than one of the three energetically close-lying 3p components. Its survival on the experimental time scale can be readily associated with the slow acetone decay component (τ_2 = 710 – 280 fs) in the transient ion profiles. In the spectra after 315 and 310 nm excitation, the 3p signal becomes weaker, but remains assignable. In the 310 nm spectrum, an additional broad band starts to appear weakly around 1 eV. Its assignment to the $3d_{yz}$ state will be discussed in the next section.

If the observed acetyl ions were created after fragmentation of the neutral molecule, the mass signals should have a delayed rise time comparable to the acetone decay times τ_1 or τ_2. Since this is not the case, the acetyl ions can only originate from fragmentation of vibrationally excited acetone cations after ionization. As already mentioned, fragmentation of the acetone ion to an acetyl ion and a neutral methyl radical requires a threshold energy of 0.8 eV in the parent ion.[64–66] But the photoelectron signal from the S_1 state, with the maximal available photoelectron energy $E_{\mathrm{avl}}^{1+2'}$, implies that the cation is vibrationally cold and thus stable. Ionization from the 3p state with one 402 nm photon would leave 0.4 – 0.6 eV in the cation, i. e. would also yield a stable cation. Hence, it is important that the transient mass spectra were recorded using 804 nm as probe wavelength: Ionization through absorption of three 804 nm photons in an above-threshold ionization (ATI) process leaves 1.9 eV of excess energy in the acetone ion, well more than the 0.8 eV threshold for fragmentation. This mechanism seems to be only remaining explanation for the appearance of the prompt acetyl fragment ion signal at zero delay time in this pump wavelength region.

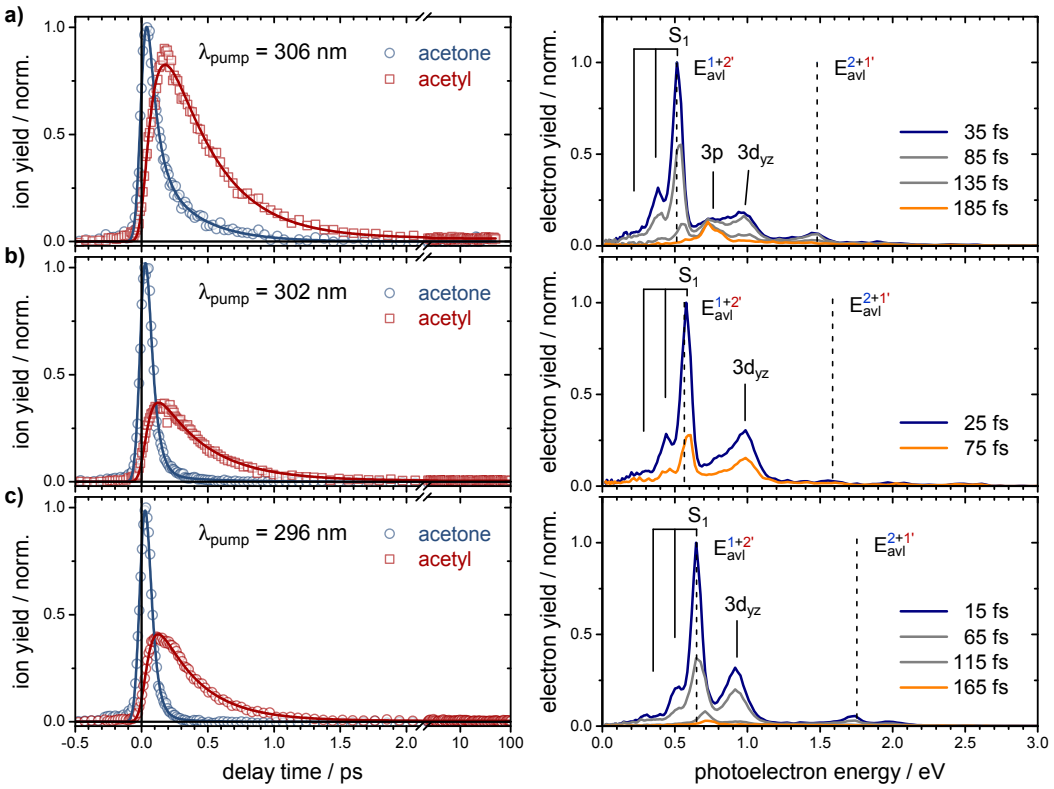

Figure 3.4. Recorded transient ion signals together with the fitted time profiles (left; acetone in blue, acetyl in red) and photoelectron spectra (right) after excitation at a) $\lambda_{\mathrm{pump}} = 306$ nm, b) 302 nm and c) 296 nm. The $3d_{yz}$ Rydberg state is reached by absorption of two pump photons, and responsible for the strong, slightly delayed acetyl signal by CC predissociation, presumably *via* the $\pi\pi^*$ state.

3.4.2 Region B: Excitation To and Above the CC Dissociation Barrier (306 nm $\geq \lambda_{\mathrm{pump}} \geq$ 296 nm)

The PE spectra recorded at $\lambda_{\mathrm{pump}} = 306$, 302 or 296 nm, depicted in Figure 3.4 a – c on the right, are in large parts similar to the spectra recorded below the 306 nm barrier height. The S_1 state signal with the CO stretch progression is still present at $E_{\mathrm{el}} = E_{\mathrm{avl}}^{1+2'}$ and decays in less than 150 femtoseconds. The transient mass signal of acetone (Figure 3.4 on the left) shows the corresponding fast ($\tau_1 = 60 - 40$ fs) decay component, associated to structural relaxation as discussed above. The long-lived PE band of the 3p state can still be assigned in the 306 nm spectrum, and while it is only weakly present around 0.77 eV in the 302 nm spectrum, it cannot be identified in the 296 nm spectrum. Its disappearance is in good agreement with the observed slow ($\tau_2 = 400 - 200$ fs) decay of the acetone ion mass signal, which decreases in amplitude with increasing excitation energy (cf. Table 3.II).

A new feature, which was not present in the spectra in region A, is the relatively broad PE band around 1 eV that already weakly showed in the 310 nm spectrum

(Figure 3.3 c). We can assign this band to the $3d_{yz}$ (A_1) Rydberg state. A PE energy of 1.1 eV is expected from this state, which corresponds to the right edge of the band. As the molecular structure in electronic Rydberg states and in the cation in the ground electronic state are usually very similar, one would expect a narrow photoelectron signal epecially from a high-lying 3d Rydberg state. A broadening due to a superposition with PE signals from neighboring states is unlikely due to their energetic separation of $\sim$0.3 eV (cf. Table 3.I). Therefore, the observed spectral shape is likely determined by unresolved vibrational structure, caused by vibronic interactions of the $3d_{yz}$ (A_1) Rydberg state with the $\pi\pi^*$ (A_1) valence state. While the perturbation of the $3p_y$ (A_1) Rydberg state by the $\pi\pi^*$ state has been observed before,[35–39] experimental evidence for its interaction with the $3d_{yz}$ Rydberg state has not been reported previously.

The acetyl ion yield increased strongly in wavelength region B, as can be seen from the transient ion signals in Figure 3.4 a – c on the left. Moreover, it shows a delayed rise with associated time constants of $\tau^{\text{rise}} = 90 - 50$ femtoseconds. We attribute these observations to a fragmentation of the neutral molecule, as dissociation of the acetone ion can be ruled out in this wavelength region because of the following considerations: (*i*) Ionization of the 3p or $3d_{yz}$ Rydberg states with 2×804 nm (or 1×402 nm) probe photons leaves 0.4 – 0.7 eV internal energy in the cation, which is below the dissociation threshold. (*ii*) The ATI process by absorption of 3×804 nm probe photons, which would result in enough internal energy for dissociation of the acetone ion, should be sensitive to the intensity of the probe pulses. Figure 3.6 shows the acetyl transient mass signals for different probe pulse intensities. When a low intensity is chosen (Figure 3.6 a), only ionization by absorption of 2×804 nm probe photons takes place, and the acetyl fragment arising from dissociation of the neutral acetone molecule is recorded. At higher probe pulse intensities (Figure 3.6 b and c), the three-photon ATI process sets in, resulting in the additional ion signal peaking around time zero. This demonstrates that acetyl signals from both processes can be distinguished in the transient mass spectra by their rise time. In summary, the only difference between the wavelength regions A and B is the two-photon excitation of the $3d_{yz}$ Rydberg state. Therefore, we conclude that there is an ultrafast pathway for the photodissociation of acetone after excitation of the $3d_{yz}$ Rydberg state, corresponding to the rise time $\tau^{\text{rise}} = 90 - 50$ fs of acetyl mass signal and in excellent agreement with the decay time of $3d_{yz}$ state PE band. The subsequent decay of the acetyl mass signal in $\tau_2 = 370 - 310$ fs is likely due to dissociation of the second CC bond.

As mentioned before, the vibronic interactions of high-lying A_1 electronic states of acetone have been the subject of theoretical studies. Merchan *et al.*[36] and Diau *et al.*[57] performed quantum-chemical calculations at the CASPT2 and CASMP2 levels of theory, respectively, and showed that the $3d_{yz}$ (A_1) Rydberg state and the

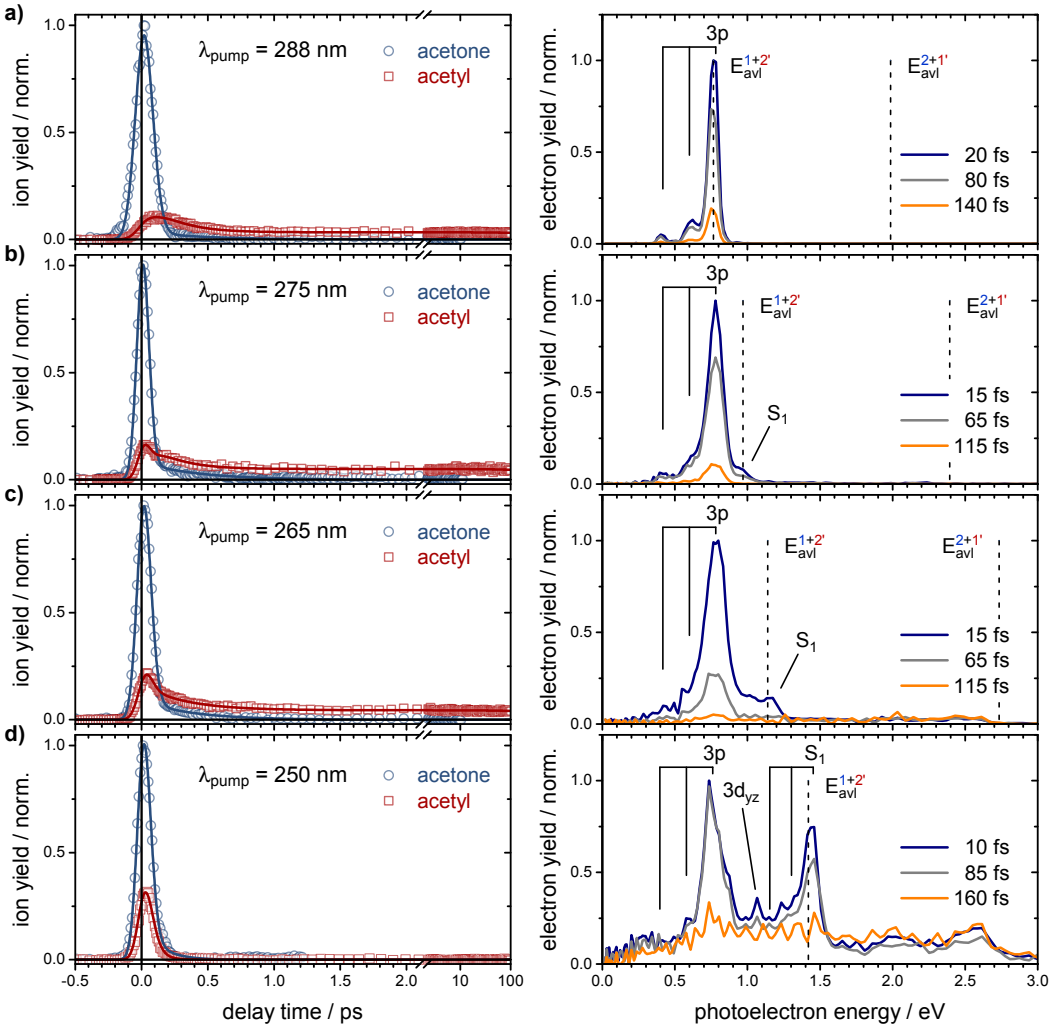

Figure 3.5. Recorded transient ion signals together with the fitted time profiles (left; acetone in blue, acetyl in red) and photoelectron spectra (right) after excitation at a) λ_{pump} = 288 nm, b) 275 nm, c) 265 nm and d) 250 nm. The fragmentation of the acetone cation obscures the dissociation of the neutral Rydberg excited molecules, giving both a prompt and a delayed contribution to the observed acetyl ion signals. The photoelectron spectra are dominated by resonance enhancement through the intermediate 3p Rydberg state in the multiphoton ionization (with 1468 cm^{-1} CO stretch vibrational progression indicated).

$\pi\pi^*$ (A_1) valence state form an avoided crossing and thus a double-well potential energy surface with a calculated barrier height of 0.7 eV along the CO stretch coordinate. The two-photon excitation of the $3d_{yz}$ state activates not only the CO stretch vibration, which guides the wavepacket over the barrier to the $\pi\pi^*$ state, but also non-totally symmetric modes, such as the CO out-of-plane bending mode, the CCO in-plane bending mode and the asymmetric CC stretch mode that are likely involved in the CC bond dissociation.[81,82] The involvement of the $\pi\pi^*$ state is affirmed by our observation that dissociation takes place only after two-photon excitation of the $3d_{yz}$ state at $\lambda_{\mathrm{pump}} < 306$ nm (i. e., at > 8.1 eV), but not at $\lambda_{\mathrm{pump}} = 310$ nm (8.0 eV), where the corresponding PE band is also present in the spectra. Considering this small energy difference and the vibrationless origin of the $3d_{yz}$ state

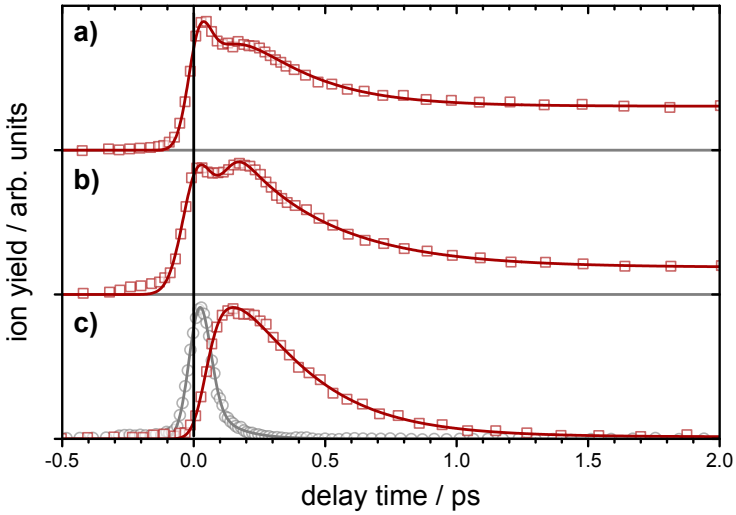

Figure 3.6. Transient mass signal of the acetyl fragment (red symbols) and the fitted model (red line) with a) high, b) medium and c) low probe pulse intensities, recorded at $\lambda_{\mathrm{pump}} = 302$ nm. The acetone transient mass signal is shown in grey on the bottom line. The dissociation of the neutral acetone molecule can be observed only with low probe pulse intensity. With higher probe pulse intensities, the signal around time zero from dissociation of the acetone cation gains in amplitude.

at 7.7 eV (see Table 3.I), we can estimate the barrier height from the $3d_{yz}$ Rydberg state to the $\pi\pi^*$ state to be on the order of 0.4 eV.

3.4.3 Region C: Excitation Well Above the CC Dissociation Barrier (288 nm $\geq \lambda_{\mathrm{pump}} \geq$ 250 nm)

The PE spectra recorded at $\lambda_{\mathrm{pump}} = 288$ nm, 275nm, 265 nm and 250 nm are depicted in Figure 3.5 a–d on the right. The PE band from the S_1 state is observed at $E_{\mathrm{el}} = E_{\mathrm{avl}}^{1+2'}$ in the PE spectra with $\lambda_{\mathrm{pump}} = 275$ nm, 265 nm and 250 nm, and probably only obscured by the PE band from the 3p Rydberg states at $\lambda_{\mathrm{pump}} = 288$ nm. In pump wavelength region C, the 3p states are resonant intermediate states in the 1+2' ionization process (see Figure 3.2). The observed PE bands at 0.77 eV are therefore assigned to the 3p states after absorption of one pump and one probe photon. The accompanying vibrational progression, with up to two quanta of excitation and a spacing of 0.18 eV, corresponds to the CO stretch vibration in these states ($\nu = 1468$ cm^{-1}, Ref. 38). A PE band from the $3d_{yz}$ state, excited by the same process, is observed at $\lambda_{\mathrm{pump}} = 250$ nm. These transitions to the 3p and $3d_{yz}$ states can only take place during the temporal overlap of the pump and probe pulses. The resonant enhancement of the multi-photon ionization process is responsible for the acetone mass signal spiking at time zero (see on the left of Figure 3.5), and the corresponding time constant τ_1 is therefore not resolved (cf. Table 3.II).

The second decay time constant τ_2 = 430 – 130 fs of the acetone mass signal in region C is likely caused by a radiationless electronic deactivaton seen after absorption of two pump photons. The acetyl mass signal could still be modeled with a delayed rise of τ^{rise} = 60 fs after excitation at λ_{pump} = 288 nm and 275nm, indicating a dissociation of the neutral molecule. Unfortunately, the PE spectra do not reveal the involved excited states after the two-photon excitation. For $\lambda_{\mathrm{pump}} \leq$ 275 nm, a prompt component, given by τ_1, needs to be included to fit the acetyl mass signal. As in regions A and B, this component corresponds to dissociation of the acetone ion. In region C, however, this process cannot be prevented by reducing the probe pulse intensity, because even the ionization with the minimal number of probe photons (see Figure 3.2) leaves enough internal energy in the ion to surmount the dissociation threshold.

3.5 Conclusions

We have excited single-photon transitions to the S_1 ($n\pi^*$) electronic state of acetone in a supersonic molecular beam using a broad range of pump wavelengths from 320 nm $\geq \lambda_{\mathrm{pump}} \geq$ 250 nm, and monitored the evolution of the excited state using femtosecond time-resolved time-of-flight mass spectrometry and photoelectron imaging spectroscopy. After the excitation, structural relaxation towards the potential energy minimum was seen to take place in less than 80 femtoseconds. This process goes hand in hand with a strongly reduced photoionization cross section that prevents monitoring of the dynamics of the relaxed species. We observed no indications for an ultrafast CC bond fission in the S_1 ($n\pi^*$) state. The commonly accepted picture of a CC bond cleavage of acetone only on the $^3n\pi^*$ potential energy surface on a time scale of at least nanoseconds is therefore fully intact. After ionization of the S_1 state, the acetone cation is found to be vibrationally cold and no further decomposition takes place.

The absorption of two pump photons excites energetically high-lying electronic Rydberg states. The photoelectron spectra revealed two distinct bands that could be assigned to the 3p and $3d_{yz}$ Rydberg states. The lifetime of the 3p states was determined to be between 700 – 200 fs, depending on the pump wavelength. Ionization of these 3p states leaves a vibrationally excited ion that dissociates during the flight time to the detector when the internal energy exceeds 0.8 eV.

After two-photon absorption at $\lambda_{\mathrm{pump}} \leq$ 310 nm, photoelectron bands corresponding to the $3d_{yz}$ state were observed. For pump wavelengths of λ_{pump} = 306 nm and below (corresponding to an excitation energy of 8.1 eV), a barrier on the $3d_{yz}$ potential energy surface can be surmounted which is formed by an avoided crossing

with the $\pi\pi^*$ state. The energy of this barrier accidentally coincides with twice the barrier height of α–CC cleavage on the $^3n\pi^*$ potential energy surface of 4.05 eV (λ = 306 nm). The decay time of the photoelectron band and the corresponding delayed rise time of the acetyl fragment indicate a subsequent CC bond fission *via* the $\pi\pi^*$ state in 90 – 50 femtoseconds.

References

1. R. G. W. Norrish, H. G. Crone, and O. D. Saltmarsh, "318. Primary photochemical reactions. Part V. The spectroscopy and photochemical decomposition of acetone," J. Chem. Soc., 1456–1464 (1934).
2. H. Okabe, *Photochemistry of small molecules* (Wiley, 1978).
3. C. E. Wayne and R. P. Wayne, *Photochemistry* (Oxford University Press, 1996).
4. R. F. Borkman and D. R. Kearns, "Electronic-Relaxation Processes in Acetone," J. Chem. Phys. **44**, 945–949 (1966).
5. G. M. Breuer and E. K. C. Lee, "Fluorescence decay times of cyclic ketones, acetone, and butanal in the gas phase," J. Phys. Chem. **75**, 989–990 (1971).
6. A. M. Halpern and W. R. Ware, "Excited Singlet State Radiative and Nonradiative Transition Probabilities for Acetone, Acetone-d_6, and Hexafluoroacetone in the Gas Phase, in Solution, and in the Neat Liquid," J. Chem. Phys. **54**, 1271–1276 (1971).
7. J. C. Miller and R. F. Borkman, "Phosphorescence Lifetimes of Partially Deuterated Ketones," J. Chem. Phys. **56**, 3727–3729 (1972).
8. M. Baba, I. Hanazaki, and U. Nagashima, "The S_1(n, π*) states of acetaldehyde and acetone in supersonic nozzle beam: Methyl internal rotation and C=O out-of-plane wagging," J. Chem. Phys. **82**, 3938–3947 (1985).
9. O. Anner, H. Zuckermann, and Y. Haas, "Fluorescence decay of jet-cooled acetone," J. Phys. Chem. **89**, 1336–1339 (1985).
10. H. Zuckermann, B. Schmitz, and Y. Haas, "The radiative lifetime of acetone: resolution of an apparent discrepancy," Chem. Phys. Lett. **151**, 323–327 (1988).
11. H. Zuckermann, B. Schmitz, and Y. Haas, "Dissociation energy of an isolated triplet acetone molecule," J. Phys. Chem. **92**, 4835–4837 (1988).
12. H. Zuckermann, B. Schmitz, and Y. Haas, "Acetone photophysics in seeded supersonic molecular beams," J. Phys. Chem. **93**, 4083–4091 (1989).
13. H. Zuckermann, Y. Haas, M. Drabbels, J. Heinze, W. L. Meerts, J. Reuss, and J. van Bladel, "Acetone, a laser-induced fluorescence study with rotational resolution at 320 nm," Chem. Phys. **163**, 193–208 (1992).
14. Y. Haas, "Photochemical α-cleavage of ketones: revisiting acetone," Photochem. Photobiol. Sci. **3**, 6–16 (2004).

15. H. B. Singh, D. O'Hara, D. Herlth, W. Sachse, D. R. Blake, J. D. Bradshaw, M. Kanakidou, and P. J. Crutzen, "Acetone in the atmosphere: Distribution, sources, and sinks," J. Geophys. Res. **99**, 1805–1819 (1994).
16. H. B. Singh, M. Kanakidou, P. J. Crutzen, and D. J. Jacob, "High concentrations and photochemical fate of oxygenated hydrocarbons in the global troposphere," Nature **378**, 50–54 (1995).
17. F. Arnold, V. Bürger, B. Droste-Fanke, F. Grimm, A. Krieger, J. Schneider, and T. Stilp, "Acetone in the upper troposphere and lower stratosphere: Impact on trace gases and aerosols," Geophys. Res. Lett. **24**, 3017–3020 (1997).
18. H. B. Singh, Y. Chen, A. Staudt, D. Jacob, D. Blake, B. Heikes, and J. Snow, "Evidence from the Pacific troposphere for large global sources of oxygenated organic compounds," Nature **410**, 1078–1081 (2001).
19. B. J. Finlayson-Pitts and J. N. Pitts, Jr., *Chemistry of the Upper and Lower Atmosphere: Theory, Experiments, and Applications* (Academic Press, 1999).
20. P. Warneck, *Chemistry of the Natural Atmosphere* (Academic Press, 1999).
21. H. Meyrahn, J. Pauly, W. Schneider, and P. Warneck, "Quantum yields for the photodissociation of acetone in air and an estimate for the life time of acetone in the lower troposphere," J. Atmospheric Chem. **4**, 277–291 (1986).
22. S. A. McKeen, T. Gierczak, J. B. Burkholder, P. O. Wennberg, T. F. Hanisco, E. R. Keim, R.-S. Gao, S. C. Liu, A. R. Ravishankara, and D. W. Fahey, "The photochemistry of acetone in the upper troposphere: A source of odd-hydrogen radicals," Geophys. Res. Lett. **24**, 3177–3180 (1997).
23. T. Gierczak, J. B. Burkholder, S. Bauerle, and A. R. Ravishankara, "Photochemistry of acetone under tropospheric conditions," Chem. Phys. **231**, 229–244 (1998).
24. M. A. Blitz, D. E. Heard, M. J. Pilling, S. R. Arnold, and M. P. Chipperfield, "Pressure and temperature-dependent quantum yields for the photodissociation of acetone between 279 and 327.5 nm," Geophys. Res. Lett. **31**, L06111 (2004).
25. M. A. Blitz, D. E. Heard, and M. J. Pilling, "Study of Acetone Photodissociation over the Wavelength Range 248–330 nm: Evidence of a Mechanism Involving Both the Singlet and Triplet Excited States," J. Phys. Chem. A **110**, 6742–6756 (2006).
26. R. Nádasdi, G. Kovács, I. Szilágyi, A. Demeter, S. Dóbé, T. Bérces, and F. Márta, "Exciplex laser photolysis study of acetone with relevance to tropospheric chemistry," Chem. Phys. Lett. **440**, 31–35 (2007).
27. A. Maranzana, J. R. Barker, and G. Tonachini, "Master equation simulations of competing unimolecular and bimolecular reactions: application to OH production in the reaction of acetyl radical with O_2," Phys. Chem. Chem. Phys. **9**, 4129–4141 (2007).
28. V. Khamaganov, R. Karunanandan, A. Rodriguez, and J. N. Crowley, "Photolysis of $CH_3C(O)CH_3$ (248 nm, 266 nm), $CH_3C(O)C_2H_5$ (248 nm) and $CH_3C(O)Br$ (248 nm): pressure dependent quantum yields of CH_3 formation," Phys. Chem.

Chem. Phys. **9**, 4098–4113 (2007).
29. B. Rajakumar, T. Gierczak, J. E. Flad, A. R. Ravishankara, and J. B. Burkholder, "The CH_3CO quantum yield in the 248 nm photolysis of acetone, methyl ethyl ketone, and biacetyl," J. Photochem. Photobiol. A **199**, 336–344 (2008).
30. V. G. Khamaganov, R. Karunanandan, A. Horowitz, T. J. Dillon, and J. N. Crowley, "Photolysis of $CH_3C(O)CH_3$ at 248 and 266 nm: pressure and temperature dependent overall quantum yields," Phys. Chem. Chem. Phys. **11**, 6173–6181 (2009).
31. H. Somnitz, T. Ufer, and R. Zellner, "Acetone photolysis at 248 nm revisited: pressure dependence of the CO and CO_2 quantum yields," Phys. Chem. Chem. Phys. **11**, 8522–8531 (2009).
32. D. W. Liao, A. M. Mebel, M. Hayashi, Y. J. Shiu, Y. T. Chen, and S. H. Lin, "Ab initio study of the n-π* electronic transition in acetone: Symmetry-forbidden vibronic spectra," J. Chem. Phys. **111**, 205–215 (1999).
33. A. B. Rocha and C. E. Bielschowsky, "Intensity of the n$\rightarrow\pi$* symmetry-forbidden electronic transition in acetone by direct vibronic coupling mechanism," Chem. Phys. Lett. **337**, 331–334 (2001).
34. M. Nobre, A. Fernandes, F. F. da Silva, R. Antunes, D. Almeida, V. Kokhan, S. V. Hoffmann, N. J. Mason, S. Eden, and P. Limão-Vieira, "The VUV electronic spectroscopy of acetone studied by synchrotron radiation," Phys. Chem. Chem. Phys. **10**, 550–560 (2008).
35. X. Xing, R. McDiarmid, J. G. Philis, and L. Goodman, "Vibrational assignments in the 3p Rydberg states of acetone," J. Chem. Phys. **99**, 7565–7573 (1993).
36. M. Merchán, B. O. Roos, R. McDiarmid, and X. Xing, "A combined theoretical and experimental determination of the electronic spectrum of acetone," J. Chem. Phys. **104**, 1791–1804 (1996).
37. R. McDiarmid and X. Xing, "Nonadiabatic coupling of the 3p Rydberg and $\pi\pi$* valence states of acetone," J. Chem. Phys. **107**, 675–679 (1997).
38. D. H. A. ter Steege, A. C. Wirtz, and W. J. Buma, "Vibronic coupling in excited states of acetone," J. Chem. Phys. **116**, 547–560 (2002).
39. S. N. Thakur, D. Guo, T. Kundu, and L. Goodman, "Two-photon photoacoustic spectroscopy of acetone 3p Rydberg states," Chem. Phys. Lett. **199**, 335–340 (1992).
40. J. G. Philis and L. Goodman, "Methyl rotor effects on acetone Rydberg spectra. II. The $^1B_2(3s\leftarrow n)\leftarrow{}^1A_1$ transition," J. Chem. Phys. **98**, 3795–3802 (1993).
41. G. A. Gaines, D. J. Donaldson, S. J. Strickler, and V. Vaida, "The (n_0-3s) Rydberg state of acetone: absorption spectroscopy of jet-cooled $(CH_3)_2CO$ and $(CD_3)_2CO$," J. Phys. Chem. **92**, 2762–2766 (1988).
42. A. Gedanken and R. McDiarmid, "Experimental one and two photon absorption properties of acetone," J. Chem. Phys. **92**, 3237–3238 (1990).
43. R. McDiarmid, "On the absorption spectrum of the 3s Rydberg state of acetone," J. Chem. Phys. **95**, 1530–1536 (1991).

44. P. Brint, L. O'Toole, S. Couris, and D. Jardine, "Multiphoton ionisation spectroscopy of the 3s(2 + 2, 1) and 4s(3 + 1) Rydberg states of acetone: evidence for a molecular valence state at 153 nm," J. Chem. Soc., Faraday Trans. **87**, 2891–2895 (1991).
45. T. Kundu, S. N. Thakur, and L. Goodman, "Methyl rotor effects on acetone Rydberg spectra. I. The $^1A_2(3p\leftarrow n)\leftarrow{}^1A_1$ transition," J. Chem. Phys. **97**, 5410–5416 (1992).
46. Y. F. Zhu, S. L. Allman, R. C. Phillips, W. R. Garrett, and C. H. Chen, "Photophysics of the acetone 3p Rydberg states utilizing two-photon resonant ionization spectroscopy," Chem. Phys. **202**, 175–184 (1996).
47. R. T. Wiedmann, L. Goodman, and M. G. White, "Two-color zero kinetic energy–pulsed field ionization spectroscopy of the acetone *n*-radical cation: the a_2 torsional vibration," Chem. Phys. Lett. **293**, 391–396 (1998).
48. A. Shastri, P. J. Singh, B. Raja Sekhar, R. D'Souza, and B. Jagatap, "The role of torsional modes in the electronic absorption spectrum of acetone," J. Quant. Spectrosc. Radiat. Transf. **113**, 1553–1565 (2012).
49. L. O'Toole, P. Brint, C. Kosmidis, G. Boulakis, and P. Tsekeris, "Vacuum-ultraviolet absorption spectra of propanone, butanone and the cyclic ketones $C_nH_{2n-2}O$ (n= 4, 5, 6, 7)," J. Chem. Soc., Faraday Trans. **87**, 3343–3351 (1991).
50. S. K. Kim, S. Pedersen, and A. H. Zewail, "Direct femtosecond observation of the transient intermediate in the α-cleavage reaction of $(CH_3)_2CO$ to $2CH_3+CO$: Resolving the issue of concertedness," J. Chem. Phys. **103**, 477–480 (1995).
51. S. A. Buzza, E. M. Snyder, and A. W. Castleman, Jr., "Further direct evidence for stepwise dissociation of acetone and acetone clusters," J. Chem. Phys. **104**, 5040–5047 (1996).
52. S. A. Buzza, E. M. Snyder, D. A. Card, D. E. Folmer, and A. W. Castleman, Jr., "Femtosecond excitation dynamics of acetone: Dissociation, ionization, and the evolution of multiply charged elemental species," J. Chem. Phys. **105**, 7425–7431 (1996).
53. T. Shibata and T. Suzuki, "Photofragment ion imaging with femtosecond laser pulses," Chem. Phys. Lett. **262**, 115–119 (1996).
54. J. C. Owrutsky and A. P. Baronavski, "Ultrafast photodissociation dynamics of the S_1 and S_2 states of acetone," J. Chem. Phys. **110**, 11206–11213 (1999).
55. Q. Zhong, L. Poth, and A. W. Castleman, Jr., "Ultrafast dissociation dynamics of acetone: A revisit to the S_1 state and 3s Rydberg state," J. Chem. Phys. **110**, 192–196 (1999).
56. P. Farmanara, V. Stert, and W. Radloff, "Ultrafast photodissociation dynamics of acetone excited by femtosecond 155 nm laser pulses," Chem. Phys. Lett. **320**, 697–702 (2000).
57. E. W.-G. Diau, C. Kötting, and A. H. Zewail, "Femtochemistry of Norrish Type-I Reactions: I. Experimental and Theoretical Studies of Acetone and Related Ketones on the S_1 Surface," ChemPhysChem **2**, 273–293 (2001).

58. A. P. Baronavski and J. C. Owrutsky, "Ketone excited state lifetimes measured by deep UV ultrafast photoionization spectroscopy," Chem. Phys. Lett. **333**, 36–40 (2001).
59. W.-K. Chen, J.-W. Ho, and P.-Y. Cheng, "Ultrafast photodissociation dynamics of the acetone 3s Rydberg state at 195 nm: a new mechanism," Chem. Phys. Lett. **380**, 411–418 (2003).
60. W.-K. Chen, J.-W. Ho, and P.-Y. Cheng, "Ultrafast Photodissociation Dynamics of Acetone at 195 nm: I. Initial-state, Intermediate, and Product Temporal Evolutions by Femtosecond Mass-Selected Multiphoton Ionization Spectroscopy," J. Phys. Chem. A **109**, 6805–6817 (2005).
61. W.-K. Chen and P.-Y. Cheng, "Ultrafast Photodissociation Dynamics of Acetone at 195 nm: II. Unraveling Complex Three-Body Dissociation Dynamics by Femtosecond Time-Resolved Photofragment Translational Spectroscopy," J. Phys. Chem. A **109**, 6818–6829 (2005).
62. N. Rusteika, K. B. Møller, and T. I. Sølling, "New insights on the photodynamics of acetone excited with 253–288 nm femtosecond pulses," Chem. Phys. Lett. **461**, 193–197 (2008).
63. R. Y. Brogaard, T. I. Sølling, and K. B. Møller, "Initial Dynamics of The Norrish Type I Reaction in Acetone: Probing Wave Packet Motion," J. Phys. Chem. A **115**, 556–561 (2011).
64. E. A. Fogleman, H. Koizumi, J. P. Kercher, B. Sztáray, and T. Baer, "Heats of Formation of the Acetyl Radical and Ion Obtained by Threshold Photoelectron Photoion Coincidence," J. Phys. Chem. A **108**, 5288–5294 (2004).
65. L. Wei, B. Yang, R. Yang, C. Huang, J. Wang, X. Shan, L. Sheng, Y. Zhang, F. Qi, C.-S. Lam, and W.-K. Li, "A Vacuum Ultraviolet Photoionization Mass Spectrometric Study of Acetone," J. Phys. Chem. A **109**, 4231–4241 (2005).
66. E. E. Rennie, A.-M. Boulanger, P. M. Mayer, D. M. P. Holland, D. A. Shaw, L. Cooper, and L. G. Shpinkova, "A Photoelectron and TPEPICO Investigation of the Acetone Radical Cation," J. Phys. Chem. A **110**, 8663–8675 (2006).
67. T. Seideman, "Time-resolved photoelectron angular distributions as a probe of coupled polyatomic dynamics," Phys. Rev. A **64**, 042504 (2001).
68. A. Stolow, A. E. Bragg, and D. M. Neumark, "Femtosecond Time-Resolved Photoelectron Spectroscopy," Chem. Rev. **104**, 1719–1758 (2004).
69. T. Suzuki, "Femtosecond time-resolved photoelectron imaging," Annu. Rev. Phys. Chem. **57**, 555–592 (2006).
70. G. Wu, P. Hockett, and A. Stolow, "Time-resolved photoelectron spectroscopy: from wavepackets to observables," Phys. Chem. Chem. Phys. **13**, 18447–18467 (2011).
71. Wolfram Research, Inc., Mathematica, Version 10.0, Champaign, IL (2014).
72. C. Bordas, F. Paulig, H. Helm, and D. L. Huestis, "Photoelectron imaging spectrometry: Principle and inversion method," Rev. Sci. Instrum. **67**, 2257–2268 (1996).

73. B.-Y. Chang, R. C. Hoetzlein, J. A. Mueller, J. D. Geiser, and P. L. Houston, "Improved two-dimensional product imaging: The real-time ion-counting method," Rev. Sci. Instrum. **69**, 1665–1670 (1998).
74. N. Yonekura, C. Gebauer, H. Kohguchi, and T. Suzuki, "A crossed molecular beam apparatus using high-resolution ion imaging," Rev. Sci. Instrum. **70**, 3265–3270 (1999).
75. W. Li, S. D. Chambreau, S. A. Lahankar, and A. G. Suits, "Megapixel ion imaging with standard video," Rev. Sci. Instrum. **76**, 063106 (2005).
76. G. A. Garcia, L. Nahon, and I. Powis, "Two-dimensional charged particle image inversion using a polar basis function expansion," Rev. Sci. Instrum. **75**, 4989–4996 (2004).
77. J. E. Hansen and W. Persson, "Revised analysis of singly ionized xenon, Xe II," Phys. Scr. **36**, 602 (1987).
78. B. J. Whitaker, ed., *Imaging in Molecular Dynamics: Technology and Applications* (Cambridge University Press, Cambridge, 2003).
79. D. B. Thompson, D. Ji, K. Lee, C.-I. Ma, and D. M. Hanson, "Excitation and decay spectra of core-excited resonances in acetone," J. Phys. B: At. Mol. Opt. Phys. **32**, 2649 (1999).
80. S. Maeda, K. Ohno, and K. Morokuma, "A Theoretical Study on the Photodissociation of Acetone: Insight into the Slow Intersystem Crossing and Exploration of Nonadiabatic Pathways to the Ground State," J. Phys. Chem. Lett. **1**, 1841–1845 (2010).
81. E. W.-G. Diau, C. Kötting, T. I. Sølling, and A. H. Zewail, "Femtochemistry of Norrish Type-I Reactions: III. Highly Excited Ketones—Theoretical," ChemPhysChem **3**, 57–78 (2002).
82. T. I. Sølling, E. W.-G. Diau, C. Kötting, S. De Feyter, and A. H. Zewail, "Femtochemistry of Norrish Type-I Reactions: IV. Highly Excited Ketones—Experimental," ChemPhysChem **3**, 79–97 (2002).

4

Ultrafast Dynamics of Electronically Highly Excited Cyclohexanone

Ole Hüter, Niklas Helle and Friedrich Temps

Institute of Physical Chemistry, Christian-Albrechts-University Kiel, Olshausenstr. 40, D-24098 Kiel, Germany

Manuscript in preparation.

Own contributions to this manuscript:

- Femtosecond time-resolved time-of-flight mass spectrometry.
- Femtosecond time-resolved photoelectron imaging spectroscopy.
- Writing of the data analysis software and analysis of all presented data.
- Writing of the manuscript.

Abstract

The radiationless decay dynamics of the first electronically excited $^1n\pi^*$ state and high-lying Rydberg states of cyclohexanone have been investigated using femtosecond time-resolved time-of-flight mass spectrometry and photoelectron imaging spectroscopy. An ultrafast population transfer was observed from the 3d and 3p Rydberg states to the 3s Rydberg state. The electronic relaxation time connected with this process was below the experimental time resolution of 35 femtoseconds. We ascribe this behavior to strong vibronic interactions between the high-lying Rydberg states, which enable an ultrafast population transfer *via* a conical intersection to the 3s Rydberg state. Subsequently, the 3s state deactivates by internal conversion to the $n\pi^*$ state, which in turn is found to be long-lived with a decay time of several hundred picoseconds.

4.1 Introduction

The investigation of the α-CC bond cleavage in the first electronically excited $^1n\pi^*$ state of aliphatic ketones, especially of the simplest ketone acetone, in the Norrish type I reaction[1–3] has led to wide research interest over the past decades.[4–12] It is commonly accepted that after photoexcitation, the $^1n\pi^*$ state is long-lived on the nanosecond time scale and deactivates by intersystem crossing (ISC) to the corresponding $^3n\pi^*$ potential energy surface,[11] where the α-cleavage reaction takes place. In cyclic ketones, this photochemical process corresponds to a ring-opening reaction.[4] It may be followed by further decomposition,[13] although, for cyclohexanone, the 5-hexenal structure obtained after the ring-opening reaction was shown to undergo no further fragmentation.[14,15]

The Norrish type I reaction of acetone has been subject to a number of experimental femtosecond time-resolved studies due to its fundamental nature.[9,16–20] Surprisingly, the nanosecond lifetime of the excited $^1n\pi^*$ state was not confirmed by many of the studies employing photoionization as probe for the molecular dynamics, and an excited-state lifetime of less than 100 fs was observed. More recent experimental and theoretical studies resolved this apparent discrepancy: while the commencing structural rearrangements after excitation to the $^1n\pi^*$ state were found to hinder photoionization,[21,22] the ultrafast α-CC bond dissociation in only 90 fs was in fact observed to take place after excitation to the $3d_{yz}$ Rydberg state.[23] Experimental[24–26] and computational[20,27] studies predicted that the $3d_{yz}$ Rydberg state strongly couples to the $\pi\pi^*$ valence state, which in turn may have a conical intersection (CoIn) with the 3s Rydberg state[20,27] on which the α-CC bond is subsequently broken. In contrast to the $^1n\pi^*$ state and the Rydberg states, the $\pi\pi^*$ valence state has not been

experimentally observed to this date to the best of our knowledge in any of the cyclic ketones. It has been subject of only few computational studies that place it at high excitation energies,[27,28] but experimentally its presence is obscured[29] and can only be indirectly deduced through its vibronic interaction with the adjacent electronic states.[24–26]

Following our work on acetone,[23] we aim to investigate the effects of vibronic Rydberg-valence couplings in larger ketones as well. Here, we report on the ultrafast deactivation dynamics of high-lying excited electronic states of cyclohexanone in a molecular beam. The molecule is excited in a two-photon process to the 3d and 3p Rydberg states, and the temporal evolution of the excited wavepacket is monitored by femtosecond time-resolved time-of-flight mass spectrometry and photoelectron imaging spectroscopy, which have proven to be valuable tools in following molecular dynamics on multiple electronic potential energy surfaces. Owing to the highly multiplexed information yielded by photoelectron imaging, we simultaneously learn about the deactivation dynamics of the $^1n\pi^*$ state that is excited with a single photon.

4.2 Experimental Methods

The experimental measurements were carried out using a femtosecond pump–probe laser system coupled to a home-built linear time-of-flight mass spectrometer (TOF-MS) and photoelectron imaging (PEI) spectrometer described in detail elsewhere.[23,30] Briefly, the required wavelength-tunable, $\sim$30 fs excitation pulses in the UV were generated in a home-built two-stage non-collinear optical parametric amplifier (NOPA) equipped with a prism compressor and a frequency-doubling crystal. The frequency-doubled fundamental of the employed Ti:Sa pump laser at 402 nm (90 fs) served as probe by multiphoton ionization in the experiments. Helium carrier gas at 2 bar was seeded with cyclohexanone (Carl Roth, $\geq$99.5% purity) and expanded into the vacuum chamber with a pulsed valve. The sample reservoir and all parts in contact with the gas mixture were heated to 130°C due to the low vapor pressure of cyclohexanone (7 mbar at room temperature[4]). The skimmed molecular beam was crossed perpendicularly by the co-propagating pump and probe laser beams between the repeller and extractor plates of a Wiley-McLaren electrode assembly. The resulting ions or electrons were detected using a microchannel plate backed by a steel anode or a phosphorescent screen viewed by a CCD camera. The energy resolution of the photoelectron (PE) spectra acquired in a one-photon pump and two-photon probe process was limited to typically 70 meV full width at half maximum (FWHM) by the spectral widths of the laser pulses.

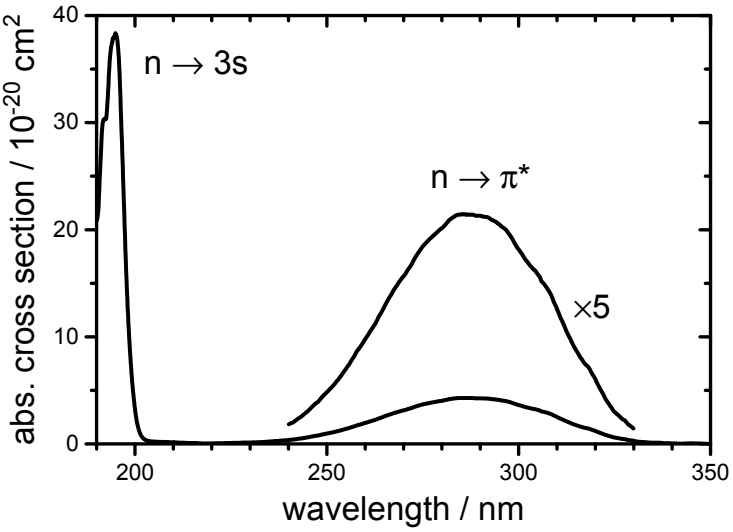

Figure 4.1. UV absorption spectrum of cyclohexanone in n-hexane. The absorption band of the ^{1}nπ^* transition, which has a maximum at around 290 nm, is scaled by a factor of 5 for better visibility. The transition to the 3s Rydberg state corresponds to the band peaking at 196 nm.

4.3 Results

The UV absorption spectrum of cyclohexanone is depicted in Figure 4.1. The absorption band of the ^{1}nπ^* state is broad and structureless, with a band maximum at around 290 nm in solution in n-hexane.[31] The ^{1}nπ^* state is constituted by the promotion of an oxygen lone pair electron from the n_y orbital to the π^* orbital. Under C_{2v} symmetry constraints, this transition is dipole-forbidden, but weakly allowed due to an intensity-borrowing mechanism.[32] It becomes increasingly allowed when the molecule deviates from C_{2v} symmetry.[33] In the energetically favorable chair conformation, cyclohexanone possesses the closely related C_s symmetry, hence the low maximum absorption cross section of 4.3×10^{-20} cm^{-2}. The adiabatic excitation energy of the ^{1}nπ^* state has not been experimentally determined. It is well known, however, for acetone (3.774 eV[6]), cyclobutanone (3.756 eV[34]), 3-cyclopenten-1-one (3.749 eV[34]) and cyclopentanone (3.754 eV[34]) from fluorescence excitation spectra of the jet-cooled molecules. Due to the similarity of absorption[31] and fluorescence emission[35] spectra of these (cyclo-)ketones, we assume the electronic origin of the ^{1}nπ^* state in cyclohexanone to be at a similar energy around 3.75 eV. Although transitions to other valence states like the $\pi\pi^*$ state are expected to occur, they have not been observed experimentally. The next spectral band in the UV absorption spectrum is the n→3s Rydberg transition peaking at 196 nm, followed by further members of the $n = 3$ Rydberg series (not depicted in Figure 4.1). The vibrationless origins of some of these states were determined using resonance-enhanced multi-photon ionization (REMPI) spectroscopy for the 3s (6.288 eV[36]) and one 3p Rydberg state (6.894 eV[37]), and using vacuum ultraviolet (VUV) absorption spectroscopy for a second 3p (6.940 eV[38]) and two 3d Rydberg states (7.424 eV and 7.531 eV[38]).

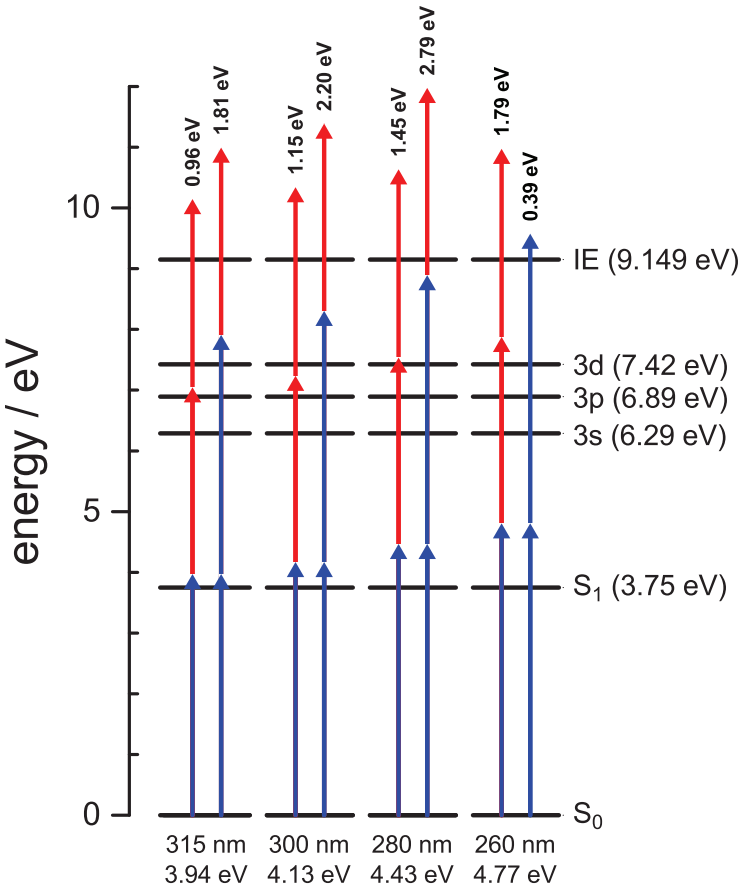

Figure 4.2. Experimentally employed pump–probe scheme showing the excitation of cyclohexanone with one or two pump photons (blue arrows) centered at the indicated wavelengths, and the subsequent ionization with two or one 402 nm probe photons (red arrows). Written vertically above the arrows is the maximum available energy E_{avl} that can be distributed between cation and photoelectron (see text).

In this work, we have excited cyclohexanone using femtosecond pump pulses centered at $\lambda_{\mathrm{pump}} = 315$ nm (3.94 eV), 300 nm (4.13 eV), 280 nm (4.43 eV) and 260 nm (4.77 eV) wavelength. A diagram of the pump and probe scheme and thereby accessible electronic states is depicted in Figure 4.2. The absorption of one pump photon excites the ^{1}nπ^* transition, while the absorption of two pump photons leads to transitions to the 3d or even higher-lying Rydberg states. Two-photon excitation at $\lambda_{\mathrm{pump}} = 260$ nm ionizes the molecule, as the ionization energy (IE) amounts to $IE = 9.149$ eV.[38] The temporal evolution of the excited ^{1}nπ^* state was monitored by multiphoton ionization with two probe photons centered at 402 nm in a (1+2') process. After the two-photon excitation at $\lambda_{\mathrm{pump}} = 315$ nm, 300 nm or 280 nm, only one probe photon was needed for ionization in a (2+1') process.

The results of the time-resolved time-of-flight mass spectrometry measurements are depicted in Figure 4.3 on the left. The observed excited-state decay curves of the cyclohexanone parent ion ($m/z = 98$ u) were fitted with a biexponential decay model, convoluted with a Gaussian that describes the instrument response function

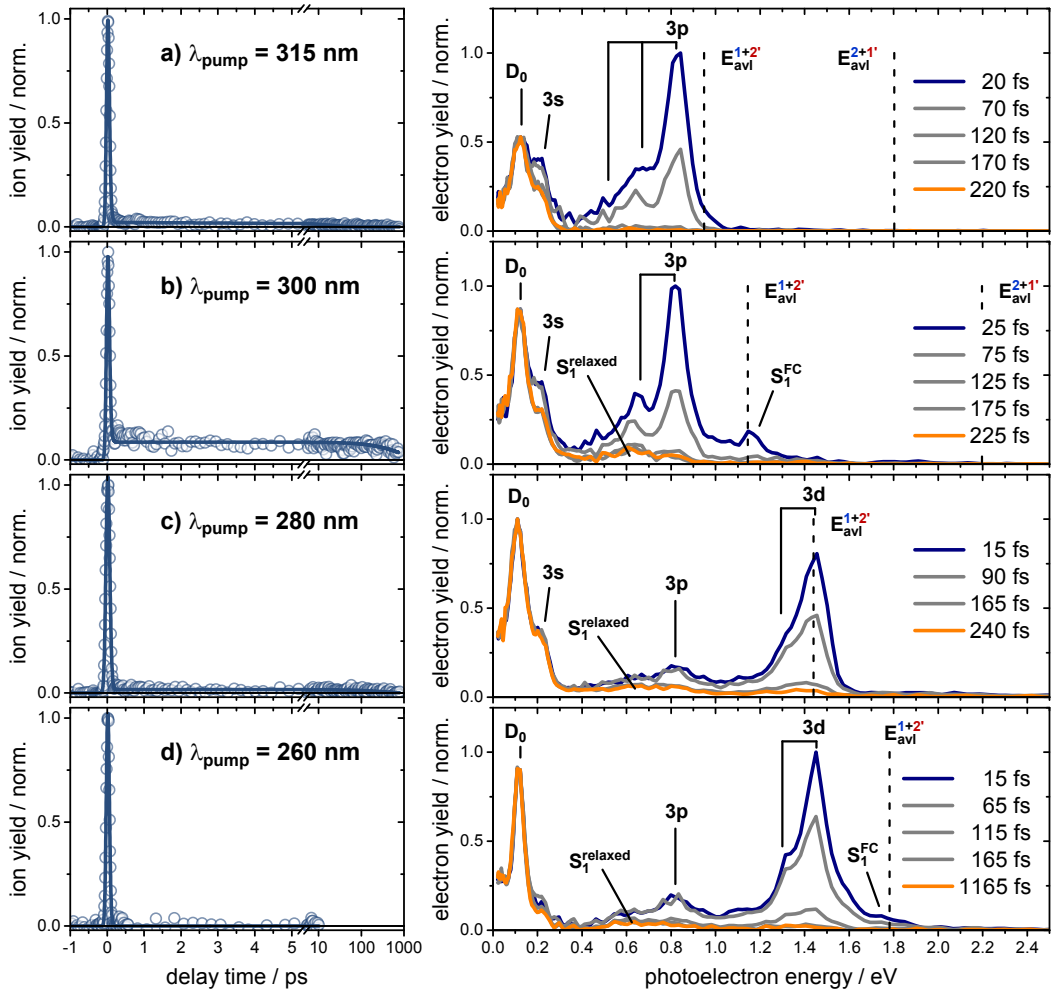

Figure 4.3. Transient mass signal and the fitted model (left side) and associated photoelectron spectra (right side) recorded after excitation with a) 315 nm, b) 300 nm, c) 280 nm and d) 260 nm pump pulses. The maximum available kinetic energy E_{avl} of the photoelectrons after the concurrent (1+2') and (2+1') pump-and-probe processes is indicated by the dashed vertical lines.

(IRF). The standard deviation σ_{IRF} of the Gaussian IRF is an appropriate measure for the experimental time resolution. The fit results are summarized in Table 4.I, with 2σ error margins given in parenthesis. The determination of the short component $\tau_1 < \sigma_{\mathrm{IRF}}$ is limited by the experimental time resolution of around 35 femtoseconds. The second decay component τ_2 varies strongly with the excitation wavelength, from $\tau_2 = 18$ ps after excitation at $\lambda_{\mathrm{pump}} = 315$ nm *via* $\tau_2 = 900$ ps at 300 nm down to $\tau_2 = 300$ ps for 280 nm excitation. The τ_2 component is not observed after 260 nm excitation. The large error values indicate that an accurate determination was experimentally very challenging.

A minor fragmentation (m/z = 42, 55, 69 and 70 u) of the parent molecule was observed in the time-of-flight mass spectra, with fragment amplitudes of less than 5% of the parent ion amplitude. Both the parent and fragment molecular ions appear

Table 4.I. Fit results for the measured excited state decay dynamics of cyclohexanone. The experimental time resolution is given by the σ_{IRF} parameter of the gaussian instrument function. The 2σ standard deviation obtained from the nonlinear least squares fit is given in parentheses.

λ_{exc} / nm	σ_{IRF} / fs	A_1 / %	τ_1 / fs	A_2 / %	τ_2 / ps
315	36(2)	0.98	$< \sigma_{\mathrm{IRF}}$	0.02	18(6)
300	37(2)	0.91	$< \sigma_{\mathrm{IRF}}$	0.09	900(400)
280	49(2)	0.98	$< \sigma_{\mathrm{IRF}}$	0.02	300(200)
260	39(2)	1.00	$< \sigma_{\mathrm{IRF}}$	—	—

at the same delay time and with the same rise time of their respective transient ion signals. Since transient ion signals of fragments arising from a photodissociation following electronic excitation are expected to show a delayed rise, the observed fragments are likely caused by the dissociation of the excited cation during the flight time from the ionization region to the detector. Dissociation of the parent ion has also been observed by Kuhlman *et al.*,[39] and was ascribed to the absorption of an additional probe photon by them.

Photoelectron images were recorded at all excitation wavelengths for several fixed delay times. The data processing procedure for the acquired photoelectron images has been described elsewhere.[23,30] In short, the images were centered and averaged, and a meridional slice through the original three-dimensional electron distribution was calculated using the pBASEX program.[40] In that way photoelectron (PE) spectra, transformed from detector pixel units to electron volts with the appropriate Jacobian transformation, as well as anisotropy parameters describing the photoelectron angular distribution (PAD) were gained. The energy bilance of a $(n+m')$ photoionization process with n pump and m probe photons can be expressed as

$$E_{\mathrm{el}} = \hbar(n \times \omega_{\mathrm{pump}} + m \times \omega_{\mathrm{probe}}) - IE - E^{+}_{\mathrm{int}}, \tag{4.1}$$

where E_{el} is the photoelectron kinetic energy, E^{+}_{int} is the internal energy remaining in the cation and IE = 9.149 eV[38] the adiabatic ionization energy of the cationic ground state. In Figure 4.2, the energy written vertically above the arrows denotes the maximum available kinetic energy E_{avl} that the photoelectrons can have when no vibrational energy is left remaining in the cation (i. e. $E_{\mathrm{avl}} \equiv E_{\mathrm{el}}$ with $E^{+}_{\mathrm{int}} = 0$).

The acquired PE spectra are shown in Figure 4.3 on the right, next to the corresponding transient mass signals on the left. The relative delay times noted in the spectra are given with respect to the time zero value gained from fitting the transient mass spectra. The values of E_{avl} are indicated with vertical dashed lines. The assignments of the observed photoelectron bands are written above the peaks. In some of the bands, a vibrational progressions is present that corresponds to the

initially active C=O stretch vibration. The second ionization energy for the removal of the second oxygen nonbonding electron from the n_z orbital is IE_2 = 11.3 eV.[41] After the (2+1') process at 300 nm and 280 nm pump wavelength, E_{avl} is larger than the required 2.15 eV for the transition to the first ionic excited state. However, a very low transition probability is expected for this process, because it would leave the molecule in an unfavorable doubly-excited configuration, and has indeed not been observed in this work.

In all recorded PE spectra, we observe the time-independent three-photon ionization to the vibrationless ionic ground state D_0 by the probe pulse. A single-color PE signal from the pump pulse was observed at λ_{pump} = 260 nm due to two-photon ionization. This signal was very small and has been subtracted from the PE spectra. Although best efforts were made to reduce both pump and probe pulse intensities to reduce these contributions, their presence could not be avoided with a decent signal-to-noise ratio of the time-dependent signals.

The time-dependent photoelectron angular distributions (PAD) could be determined with anisotropy parameters of $\beta_2 \approx 1$, $\beta_4 \approx 0$ and $\beta_6 \approx 0$ for all observed bands in all PADs that had sufficient signal amplitude to be evaluated. The value of β_2 likely is governed by the parallel alignment of the transition dipole moment to the laser polarization, causing a $\cos^2\theta$ angular distribution.

4.4 Assignments and Discussion

In general, the PE spectra feature a similar spectral band structure at all pump wavelengths. Their temporal evolutions indicate very fast commencing dynamics. The spectra after excitation at λ_{pump} = 315 nm and 300 nm display PE bands at 0.80 eV from the 3p Rydberg states. After 280 nm and 260 nm excitation, in contrast, the spectra display PE bands at 1.45 eV from the 3d Rydberg states, although the signature of the 3p Rydberg states is observed with smaller amplitude as well. The vibrational progression indicated above the 3p and 3d PE bands in Figure 4.3 has a level spacing of 0.15 eV, corresponding to ~1210 cm^{-1}. As the photoexcitation of the n electron from the oxygen atom weakens the C=O double bond, the C=O stretch vibration ν_{CO} can be expected to be predominantly active after excitation. The ground state frequency ν_{CO} = 1709 cm^{-1} is well known,[42] and as a value of ν_{CO} = 1232 cm^{-1} in the 3p Rydberg states was determined,[37] a similar value can be expected for the 3d Rydberg states. Most of the intensity of the 3p and 3d state PE bands probably arises from their excitation with one pump and one probe photon during the temporal overlap of both laser pulses. As can be seen from Figure 4.2, the energy of this process is sufficient for the excitation of the 3p states at 315 nm and

300 nm, and for the 3d states at 280 nm and 260 nm. This resonant enhancement also explains the spiking signal around time zero in the transient ion mass signals. We note as an important fact, however, that the excited 3p state signal is clearly present in the 280 nm and 260 nm PE spectra, although the $(1 + 1')$ photon energy is above the excitation energy of the 3d states, and the 3p and 3d Rydberg states are energetically well separated.

In the spectra recorded using λ_{pump} = 315 nm, 300 nm and 280 nm, a narrow PE band at 0.20 eV is observed that we assign to the excited 3s Rydberg state. It is not immediately evident how this state is populated in our pump-and-probe scheme. The 3s state PE band is still present when the bands generated in the $(1 + 1')$ process have vanished. A long-lived photoelectron signal from an excited state has to be due to transitions initiated by the pump pulse only. The absorption of two 315 nm or 300 nm photons leads to the excitation of the 3d Rydberg states, and a PE band would be expected around 1.45 eV. Such a band is not observed, however, in the corresponding spectra. In the 280 nm and 260 nm spectra, it is indeed observed, but cannot be separated from the 3p and 3d state bands excited in the $(1 + 1')$ process. The 3s state is not observed in the PE spectrum after 260 nm excitation, because the two-photon absorption directly ionizes the molecule. The only remaining possibility is that the 3s Rydberg state is populated after the two-photon excitation of either the 3p or the 3d Rydberg states. Therefore, an efficient electronic relaxation pathway from the higher-lying Rydberg states to 3s Rydberg state has to exist to explain the observed ultrafast population transfer.

In the literature, there are no experimental or theoretical studies on the ultrafast dynamics of the high-lying Rydberg states in cyclic ketones. We therefore compare the observed phenoma to the well-investigated acetone molecule. In acetone (C_{2v} symmetry), the Rydberg states of A_1 symmetry were experimentally found to interact strongly with the $\pi\pi^*$ state of A_1 symmetry.[24–26] O'Toole *et al.*[38] noted that the unusually extensive vibronic structure of 3p and 3d Rydberg states observed in their VUV absorption spectra is probably caused by a vibronic coupling mechanism. The vibronic interaction between high-lying A_1 states has been subject to some theoretical studies as well. Merchán *et al.*[24] performed CASSCF/CASPT2 calculations and proposed that the potential energy surfaces of the $3p_y$ and $3d_{yz}$ (both A_1) Rydberg states and the $\pi\pi^*$ valence state form avoided crossings and thus double-well potential energy surfaces along the C=O stretch coordinate. They proposed that the $\pi\pi^*$ state was short-lived to explain unexpected intensity anomalies in their $(3 + 1)$ REMPI spectra of the 3p and 3d Rydberg states. Calculations at the CASSCF/CASPT2 level of theory with a larger active space were also performed by Diau *et al.*[27] They followed the radiationless deactivation pathway from the excited $\pi\pi^*$ state and found a low-lying conical intersection with the 3s Rydberg state at a large C=O bond length. In our study of the electronic deactivation dynamics of

the excited $3d_{yz}$ (A_1) Rydberg state of acetone, we observed that the CoIn to the 3s Rydberg state can be efficiently accessed in less than 100 femtoseconds.[23]

The PE spectra of the present work indicate that these findings may be directly applied to cyclohexanone as well. The excited 3d and 3p Rydberg states deactivate in less than $\sigma_{\mathrm{IRF}} = 35$ fs to the 3s Rydberg state, although an involvement of the $\pi\pi^*$ state can not be directly deduced from our data. The lifetime of the excited 3s Rydberg state was determined to be 9.7 ps after one-photon excitation close the its vibrationless origin by Kuhlman *et al.*,[39] and it has been shown to undergo further internal conversion (IC) to the $^1n\pi^*$ state.[39,43] This finally brings us to the fate of the excited $^1n\pi^*$ state. In the PE spectra recorded using λ_{pump} = 300 nm and 260 nm in Figure 4.3, the Franck–Condon species, denoted S_1^{FC}, is observed at 1.15 eV and 1.78 eV, respectively. In the PE spectra recorded at λ_{pump} = 315 nm and 280 nm, it is obscured by the more intense 3p and 3d Rydberg state PE bands. The signal disappears in only 75 fs, which is well-known from acetone. Upon excitation to the $^1n\pi^*$ state, the molecular structure changes by a pyramidalization of the C–CO–C atoms out of the molecular plane.[6,44,45] The ionization probability is drastically reduced in the pyramidalized equilibrium structure,[22] which is reached in less than 30 femtoseconds.[21,23] The cyclic ketones appear to undergo pyramidalization in the $^1n\pi^*$ state as well, and the impact on the ionization probability can be suspected to be similar. The carbon atom, which is initially sp^2-hybridized, relaxes to a more sp^3-like hybridization when the n_y electron is promoted to a higher orbital. This leads not only to the deplanarization around this atom, but also to a relaxation of the adjacent C–C bonds.[36] The release of ring strain induces nuclear motions in the ring system, mainly the low-frequency vibrational ring puckering mode. The activity of this mode directly after excitation with femtosecond laser pulses has been observed in cyclobutanone and cyclopentanone.[39]

The vibrationally excited $^1n\pi^*$ state in a relaxed structure is expected to show up in our photoelectron spectra as a broad band around 0.75 eV. We can indeed observe such a band, denoted S_1^{relaxed}, in the PE spectra recorded using λ_{pump} = 300 nm, 280 nm and 260 nm in Figure 4.3. In the 260 nm spectrum, the band from the relaxed $^1n\pi^*$ state is still present after more than one picosecond. Because the population from the 3s Rydberg state was shown to decay in 10 ps or less, the second decay component of $\tau_2 \gg 10$ ps, obtained from fitting the measured transient ion yield, likely corresponds to the deactivation time of the excited $^1n\pi^*$ state. The determination of the τ_2 component clearly is subject to large experimental uncertainties, and we only claim that the excited $^1n\pi^*$ state has a lifetime of at least several hundred picoseconds. The rate-limiting step in the decay of the $^1n\pi^*$ state is the intersystem crossing to the $^3n\pi^*$ state, for which a quantum yield of unity was determined.[35] The ring-opening reaction then takes place on the triplet surface,[14] which is also supported by a recent computational CASSCF/CASPT2 study that found

the ring-opening reaction to be blocked on the singlet $n\pi^*$ potential energy surface due to the small ring strain in the cyclohexanone molecule.[46]

4.5 Conclusions

The excitation with femtosecond laser pulses at wavelengths of $\lambda_{\mathrm{pump}} = 315-260$ nm leads not only to a one-photon transition to the $^1n\pi^*$ state, but also to two-photon transitions to high-lying Rydberg states. The population of these states was not directly evident from the photoelectron spectra in terms of discrete band structures, but could be indirectly referred to by a signal assigned to the 3s Rydberg state. This state was found to live fore more than 240 fs (the maximum delay time of the relevant spectra), and could therefore not be populated in any other way than by an internal conversion process from energetically higher-lying states. The time scale on which this conversion process takes place is below our experimental time resolution of 35 femtoseconds. By comparison with calculations and experimental observations of acetone, we attribute this ultrafast electronic population transfer to vibronic interactions with the higher-lying Rydberg states, enabling the passage through a conical intersection to the 3s Rydberg state in only one vibrational period of the C=O stretch vibration. The role of the $\pi\pi^*$ state in the occurring ultrafast dynamics can not be deduced from our observations.

After internal conversion from the 3s Rydberg state to the $^1n\pi^*$ valence state, the excited $^1n\pi^*$ state is found to be long-lived with a decay time of several hundred picoseconds or more. An excited-state lifetime on this timescale has also been assumed for acetone, but could so far not be directly observed in ultrafast experiments utilizing an ionizing probe process, because the relaxation to the pyramidially distorted equilibrium structure effectively hinders ionization. This effect is seen to be weakened in cyclohexanone, where the vibrationally excited $^1n\pi^*$ state in its relaxed structure can be observed as a weak, broad band in the photoelectron spectra. The decay of the excited $^1n\pi^*$ state signal is attributed to intersystem crossing to the corresponding triplet state.

References

1. R. G. W. Norrish, H. G. Crone, and O. D. Saltmarsh, “318. Primary photochemical reactions. Part V. The spectroscopy and photochemical decomposition of acetone,” J. Chem. Soc., 1456–1464 (1934).
2. O. D. Saltmarsh and R. G. W. Norrish, “98. Primary photochemical reactions. Part VI. The photochemical decomposition of certain cyclic ketones,” J. Chem.

Soc., 455–459 (1935).
3. C. H. Bamford and R. G. W. Norrish, "287. Primary photochemical reactions. Part X. The photolysis of cyclic ketones in the gas phase," J. Chem. Soc., 1521–1531 (1938).
4. S. W. Benson and G. B. Kistiakowsky, "The Photochemical Decomposition of Cyclic Ketones," J. Am. Chem. Soc. **64**, 80–86 (1942).
5. J. C. Dalton and N. J. Turro, "Photoreactivity of n,π* Excited States of Alkyl Ketones," Annu. Rev. Phys. Chem. **21**, 499–560 (1970).
6. H. Zuckermann, Y. Haas, M. Drabbels, J. Heinze, W. L. Meerts, J. Reuss, and J. van Bladel, "Acetone, a laser-induced fluorescence study with rotational resolution at 320 nm," Chem. Phys. **163**, 193–208 (1992).
7. S. Pedersen, J. L. Herek, and A. H. Zewail, "The Validity of the 'Diradical' Hypothesis: Direct Femtoscond Studies of the Transition-State Structures," Science **266**, 1359–1364 (1994).
8. E. W.-G. Diau, J. L. Herek, Z. H. Kim, and A. H. Zewail, "Femtosecond Activation of Reactions and the Concept of Nonergodic Molecules," Science **279**, 847–851 (1998).
9. E. W.-G. Diau, C. Kötting, and A. H. Zewail, "Femtochemistry of Norrish Type-I Reactions: I. Experimental and Theoretical Studies of Acetone and Related Ketones on the S_1 Surface," ChemPhysChem **2**, 273–293 (2001).
10. E. W.-G. Diau, C. Kötting, and A. H. Zewail, "Femtochemistry of Norrish Type-I Reactions: II. The Anomalous Predissociation Dynamics of Cyclobutanone on the S_1 Surface," ChemPhysChem **2**, 294–309 (2001).
11. Y. Haas, "Photochemical α-cleavage of ketones: revisiting acetone," Photochem. Photobiol. Sci. **3**, 6–16 (2004).
12. V. Goncharov, N. Herath, and A. G. Suits, "Roaming Dynamics in Acetone Dissociation," J. Phys. Chem. A **112**, 9423–9428 (2008).
13. A. A. Scala and D. G. Ballan, "The Vacuum Ultraviolet Photolysis of Cyclopentanone," Can. J. Chem. **50**, 3938–3943 (1972).
14. A. Singh and G. R. Freeman, "γ-Radiation-Induced Isomerization of Cyclohexanone to 5-Hexenal in the Liquid Phase," J. Phys. Chem. **69**, 666–668 (1965).
15. A. A. Scala and D. G. Ballan, "Vacuum Ultraviolet Photochemistry of Cyclobutanone," J. Chem. Phys. **57**, 2162–2167 (1972).
16. S. K. Kim, S. Pedersen, and A. H. Zewail, "Direct femtosecond observation of the transient intermediate in the α-cleavage reaction of $(CH_3)_2CO$ to $2CH_3+CO$: Resolving the issue of concertedness," J. Chem. Phys. **103**, 477–480 (1995).
17. T. Shibata and T. Suzuki, "Photofragment ion imaging with femtosecond laser pulses," Chem. Phys. Lett. **262**, 115–119 (1996).
18. J. C. Owrutsky and A. P. Baronavski, "Ultrafast photodissociation dynamics of the S_1 and S_2 states of acetone," J. Chem. Phys. **110**, 11206–11213 (1999).
19. Q. Zhong, L. Poth, and A. W. Castleman, Jr., "Ultrafast dissociation dynamics of acetone: A revisit to the S_1 state and 3s Rydberg state," J. Chem. Phys. **110**,

192–196 (1999).
20. T. I. Sølling, E. W.-G. Diau, C. Kötting, S. De Feyter, and A. H. Zewail, "Femtochemistry of Norrish Type-I Reactions: IV. Highly Excited Ketones—Experimental," ChemPhysChem **3**, 79–97 (2002).
21. N. Rusteika, K. B. Møller, and T. I. Sølling, "New insights on the photodynamics of acetone excited with 253–288 nm femtosecond pulses," Chem. Phys. Lett. **461**, 193–197 (2008).
22. R. Y. Brogaard, T. I. Sølling, and K. B. Møller, "Initial Dynamics of The Norrish Type I Reaction in Acetone: Probing Wave Packet Motion," J. Phys. Chem. A **115**, 556–561 (2011).
23. O. Hüter and F. Temps, "Ultrafast α-CC bond cleavage of acetone upon excitation to the $3d_{yz}$ Rydberg state by femtosecond time-resolved photoelectron imaging," manuscript in preparation (2016).
24. M. Merchán, B. O. Roos, R. McDiarmid, and X. Xing, "A combined theoretical and experimental determination of the electronic spectrum of acetone," J. Chem. Phys. **104**, 1791–1804 (1996).
25. R. McDiarmid and X. Xing, "Nonadiabatic coupling of the 3p Rydberg and $\pi\pi^*$ valence states of acetone," J. Chem. Phys. **107**, 675–679 (1997).
26. D. H. A. ter Steege, A. C. Wirtz, and W. J. Buma, "Vibronic coupling in excited states of acetone," J. Chem. Phys. **116**, 547–560 (2002).
27. E. W.-G. Diau, C. Kötting, T. I. Sølling, and A. H. Zewail, "Femtochemistry of Norrish Type-I Reactions: III. Highly Excited Ketones—Theoretical," ChemPhysChem **3**, 57–78 (2002).
28. C. Angeli, S. Borini, L. Ferrighi, and R. Cimiraglia, "A CASSCF theoretical study of the vibrational frequencies and structure of formaldehyde, acetaldehyde and acetone valence excited states," THEOCHEM **718**, 55–69 (2005).
29. M. Nobre, A. Fernandes, F. F. da Silva, R. Antunes, D. Almeida, V. Kokhan, S. V. Hoffmann, N. J. Mason, S. Eden, and P. Limão-Vieira, "The VUV electronic spectroscopy of acetone studied by synchrotron radiation," Phys. Chem. Chem. Phys. **10**, 550–560 (2008).
30. O. Hüter, M. Sala, H. Neumann, S. Zhang, H. Studzinski, D. Egorova, and F. Temps, "Long-lived coherence in pentafluorobenzene as a probe of $\pi\pi^*$–$\pi\sigma^*$ vibronic coupling," submitted to J. Chem. Phys. (2016).
31. M. O'Sullivan and A. C. Testa, "Fluorescence of cycloalkanones," J. Phys. Chem. **77**, 1830–1833 (1973).
32. A. B. Rocha and C. E. Bielschowsky, "Intensity of the n$\rightarrow\pi^*$ symmetry-forbidden electronic transition in acetone by direct vibronic coupling mechanism," Chem. Phys. Lett. **337**, 331–334 (2001).
33. W. D. Chandler and L. Goodman, "Allowed and forbidden character in $\pi^*\leftarrow$n spectra of cycloalkanones," J. Mol. Spectrosc. **35**, 232–243 (1970).
34. J. Zhang, W. Y. Chiang, P. Sagear, and J. Laane, "Jet-cooled fluorescence excitation spectra and carbonyl wagging potential energy functions of several

cyclic ketones in their $S_1(n, \pi^*)$ electronic excited states," Chem. Phys. Lett. **196**, 573–577 (1992).
35. E. K. C. Lee, R. G. Shortridge, and C. F. Rusbult, "Fluorescence excitation study of cyclobutanone, cyclopentanone, and cyclohexanone in the gas phase," J. Am. Chem. Soc. **93**, 1863–1867 (1971).
36. T. J. Cornish and T. Baer, "2 + 1 REMPI spectra of cyclic ketones in a cold molecular beam. 1. Structural studies of the 3s Rydberg state in unsubstituted rings," J. Am. Chem. Soc. **109**, 6915–6920 (1987).
37. C. Kosmidis, G. Boulakis, A. Bolovinos, P. Tsekeris, and P. Brint, "MPI spectroscopy in the region of the 3p Rydberg state of some cycloketones," J. Mol. Struct. **266**, 133–140 (1992).
38. L. O'Toole, P. Brint, C. Kosmidis, G. Boulakis, and P. Tsekeris, "Vacuum-ultraviolet absorption spectra of propanone, butanone and the cyclic ketones $C_nH_{2n-2}O$ (n= 4, 5, 6, 7)," J. Chem. Soc., Faraday Trans. **87**, 3343–3351 (1991).
39. T. S. Kuhlman, T. I. Sølling, and K. B. Møller, "Coherent Motion Reveals Non-Ergodic Nature of Internal Conversion between Excited States," ChemPhysChem **13**, 820–827 (2012).
40. G. A. Garcia, L. Nahon, and I. Powis, "Two-dimensional charged particle image inversion using a polar basis function expansion," Rev. Sci. Instrum. **75**, 4989–4996 (2004).
41. S. X. Tian, N. Kishimoto, and K. Ohno, "Electronic structures of 1-adamantanol, cyclohexanol and cyclohexanone and anisotropic interactions with $He^*(2^3S)$ atoms: collision-energy-resolved Penning ionization electron spectroscopy combined with quantum chemistry calculations," J. Electron Spectrosc. Relat. Phenom. **127**, 167–181 (2002).
42. H. Fuhrer, V. B. Kartha, P. J. Krueger, H. H. Mantsch, and R. N. Jones, "Normal modes and group frequencies. Conflict or compromise? In-depth vibrational analysis of cyclohexanone," Chem. Rev. **72**, 439–456 (1972).
43. T. S. Kuhlman, S. P. A. Sauer, T. I. Sølling, and K. B. Møller, "Symmetry, vibrational energy redistribution and vibronic coupling: The internal conversion processes of cycloketones," J. Chem. Phys. **137**, 22A522 (2012).
44. A. D. Walsh, "471. The electronic orbitals, shapes, and spectra of polyatomic molecules. Part VI. H_2AB molecules," J. Chem. Soc., 2306–2317 (1953).
45. M. Baba, I. Hanazaki, and U. Nagashima, "The $S_1(n, \pi^*)$ states of acetaldehyde and acetone in supersonic nozzle beam: Methyl internal rotation and C=O out-of-plane wagging," J. Chem. Phys. **82**, 3938–3947 (1985).
46. S.-H. Xia, X.-Y. Liu, Q. Fang, and G. Cui, "Excited-State Ring-Opening Mechanism of Cyclic Ketones: A MS-CASPT2//CASSCF Study," J. Phys. Chem. A **119**, 3569–3576 (2015).

5

Long-Lived Coherence in Pentafluorobenzene as a Probe of $\pi\pi^*-\pi\sigma^*$ Vibronic Coupling

Ole Hüter,[1] Matthieu Sala,[1] Hendrikje Neumann,[1,2] Song Zhang,[1,3] Harald Studzinski,[1,4] Dassia Egorova[1] and Friedrich Temps[1]

[1] Institute of Physical Chemistry, Christian-Albrechts-University Kiel, Olshausenstr. 40, D-24098 Kiel, Germany
[2] Present address: Institute of Materials Science, Christian-Albrechts-University Kiel, Kaiserstr. 2, D-24143 Kiel, Germany
[3] Present address: State Key Laboratory of Magnetic Resonance and Atomic and Molecular Physics, Wuhan Institute of Physics and Mathematics, Chinese Academy of Sciences, Wuhan 430071, P. R. China
[4] Present address: Bosch Transmission Technology B.V., Dr. Hub van Coorneweg 120, 5026 RA Tilburg, The Netherlands

Manuscript submitted to The Journal of Chemical Physics (AIP Publishing LLC).

Own contributions to this manuscript:

- Femtosecond time-resolved time-of-flight mass spectrometry.
- Femtosecond time-resolved photoelectron imaging spectroscopy.
- Writing of the data analysis software and analysis of all experimental data.
- Quantum chemical calculations at the RI-SCS-MP2/-CC2 levels of theory.
- Analysis of all presented data calculated on the aforementioned levels of theory.
- Writing of the manuscript.

Abstract

The dynamics of pentafluorobenzene (PFB) after femtosecond laser excitation to the optically bright $\pi\pi^*$ first excited electronic state have been investigated by femtosecond time-resolved time-of-flight mass spectrometry and femtosecond time-resolved photoelectron imaging spectroscopy. The observed temporal profiles exhibit a bi-exponential decay behavior with a superimposed, long-lived, large-amplitude oscillation with a frequency of $\nu_{\mathrm{osc}} = 78-74\ \mathrm{cm}^{-1}$ and a damping time of $\tau_{\mathrm{D}} = 5-2$ ps. On the basis of electronic structure and quantum dynamics calculations, the oscillations have been shown to arise due to vibronic coupling between the optically bright $\pi\pi^*$ state and the energetically close-lying optically dark $\pi\sigma^*$ state. The coupling leads to a pronounced double-well character of the lowest excited adiabatic potential energy surface along several out-of-plane modes of b_1 symmetry. The optical electronic excitation initiates periodic wavepacket motion along these modes. In the out-of-plane distorted molecular configuration, the excited state acquires substantial $\pi\sigma^*$ character, thus modulating the ionization probability. The photoelectron spectra and the anisotropy of their angular distribution confirm the periodically changing electronic character. The ionizing probe laser pulse directly maps the coupled electron-nuclear motion into the observed signal oscillations.

5.1 Introduction

Since the seminal paper of Sobolewski et al.,[1] the role of $\pi\sigma^*$ electronic states in the ultrafast radiationless dynamics and photochemistry of (hetero)aromatic molecules such as azoles, phenols, amines, the aromatic amino acids and the DNA bases after excitation by ultraviolet (UV) light has attracted major attention (see, e. g., the reviews by Ashfold et al.,[2,3] Roberts and Stavros,[4] and references therein). Important prototypical molecules, for which the ensuing processes have been explored in considerable detail, are pyrrole,[5–11] aniline,[12–17] phenols,[18–23] imidazoles[24–26] and indoles.[27–29] On the one hand, energetically low-lying $\pi\sigma^*$ states have been seen to open previously unexpected bond fission channels on the femtosecond time scale governed by highly vibrational mode-specific mechanisms. While direct photoexcitation from the S_0 ground state to the first $\pi\sigma^*$ state is usually electric dipole forbidden (and weakly enabled by vibronic intensity borrowing only in rare cases, e. g. pyrrole), the strongly absorbing $\pi\pi^*$ excited states of the molecules often exhibit an easily accessible conical intersection (CoIn) mediating an ultrafast internal conversion (IC) to the $\pi\sigma^*$ state and subsequent predissociation on the $\pi\sigma^*$ potential energy surface (PES). On the other hand, the molecules may acquire a pronounced stability to photochemical damage by the existence of highly efficient ultrafast electronic relaxation pathways through the $\pi\sigma^*$ state back to the S_0 ground state.[1,30–35]

Of special interest are highly fluorinated benzenes, where the so-called perfluoro effect due to the strong electronegativity of the F atoms lowers the σ^* molecular orbitals (MOs) in energy relative to the π^* MOs.[36–38] In pentafluorobenzene (PFB) and in hexafluorobenzene (HFB), the lowest $\pi\sigma^*$ state, formed by promotion from the π system to a σ^* orbital on a C–F bond, thus becomes almost isoenergetic with the first $\pi\pi^*$ excited electronic state.[38–41] Fluorobenzenes are therefore well-suited for detailed investigations of the vibronic coupling mechanisms between energetically increasingly close $\pi\pi^*$ and $\pi\sigma^*$ states. In particular, while the first absorption bands in the UV spectra of fluorobenzenes with up to four F atoms display well-defined vibrational structures, the spectra of PFB and HFB are broad and structureless.[42] This also applies to the fluorescence spectra, which show large Stokes shifts and no noticeable spectral overlap with the absorption band.[39] The lack of identifiable electronic origin bands in resonance-enhanced multiphoton ionization (REMPI) spectra of PFB and HFB despite careful searches indicates large structural differences between the S_0 ground state and the $\pi\pi^*$ excited states.[43] Taken together with the short ($\sim$ nanosecond) fluorescence lifetimes, low fluorescence quantum yields,[44] and absence of significant phosphorescence from HFB and PFB,[45] these results indicate a prominent role of radiationless processes in the electronic dynamics involving the low-lying $\pi\sigma^*$ state.

Moreover, Kovalenko et al. reported the observation of long-lived temporal amplitude oscillations in the femtosecond transient absorption spectra of HFB, PFB, as well as 1,2,3,4-tetrafluorobenzene (TFB) after excitation to the lowest $\pi\pi^*$ state.[46] For PFB, they found oscillation frequencies corresponding to 94 cm^{-1} in acetonitrile and 86 cm^{-1} in *n*-hexane, respectively, which they assigned to electronic coherence between the initially optically excited (OE) bright state and an optically dark electron transfer (ET) state. Similar oscillations of $\sim$100 cm^{-1} were observed for HFB by time-resolved time-of-flight transient ion yield measurements in a molecular beam study by Studzinski et al.,[40] who attributed their observation to a modulation of the photoionization probability by the probe pulse through an out-of-plane motion along the vibrational coupling mode between the $\pi\pi^*$ and $\pi\sigma^*$ states. No such unusual observations have been made for the series of mono- to tetrafluorobenzenes (except the mentioned case of 1,2,3,4-TFB). Due to the lack of sufficiently accurate information on the excited electronic states of 1,2,3,4-TFB, PFB and HFB, however, the proposed pictures for the ensuing dynamics remained vague and merely qualitative. Newer high level *ab initio* calculations for PFB[47,48] and HFB,[49] for example, placed the $\pi\sigma^*$ state sufficiently high above the $\pi\pi^*$ state that a direct role of a $\pi\pi^*/\pi\sigma^*$ CoIn in the dynamics appears less likely and the proposed mechanisms have become questionable.

In this paper, we report on a joint experimental and theoretical study of the unusual excited-state dynamics of PFB in the gas phase after excitation to the optically bright

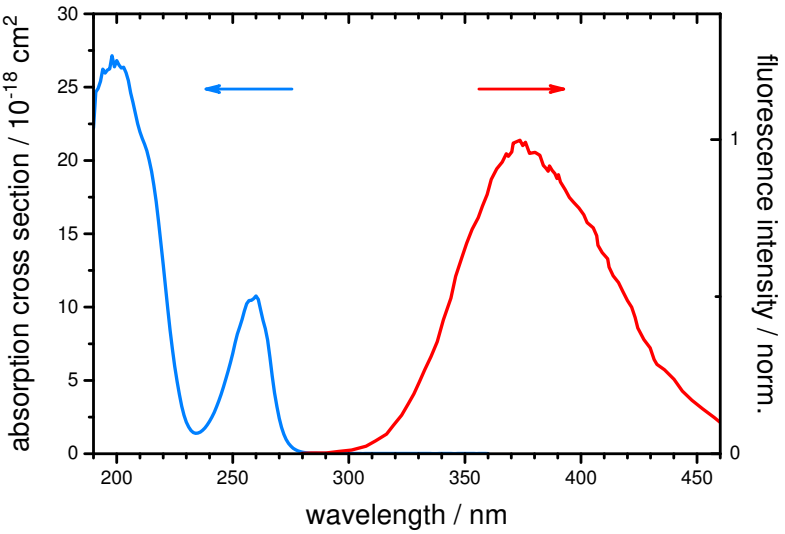

Figure 5.1. Gas phase UV absorption spectrum (p = 5 mbar) and dispersed fluorescence spectrum (supersonic free jet, λ_{exc} = 255 nm) of PFB. The dispersed fluorescence spectrum was adapted from Zgierski et al. (Ref. 39).

$\pi\pi^*$ ($^1B_2$) electronic state. We employ femtosecond time-resolved time-of-flight mass spectrometry and photoelectron imaging spectroscopy to monitor the temporal evolution of the excited wavepacket and the changing electronic character during its periodic motion. In addition, we investigate the role of the energetically low-lying $\pi\sigma^*$ ($^1A_2$) state by *ab initio* electronic structure calculations at the RI-SCS-CC2 and XMCQDPT2 levels of theory. We present high level quantum dynamics simulations which rationalize the observed coherent oscillation using a three-mode and a six-mode vibronic coupling model including the $^1B_2$ and $^1A_2$ excited electronic states and the vibrational modes of b_1 symmetry nearly quantitatively.

5.2 Experimental and Computational Methods

The experimental measurements were carried out using a femtosecond pump-probe laser system coupled to a home-built linear time-of-flight mass spectrometer (TOF-MS) and photoelectron imaging (PEI) spectrometer. Details of the experimental methods and the data analysis can be found in the Supplemental Material.[50] Briefly, the required wavelength-tunable, ~30 fs excitation pulses in the UV were generated in a home-built two-stage non-collinear optical parametric amplifier (NOPA) equipped with a prism compressor and a frequency-doubling crystal. The fundamental of the employed Ti:Sa pump laser at 804 nm (90 fs) served as probe by multiphoton ionization in the TOF-MS experiments, while frequency-doubled pulses at 402 nm were used for the PEI measurements. Helium carrier gas at 2 bar was seeded with PFB (Aldrich, ≥98% purity) and expanded into the vacuum chamber through a pulsed valve. The skimmed molecular beam was crossed perpendicularly

by the co-propagating pump and probe laser beams between the repeller and extractor plates of a Wiley-McLaren electrode assembly. The resulting ions or electrons were detected using a microchannel plate backed by a steel anode or a phosphor-coated vacuum window viewed by a CCD camera. The energy resolution of the photoelectron (PE) spectra acquired in a one-photon pump and two-photon probe process was limited to typically 70 meV full width at half maximum (FWHM) by the spectral widths of the laser pulses.

The neutral ($^1A_1$) and ionic ($^2A_2$) ground state equilibrium structures of the PFB molecule were computed using second-order Møller-Plesset perturbation theory (MP2) under the resolution of the identity (RI) approximation and the spin-component scaling (SCS) modification (RI-SCS-MP2)[51–55] with a def2-TZVPPD[56–58] basis set. Vertical excitation energies (VEEs), the excited-state equilibrium structures of the neutral $^1B_2$ ($\pi\pi^*$) and $^1A_2$ ($\pi\sigma^*$) states and of the lowest two excited ionic states (both of $^2B_1$ symmetry) were calculated using the second-order approximate coupled-cluster method in the same variant (RI-SCS-CC2).[59–64] The VEEs and the potential energy curves along the vibrational modes of b_1 symmetry were calculated using the extended multi-configuration quasi-degenerate second-order perturbation theory (XMCQDPT2) method[65] with an active space of six electrons in seven orbitals, including the three highest occupied π orbitals, the three lowest unoccupied π^* orbitals, a σ^* orbital and the aug-cc-pVDZ basis set.[66] The quantum dynamics simulations were performed using the multi-configuration time-dependent Hartree method[67–69] as implemented in the Heidelberg MCTDH program package.[70] Details of the calculations with all relevant related parameters are given in the Supplementary Information.

5.3 Results

5.3.1 Stationary Spectra and Computed Electronically Excited States

The UV absorption and dispersed fluorescence spectra of PFB are depicted in Figure 5.1. The broad absorption band by the $^1B_2$ ($\pi\pi^*$) state ranges from ~280 to 240 nm without resolved vibrational structure. The band maximum at $\lambda = 259$ nm corresponds to an excitation by 4.79 eV. The 0–0 transition has previously been estimated to be at ~4.50 eV.[42,43] The very weak fluorescence[45,76] of PFB exhibits a 12 000 cm^{-1} Stokes shift and decays with a 1.9 ns lifetime under jet-cooled conditions.[39] A sizable solvatochromic red-shift of the emission of the molecules in solution with increasing solvent polarity has been interpreted in terms of the changing electronic character of the initially excited state during the assumed internal conversion to the $^1A_2$ ($\pi\sigma^*$) state.[39,46,47] As already noted, the transition from the $^1A_1$ ground state to

Table 5.I. Calculated vertical and adiabatic transition energies (in eV) from the S_0 ($^1A_1$) ground electronic state to the lowest four valence excited states of the neutral molecule, to the electronic ground state of the ion, and to the lowest two excited electronic states of the ion. Experimental values are given for comparison where available.

Method	S_1 ($^1B_2$, $\pi\pi^*$)	S_2 ($^1A_2$, $\pi\sigma^*$)	S_3 ($^1B_1$, $\pi\sigma^*$)	S_4 ($^1A_1$, $\pi\pi^*$)	D_0 ($^2A_2$, π^{-1})	D_1 ($^2B_1$, π^{-1})	D_2 ($^2B_1$, π^{-1})
Vertical excitation energies:							
RI-SCS-CC2 [a]	5.07	6.01	6.34	6.47	9.86	10.49	12.63
CASSCF [a]	4.96	7.10	7.26	8.42			
XMCQDPT2 [a]	4.85	5.93	6.20	6.29			
EOM-CCSD [b]	5.11	—	6.31	6.60			
TD-BP86 [c]	4.91	4.94	—	—			
Experimental	4.79 [d]	—	5.85 [d]	6.36 [d]	9.90 [e]	10.06 [a]	12.74 [e]
Adiabatic excitation energies:							
RI-SCS-CC2 [a]	4.55	5.33 [f]	—	—	9.57	9.93	12.43
XMCQDPT2 [a]	4.27	5.04 [f]					
Experimental	4.26,[a] 4.50 [g]	—	—	—	9.64 [h]	9.82 [e]	12.51 [i]

[a] This work. [b] Ref. 47. [c] Ref. 39. [d] Refs. 42, 71. [e] Ref. 72. [f] Saddle point with $\nu_{14} = 50i$ cm^{-1} (see SI). [g] Refs. 42, 43. [h] Ref. 73. [i] Refs. 74, 75.

the $^1A_2$ ($\pi\sigma^*$) state is forbidden in C_{2v} symmetry. The transition to the higher $^1B_1$ ($\pi\sigma^*$) state gives rise to the second absorption band seen in Figure 5.1 as a shoulder around 5.85 eV (212 nm).[42] This band strongly overlaps with the intense absorption by the $^1A_1$ ($\pi\pi^*$) state around 6.30 eV ($\sim$197 nm).[42]

The computational results for the vertical excitation energies and the electronic character of the transitions are listed in Table 5.I. Values obtained by Zgierski et al.[39] at the TD-BP86 level of theory and by Mondal et al.[48] at the EOM-CCSD level of theory are given for comparison. The RI-SCS-CC2, EOM-CCSD and XMCQDPT2 methods give results in very good agreement with each other. The four lowest-lying excited states are found to be the $^1B_2$ ($\pi\pi^*$), $^1A_2$ ($\pi\sigma^*$), $^1B_1$ ($\pi\sigma^*$) and $^1A_1$ ($\pi\pi^*$) states in order of increasing energy. The VEE of the $^1B_2$ ($\pi\pi^*$) state calculated with the XMCQDPT2 method closely matches the experimental band maximum, whereas the RI-SCS-CC2 and EOM-CCSD values slightly overestimate the experiment. The RI-SCS-CC2 and XMCQDPT2 VEEs of the $^1A_2$ ($\pi\sigma^*$) state agree with each other within 0.1 eV. These values are almost 1 eV higher than the TD-BP86 value of Ref. 39. This disagreement has important consequences regarding the interpretation of the fluorescence spectrum and the deactivation mechanism of the excited $^1B_2$ ($\pi\pi^*$) state, as will be discussed in more detail below. The calculated VEEs for the $^1B_1$ ($\pi\sigma^*$) state are again in good agreement with each other. These values appear slightly high, however, with respect to the experimental band maximum of 5.85 eV.[42,71] The EOM-CCSD calculations performed by Mondal et al. were used to

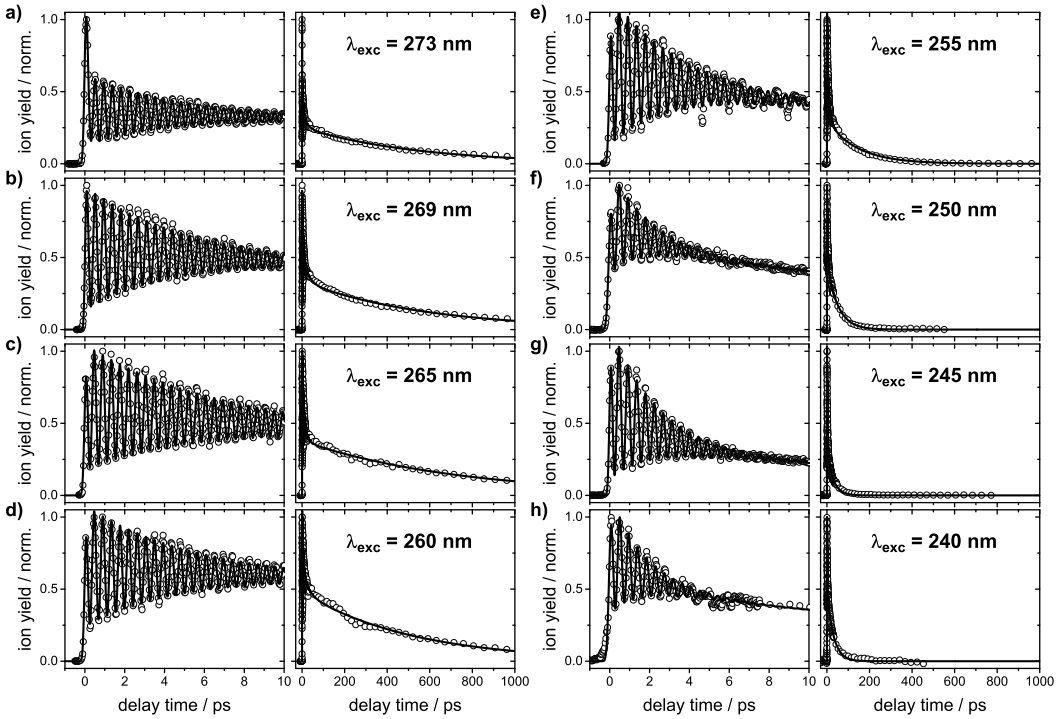

Figure 5.2. Measured temporal PFB ion yield profiles after excitation at the selected pump wavelengths. The data are plotted on time scales from 0 – 10 ps to reveal the initial oscillations and from 0 – 1000 ps to show the subsequent decay. The signals could be fitted using two exponential decay terms and an additional exponentially damped oscillatory cosine term (see text).

derive a model Hamiltonian for subsequent quantum dynamics simulations of the UV absorption spectrum.[48] The authors adjusted the VEE of the $^1B_1$ ($\pi\sigma^*$) state to 6.01 eV for best reproduction of the experimental absorption spectrum. Thus, while slightly overestimated, our VEEs of the $^1B_1$ ($\pi\sigma^*$) state are reasonably accurate with respect to what may be commonly expected of coupled-cluster and multi-reference perturbation methods. The RI-SCS-CC2, XMQCDPT2 and EOM-CCSD values for the VEE of the $^1A_1$ ($\pi\pi^*$) state appear in good agreement with the experimental band maximum.

5.3.2 Time-Resolved Time-of-Flight Mass Spectrometry Results

Time-resolved ion yield measurements were carried out following excitation of PFB in the molecular beam to the S_1 ($^1B_2$, $\pi\pi^*$) state at eight selected wavelengths in the range between λ_{pump} = 273 nm to 240 nm, distributed evenly over the UV absorption band. At all pump wavelengths, the recorded time-of-flight mass spectra showed negligible fragmentation of the excited neutral parent molecules or the PFB^+ ions after the ionization (unlike Ridley et al.,[43] who encountered severe fragmentation of the molecular ions by nanosecond laser excitation), and no signs for cluster formation (see Figure 5.S1). The transient PFB^+ ion yields from all measurements are depicted as function of time in Figure 5.2. The recorded

Table 5.II. Fit results for the measured excited state decay dynamics of PFB (with 2σ error values in parentheses).

λ_{pump} / nm	σ_{IRF} [a] / fs	A_1 / %	τ_1 / ps	A_2 / %	τ_2 / ps	A_{osc} / %	τ_D / ps	ν_{osc} / cm^{-1}	φ_{osc} / π
273 [b]	71(1)	0.15(2)	21(2)	0.32(3)	539(26)	0.53(6)	4.5(1)	77.64(5)	-0.42(2)
269	52(5)	0.20(3)	24(3)	0.30(3)	584(60)	0.50(6)	4.7(2)	77.54(4)	-0.40(2)
265	85(8)	0.16(2)	22(5)	0.26(3)	870(85)	0.58(9)	6.5(4)	77.57(5)	-0.13(3)
260	81(7)	0.13(4)	20(5)	0.31(6)	562(79)	0.56(14)	5.5(3)	77.21(6)	-0.13(3)
255	79(6)	0.22(4)	11(2)	0.18(4)	144(31)	0.60(12)	3.3(2)	75.87(8)	-0.14(2)
250	108(3)	0.16(1)	4.0(4)	0.24(2)	50(4)	0.60(8)	1.9(1)	75.6(1)	-0.14(1)
245	69(2)	0.23(1)	2.8(1)	0.20(1)	29(1)	0.57(4)	2.2(1)	75.27(5)	-0.11(1)
240	103(7)	0.14(3)	2.5(5)	0.26(4)	31(3)	0.60(17)	1.7(1)	74.4(3)	-0.24(4)

[a] Width parameter of the Gaussian describing the instrument response function (IRF).

[b] At $\lambda_{\mathrm{pump}} = 273$ nm, an additional component with a time constant on the order of σ_{IRF} was needed to fit the resonant multi-photon ionization spike at $t = 0$. This component is omitted from the list because it corresponds to the cross-correlation of the pump and probe pulse and does not actually describe a molecular relaxation process.

signals exhibit bi-exponential decay behaviors with a superimposed large-amplitude oscillation. The parameters derived by a least squares fit analysis (see Section 5.S1.2 in the Supplementary Information) of the experimental time profiles are compiled in Table 5.II. At the longest pump wavelength ($\lambda_{\mathrm{pump}} = 273$ nm), the data are described by one fast decay component with lifetime $\tau_1 = 21$ ps and a rather long-lived decay component with $\tau_2 = 539$ ps. With increasing excitation energy, the decay times decrease rapidly. At the shortest pump wavelength ($\lambda_{\mathrm{pump}} = 240$ nm), the lifetime of the fast component is only $\tau_1 = 2.5$ ps, whereas the slow component has dropped to $\tau_2 = 31$ ps. The superimposed oscillation has a period of $T_{\mathrm{osc}} = 0.43$ ps, nearly constant for the employed excitation wavelengths and corresponding to a mode of $\nu_{\mathrm{osc}} = 78 - 74\ \mathrm{cm}^{-1}$. The damping time of the oscillation drops from $\tau_{\mathrm{D}} = 4.5$ ps at 273 nm to $\tau_{\mathrm{D}} = 1.7$ ps at 240 nm.

5.3.3 Time-Resolved Photoelectron Imaging Results

Photoelectron images of PFB were taken at several fixed delay times following excitation to the S_1 ($^1B_2$, $\pi\pi^*$) state at $\lambda_{\mathrm{pump}} = 265$ nm, near the center of the UV absorption band. A typical image measured at the delay time $\Delta t = 0.46$ ps, which corresponds to the second oscillation maximum in the ion yield time profile, and the recovered meridional slice through the three-dimensional PE cloud after image inversion by pBASEX[77] are displayed in Figure 5.3. The resulting PE spectrum obtained by integration of the imaged photoelectron intensity over the angular coordinates and Jacobian transformation to the photoelectron energy scale is given in Figure 5.4. As can be seen, the main spectral features are a rather broad band

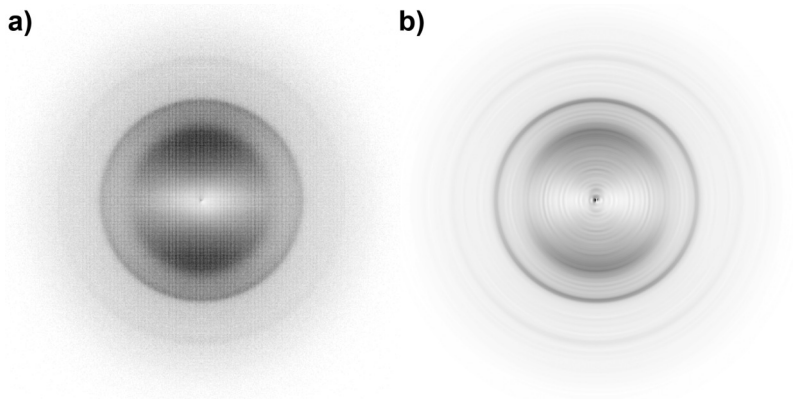

Figure 5.3. a) Photoelectron image with 4.6×10^6 recorded electrons after excitation at $\lambda_{\mathrm{pump}} = 265$ nm at delay time $\Delta t = 0.46$ ps. b) Meridional slice through the recovered three-dimensional photoelectron distribution from a), calculated with the pBASEX program. The data were radially scaled with the radius r for a better visual appearance.

with maximum at a photoelectron energy around 0.4 eV and a well-defined narrow band peaking around 0.8 eV. A broad and mostly structureless background ranges from 0 eV to about 3 eV.

To investigate the temporal evolution of the PE spectra, additional images were recorded at delay times ranging from the first ion signal maximum at $\Delta t = 0.05$ ps to the 18$^{\mathrm{th}}$ ion maximum at $\Delta t = 7.38$ ps. The corresponding spectra are overlayed in Figure 5.4. The different traces clearly show that the observed band structure does not change from maximum to maximum. Moreover, the PE spectra were examined in detail around the first revival of the ion yield (i. e. around the second ion signal maximum at $\Delta t = 0.46$ ps) in steps of $\Delta(\Delta t) = 55$ fs starting from the preceding minimum at $\Delta t = 0.24$ ps to the following minimum at $\Delta t = 0.68$ ps (Figure 5.5). Accordingly, the intensities of both PE bands strongly decrease near the ion signal minima, while the unstructured background changes little.

5.3.4 Assignment of the PE Spectral Bands

Conservation of energy in an $n + m$ photoionization scheme with n pump and m probe photons dictates that the photoelectron kinetic energy E_{el} is determined by

$$E_{\mathrm{el}} = \hbar\,(n \times \omega_{\mathrm{pump}} + m \times \omega_{\mathrm{probe}}) - IE_i - E^+_{i,\mathrm{int}}, \tag{5.1}$$

where $E^+_{i,\mathrm{int}}$ is the internal energy remaining in the cation and IE_i is the adiabatic ionization energy of the i-th ionic state. The available maximal PE kinetic energy, when no vibrational energy remains in the cation, is denoted E_{avl} in the following (i. e. $E_{\mathrm{avl}} \equiv E_{\mathrm{el}}$ for $E^+_{i,\mathrm{int}} = 0$). The first adiabatic ionization energy IE_1 of PFB (which belongs to the D_0 state) has been experimentally determined to be 9.64

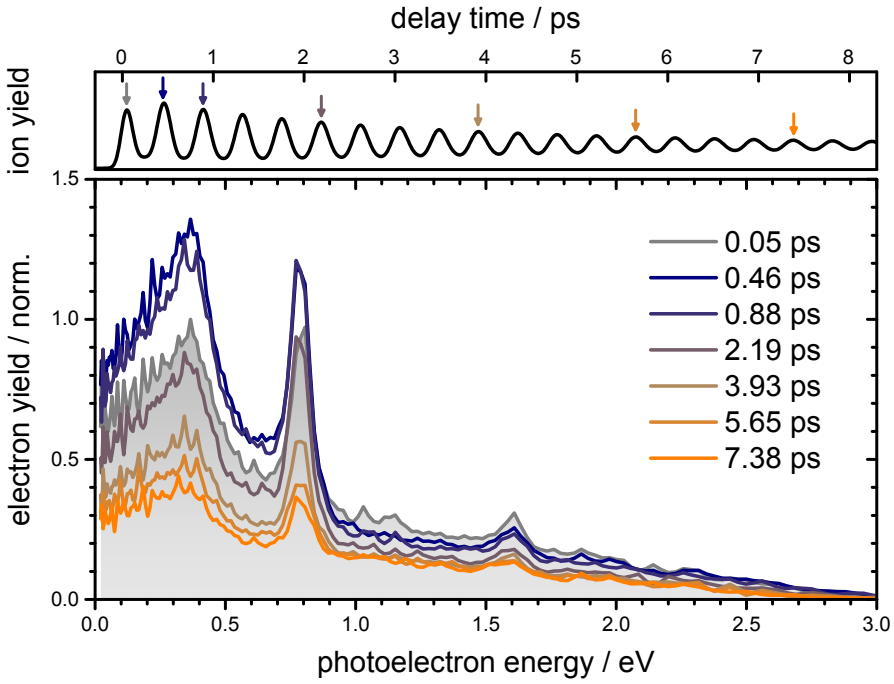

Figure 5.4. Photoelectron spectra after 265 nm excitation at seven different delay times corresponding to seven oscillation maxima of the transient ion yield signal (shown above for orientation with color-coded arrows indicating the delay times). The spectrum at $\Delta t = 0.05$ ps is displayed with a gray filling to visually set it apart from the other spectra. The small peak at $E = 1.6$ eV is an artifact due to $(2 + 1')$ ionization (see text).

eV.[73] For the second ionization energy IE_2 (belonging to the D_1 state), values of 12.50 – 12.74 eV[72,73] and a value of ∼10.2 eV[74] can be found. The 10.2 eV value seems much more likely, as an energetically very close excited cationic state above D_0 is expected for the following reason: The ionic ground and first electronically excited states of the cation arise by loss of an electron from one of the two highest occupied molecular orbitals (HOMOs). These π MOs are degenerate in benzene and HFB (e_{1g} symmetry in the D_{6h} point group).[78] The five-fold fluorine substitution in PFB lowers the symmetry to C_{2v} and lifts the orbital degeneracy so that the HOMO splits into two energetically close MOs of a_2 and b_1 symmetry.[78] Accordingly, two cationic states with comparable ionization energies are expected to exist. Because of the strong vibronic overlap and interaction of the cationic ground state and the first excited state,[79] the value of $IE_2 \approx 10.2$ eV could be determined only approximately.[74] The values of 12.50 – 12.74 eV[72,73] thus correspond to the third ionization energy (i. e. the D_2 state).

The computational results for the lowest three vertical ionization energies calculated at the RI-SCS-CC2 level of theory are included in Table 5.I. In the order of increasing energy, the ionic states are $1\,^2A_2$ (π^{-1}), $1\,^2B_1$ (π^{-1}) and $2\,^2B_1$ (π^{-1}). The calculated IE_1 and IE_3 values are in very good agreement with the experimental values. IE_2 is found to be very close to IE_1, confirming our conclusion on the D_1 ionic state

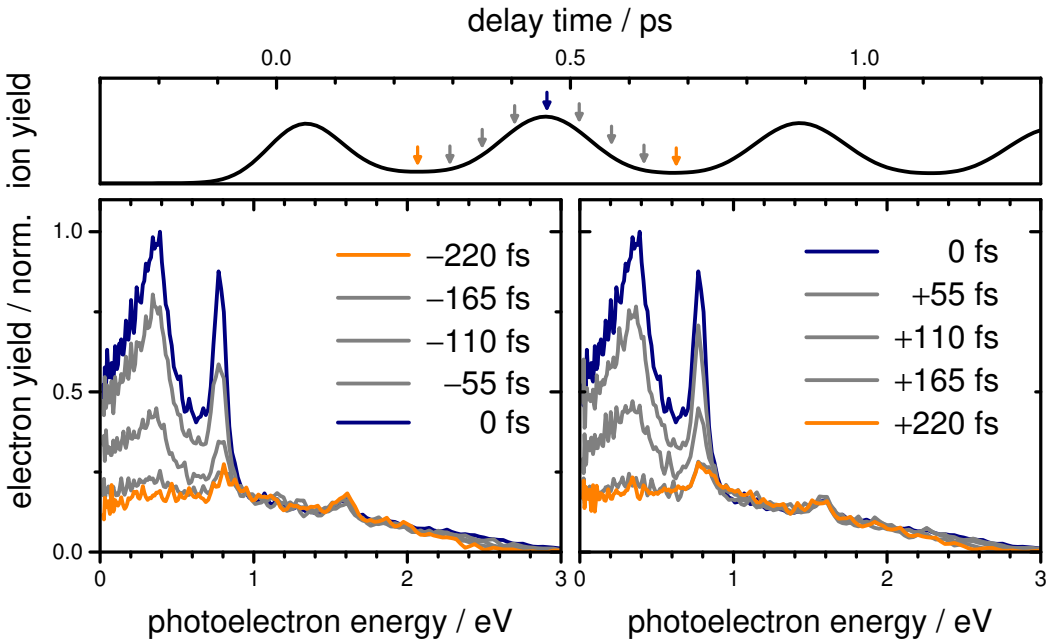

Figure 5.5. Photoelectron spectra after 265 nm excitation recorded from the first ion yield minimum at $\Delta t = 0.24$ ps to the next minimum at $\Delta t = 0.68$ ps in steps of $\Delta(\Delta t) = 55$ fs. The time delays in the plotted spectra are given relative to the ion yield maximum at $\Delta t = 0.46$ ps. The ion signal as function of delay time is given above, with color-coded arrows for orientation.

above. In the geometry optimization, the ionic states retain planar structures. The diagonalization of the Hessian matrix confirms that they are true minima. The D_2 ($^2B_1$) state has an adiabatic excitation energy of 12.43 eV compared to the experimental 12.51 eV,[74] meaning that it cannot be reached by our pump–probe photoionization scheme, so that it will not be considered further in the following. The recorded PE spectra therefore can be divided into two distinct regimes: (*i*) a low energy region up to $E_{\mathrm{avl}}^{(1+2')} = 1.21$ eV with contributions from the main $(1+2')$ ionization process, and (*ii*) a high energy region up to $E_{\mathrm{avl}}^{(2+1')} = 2.80$ eV with contributions from $(2+1')$ ionization. The photoelectrons resulting from the second scheme give rise to the broad background signal, probably due to the high density of vibronic states in the highly excited molecules.

Figure 5.6 shows the PE spectrum recorded at $\Delta t = 0.05$ ps in the energy region of the $(1+2')$ process on an enlarged scale. Following Stolow and co-workers,[80,81] we may use the calculated one-electron configurations of the excited states to determine their correlation with the ionic states upon photoionization. The configurations of the lowest two neutral and cationic states at the RI-SCS-CC2 level of theory are summarized in Table 5.III. Accordingly, the $^1B_2$ ($\pi\pi^*$) state has major contributions from the $3a_2 \rightarrow 6b_1$ (59%) and $5b_1 \rightarrow 4a_2$ (34%) configurations. By comparison of the molecular orbital occupancies, the S_1 ($\pi\pi^*$) state therefore correlates with both the D_0 and D_1 states of the cation, while the S_2 ($\pi\sigma^*$) state correlates only with the

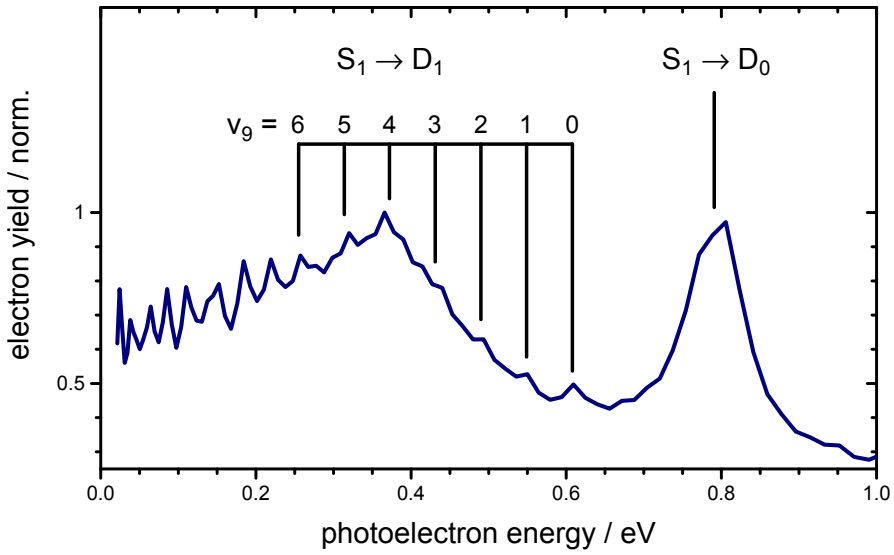

Figure 5.6. Assignment of the photoelectron spectrum recorded at Δt = 0.05 ps. The ionic ground state D_0 has a molecular structure similar to the Franck–Condon geometry, resulting in a sharp peak. The first excited ionic state D_1 has a slightly different equilibrium structure, which leads to an activation of the totally symmetric mode ν_9.

D_0 state. Both PE bands are assigned to the ionization of the excited $^1B_2$ ($\pi\pi^*$) state to the lowest two cationic states, (*i*) because of the calculated ionization correlations, (*ii*) because of the good agreement of the energy difference between the two PE band maxima with the difference of the ionization energies IE_1 and IE_2, and (*iii*) because the PE band energy difference does not agree with the calculated energy splitting between the $^1B_2$ ($\pi\pi^*$) and $^1A_2$ ($\pi\sigma^*$) excited states. Specifically, the 0.4 eV PE band is attributed to the S_1 ($^1B_2$, $\pi\pi^*$) $\rightarrow$ D_1 ($^2B_1$, π^{-1}) transition, and the 0.8 eV band is assigned to the S_1 ($^1B_2$, $\pi\pi^*$) $\rightarrow$ D_0 ($^2A_2$, π^{-1}) transition.

The $S_1 \rightarrow D_1$ PE band displays a vibrational progression that can be assigned to the totally symmetric ν_9 mode (ν_{6a} in Wilson notation[82]). The vibrational frequency is known to be ν_9 = 474 cm^{-1} in the neutral ground state,[83] and was computed to be 475 cm^{-1} in the D_1 state. The progression indicates a significant structural rearrangement from S_1 to D_1. The first member of the progression is labeled v_9 = 0, although there is no conclusive evidence for this assignment. Under this assumption, the energy difference between the adiabatic ionization energies of the D_0 (9.64 eV[73]) and D_1 (9.82 eV) ionic states is 0.2 eV, which is in good agreement with VUV absorption experiments[78,84] and with the computational results.

With the above assignments, the adiabatic excitation energy of the S_1 state is determined from our PE spectra to amount to 4.26 eV. This new value, which we include in Table 5.I, is substantially lower than the previous estimate of 4.50 eV.[42,43] Further, our geometry optimization of the S_1 excited state at the RI-SCS-CC2 level of theory yielded one stationary point, which was confirmed as a true minimum by

Table 5.III. Molecular orbital configurations and their contribution (weight) to the electronic excitations at the RI-SCS-CC2 level of theory. The correlated ion state was determined with the assumption of a single active electron ionization without rearrangement of the core electrons (Koopmans' picture). The two configurations of the S_1 excited state are found to correlate with different ionic states, explaining the two bands in the photoelectron spectra.

	Occupied orbitals			Unoccupied orbitals					
									
Neutral state	$4b_1$ (π)	$5b_1$ (π)	$3a_2$ (π)	$6b_1$ (π^*)	$4a_2$ (π^*)	$20a_1$ (σ^*)	$21a_1$ (σ^*)	Weight	Correlated ion state
S_0 ($^1A_1$)	2	2	2						
S_1 ($^1B_2$, $\pi\pi^*$)	2	2	1	1				59 %	D_0 ($^2A_2$)
	2	1	2	0	1			34 %	D_1 ($^2B_1$)
S_2 ($^1A_2$, $\pi\sigma^*$)	2	2	1	0	0	1		53 %	D_0 ($^2A_2$)
	2	2	1	0	0	0	1	26 %	D_0 ($^2A_2$)
Ionic state									
D_0 ($^2A_2$, π^{-1})	2	2	1						
D_1 ($^2B_1$, π^{-1})	2	1	2					98 %	
D_2 ($^2B_1$, π^{-1})	1	2	2					82 %	

the Hessian matrix diagonalization. In the calculated equilibrium structure, the F atom opposing the single H atom is bent out of the molecular plane by 33°, and the adjacent F atoms are bent out of plane in the opposite direction by 8°. Adiabatic excitation energies of 4.55 eV and 4.27 eV were computed at the RI-SCS-CC2 and XMQCDPT2 levels of theory. The latter one is in excellent agreement with the experimental result from our PE spectra.

5.4 Discussion

To investigate the molecular mechanisms giving rise to the marked oscillations in the measured ion yield spectra, we note first that the $^1B_2$ ($\pi\pi^*$) and $^1A_2$ ($\pi\sigma^*$) excited electronic states of the PFB molecule may be vibronically coupled by out-of-plane vibrational modes with b_1 symmetry. With this premise, we present MCTDH quantum dynamics simulations based on a vibronic coupling model Hamiltonian[85,86] parametrized from the results of the XMCQDPT2 calculations. The computational results are discussed in relation to the experimental findings.

5.4.1 Vibronic Coupling Model and Quantum Dynamics Simulations

The adiabatic and diabatic potential energy curves of the $^1B_2$ ($\pi\pi^*$) and $^1A_2$ ($\pi\sigma^*$) electronic states along the out-of-plane b_1 modes are presented in Figure 5.7. The diabatic potential energy curves of the first excited state all have their minimum at the planar Franck–Condon (FC) structure, while the first adiabatic electronic state exhibits symmetric double wells along the Q_{20}, Q_{18}, Q_{17} and Q_{16} modes with minima at distorted geometries (the displacement vectors of the b_1 modes are illustrated in Figure 5.S7). This symmetry breaking effect, known as pseudo Jahn-Teller effect,[87] is caused by the strong vibronic couplings between the $^1B_2$ ($\pi\pi^*$) and $^1A_2$ ($\pi\sigma^*$) states induced by the b_1 modes. These couplings induce a repelling of the first and second adiabatic potential energy curves. In case of the Q_{20}, Q_{18}, Q_{17} and Q_{16} modes, the couplings are strong enough to stabilize out-of-plane distorted geometries in the first excited state. In contrast, the diabatic and adiabatic potential energy curves along the Q_{19} and Q_{15} modes are almost identical, because the vibronic couplings along these modes are comparatively smaller (the first-order coupling constants are given in Table 5.SIII).

Two different quantum dynamics models were considered: A first model, called 3D, included only the three lowest-frequency b_1 modes Q_{20}, Q_{19} and Q_{18}, while the second model, called 6D, included all six b_1 modes. In both cases, the wavefunction was propagated for 5 picoseconds. The quantum dynamics results obtained from the 3D model are depicted in Figure 5.8 a – c. As can be seen, the diabatic electronic state populations in Figure 5.8 a exhibit clear long-lived oscillations, reflecting a periodic change between $\pi\pi^*$ and $\pi\sigma^*$ characters. A fit to the first excited diabatic state population (blue line in Figure 5.8 a) assuming a suitable analytical expression (cf. Section 5.S2.6) gave a frequency $\nu_{\mathrm{osc}} = 92$ cm^{-1} for the oscillation and a damping time constant $\tau_{\mathrm{D}} = 2.36$ ps (cf. Table 5.SVI), in very good agreement with the experimental values extracted from the transient ion yield measurement.

The evolving wavepacket was further analyzed to investigate the physical mechanism behind those long-lived oscillations. Figure 5.8 b presents a contour plot of the reduced density of the component of the wavepacket corresponding to the first diabatic electronic state ($\pi\pi^*$ character), denoted $\psi^{(1)}(\boldsymbol{Q}, t)$, along the Q_{20} coordinate as a function of time. The reduced density along a given coordinate Q_i is simply the density $\langle\psi^{(1)}(\boldsymbol{Q}, t)|\psi^{(1)}(\boldsymbol{Q}, t)\rangle$ integrated over all the coordinates except Q_i. Immediately after excitation, the wavepacket is localized in the FC region around $Q_{20} = 0$, but is then split into two components, one moving towards positive and the other moving towards negative values up to $Q_{20} \approx \pm 10$. This behavior is purely quantum, and corresponds to a strong out-of-plane distortion occurring

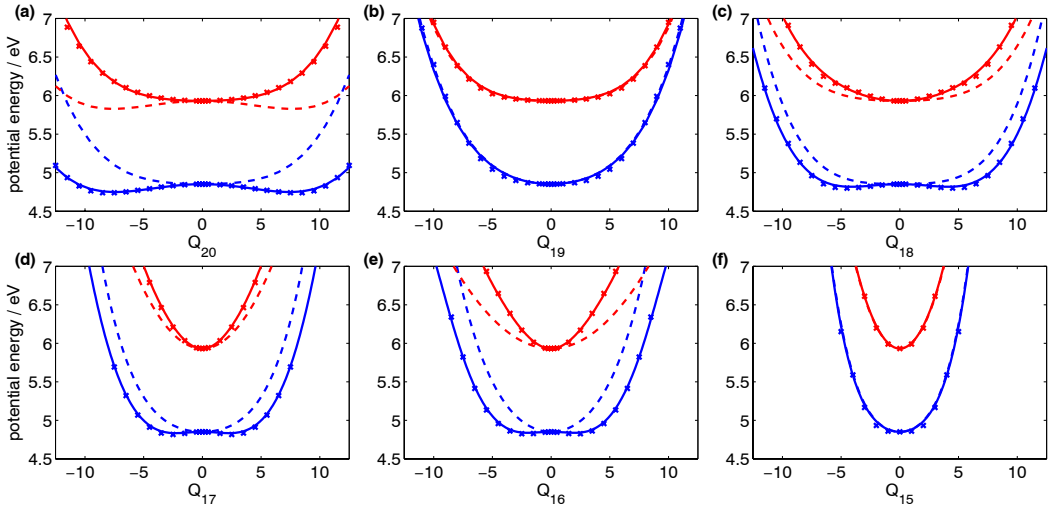

Figure 5.7. a) – f) Diabatic (dashed lines) and adiabatic (solid lines) potential energy curves of the two lowest excited electronic states along the vibrational modes of b_1 symmetry Q_{20} to Q_{15}. The electronic states continuously connected to the $^1B_2$ ($\pi\pi^*$) and $^1A_2$ ($\pi\sigma^*$) states at the FC structure are shown in blue and red, respectively. The crosses represent the XMCQDPT2 energies, and the lines are obtained from the vibronic coupling model.

simultaneously on both sides of the molecular plane. The two components then start to move back towards the FC region, where they recombine. This motion is repeated periodically. After a few oscillations, however, a dephasing of the various components of the wavepacket occurs, which leads to a spreading of the wavepacket and damping of the oscillation.

The oscillatory behavior of the wavepacket can also be seen from the expectation values of the squared position operators, $\langle\psi^{(1)}(\boldsymbol{Q},t)|Q_i^2|\psi^{(1)}(\boldsymbol{Q},t)\rangle$, which reflect the spreading of the wavepacket along the coordinates Q_i. Note that the expectation value of the position operators Q_i is zero by symmetry. As shown in Figure 5.8 c, one can see large and regular oscillations for the Q_{20} mode that match the oscillations of the diabatic electronic state populations. In contrast, little oscillatory motion is observed along the two other modes. These results thus provide a clear interpretation of the physical mechanism at the origin of the oscillations seen in the diabatic state populations (Figure 5.8 a): Upon excitation to the first excited electronic state, which is of $\pi\pi^*$ character at the FC geometry, the molecule undergoes a periodic out-of-plane motion, preferentially along the Q_{20} mode. As the wavepacket moves from the FC region towards the two symmetry-related minima of the lowest adiabatic state, the electronic wavefunction acquires a more and more pronounced $\pi\sigma^*$ character. The oscillation of the diabatic state populations is therefore driven by the periodic out-of-plane molecular distortion.

The above 3D model was found to be the simplest model that qualitatively reproduces the long-lived regular oscillations observed in the transient ion yield measurements. A one-dimensional model including only the Q_{20} mode does not provide a long-

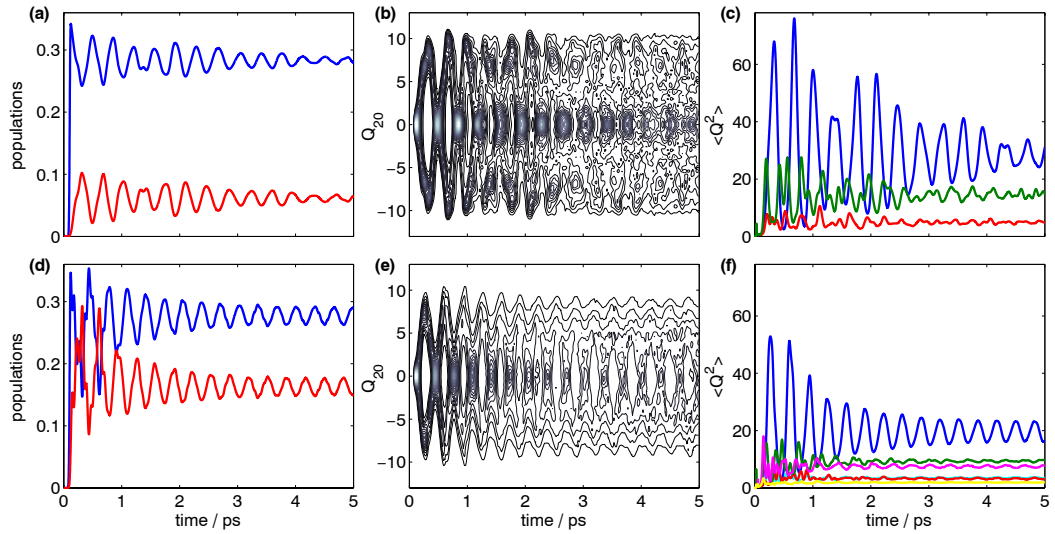

Figure 5.8. Quantum dynamics results obtained from the 3D (upper row, a – c) and 6D (lower row, d – e) models. a) and d): Populations of the $\pi\pi^*$ (blue) and $\pi\sigma^*$ (red) diabatic electronic states. b) and (e): Contour plot of the reduced density of the component of the wavepacket corresponding to the $\pi\pi^*$ diabatic electronic state along the Q_{20} coordinate. c) and f): Expectation values of the squared position operators of the b_1 modes Q_{20} (blue), Q_{19} (red), Q_{18} (green), Q_{17} (magenta), Q_{16} (cyan) and Q_{15} (yellow).

lived and regular oscillatory pattern as does the 3D model. This indicates that the couplings between the different vibrational modes need to be accounted for to properly describe the excited-state dynamics. The oscillations of the diabatic state populations obtained from the 3D model are of small amplitude when compared to the large amplitude oscillations observed in the experiment. We therefore turned to the 6D model, the results of which are presented in Figure 5.8 d – e. As before, the model predicts a long-lived oscillation of the diabatic electronic state populations. A fit to the first excited diabatic electronic state population yielded $\nu_{\mathrm{osc}} = 103$ cm^{-1} and $\tau_{\mathrm{D}} = 1.96$ ps for the frequency and damping time constant (cf. Table 5.SVI), again in good agreement with the values obtained experimentally. The reduced density of the first diabatic excited state component of the wavepacket along the Q_{20} mode and the expectation values of the squared position operators are given in Figure 5.8 e and f, respectively. As in the 3D model, a wide amplitude oscillatory motion along Q_{20} is observed, while irregular motion is encountered along the other modes. However, the amplitude of the oscillation of the diabatic electronic state populations obtained from the 6D model is larger during the first 2 picoseconds, and a larger amount of population is transferred to the second excited diabatic state. This was found to be a consequence of the large coupling between the two diabatic electronic states induced by motion along the Q_{17} and Q_{16} modes (see Table 5.SIII), which were not taken into account in the 3D model.

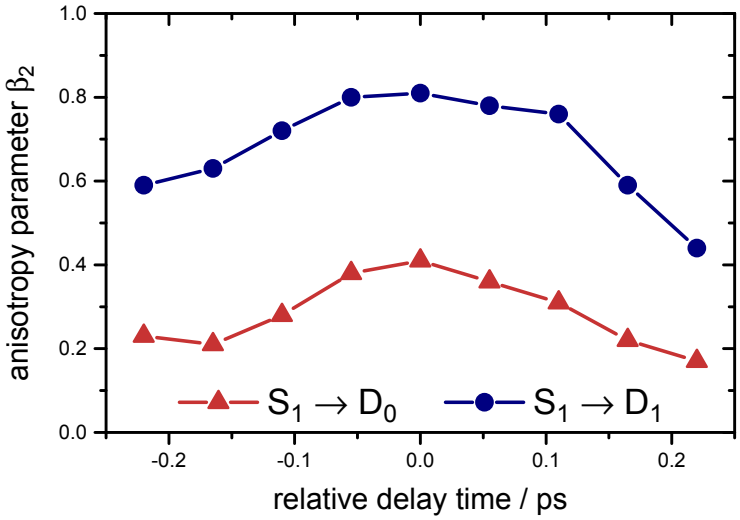

Figure 5.9. Anisotropy of the photoelectron angular distribution (PAD) in terms of the β_2 anisotropy parameter from both bands observed in the PE spectra presented in Fig. 5.5. The delay time is given relative to the ion yield maximum at $\Delta t = 0.46$ ps. The periodically changing electronic character of the emitting electronic state from the minimum to the maximum, and back to the following minimum is clearly evident from the temporal evolution of β_2.

5.4.2 Mapping of the Dynamics to the Experimental Signal

According to the computational results, the lowest adiabatic (S_1) state is of $\pi\pi^*$ character in the FC region (planar molecular structure), and aquires a strongly mixed $\pi\pi^*/\pi\sigma^*$ character in the minima corresponding to strong out-of-plane distortions due to b_1 modes. The molecular out-of-plane vibrations lead, therefore, to a periodic change of the electronic character of the S_1 state, affecting the electronic transition moment for photoionization. Assuming that ionization may preferentially occur from the $\pi\pi^*$ electronic configuration, the long-lived oscillations observed in the transient ion yield provide a direct mapping of the strongly coupled electron-nuclear dynamics. This assumption is corroborated by the temporal evolution of the anisotropy parameter β_2 of the photoelectron angular distribution (PAD), although we note that the interpretation of absolute β_2 values is hampered by the additional anisotropy introduced in the two-photon ionization process. In Figure 5.9, the β_2 parameter of the $S_1 \rightarrow D_0$ and $S_1 \rightarrow D_1$ PE bands from the scan of a single oscillation period in $\Delta(\Delta t) = 55$ fs steps is shown, corresponding to the PE spectra depicted in Figure 5.5. The β_4 parameter was found to be nearly delay time independent with values around 0.0 and was thus omitted. As can be seen, the temporal evolution of the β_2 values of both bands closely resembles the oscillation of the transient ion yield. As rotational dynamics may be neglected on this fast time scale (the PAD can be affected by the electronic character of the emitting state, and by rotational dynamics[88]), the value of β_2 is determined by the electronic character of the S_1 state.

This observation directly provides the connection between the experimental data and the computational results.

Nonetheless, we also checked for an energetic origin of the signal oscillation, i. e. if the absorption of 4 $\times$ 804 nm (or 2 $\times$ 402 nm, respectively) photons may not provide the necessary ionization energy at the outer turning points of the excited wavepacket. Calculating this ionization energy is computationally challenging, but an upper bound is provided by the ionization energy of the S_1 state in its relaxed equilibrium structure. The calculated value $IE_{S_1}^{rel}$ = 6.81 eV at the RI-SCS-CC2 level of theory is close to the energy of four 804 nm probe photons (6.17 eV). Furthermore, the amplitude of the transient ion yield oscillation would be very sensitive to the probe pulse intensity. Such a dependence could not be experimentally observed, thus rendering energetic effects unlikely.

5.4.3 Radiationless Electronic Deactivation Dynamics

The excitation energy dependencies of the decay time constants τ_1, τ_2 and τ_D describing the vibrational and electronic decay dynamics of the $^1B_2$ ($\pi\pi^*$) state are found to follow similar patterns, as depicted in Figure 5.10. The values of all three decay time constants exhibit a plateau between 273 – 265 nm, and decrease sharply for shorter excitation wavelengths. The slower decay time constant τ_2 can be assigned to the S_0 electronic ground state recovery. As shown in Figure 5.10 a, the values of $\tau_2 > 500$ ps in the excitation wavelength range of 273 – 260 nm drop to τ_2 = 29 – 50 ps for wavelengths shorter than 255 nm. The small τ_2 values likely correspond to an electronic deactivation pathway through a low-lying CoIn of the $\pi\pi^*$ potential energy surface with the S_0 state, which is inaccessible at lower excitation energies. The faster decay time constant τ_1, with values of τ_1 = 20 – 24 ps in the excitation wavelength range of 273 – 260 nm as shown in Figure 5.10 b, may reflect an intramolecular vibrational energy redistribution (IVR) process. This process becomes much faster with τ_1 = 2.5 – 4.0 ps for excitation wavelengths 255 – 240 nm in line with the increasing density of vibrational states.

The excitation wavelength dependence of the oscillation damping time constant τ_D, which describes the dephasing time of the various components of the wavepacket, is shown in Figure 5.10 c. We determined values of τ_D = 4.5 – 6.5 ps for excitation wavelengths of 273 – 260 nm, while τ_D decreases to 3.3 – 1.7 ps in the 255 – 240 nm range. The relatively slow dephasing can be understood because as Q_{20} is the lowest-frequency mode, the IVR process must therefore involve higher-frequency modes. On the other hand, IVR from the other b_1 modes ($Q_{19} - Q_{15}$) may well affect the damping time constant: the quantum dynamics simulations indicated that these modes are necessary to form the oscillating wavepacket. Presently, it cannot be unambiguously

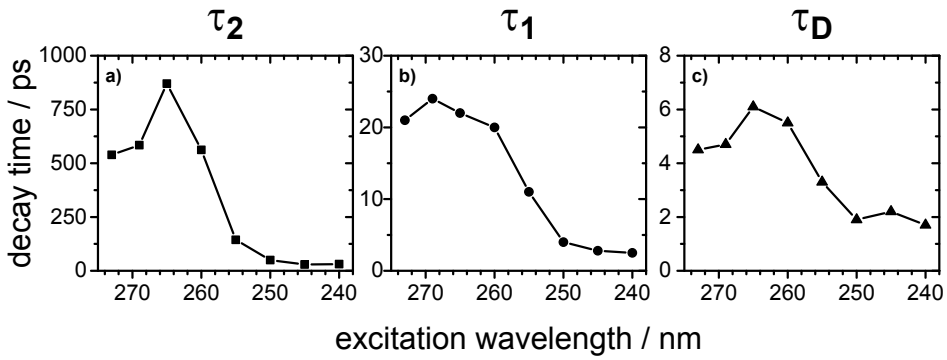

Figure 5.10. a) – c) Excitation wavelength dependence of the transient ion yield decay time constants τ_2, τ_1 and τ_D, respectively. All time constants exhibit a similar dependence on λ_{pump} with a maximum around 265 nm. The sharp decrease beginning from 255 nm is attributed to the accessibility of a conical intersection between the electronically excited state and the ground state.

discerned if the pronounced excitation wavelength dependence of the τ_D and τ_1 time constants is due to the influence of the higher density of vibrational states at higher excitation energies on the occurring IVR, or to the energetic accessibility of the CoIn with the S_0 state. In any case, the $\pi\pi^*/S_0$ CoIn seems to be of crucial importance for the excited-state vibrational and electronic deactivation dynamics. When the CoIn is not accessed by the excited wavepacket, the $\pi\pi^*$ state may deactivate by emitting vibrationally structureless fluorescence with a large Stokes shift (see Figure 5.1) after relaxation into the S_1 equilibrium structure, where the diabatic $\pi\pi^*$ state was found to be mixed with the $\pi\sigma^*$ state. This likely explains the solvatochromic red-shift of the emission in polar solvents. These issues are the subject of ongoing investigations in our group.

5.5 Conclusions

The excited-state dynamics of pentafluorobenzene have been studied experimentally by femtosecond time-resolved time-of-flight mass spectrometry and photoelectron imaging spectroscopy and theoretically by a vibronic coupling model and MCTDH simulations. The measured transient ion yields were found to exhibit a biexponential decay behavior, superimposed with a long-lived, large amplitude oscillation of 78 – 74 cm^{-1} frequency. Photoelectron spectral bands were best resolved in the maxima of the oscillation, and gradually vanishing towards the minima. The anisotropy of the photoelectron angular distribution indicated a periodically changing electronic character of the emitting state, which modulates the ionization transition moment correspondingly.

The physical mechanism of the signal oscillation was revealed by XMCQDPT2 electronic structure calculations and MCTDH quantum dynamics simulations. The results showed that the lowest adiabatic excited-state potential energy curves exhibit a symmetric double-well character along certain b_1 modes. The reason is a strong vibronic coupling between the $^1B_2$ ($\pi\pi^*$) state and the energetically higher-lying $^1A_2$ ($\pi\sigma^*$) state. The excitation laser pulse creates a highly localized wavepacket in the Franck–Condon region of the excited state, which is of $\pi\pi^*$ character in this structure. The wavepacket is then split into two symmetric components that simultaneously move in opposite directions out of the Franck–Condon region, and then return to recombine. This motion is repeated periodically and causes an oscillatory change of the electronic character between $\pi\pi^*$ (at the planar structure) and mixed $\pi\pi^*/\pi\sigma^*$, with the largest $\pi\sigma^*$ contribution at maximal displacements of the b_1 modes (out-of-plane distortions). As the ionization occurs preferentially from the $\pi\pi^*$ electronic configuration, the ionizing probe laser pulse provides a direct mapping of the observed periodic motion. The detected oscillation of the time-resolved signals is essentially an electronic coherence driven by molecular vibrations, and can thus be denoted as a "vibronic coherence". Additional theoretical work, including simulations of the time-resolved photoelectron spectra based on an extended model, is in progress in our group and will provide further details on the relation between the non-adiabatically driven periodic out-of-plane motion and the long-lived oscillations observed experimentally.

Recently, similar long-lived oscillations were observed in catechol[89] and in the lignin building blocks syringol and guaiacol,[90] where symmetric double-well potential energy surfaces of the S_1 excited states were calculated as well. Among others, these molecules may also turn as interesting candidates to study the coherent excited-state dynamics induced by vibronic coupling of energetically close-lying electronic states of $\pi\pi^*$ and $\pi\sigma^*$ character.

Acknowledgements

This work has been supported by the Deutsche Forschungsgemeinschaft. SZ thanks the Alexander von Humboldt foundation for a fellowship.

References

1. A. L. Sobolewski, W. Domcke, C. Dedonder-Lardeux, and C. Jouvet, "Excited-state hydrogen detachment and hydrogen transfer driven by repulsive $^1\pi\sigma^*$

states: A new paradigm for nonradiative decay in aromatic biomolecules," Phys. Chem. Chem. Phys. **4**, 1093–1100 (2002).
2. M. N. R. Ashfold, B. Cronin, A. L. Devine, R. N. Dixon, and M. G. D. Nix, "The Role of $\pi\sigma^*$ Excited States in the Photodissociation of Heteroaromatic Molecules," Science **312**, 1637–1640 (2006).
3. M. N. R. Ashfold, G. A. King, D. Murdock, M. G. D. Nix, T. A. A. Oliver, and A. G. Sage, "$\pi\sigma^*$ excited states in molecular photochemistry," Phys. Chem. Chem. Phys. **12**, 1218–1238 (2010).
4. G. M. Roberts and V. G. Stavros, "The role of $\pi\sigma^*$ states in the photochemistry of heteroaromatic biomolecules and their subunits: insights from gas-phase femtosecond spectroscopy," Chem. Sci. **5**, 1698–1722 (2014).
5. J. Wei, A. Kuczmann, J. Riedel, F. Renth, and F. Temps, "Photofragment velocity map imaging of H atom elimination in the first excited state of pyrrole," Phys. Chem. Chem. Phys. **5**, 315–320 (2003).
6. J. Wei, J. Riedel, A. Kuczmann, F. Renth, and F. Temps, "Photodissociation dynamics of pyrrole: Evidence for mode specific dynamics from conical intersections," Faraday Discuss. **127**, 267–282 (2004).
7. B. Cronin, M. G. D. Nix, R. H. Qadiri, and M. N. R. Ashfold, "High resolution photofragment translational spectroscopy studies of the near ultraviolet photolysis of pyrrole," Phys. Chem. Chem. Phys. **6**, 5031–5041 (2004).
8. H. Lippert, H.-H. Ritze, I. V. Hertel, and W. Radloff, "Femtosecond Time-Resolved Hydrogen-Atom Elimination from Photoexcited Pyrrole Molecules," ChemPhysChem **5**, 1423–1427 (2004).
9. V. Vallet, Z. Lan, S. Mahapatra, A. L. Sobolewski, and W. Domcke, "Photochemistry of pyrrole: Time-dependent quantum wave-packet description of the dynamics at the $^1\pi\sigma^*$-S_0 conical intersections," J. Chem. Phys. **123**, 144307 (2005).
10. R. Montero, Á. Peralta Conde, V. Ovejas, M. Fernández-Fernández, F. Castaño, J. R. Vázquez de Aldana, and A. Longarte, "Femtosecond evolution of the pyrrole molecule excited in the near part of its UV spectrum," J. Chem. Phys. **137**, 064317 (2012).
11. G. Wu, S. P. Neville, O. Schalk, T. Sekikawa, M. N. R. Ashfold, G. A. Worth, and A. Stolow, "Excited state non-adiabatic dynamics of pyrrole: A time-resolved photoelectron spectroscopy and quantum dynamics study," J. Chem. Phys. **142**, 074302 (2015).
12. G. A. King, T. A. A. Oliver, and M. N. R. Ashfold, "Dynamical insights into $^1\pi\sigma^*$ state mediated photodissociation of aniline," J. Chem. Phys. **132**, 214307 (2010).
13. R. Montero, Á. P. Conde, V. Ovejas, R. Martínez, F. Castaño, and A. Longarte, "Ultrafast dynamics of aniline in the 294-234 nm excitation range: The role of the $\pi\sigma^*$ state," J. Chem. Phys. **135**, 054308 (2011).

14. G. M. Roberts, C. A. Williams, J. D. Young, S. Ullrich, M. J. Paterson, and V. G. Stavros, "Unraveling Ultrafast Dynamics in Photoexcited Aniline," J. Am. Chem. Soc. **134**, 12578–12589 (2012).
15. F. Wang, S. P. Neville, R. Wang, and G. A. Worth, "Quantum Dynamics Study of Photoexcited Aniline," J. Phys. Chem. A **117**, 7298–7307 (2013).
16. M. Sala, O. M. Kirkby, S. Guérin, and H. H. Fielding, "New insight into the potential energy landscape and relaxation pathways of photoexcited aniline from CASSCF and XMCQDPT2 electronic structure calculations," Phys. Chem. Chem. Phys. **16**, 3122–3133 (2014).
17. O. M. Kirkby, M. Sala, G. Balerdi, R. de Nalda, L. Bañares, S. Guérin, and H. H. Fielding, "Comparing the electronic relaxation dynamics of aniline and d_7-aniline following excitation at 272–238 nm," Phys. Chem. Chem. Phys. **17**, 16270–16276 (2015).
18. Z. Lan, W. Domcke, V. Vallet, A. L. Sobolewski, and S. Mahapatra, "Time-dependent quantum wave-packet description of the $^1\pi\sigma^*$ photochemistry of phenol," J. Chem. Phys. **122**, 224315 (2005).
19. M. G. D. Nix, A. L. Devine, B. Cronin, R. N. Dixon, and M. N. R. Ashfold, "High resolution photofragment translational spectroscopy studies of the near ultraviolet photolysis of phenol," J. Chem. Phys. **125**, 133318 (2006).
20. A. Iqbal, M. S. Y. Cheung, M. G. D. Nix, and V. G. Stavros, "Exploring the Time-Scales of H-Atom Detachment from Photoexcited Phenol-h_6 and Phenol-d_5: Statistical vs Nonstatistical Decay," J. Phys. Chem. A **113**, 8157–8163 (2009).
21. R. N. Dixon, T. A. A. Oliver, and M. N. R. Ashfold, "Tunnelling under a conical intersection: Application to the product vibrational state distributions in the UV photodissociation of phenols," J. Chem. Phys. **134**, 194303 (2011).
22. G. M. Roberts, A. S. Chatterley, J. D. Young, and V. G. Stavros, "Direct Observation of Hydrogen Tunneling Dynamics in Photoexcited Phenol," J. Phys. Chem. Lett. **3**, 348–352 (2012).
23. A. S. Chatterley, J. D. Young, D. Townsend, J. M. Żurek, M. J. Paterson, G. M. Roberts, and V. G. Stavros, "Manipulating dynamics with chemical structure: probing vibrationally-enhanced tunnelling in photoexcited catechol," Phys. Chem. Chem. Phys. **15**, 6879–6892 (2013).
24. D. J. Hadden, K. L. Wells, G. M. Roberts, L. T. Bergendahl, M. J. Paterson, and V. G. Stavros, "Time resolved velocity map imaging of H-atom elimination from photoexcited imidazole and its methyl substituted derivatives," Phys. Chem. Chem. Phys. **13**, 10342–10349 (2011).
25. R. Crespo-Otero, M. Barbatti, H. Yu, N. L. Evans, and S. Ullrich, "Ultrafast Dynamics of UV-Excited Imidazole," ChemPhysChem **12**, 3365–3375 (2011).
26. R. Montero, Á. P. Conde, V. Ovejas, M. Fernández-Fernández, F. Castaño, and A. Longarte, "Ultrafast Evolution of Imidazole after Electronic Excitation," J. Phys. Chem. A **116**, 10752–10758 (2012).

27. H. Lippert, H. H. Ritze, I. V. Hertel, and W. Radloff, "Femtosecond time-resolved analysis of the photophysics of the indole molecule," Chem. Phys. Lett. **398**, 526–531 (2004).
28. R. Livingstone, O. Schalk, A. E. Boguslavskiy, G. Wu, L. Therese Bergendahl, A. Stolow, M. J. Paterson, and D. Townsend, "Following the excited state relaxation dynamics of indole and 5-hydroxyindole using time-resolved photoelectron spectroscopy," J. Chem. Phys. **135**, 194307 (2011).
29. T. A. A. Oliver, G. A. King, and M. N. R. Ashfold, "Position matters: competing O–H and N–H photodissociation pathways in hydroxy- and methoxy-substituted indoles," Phys. Chem. Chem. Phys. **13**, 14646–14662 (2011).
30. A. L. Sobolewski and W. Domcke, "On the mechanism of nonradiative decay of DNA bases: ab initio and TDDFT results for the excited states of 9H-adenine," Eur. Phys. J. D **20**, 369–374 (2002).
31. C. E. Crespo-Hernández, B. Cohen, P. M. Hare, and B. Kohler, "Ultrafast Excited-State Dynamics in Nucleic Acids," Chem. Rev. **104**, 1977–2020 (2004).
32. S. Perun, A. L. Sobolewski, and W. Domcke, "Ab Initio Studies on the Radiationless Decay Mechanisms of the Lowest Excited Singlet States of 9H-Adenine," J. Am. Chem. Soc. **127**, 6257–6265 (2005).
33. S. Perun, A. L. Sobolewski, and W. Domcke, "Photostability of 9H-adenine: mechanisms of the radiationless deactivation of the lowest excited singlet states," Chem. Phys. **313**, 107–112 (2005).
34. W. C. Chung, Z. Lan, Y. Ohtsuki, N. Shimakura, W. Domcke, and Y. Fujimura, "Conical intersections involving the dissociative $^1\pi\sigma^*$ state in 9H-adenine: a quantum chemical ab initio study," Phys. Chem. Chem. Phys. **9**, 2075–2084 (2007).
35. C. T. Middleton, K. d. L. Harpe, C. Su, Y. K. Law, C. E. Crespo-Hernández, and B. Kohler, "DNA Excited-State Dynamics: From Single Bases to the Double Helix," Annu. Rev. Phys. Chem. **60**, 217–239 (2009).
36. C. R. Brundle, M. B. Robin, N. A. Kuebler, and H. Basch, "Perfluoro effect in photoelectron spectroscopy. I. Nonaromatic molecules," J. Am. Chem. Soc. **94**, 1451–1465 (1972).
37. C. R. Brundle, M. B. Robin, and N. A. Kuebler, "Perfluoro effect in photoelectron spectroscopy. II. Aromatic molecules," J. Am. Chem. Soc. **94**, 1466–1475 (1972).
38. A. P. Hitchcock, P. Fischer, A. Gedanken, and M. B. Robin, "Antibonding σ^* valence MOs in the inner-shell and outer-shell spectra of the fluorobenzenes," J. Phys. Chem. **91**, 531–540 (1987).
39. M. Z. Zgierski, T. Fujiwara, and E. C. Lim, "Photophysics of aromatic molecules with low-lying $\pi\sigma^*$ states: Fluorinated benzenes," J. Chem. Phys. **122**, 144312–144312–6 (2005).
40. H. Studzinski, S. Zhang, Y. Wang, and F. Temps, "Ultrafast nonradiative dynamics in electronically excited hexafluorobenzene by femtosecond time-resolved mass spectrometry," J. Chem. Phys. **128**, 164314 (2008).

41. M. Z. Zgierski, T. Fujiwara, and E. C. Lim, "Role of the $\pi\sigma^*$ State in Molecular Photophysics," Acc Chem Res **43**, 506–517 (2010).
42. J. Philis, A. Bolovinos, G. Andritsopoulos, E. Pantos, and P. Tsekeris, "A comparison of the absorption spectra of the fluorobenzenes and benzene in the region 4.5-9.5 eV," J. Phys. B **14**, 3621–3635 (1981).
43. T. Ridley, D. M. Rogers, and K. P. Lawley, "A combined resonance enhanced multiphoton ionization and ab initio study of the first absorption band of 1,2,4,5-tetrafluorobenzene, pentafluorobenzene, and hexafluorobenzene," J. Chem. Phys. **141**, 154310 (2014).
44. D. V. O'Connor, M. Sumitani, J. M. Morris, and K. Yoshihara, "Non-exponential picosecond fluorescence decay in isolated pentafluorobenzene and hexafluorobenzene," Chem. Phys. Lett. **93**, 350–354 (1982).
45. D. Phillips and K. Al-Ani, "Photochemistry of pentafluorobenzene in the vapor phase," J. Phys. Chem. **74**, 4046–4052 (1970).
46. S. A. Kovalenko, A. L. Dobryakov, and V. Farztdinov, "Detecting Electronic Coherence in Excited-State Electron Transfer in Fluorinated Benzenes," Phys. Rev. Lett. **96**, 068301 (2006).
47. T. Mondal and S. Mahapatra, "Photophysics of fluorinated benzene. I. Quantum chemistry," J. Chem. Phys. **133**, 084304 (2010).
48. T. Mondal and S. Mahapatra, "Photophysics of fluorinated benzene. II. Quantum dynamics," J. Chem. Phys. **133**, 084305 (2010).
49. T. Mondal, S. R. Reddy, and S. Mahapatra, "Photophysics of fluorinated benzene. III. Hexafluorobenzene," J. Chem. Phys. **137**, 054311–054311–17 (2012).
50. See supplemental material at [URL will be inserted by AIP] for detailed descriptions of the experimental and computational methods and the data analysis employed in this work.
51. M. Häser and R. Ahlrichs, "Improvements on the direct SCF method," J. Comput. Chem. **10**, 104–111 (1989).
52. F. Weigend and M. Häser, "RI-MP2: first derivatives and global consistency," Theor. Chem. Acc. **97**, 331–340 (1997).
53. F. Weigend, M. Häser, H. Patzelt, and R. Ahlrichs, "RI-MP2: optimized auxiliary basis sets and demonstration of efficiency," Chem. Phys. Lett. **294**, 143–152 (1998).
54. S. Grimme, "Improved second-order Møller–Plesset perturbation theory by separate scaling of parallel- and antiparallel-spin pair correlation energies," J. Chem. Phys. **118**, 9095–9102 (2003).
55. C. Hättig, A. Hellweg, and A. Köhn, "Distributed memory parallel implementation of energies and gradients for second-order Møller–Plesset perturbation theory with the resolution-of-the-identity approximation," Phys. Chem. Chem. Phys. **8**, 1159–1169 (2006).
56. A. Schäfer, C. Huber, and R. Ahlrichs, "Fully optimized contracted Gaussian basis sets of triple zeta valence quality for atoms Li to Kr," J. Chem. Phys. **100**,

5829–5835 (1994).
57. F. Weigend and R. Ahlrichs, "Balanced basis sets of split valence, triple zeta valence and quadruple zeta valence quality for H to Rn: Design and assessment of accuracy," Phys. Chem. Chem. Phys. **7**, 3297–3305 (2005).
58. D. Rappoport and F. Furche, "Property-optimized Gaussian basis sets for molecular response calculations," J. Chem. Phys. **133**, 134105 (2010).
59. O. Christiansen, H. Koch, and P. Jørgensen, "The second-order approximate coupled cluster singles and doubles model CC2," Chem. Phys. Lett. **243**, 409–418 (1995).
60. C. Hättig and F. Weigend, "CC2 excitation energy calculations on large molecules using the resolution of the identity approximation," J. Chem. Phys. **113**, 5154–5161 (2000).
61. C. Hättig and A. Köhn, "Transition moments and excited-state first-order properties in the coupled-cluster model CC2 using the resolution-of-the-identity approximation," J. Chem. Phys. **117**, 6939–6951 (2002).
62. A. Köhn and C. Hättig, "Analytic gradients for excited states in the coupled-cluster model CC2 employing the resolution-of-the-identity approximation," J. Chem. Phys. **119**, 5021–5036 (2003).
63. R. Ahlrichs, "Efficient evaluation of three-center two-electron integrals over Gaussian functions," Phys. Chem. Chem. Phys. **6**, 5119–5121 (2004).
64. A. Hellweg, S. A. Grün, and C. Hättig, "Benchmarking the performance of spin-component scaled CC2 in ground and electronically excited states," Phys. Chem. Chem. Phys. **10**, 4119–4127 (2008).
65. A. A. Granovsky, "Extended multi-configuration quasi-degenerate perturbation theory: The new approach to multi-state multi-reference perturbation theory," J. Chem. Phys. **134**, 214113 (2011).
66. R. A. Kendall, T. H. Dunning Jr., and R. J. Harrison, "Electron affinities of the first-row atoms revisited. Systematic basis sets and wave functions," J. Chem. Phys. **96**, 6796–6806 (1992).
67. H.-D. Meyer, U. Manthe, and L. S. Cederbaum, "The multi-configurational time-dependent Hartree approach," Chem. Phys. Lett. **165**, 73–78 (1990).
68. M. H. Beck, A. Jäckle, G. A. Worth, and H. D. Meyer, "The multiconfiguration time-dependent Hartree (MCTDH) method: a highly efficient algorithm for propagating wavepackets," Phys. Rep. **324**, 1–105 (2000).
69. H.-D. Meyer, F. Gatti, and G. A. Worth, *Multidimensional Quantum Dynamics: MCTDH Theory and Applications* (Wiley-VCH, Weinheim, 2009).
70. G.A. Worth, M.H. Beck, A. Jäckle, and H.-D. Meyer, computer code, The MCTDH Package, Version 8.2, University of Heidelberg, Heidelberg, Germany, 2000; H.-D. Meyer, computer code, The MCTDH Package, Version 8.3 (2002), Version 8.4 (2007). [`http://mctdh.uni-hd.de`].
71. R. P. Frueholz, W. M. Flicker, O. A. Mosher, and A. Kuppermann, "Electronic spectroscopy of benzene and the fluorobenzenes by variable angle electron

impact," J. Chem. Phys. **70**, 3057–3070 (1979).
72. B. C. Trudell and S. J. W. Price, "The ultraviolet photoelectron spectra of C_6F_5X compounds, X = (F, Cl, Br, I, H, CH_3)," Can. J. Chem. **57**, 2256–2259 (1979).
73. D. Streets and G. P. Ceasar, "Inductive and mesomeric effects on the π orbitals of halobenzenes," Mol. Phys. **26**, 1037–1052 (1973).
74. M. Allan and J. P. Maier, "Emission spectra of the radical cations of hexa-, penta-, tetra-, and tri-fluorobenzenes," Chem. Phys. Lett. **34**, 442–446 (1975).
75. M. Allan, J. P. Maier, and O. Marthaler, "Radative relaxation of the $\tilde{B}(\pi^{-1})$ excited electronic states of the radical cations of hexafluorobenzene, pentafluorobenzene, 1,2,3,4-, 1,2,3,5-, 1,2,4,5-tetrafluorobenzene, 1,3,5-, 1,2,4-trifluorobenzene and 1,3-difluorobenzene," Chem. Phys. **26**, 131–140 (1977).
76. G. Loper and E. Lee, "Fluorescence decay and radiative lifetimes of fluorinated aromatic molecules," Chem. Phys. Lett. **13**, 140–143 (1972).
77. G. A. Garcia, L. Nahon, and I. Powis, "Two-dimensional charged particle image inversion using a polar basis function expansion," Rev. Sci. Instrum. **75**, 4989–4996 (2004).
78. N. V. Davydova and V. D. Yumatov, "A study of the electronic structure of the hexafluorobenzene and pentafluorobenzene molecules by ultrasoft X-ray emission spectroscopy," Russ. J. Phys. Chem. **84**, 33–38 (2010).
79. C. Cossart-Magos, D. Cossart, and S. Leach, "Emission spectra of seven fluorobenzene cations," Mol. Phys. **37**, 793–830 (1979).
80. V. Blanchet, M. Z. Zgierski, and A. Stolow, "Electronic continua in time-resolved photoelectron spectroscopy. I. Complementary ionization correlations," J. Chem. Phys. **114**, 1194–1205 (2001).
81. M. Schmitt, S. Lochbrunner, J. P. Shaffer, J. J. Larsen, M. Z. Zgierski, and A. Stolow, "Electronic continua in time-resolved photoelectron spectroscopy. II. Corresponding ionization correlations," J. Chem. Phys. **114**, 1206–1213 (2001).
82. A. M. Gardner and T. G. Wright, "Consistent assignment of the vibrations of monosubstituted benzenes," J. Chem. Phys. **135**, 114305 (2011).
83. S. Frankiss and D. Harrison, "Thermodynamic properties of fluorine compounds—XVI. The vibrational spectra and thermodynamic functions of pentafluorobenzene, chloropentafluorobenzene, bromopentafluorobenzene and methylpentafluorobenzene," Spectrochim. Acta Mol. Spectrosc. **31**, 1839–1864 (1975).
84. C. B. Duke, K. L. Yip, G. P. Ceasar, A. W. Potts, and D. G. Streets, "Electronic structure of the fluorobenzenes, ethylene, and tetrafluoroethylene," J. Chem. Phys. **66**, 256–268 (1977).
85. H. Köppel, W. Domcke, and L. S. Cederbaum, "Multimode Molecular Dynamics Beyond the Born-Oppenheimer Approximation," in *Advances in Chemical Physics*, Vol. 57, edited by I. Prigogine and S. A. Rice (John Wiley & Sons, Inc., 1984) pp. 59–246.

86. G. A. Worth, H.-D. Meyer, H. Köppel, L. S. Cederbaum, and I. Burghardt, "Using the MCTDH wavepacket propagation method to describe multimode non-adiabatic dynamics," Int. Rev. Phys. Chem. **27**, 569–606 (2008).
87. I. B. Bersuker, "Pseudo-Jahn–Teller Effect—A Two-State Paradigm in Formation, Deformation, and Transformation of Molecular Systems and Solids," Chem. Rev. **113**, 1351–1390 (2013).
88. T. Seideman, "Time-Resolved Photoelectron Angular Distributions: Concepts, Applications, and Directions," Annu. Rev. Phys. Chem. **53**, 41–65 (2002).
89. J. Young, M. Staniforth, M. Paterson, and V. Stavros, "Torsional Motion of the Chromophore Catechol following the Absorption of Ultraviolet Light," Phys. Rev. Lett. **114**, 233001 (2015).
90. J. D. Young, M. Staniforth, J. C. Dean, G. M. Roberts, F. Mazzoni, T. N. V. Karsili, M. N. R. Ashfold, T. S. Zwier, and V. G. Stavros, "Towards Understanding Photodegradation Pathways in Lignins: The Role of Intramolecular Hydrogen Bonding in Excited States," J. Phys. Chem. Lett. **5**, 2138–2143 (2014).

Electronic Supplemental Material

5.S1 Experimental Methods and Data Analysis

5.S1.1 Experimental Setup

All experiments were carried out using a home-built linear time-of-flight mass spectrometer (TOF-MS) and photoelectron imaging (PEI) apparatus. The setup consists of two differentially pumped stainless steel high vacuum chambers used for the ultrasonic expansion of the sample molecules and the detection of the ions and hot electrons. The typical pressures in the entrance and detection compartments under operating conditions were of the order of 1×10^{-5} mbar and 3×10^{-7} mbar. Pentafluorobenzene (PFB) was used as supplied by Sigma-Aldrich ($\geq$98% purity). A gas mixture was prepared by flowing Helium carrier gas at 2 bar pressure over the liquid kept in a glass reservoir. The seeded gas was expanded into the vacuum chamber through a solenoid actuated pulsed valve (Parker series 9, 0.5 mm orifice diameter) driven by a home-built power supply and operated at 100 Hz repetition rate with 65 µs opening time. A molecular beam was formed by a 0.5 mm orifice diameter skimmer (Beam Dynamics) through which it entered the ion source in the detection chamber. Here, the beam was crossed perpendicularly by the pump and probe laser beams between the repeller and extractor plates, which were surrounded by a liquid N_2-filled cold trap. The field-free flight path was shielded by a µ-metal tube from stray magnetic fields. The microchannel plate (MCP) detector was backed by a steel anode for ion time-of-flight measurements or by a fiber-optical vacuum window coated with a P43 phosphorescence screen for photoelectron imaging.

The pump and probe laser pulses were derived from a regeneratively amplified Ti:Sa femtosecond laser system (Coherent Libra-HE) producing pulses of 90 fs length (full width at half-maximum, FWHM) at $\lambda = 804$ nm with energies of 3.7 mJ at 1 kHz repetition rate. The required ultraviolet (UV) pump pulses were generated by frequency-doubling the output of a home-built, two-stage, non-collinear optical parametric amplifier (NOPA). The pulses were compressed to 20 – 30 fs length in a prism compressor and focused into the vacuum chamber with a concave mirror of 50 cm focal length. The excited molecules were probed by multiphoton ionization at 804 nm (TOF-MS) using the Ti:Sa laser fundamental or at 402 nm (PEI and additional TOF-MS measurements) from the second harmonic. The respective pulses were focused into the vacuum chamber with a 100 cm focal length lens. The pump and probe polarizations were set parallel to the detector surface. The obtained molecular ion current was amplified and then digitized on a 1 GSa/s digital storage oscilloscope (LeCroy LT264). For photoelectron (PE) imaging, the high voltage

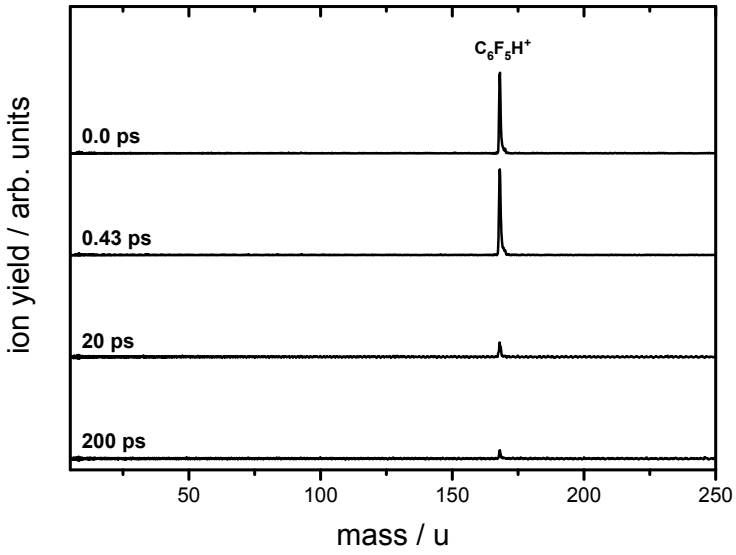

Figure 5.S1. Femtosecond time-of-flight mass spectra of PFB by excitation at λ_{pump} = 265 nm and ionization at λ_{probe} = 402 nm at selected delay times showing the absence of any measurable fragmentation of the parent molecules.

applied to the MCPs was gated by a fast transistor switch (Behlke HTS 31-03-GSM, 6 ns rise time). The emittance from the phosphor screen was recorded by a CCD camera (pco.1600, 1600 $\times$ 1200 pixels, 14-bit digitization) with the sensor cooled to $-20°$C. The timing of all components was controlled by a digital delay generator (Stanford Research DG645). The recorded mass spectra given for several delay times in Figure 5.S1 did not reveal any signs for fragmentation of the PFB molecules.

Temporal profiles as function of pump–probe time delay were recorded using a linear translation stage (Physik Instrumente M-521.DG) reaching up to a maximum delay time of $\Delta t = 1.38$ ns. At each pump–probe delay, ion mass spectra were typically accumulated over 500 laser shots. Photoelectron images were taken over 50,000 laser shots. The mass spectra were gated over individual time-of-flight mass peaks, integrated and stored on a computer. The acquired PE images were background-subtracted and thresholded, followed by application of a peak finding and centroiding algorithm implemented in the LabView software that controlled the experiment. Only the detected peak coordinates were stored on the computer for subsequent further processing and analysis.[1–3] The calibration of the images was performed by measurement of the $^2P_{3/2}$ and $^2P_{1/2}$ lines from ionization of Xenon[4] in a multi-photon above-threshold ionization (ATI) process. The energy resolution of the PE spectra gained in a one-photon pump and two-photon probe process was limited to typically 70 meV (FWHM) by the spectral widths of the laser pulses. A temporal resolution of $\Delta t = 30$ fs was reached under optimal conditions.

5.S1.2 Analysis of Transient Ion Mass Signals

The measured excited-state relaxation dynamics were modeled using a kinetic scheme consisting of the sum of two exponential decay functions

$$M_i(t) = a_i \, e^{-t/\tau_i}, \tag{5.2}$$

with the τ_i as the respective lifetime constants and a_i as amplitudes. The coherent oscillation was fitted using exponentially damped cosine terms of the form

$$C_i(t) = a_i \cos(\omega_i t + \varphi_i) \, e^{-t/\tau_D}, \tag{5.3}$$

of which usually one term sufficed to achieve a satisfactory fit. These expressions were convoluted with a Gaussian

$$G(t) = \frac{1}{\sqrt{2\pi}\sigma_{\mathrm{IRF}}} \exp\left(-\frac{t-t_0}{2\sigma_{\mathrm{IRF}}}\right)^2 \tag{5.4}$$

describing the instrument response function (IRF) to give the experimentally acquired signal $S(t)$ in the form

$$S(t) = G(t) \otimes \left(\sum_i M_i(t) + \sum_j C_j(t)\right), \tag{5.5}$$

where the t_0 parameter determines the point of zero temporal delay between pump and probe. The standard deviation σ_{IRF} of the Gaussian IRF is an appropriate measure for the experimental time resolution. The model function $S(t)$ was fitted to the data points of the transient mass signal acquired at a given excitation wavelength using the Levenberg-Marquard algorithm implemented in Wolfram Mathematica 10.[5]

5.S1.3 Oscillation Frequencies

Upon closer inspection, the fit to the transient mass signals using only one oscillatory component does not follow the data to full extent. A measurement of the transient ion yield after excitation at 265 nm is depicted in Figure 5.S2 on an enlarged scale for the first 5 ps. The fit with one cosine component of $\tilde{\nu}_{\mathrm{osc}}^{(1)} = 77$ cm^{-1} displayed in panel (a) clearly underestimates/overestimates the maxima/minima of the oscillation and, as becomes evident from the residuals, leaves a remaining oscillatory component. As displayed in panel (b), the quality of the fit was significantly improved by addition of a second cosine component. The frequencies of both oscillations were taken as free fit parameters, yet the second cosine component converged to twice the frequency of the first component, $\tilde{\nu}_{\mathrm{osc}}^{(2)} = 155$ cm^{-1}. The Fourier transform of the transients in

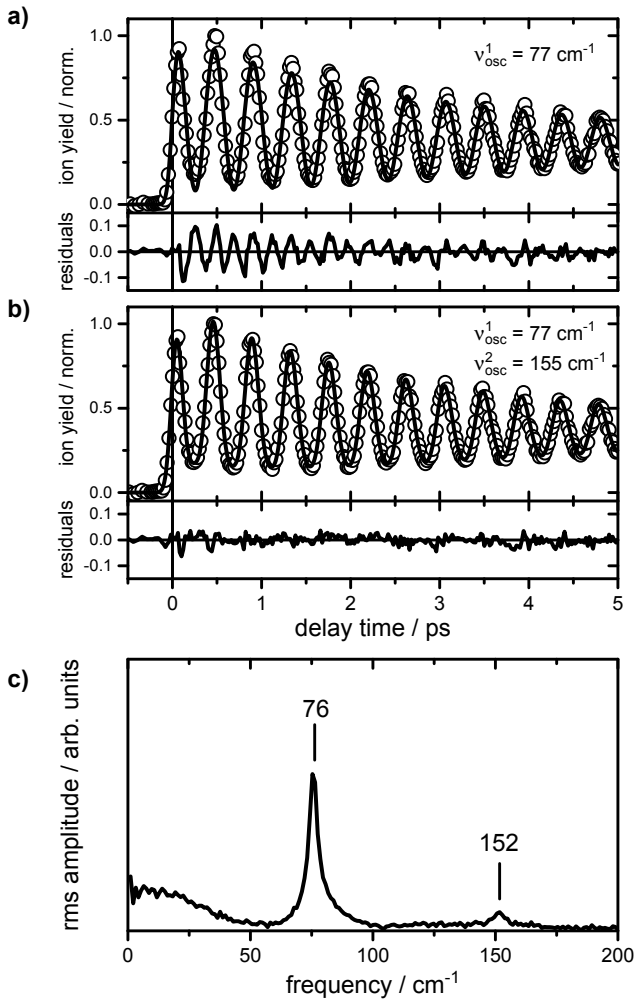

Figure 5.S2. Fits to the oscillating transient mass signal after excitation at $\lambda_{\mathrm{pump}} = 265$ nm. a) Result with one frequency component, $\tilde{\nu}^{(1)}_{\mathrm{osc}} = 77$ cm^{-1}, and fit residuals exhibiting an additional higher frequency oscillation term. b) Result with two frequency components, $\tilde{\nu}^{(1)}_{\mathrm{osc}} = 77$ cm^{-1} and $\tilde{\nu}^{(2)}_{\mathrm{osc}} = 155$ cm^{-1} frequency, and fit residuals showing excellent agreement. c) Fourier transform of the transient mass signal revealing two frequency components.

panel (c) gives nearly identical frequencies. The appearance of the second harmonic frequency likely is a consequence of the anharmonic electronic potential of the ν_{20} mode, as the solution of the equation of motion for an anharmonic oscillator with perturbational methods is well known to provide additional terms with multiples of the harmonic frequency.[6]

5.S1.4 Analysis of the Photoelectron Images

The acquired PE images were centered using the algorithm of Bordas[7] and averaged over their four quadrants. Meridional slices through the original three-dimensional electron distributions were then obtained using the polar basis function expansion method implemented in the pBASEX program.[8] In that way, PE spectra as well as

anisotropy parameters describing the photoelectron angular distribution (PAD) were gained. For conversion from detector pixel to energy units in eV, the appropiate Jacobian transformation was applied. The PE spectrum recorded at zero time delay was normalized to unity, all other spectra were scaled relative to that according to the number of measured electrons and the area under the curve. The relative delay times noted in the spectra are given with respect to the t_0 value determined from the fit to the transient mass signals.

In general, the time-dependent PAD for a three-photon ionization scheme using linear polarization should be described as function of the angle between the laser polarization and the direction of the ejected eletrons θ in terms of three anisotropy parameters β_2, β_4 and β_6 by an expression of the form

$$I(t,\theta) = \frac{\sigma(t)}{4\pi}\left(1 + \sum_{L=2,4,6} \beta_L(t) P_L(\cos\theta)\right), \tag{5.6}$$

with the associated L-th order Legendre polynomials $P_L(\cos\theta)$ and the photoionization cross section σ.[9] However, because the retrieved PADs showed only a very weak (and not significant) contribution of the fourth-order term and no higher order contributions, the sixth-order term was omitted in our pBASEX image inversions.

5.S2 Computational Methods and Results

5.S2.1 Electronic Structure Calculations

The neutral $^1A_1$ (S_0) and ionic $^2A_2$ (D_0) ground state equilibrium structures of the PFB molecule were optimized ab initio using second-order Møller-Plesset perturbation theory under the resolution of the identy (RI) approximation and the spin-component scaling (SCS) modification (RI-SCS-MP2).[10–14] The excited-state equilibrium structures of the neutral $^1B_2$ ($\pi\pi^*$) and $^1A_2$ ($\pi\sigma^*$) states and the lowest two excited ionic states D_1 and D_2 (both of $^2B_1$ symmetry) were calculated using the second-order approximate coupled-cluster method in the same variant (RI-SCS-CC2).[15–20] The employed coordinate system and atom numbering scheme are defined in Figure 5.S3. The results of the optimizations are given in Figures 5.S4 – 5.S5 and Table 5.SI and detailed in Section 5.S3.

The optimization of the $^1A_2$ ($\pi\sigma^*$) excited state structure yielded one imaginary frequency of $50i$ cm^{-1} in the ν_{14} mode (a_2 symmetry, ν_{16a} in Wilson notation). Optimizations with tightened convergence criteria for the energy and gradient produced the same result, indicating that the imaginary frequency, albeit rather small, is not a numerical artifact. Our attempts to resume the optimization from

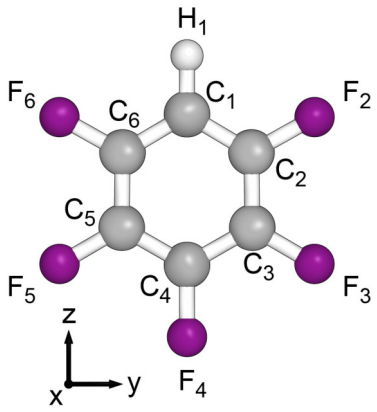

Figure 5.S3. Coordinate system and atom numbering scheme employed in this work.

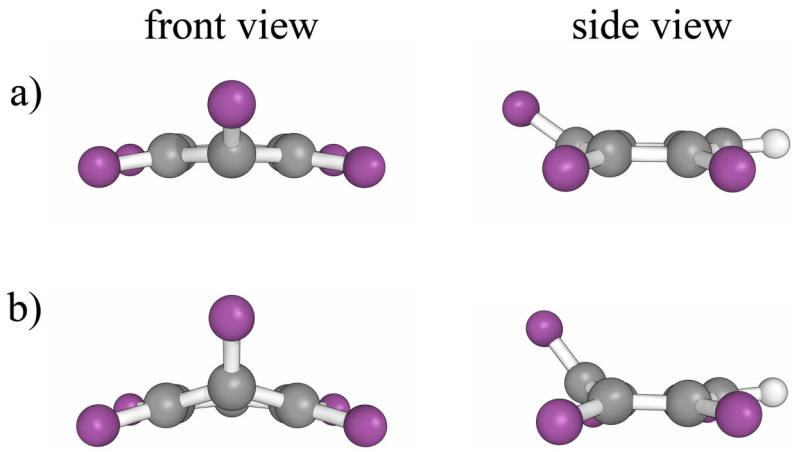

Figure 5.S4. RI-SCS-CC2 optimized molecular structures of the a) S_1 ($^1B_2$, $\pi\pi^*$) state (potential minimum) and b) the S_2 ($^1A_2$, $\pi\sigma^*$) state (stationary point with $\nu_{14} = 50i$ cm^{-1}).

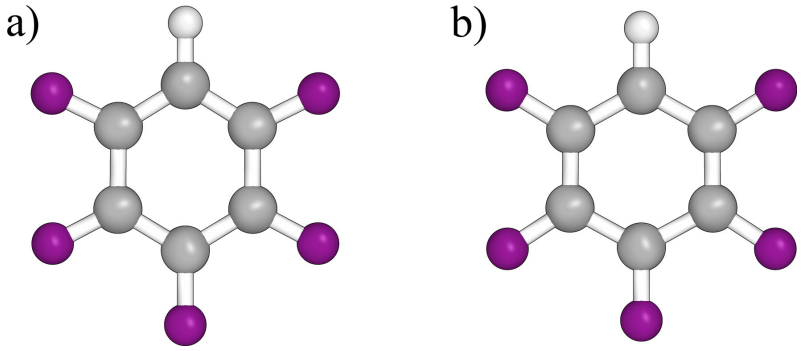

Figure 5.S5. RI-SCS-MP2 and RI-SCS-CC2 optimized molecular structures of the a) D_0 and b) D_1 ionic states, respectively.

Table 5.SI. Atomic distances and out-of-plane bending angles of the calculated electronic ground, excited and ionic states in the equilibrium structures.

parameter [a,b]	S_0 / Å	S_1 ($\pi\pi^*$) / Å	S_2 ($\pi\sigma^*$) [c] / Å	D_0 / Å	D_1 / Å
C_1-C_2	1.387	1.403	1.431	1.380	1.418
C_2-C_3	1.390	1.429	1.373	1.450	1.373
C_3-C_4	1.392	1.420	1.415	1.381	1.425
C_4-H_1	1.079	1.077	1.083	1.081	1.085
C_2-F_2	1.337	1.331	1.350	1.298	1.316
C_3-F_3	1.332	1.336	1.345	1.290	1.307
C_4-F_4	1.331	1.378	1.367	1.308	1.284
δC_1 [d]	0.0°	2.8°	4.4°	0.0°	0.0°
δH_1 [e]	0.0°	0.5°	1.0°	0.0°	0.0°
δC_4 [d]	0.0°	2.3°	13.7°	0.0°	0.0°
δF_4 [f]	0.0°	30.6°	22.5°	0.0°	0.0°

[a] Values for the ground state at the RI-SCS-MP2 and the excited states at the RI-SCS-CC2 levels of theory with the def2-TZVPPD bases using Turbomole 6.6.

[b] The molecular symmetry with respect to the σ_v (xz) mirror plane is retained in all states, therefore only distances for one side of the molecule are given.

[c] Stationary point with $\nu_{14} = 50i$ cm^{-1}.

[d] Out-of-plane angle relative to the plane defined by C_2,C_3, C_5, C_6.

[e] Out-of-plane angle relative to the plane defined by C_1,C_2,C_6.

[f] Out-of-plane angle relative to the plane defined by C_3,C_4, C_5.

a slightly distorted molecular structure did not converge. During the ongoing iterations, the molecular structure took a twisted shape, largely corresponding to an elongation of the ν_{14} (a_2) mode. Modes of a_2 symmetry couple the $^1A_2$ ($\pi\sigma^*$) state with the higher-lying $^1A_1$ ($\pi\pi^*$) state. The failed structural optimization is therefore not relevant for the coupling to the $^1B_2$ ($\pi\pi^*$) state of interest.

Vertical excitation energies (VEEs) were calculated with the RI-SCS-CC2 method and with the extended multi-configuration quasi-degenerate second-order perturbation theory (XMCQDPT2) method.[21] The latter method uses a complete active space self-consistent field (CASSCF) wavefunction obtained with an active space of six electrons in seven orbitals, including the three highest occupied π orbitals, the three lowest unoccupied π^* orbitals and a σ^* orbital with significant Rydberg character (see Figure 5.S6). State averaging over the seven lowest CASSCF states was found necessary as the CASSCF method gives a wrong ordering of the excited states.

The MP2 and CC2 calculations were performed using a def2-TZVPPD[22–24] basis set in the TURBOMOLE 6.6 program package.[25,26] The XMCQDPT2 calculations were

performed with a aug-cc-pVDZ[27] basis set, using the Firefly[28] program package, which is partially based on the GAMESS (US) source code. Diffuse basis functions were essential to account for the significant Rydberg character of the $\pi\sigma^*$ states. The nature of the stationary points obtained from the geometry optimizations was checked by Hessian diagonalizations. The second derivates of the energy were computed as finite differences of the first derivatives, because analytic second derivatives are not available at the CC2 level of theory.

5.S2.2 Normal Modes

A listing of the calculated normal mode vibrational frequencies of the PFB molecule in the interesting electronic states at the RI-SCS-MP2/def2-TZVPPD (S_0, D_0) and RI-SCS-CC2/def2-TZVPPD (S_1, S_2, D_1) levels of theory, respectively, is given in Table 5.SII. The corresponding normal mode displacement vectors of the ν_9 (a_1) mode and the b_1 modes in the electronic ground state are displayed in Figure 5.S7.

5.S2.3 Vibronic Coupling Model Hamiltonian

In the vibronic coupling model,[30] we adopt a diabatic Hamiltonian of the general form

$$H_s(\boldsymbol{Q}) = H_0(\boldsymbol{Q})I + W(\boldsymbol{Q}), \tag{5.7}$$

where $\boldsymbol{Q}$ is a vector gathering the ground state dimensionless normal coordinates, $H_0(\boldsymbol{Q})$ is the ground state Hamiltonian in the harmonic approximation

$$H_0(\boldsymbol{Q}) = \sum_i \frac{\omega_i}{2}\left(\frac{\partial^2}{\partial Q_i^2} + Q_i^2\right), \tag{5.8}$$

I denotes the identity matrix, and $W(\boldsymbol{Q})$ is the diabatic potential energy matrix. The elements of $W(\boldsymbol{Q})$ are expressed as a Taylor expansion in $\boldsymbol{Q}$. To correctly account for the high anharmonicity of the potential energy surfaces along the b_1 modes that mediate the vibronic coupling, it was found necessary to include terms up to fourth order in the definition of the diabatic potential matrix elements. Specifically, in our case, the diagonal elements of $W(\boldsymbol{Q})$ read

$$W_{nn}(\boldsymbol{Q}) = E_n + \sum_{i,j>i} \gamma_{ij}^{(n)} Q_i Q_j + \sum_{i,j>i} \sigma_{ij}^{(n)} Q_i^2 Q_j^2, \tag{5.9}$$

and the off-diagonal elements

$$W_{12}(\boldsymbol{Q}) = \sum_i \lambda_i^{(12)} Q_i + \sum_{i,j>i} \eta_{ij}^{(12)} Q_i^2 Q_j. \tag{5.10}$$

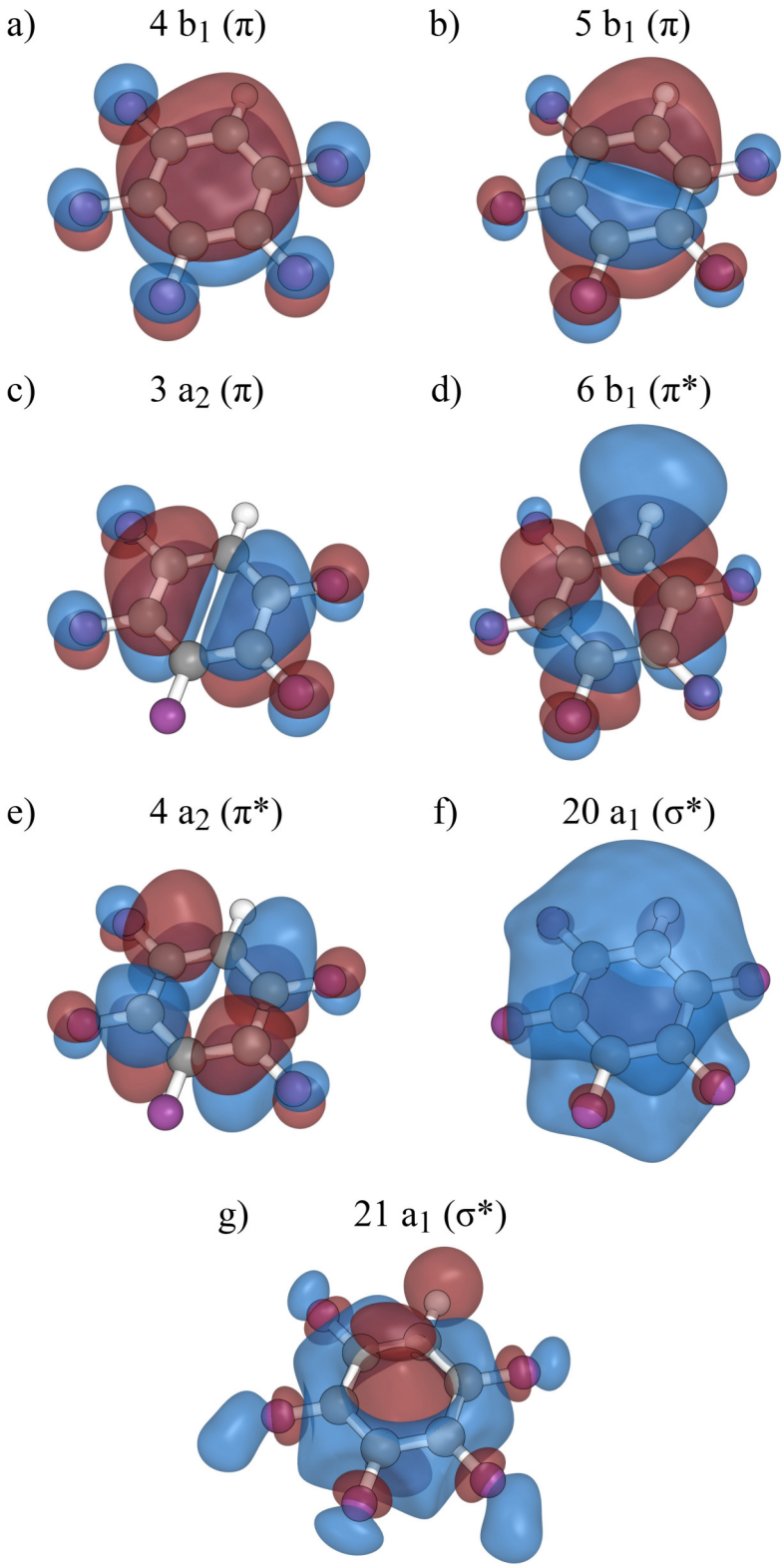

Figure 5.S6. Optimized molecular orbitals (isosurface ±0.02 a.u.) at the MP2-optimized ground state structure.

Table 5.SII. Calculated harmonic vibrational frequencies from numerical second derivatives of the total energy in the ground, excited and ionic state equilibrium structures of PFB. All values are given in cm^{-1}.

	no.	expt. [a]	S_0 ($^1A_1$)	S_1 ($^1B_2$)	S_2 ($^1A_2$)	D_0 ($^2A_2$)	D_1 ($^2B_1$)
a_1	1	3103	3261	3275	3216	3267	3218
	2	1648	1683	1547	1646	1685	1749
	3	1516	1550	1349	1275	1557	1570
	4	1413	1441	1400	1325	1530	1394
	5	1291	1298	1195	1138	1302	1330
	6	1078	1089	967	934	1130	1170
	7	719	726	699	704	747	738
	8	577	581	642	566	589	584
	9	(474)	475	414	472	466	475
	10	327	328	333	317	347	330
	11	272	271	273	246	279	264
a_2	12	661	669	580	654	807	663
	13	387	400	428	432	332	389
	14	142	133	94	$50i$	155	117
b_1	15	837	843	642	808	956	889
	16	715	584	490	480	574	663
	17	556	480	620	664	690	494
	18	321	318	233	275	272	296
	19	206	204	145	150	118	193
	20	158	147	84	110	169	106
b_2	21	1648	1686	1513	1847	1529	2504
	22	1540	1572	1382	1443	1057	1592
	23	1269	1338	1866	1568	1485	1440
	24	1182	1211	1173	1194	1248	1274
	25	1143	1161	1116	1078	1366	1204
	26	958	966	904	890	987	986
	27	692	693	667	689	711	701
	28	433	437	368	432	145	509
	29	303	304	305	280	306	314
	30	256	276	239	210	319	283

[a] Values in the S_0 state from Frankiss and Harrison, Ref. 29.

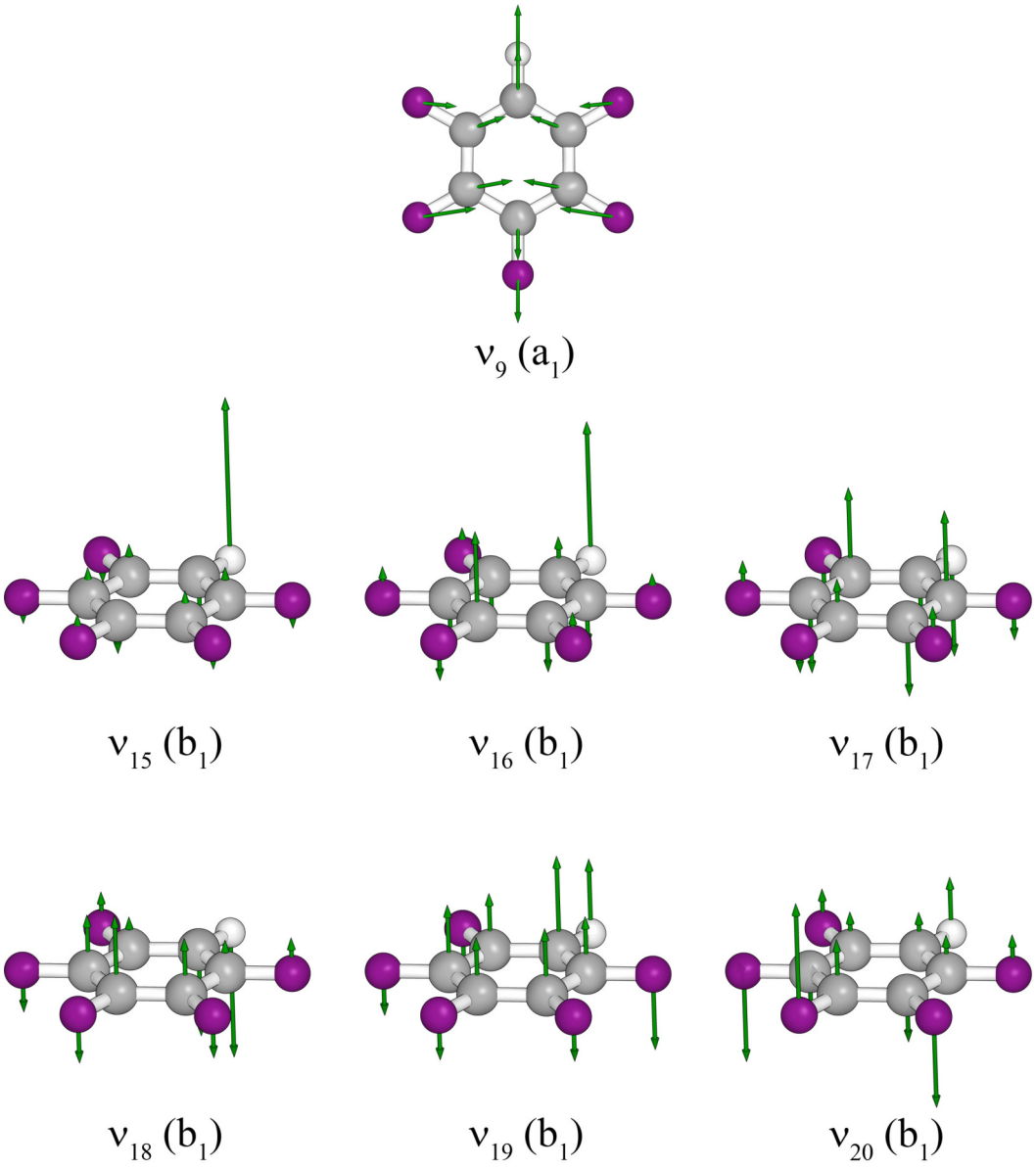

Figure 5.S7. Illustration of the vibrational normal mode displacement vectors of the ν_9 (a_1) mode and all b_1 modes.

We then simulated the dynamics of PFB after excitation to its first excited state by a linearly polarized short resonant laser pulse. The total Hamiltonian thus reads

$$H(\boldsymbol{Q}, t) = H_s(\boldsymbol{Q}) + H_{\text{int}}(t), \tag{5.11}$$

with $H_{\text{int}}(t)$ describing the interaction of the molecule with the electric field in the dipolar approximation

$$H_{\text{int}}(t) = -\mu^{01}\mathcal{E}(t), \tag{5.12}$$

where $\mathcal{E}(t)$ is the electric field and μ^{01} denotes the transition dipole moment between the ground and first excited diabatic electronic states. The Franck–Condon approximation is assumed, i. e. the dependence of the transition dipole moment

on the vibrational coordinates is neglected. The permanent dipole moments in the ground and excited states are also neglected, because the laser pulse is non-resonant with respect to vibrational transitions. A Gaussian pulse shape

$$\mathcal{E}(t) = \mathcal{E}_0 e^{-4\ln(2)\left(\frac{t-t_0}{\tau}\right)^2} \cos(\omega t), \tag{5.13}$$

centered at t_0 = 100 fs with length τ = 35 fs (FWHM) and photon energy $\hbar\omega$ = 4.8 eV was explicitly included in our simulations. The resulting time-dependent Schrödinger equation

$$H(\boldsymbol{Q}, t)\Psi(\boldsymbol{Q}, t) = i\hbar\frac{\partial}{\partial t}\Psi(\boldsymbol{Q}, t) \tag{5.14}$$

was solved using the multi-configuration time-dependent Hartree (MCTDH) method as implemented in the Heidelberg program package.[31] The interested reader is referred to the abundant literature on MCTDH (see e. g. Refs. 32–34 and references therein) for a description of the method and its application to the excited-state non-adiabatic dynamics of molecular systems.[35]

5.S2.4 Fitting Details

The parameters entering into Eqs. (5.9) and (5.10) were obtained through a least-square fit against adiabatic electronic energies computed at the XMCQDPT2 level of theory. The quantity optimized is expressed as

$$\Delta = \sum_{\alpha}\sum_{i}^{n_p}\left(V_i^{(\alpha)} - V_i^{(\alpha),\mathrm{mod}}\right)^2 F_i^{(\alpha)}, \tag{5.15}$$

where α labels the two excited electronic states, n_p is the number of ab initio points used in the fit, $V_i^{(\alpha)}$ is the ab initio adiabatic energy of the electronic state α at point i, and $V_i^{(\alpha),\mathrm{mod}}$ is the corresponding adiabatic energy obtained from the model. The function

$$F_i^{(\alpha)} = \exp\left[-\left(V_i^{(\alpha)} - V_0^{(\alpha)}\right)\right], \tag{5.16}$$

where $V_0^{(\alpha)}$ is the value of the α^{th} adiabatic potential at the ground state equilibrium geometry, is a weight function used to ensure a preferential accuracy of the fit in low energy regions of the potentials.

The required input parameters for our three-dimensional (3D) and six-dimensional (6D) models were obtained from separate fits. For the 3D model, 36 parameters were fitted against XMCQDPT2 energies obtained at 134 symmetry independent geometries with a weighted root mean square deviation (RMSD) of 0.033 eV. For the 6D model, 126 parameters were fitted against XMCQDPT2 energies obtained

Table 5.SIII. Coupling constants λ_i in eV obtained from our fits for the 3D and 6D models.

	λ_{20}	λ_{19}	λ_{18}	λ_{17}	λ_{16}	λ_{15}
3D	0.086	−0.015	−0.075	—	—	—
6D	0.078	−0.016	−0.078	0.145	0.175	−0.044

at 427 symmetry independent geometries with a weighted RMSD of 0.045 eV. The obtained first-order off-diagonal coupling constants λ_i are given in Table 5.SIII.

5.S2.5 Details for the Quantum Dynamics Simulations

For the representation of the Hamiltonian and the wavefunction, a Hermite polynomial DVR scheme[36] was used for all the degrees of freedom. The so-called multi-set formalism, where a different single-particle function (SPF) basis is used for each electronic state, was used for the calculations. The details of the primitive and single-particle bases for the calculations using the 3D and 6D models are given in Tables 5.SIV and 5.SV.

5.S2.6 Fits to the Simulated Diabatic Electronic Populations

For a comparison of our computational and experimental results, the simulated electronic population of the first excited diabatic state was fitted against the expression

$$P(t) = c_1\ e^{-4\ln(2)\left(\frac{t-t_0}{\tau}\right)^2} \otimes \left(c_2 + c_3\ \cos(2\pi\nu_{\text{osc}}t + \varphi)e^{-t/\tau_{\text{osc}}}\right), \tag{5.17}$$

where the c_i (with $i = 1-3$), ν_{osc}, φ and τ_{osc} are the parameters to be optimized. The computed and fitted populations of the first diabatic excited electronic states for the 3D and 6D models are presented in Figure 5.S8. The parameters obtained from our fits are given in Table 5.SVI.

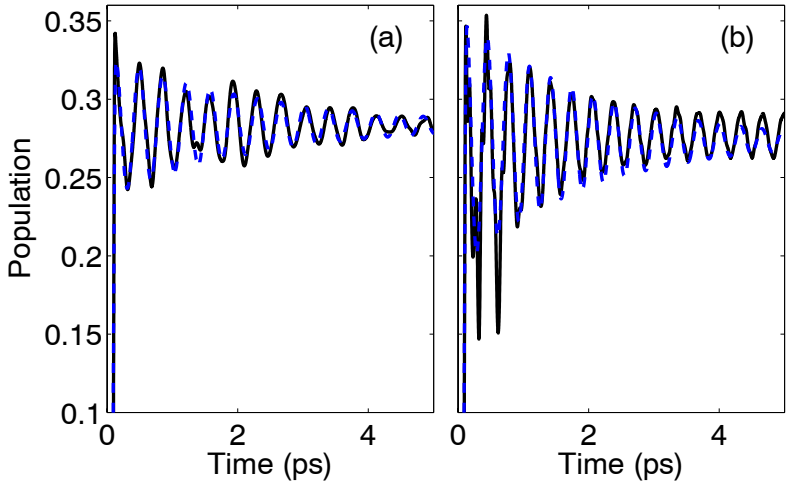

Figure 5.S8. Population of the first diabatic excited electronic state obtained from the MCTDH computation (black solid lines) and from the fit (blue dashed lines) for a) the 3D model and b) the 6D model.

Table 5.SIV. Number of SPF and primitive basis functions for the ground, first and second diabatic excited electronic states used for the 3D model.

modes	SPF basis	primitive basis
Q_{20}	[4,28,28]	60
Q_{19}	[4,20,20]	30
Q_{18}	[4,23,23]	50

Table 5.SV. Number of SPF and primitive basis functions for the ground, first and second diabatic excited electronic states used for the 6D model. The physical modes were combined to form multi-dimensional SPF bases (see Ref. 35).

modes	SPF basis	primitive basis
Q_{20}	[4,28,26]	56
(Q_{19}, Q_{16})	[4,26,24]	(26,26)
Q_{18}	[4,19,19]	46
(Q_{17}, Q_{15})	[5,22,20]	(32,18)

Table 5.SVI. Parameters obtained from our fits of Eq. (5.17) against the computed population of the first diabatic excited electronic state for the 3D and 6D models.

model	c_1	c_2	c_3	ν_{osc} (cm^{-1})	φ (rad)	τ_{osc} (ps)
3D	0.0217	0.350	0.056	92	-0.47	2.36
6D	0.0201	0.365	0.110	103	-0.45	1.96

5.S3 Listings of the Cartesian Atomic Coordinates of the Optimized Geometries

Listing 5.S1 MP2-optimized atomic cartesian coordinates of the S_0 ($^1A_1$) state in Å.

F	−0.0000007	0.0000000	2.6963593
F	0.0000025	−2.3576130	1.3459102
F	−0.0000017	2.3576130	1.3459102
F	0.0000022	2.3589515	−1.3703688
F	−0.0000020	−2.3589515	−1.3703688
C	−0.0000001	−0.0000000	1.3656467
C	0.0000006	−1.2074144	0.6737368
C	−0.0000004	1.2074144	0.6737368
C	0.0000004	1.1924503	−0.7162537
C	−0.0000004	−1.1924503	−0.7162537
C	−0.0000001	−0.0000000	−1.4243561
H	−0.0000004	0.0000000	−2.5036988

Listing 5.S2 CC2-optimized atomic cartesian coordinates of the S_1 ($^1B_2$) state in Å.

F	−0.5128857	−0.0013816	2.6963589
F	0.3602727	−2.3658671	1.2727225
F	0.3636948	2.3636848	1.2758023
F	0.0632657	2.3442797	−1.3441950
F	0.0598710	−2.3426260	−1.3472282
C	0.1434341	−0.0010724	1.4851613
C	0.1133946	−1.1843933	0.6999020
C	0.1151151	1.1833166	0.7014403
C	−0.0425639	1.1741354	−0.7189106
C	−0.0442679	−1.1731426	−0.7204348
C	−0.1971874	0.0010965	−1.4735175
H	−0.4221431	0.0019699	−2.5271011

Listing 5.S3 CC2-optimized atomic cartesian coordinates of the S_2 ($^1A_2$) state in Å.

F	−0.9184180	−0.0009081	2.3859774
F	0.6630153	−2.3414515	1.3362687
F	0.6669398	2.3386343	1.3391825
F	0.0015940	2.3549750	−1.3881186
F	−0.0013598	−2.3531036	−1.3912060
C	−0.0131007	−0.0008627	1.3619334
C	0.2162337	−1.2433471	0.6909145
C	0.2180181	1.2421575	0.6925139
C	−0.0133881	1.2237048	−0.6606148
C	−0.0149910	−1.2227949	−0.6622007
C	−0.2393571	0.0010577	−1.3359819
H	−0.5651863	0.0019384	−2.3686684

Listing 5.S4 MP2-optimized atomic cartesian coordinates of the D_0 ($^2A_2$) state in Å.

F	−0.0001345	−0.0001519	2.7277000
F	0.0001094	−2.3221855	1.3050672
F	−0.0000831	2.3227121	1.3050618
F	0.0000906	2.3346846	−1.3225004
F	−0.0000187	−2.3351090	−1.3226072
C	−0.0000436	0.0002538	1.4193310
C	0.0000016	−1.1813284	0.7036098
C	−0.0000143	1.1814937	0.7039366
C	0.0000391	1.1724237	−0.7456667
C	0.0000009	−1.1726140	−0.7460532
C	0.0000253	−0.0001921	−1.4736054
H	0.0000274	0.0000130	−2.5542734

Listing 5.S5 CC2-optimized atomic cartesian coordinates of the D_1 ($^2B_1$) state in Å.

F	−0.0000651	0.0000309	2.6339402
F	0.0000056	−2.3445171	1.3820960
F	−0.0000592	2.3445451	1.3820367
F	0.0000318	2.3569537	−1.3961396
F	0.0000207	−2.3569838	−1.3960820
C	−0.0000309	0.0000150	1.3500156
C	0.0000007	−1.2504005	0.6673443
C	−0.0000257	1.2504126	0.6673118
C	0.0000124	1.2371552	−0.7054412
C	0.0000164	−1.2371699	−0.7054109
C	0.0000318	−0.0000163	−1.3974504
H	0.0000614	−0.0000248	−2.4822204

Listing 5.S6 CC2-optimized atomic cartesian coordinates of the D_2 ($^2B_1$) state in Å.

F	−0.0000795	−0.0000573	2.7051613
F	−0.0000129	−2.3505197	1.3529736
F	−0.0000532	2.3508139	1.3530104
F	0.0000287	2.3661452	−1.3673015
F	0.0000463	−2.3664036	−1.3673084
C	−0.0000400	0.0001643	1.4007205
C	−0.0000094	−1.2246896	0.6952175
C	−0.0000277	1.2248072	0.6954199
C	0.0000135	1.2209783	−0.7292272
C	0.0000259	−1.2210706	−0.7294463
C	0.0000390	−0.0001471	−1.4632621
H	0.0000691	−0.0000211	−2.5459578

References

1. B.-Y. Chang, R. C. Hoetzlein, J. A. Mueller, J. D. Geiser, and P. L. Houston, "Improved two-dimensional product imaging: The real-time ion-counting method," Rev. Sci. Instrum. **69**, 1665–1670 (1998).
2. N. Yonekura, C. Gebauer, H. Kohguchi, and T. Suzuki, "A crossed molecular beam apparatus using high-resolution ion imaging," Rev. Sci. Instrum. **70**, 3265–3270 (1999).
3. W. Li, S. D. Chambreau, S. A. Lahankar, and A. G. Suits, "Megapixel ion imaging with standard video," Rev. Sci. Instrum. **76**, 063106 (2005).
4. J. E. Hansen and W. Persson, "Revised analysis of singly ionized xenon, Xe II," Phys. Scr. **36**, 602 (1987).
5. Wolfram Research, Inc., Mathematica, Version 10.0, Champaign, IL (2014).
6. L. D. Landau and E. M. Lifshitz, *Mechanics* (Butterworth-Heinemann, 1976).
7. C. Bordas, F. Paulig, H. Helm, and D. L. Huestis, "Photoelectron imaging spectrometry: Principle and inversion method," Rev. Sci. Instrum. **67**, 2257–2268 (1996).
8. G. A. Garcia, L. Nahon, and I. Powis, "Two-dimensional charged particle image inversion using a polar basis function expansion," Rev. Sci. Instrum. **75**, 4989–4996 (2004).
9. B. J. Whitaker, ed., *Imaging in Molecular Dynamics: Technology and Applications* (Cambridge University Press, Cambridge, 2003).
10. M. Häser and R. Ahlrichs, "Improvements on the direct SCF method," J. Comput. Chem. **10**, 104–111 (1989).
11. F. Weigend and M. Häser, "RI-MP2: first derivatives and global consistency," Theor. Chem. Acc. **97**, 331–340 (1997).
12. F. Weigend, M. Häser, H. Patzelt, and R. Ahlrichs, "RI-MP2: optimized auxiliary basis sets and demonstration of efficiency," Chem. Phys. Lett. **294**, 143–152 (1998).
13. S. Grimme, "Improved second-order Møller–Plesset perturbation theory by separate scaling of parallel- and antiparallel-spin pair correlation energies," J. Chem. Phys. **118**, 9095–9102 (2003).
14. C. Hättig, A. Hellweg, and A. Köhn, "Distributed memory parallel implementation of energies and gradients for second-order Møller–Plesset perturbation theory with the resolution-of-the-identity approximation," Phys. Chem. Chem. Phys. **8**, 1159–1169 (2006).
15. O. Christiansen, H. Koch, and P. Jørgensen, "The second-order approximate coupled cluster singles and doubles model CC2," Chem. Phys. Lett. **243**, 409–418 (1995).
16. C. Hättig and F. Weigend, "CC2 excitation energy calculations on large molecules using the resolution of the identity approximation," J. Chem. Phys. **113**, 5154–

5161 (2000).
17. C. Hättig and A. Köhn, "Transition moments and excited-state first-order properties in the coupled-cluster model CC2 using the resolution-of-the-identity approximation," J. Chem. Phys. **117**, 6939–6951 (2002).
18. A. Köhn and C. Hättig, "Analytic gradients for excited states in the coupled-cluster model CC2 employing the resolution-of-the-identity approximation," J. Chem. Phys. **119**, 5021–5036 (2003).
19. R. Ahlrichs, "Efficient evaluation of three-center two-electron integrals over Gaussian functions," Phys. Chem. Chem. Phys. **6**, 5119–5121 (2004).
20. A. Hellweg, S. A. Grün, and C. Hättig, "Benchmarking the performance of spin-component scaled CC2 in ground and electronically excited states," Phys. Chem. Chem. Phys. **10**, 4119–4127 (2008).
21. A. A. Granovsky, "Extended multi-configuration quasi-degenerate perturbation theory: The new approach to multi-state multi-reference perturbation theory," J. Chem. Phys. **134**, 214113 (2011).
22. A. Schäfer, C. Huber, and R. Ahlrichs, "Fully optimized contracted Gaussian basis sets of triple zeta valence quality for atoms Li to Kr," J. Chem. Phys. **100**, 5829–5835 (1994).
23. F. Weigend and R. Ahlrichs, "Balanced basis sets of split valence, triple zeta valence and quadruple zeta valence quality for H to Rn: Design and assessment of accuracy," Phys. Chem. Chem. Phys. **7**, 3297–3305 (2005).
24. D. Rappoport and F. Furche, "Property-optimized Gaussian basis sets for molecular response calculations," J. Chem. Phys. **133**, 134105 (2010).
25. TURBOMOLE V6.6 2014, a development of University of Karlsruhe and Forschungszentrum Karlsruhe GmbH, 1989-2007, TURBOMOLE GmbH, since 2007; available from `http://www.turbomole.com`.
26. R. Ahlrichs, M. Bär, M. Häser, H. Horn, and C. Kölmel, "Electronic structure calculations on workstation computers: The program system turbomole," Chem. Phys. Lett. **162**, 165–169 (1989).
27. R. A. Kendall, T. H. Dunning Jr., and R. J. Harrison, "Electron affinities of the first-row atoms revisited. Systematic basis sets and wave functions," J. Chem. Phys. **96**, 6796–6806 (1992).
28. A. A. Granovsky, Firefly version 8, www `http://classic.chem.msu.su/gran/firefly/`.
29. S. Frankiss and D. Harrison, "Thermodynamic properties of fluorine compounds—XVI. The vibrational spectra and thermodynamic functions of pentafluorobenzene, chloropentafluorobenzene, bromopentafluorobenzene and methylpentafluorobenzene," Spectrochim. Acta Mol. Spectrosc. **31**, 1839–1864 (1975).
30. H. Köppel, W. Domcke, and L. S. Cederbaum, "Multimode Molecular Dynamics Beyond the Born-Oppenheimer Approximation," in *Advances in Chemical Physics*, Vol. 57, edited by I. Prigogine and S. A. Rice (John Wiley & Sons, Inc., 1984) pp.

59–246.

31. G.A. Worth, M.H. Beck, A. Jäckle, and H.-D. Meyer, computer code, The MCTDH Package, Version 8.2, University of Heidelberg, Heidelberg, Germany, 2000; H.-D. Meyer, computer code, The MCTDH Package, Version 8.3 (2002), Version 8.4 (2007). [`http://mctdh.uni-hd.de`].
32. H.-D. Meyer, U. Manthe, and L. S. Cederbaum, "The multi-configurational time-dependent Hartree approach," Chem. Phys. Lett. **165**, 73–78 (1990).
33. M. H. Beck, A. Jäckle, G. A. Worth, and H. D. Meyer, "The multiconfiguration time-dependent Hartree (MCTDH) method: a highly efficient algorithm for propagating wavepackets," Phys. Rep. **324**, 1–105 (2000).
34. H.-D. Meyer, F. Gatti, and G. A. Worth, *Multidimensional Quantum Dynamics: MCTDH Theory and Applications* (Wiley-VCH, Weinheim, 2009).
35. G. A. Worth, H.-D. Meyer, H. Köppel, L. S. Cederbaum, and I. Burghardt, "Using the MCTDH wavepacket propagation method to describe multimode non-adiabatic dynamics," Int. Rev. Phys. Chem. **27**, 569–606 (2008).
36. J. C. Light, I. P. Hamilton, and J. V. Lill, "Generalized discrete variable approximation in quantum mechanics," J. Chem. Phys. **82**, 1400–1409 (1985).

6 Summary and Outlook

The wavepacket dynamics in two different classes of molecules in their excited electronic states after excitation with ultraviolet femtosecond laser pulses have been investigated using the time-resolved time-of-flight mass spectrometry and photoelectron imaging spectroscopy techniques. Of particular interest were excitations to predissociative states, and vibronically induced interstate coupling effects between the initially optically excited state and a second, optically dark state.

The employed techniques turned out to be particularly powerful in this respect. The resulting fragments of a bond dissociation reaction can be readily distinguished by their respective time of flight. The rise and decay time constants of the transient mass signals yield information on the time scales of the involved photochemical processes and tell us whether the fragments were generated before or after interaction with the ionizing probe laser pulses. The recorded photoelectron spectra and angular distribution allowed us to follow radiationless population transfer processes between excited electronic states. By combining both techniques, different photophysical and photochemical phenomena could be successfully investigated.

The α–CC Cleavage Reaction in Acetone and Cyclohexanone

The proposed photochemical reaction pathway of the α–CC cleavage in acetone and cyclohexanone after excitation to the ^{1}nπ^* state via intersystem crossing to the ^{3}nπ^* state and the subsequent surmounting of an energy barrier on the nanosecond time scale has been widely accepted, although femtosecond time-resolved investigations seemed to suggest a CC bond dissociation in less than 200 femtoseconds. This apparent discrepancy could be resolved in the present work. It was found that the observation of the dynamics on the potential energy surface of the ^{1}nπ^* state is obscured by the parallel occurrence of dynamics induced by two-photon transitions to high-lying Rydberg states, and the decomposition of the acetone cation following the ionizing probe laser pulse in certain experimental configurations. The simultaneous dynamics could not be disentangled by the transient ion yields recorded in previous studies alone. Only in combination with the frequency-resolved photoelectron imaging method it was possible to distinguish the three processes from each other and isolate their effects:

(i) It was confirmed that there is no ultrafast α–CC bond dissociation on the $^1n\pi^*$ electronic potential energy surface, as no photodissociation products of this state were found on a time scale of several hundred picoseconds. The vibrational energy of the initially excited CO stretch mode is redistributed in less than 80 femtoseconds, and the molecular structure relaxes towards the $^1n\pi^*$ potential energy minimum. This process goes hand in hand with a strongly reduced photoionization cross section that prevents us to follow the ensuing dynamics after the departure of the excited wavepacket from the Franck–Condon region. Photoionization of the $^1n\pi^*$ state leaves the molecular cation vibrationally cold and no further decomposition takes place.

(ii) The two-photon absorption of light with wavelengths of $\lambda > 306$ nm excites transitions to the 3p Rydberg states. Depending on the excitation energy, the lifetime of these states was determined to be $\tau = 700 - 200$ fs. Their photoionization leaves a hot ground state ion that can dissociate during the flight time to the detector if the deposited vibrational energy exceeds 0.8 eV.

(iii) With a two-photon excitation energy of 8.1 eV, a barrier on the $3d_{yz}$ Rydberg state can be surmounted, which is formed by an avoided crossing with the $\pi\pi^*$ valence state. This energy accidentally coincides with two times the barrier height for α–CC cleavage on the $^3n\pi^*$ potential energy surface of 4.05 eV ($\lambda = 306$ nm). From the $\pi\pi^*$ potential energy surface, an ultrafast reaction pathway to breaking the α–CC bond in $\tau = 90 - 50$ fs is taken.

In summary, we could elucidate all reaction pathways leading to the observations of previous investigations, while leaving the commonly accepted picture of the CC bond cleavage of acetone fully intact.

Similar ultrafast electronic relaxation pathways from high-lying Rydberg states were observed in cyclohexanone as well. The two-photon excitation of the 3p and 3d Rydberg states lead to internal conversion to the 3s Rydberg state on a time scale faster than the experimental time resolution of 35 femtoseconds. Although it could not be directly deduced from the photoelectron spectra, it is very likely that this ultrafast electronic relaxation is facilitated by similar vibronic interactions with the $\pi\pi^*$ state as in acetone: The population of the excited Rydberg states is thus transferred in only about one vibrational period of the CO stretching vibration to the $\pi\pi^*$ state potential energy surface and through a conical intersection to the 3s Rydberg state. From previous research it is known that the excited 3s Rydberg state deactivates to the $^1n\pi^*$ electronic state by internal conversion in $\sim$10 picoseconds. The excited $^1n\pi^*$ state is found to be long-lived with a decay time of more than several hundred picoseconds, as was seen from its weak, broad band in the photoelectron spectra recorded in the present work.

Aside from the contribution of these findings to the solution of the initially presented α–CC cleavage problem, the observed phenomena can also be interpreted in terms of the paradigms introduced by the anthracence and NaI experiments presented in the introduction of this Thesis. The dynamics of these aliphatic ketones in high-lying Rydberg states can be pictured as textbook examples of very directional phase-space trajectories. The nuclear motion along the CO stretching coordinate in the form of a highly localized wavepacket drives the system to a configuration where the electronic interstate couplings are so strong that the CC bond is broken in only few vibrational periods.

Vibronic Interaction of the $\pi\pi^*$ and $\pi\sigma^*$ Excited States in Pentafluorobenzene

The first optically bright $\pi\pi^*$ electronic state of pentafluorobenzene was excited using femtosecond laser pulses at wavelengths between 273 and 240 nm. The subsequently recorded transient parent ion yield showed a long-lived, large-amplitude coherent oscillation of 78 – 74 cm-1 frequency. Interestingly, the photoelectron spectra evidenced the population of the initially excited $\pi\pi^*$ state only in the maxima of the oscillation, as the corresponding photoelectron bands vanished in the minima. The oscillation is mirrored in the anisotropy of the photoelectron angular distribution, which indicates a periodically changing electronic character of the emitting state.

The interpretation of the experimental observations has been confirmed by the performed quantum-chemical calculations on the system. The computational results have shown that the $\pi\pi^*$ state strongly vibronically couples to the $\pi\sigma^*$ state along several vibrational out-of-plane modes. In the adiabatic picture, this coupling distorts the $\pi\pi^*$ potential energy surface to acquire a pronounced double-well character along these modes. The quantum dynamics simulations yielded a long-lived, localized wavepacket oscillating in the double-well potential of the lowest-frequency out-of-plane mode. While the first diabatic excited state of the planar molecule is of purely $\pi\pi^*$ electronic character, a population transfer to the second diabatic $\pi\sigma^*$ electronic state occurs during the vibrational out-of-plane motion. The ionizing probe laser pulse directly maps the evolving wavepacket into the observed signal oscillations.

The goal of this work was to investigate the interaction of electronic $\pi\pi^*$ states with neighboring optically dark $\pi\sigma^*$ states in the sense of a quantum-mechanical model system for biologically relevant molecules that show very efficient electronic relaxation pathways by exploiting similar electronic excited-state configurations. In these systems, the $\pi\pi^*$ and $\pi\sigma^*$ potential energy surfaces conically intersect each other, forming a “photochemical funnel” that facilitates the ultrafast electronic deactivation reaction. It could be shown that in pentafluorobenzene, although the potential energy surfaces of both states do not intersect in the investigated excitation energy regime, the vicinity of the $\pi\sigma^*$ state has a strong influence on the

$\pi\pi^*$ state by the large vibronic coupling coefficients of certain nuclear coordinates. The periodic population transfer between the two electronic states corresponds to an electronic coherence that is driven by a molecular vibration. Therefore, the term "vibronic coherence" was chosen as the most appropriate description for the observed behavior.

Concluding Remarks and Outlook

During the work on this Thesis, many technical improvements were introduced to the mass spectrometry and photoelectron imaging experimental setups. The data acquisition rate was initially raised to 100 Hz, and during the writing of this Thesis, a further increase to 200 Hz was possible. Work is under way to further increase the data rate, possibly up to the laser repitition rate of 1 kHz. These improvements do not only affect the duty cycle of the pulsed valve that produces the molecular beam. Attention must also be paid that the subsequent digitizing electronics and computer software do not pose a bottleneck limiting the acquisition rate. Only with this experimental fine tuning did the demanding measurements on molecules like the aliphatic ketones, with extraordinarily weak absorption cross sections resulting in charged particle count rates of at most five per laser shot, become possible.

The photoelectron imaging technique provided highly valuable insight into the electronic structure and the ensuing non-adiabatic wavepacket dynamics on the electronic potential energy surfaces of the investigated molecules that can not be gained from the frequency-integrated transient ion signals alone. In the context of the photochemical mechanisms behind the unusual excited-state dynamics in the $\pi\pi^*$ electronic state of pentafluorobenzene, it would be interesting to apply this technique to 1,2,3,4-tetrafluorobenzene and to hexafluorobenzene. In these molecules, the $\pi\sigma^*$ state is energetically shifted to higher or lower energies, respectively. Coherent signal oscillations have been observed in both molecules (Kovalenko *et al.*, Phys. Rev. Lett. 96, 68301, 2006; Studzinski *et al.*, J. Chem. Phys. 128, 164314, 2008), although the exact mechanisms have so far remained unresolved. The photoelectron spectra and angular distributions would reveal whether a similar vibronic coherence is responsible for the observed phenomena.

Increasing the temporal resolution of the experiment might reveal nuclear motion in terms of vibrational modes that contribute to coupling between excited electronic states that could so far not be resolved. In the guanine-cytosine Watson-Crick base pair for example, electron-induced proton transfer has only very recently been shown to be an important pathway for electronic deactivation (Röttger *et al.*, Angew. Chem. Int. Ed. 54, 14719, 2015). The vibrational period of a N–H vibration is typically located around 10 femtoseconds, making it experimentally very challenging to monitor the corresponding nuclear wavepacket dynamics in real time. The obvious

way to improve the temporal resolution of the time-resolved mass spectrometry and photoelectron imaging experiment to enable such observations would be a temporally shorter probe laser pulse. Its generation, for example by sum-frequency generation of a frequency-doubled NOPA laser pulse and a fundamental laser pulse, would result in ultraviolet laser pulses of $\sim$30 fs duration, tuneable in the range from 190 nm $\leq \lambda \leq$ 230 nm. Furthermore, these high photon energies would facilitate a one-photon ionization of most excited molecules, thus avoiding the resonant intermediate steps that may introduce additional complexity to the photoelectron spectra and angular distributions.

Danksagung

Mein großer Dank gebührt an erster Stelle meinem Doktorvater Friedrich Temps, der mich ohne mich vorher gekannt zu haben in seine Arbeitsgruppe aufnahm und sogar eine bezahlte Stelle aus dem Hut zauberte. Herzlichen Dank für Ihr Vertrauen, für die vielen Diskussionen und Anregungen, sowie für Ihre stets hilfsbereite und verständnisvolle Art!

Ich danke Hendrikje Neumann für ihre Einführung in die Vakuumtechnik des Massenspektrometrie-Experiments. Ebenfalls großer Dank gebührt Julia Bahrenburg, Katharina Röttger und Mayra Stuhldreier für ihre Einführung in die Arbeitspraxis in den Laserlaboren. Ihr habt mir damals den Start sehr erleichtert, vor allem mit eurer Herzlichkeit!

Für jede weitere Hilfe in Fragen der Vakuumtechnik sowie die Versorgung mit allen denkbaren und undenkbaren Vakuumkomponenten wie Verschraubungen, Ventilen, Leitungen, Dichtungen, Flanschen, Detektoren, Meßköpfen, Maßzeichnungen, Schlauchschellen und was ich Euch sonst noch alles abgeschwatzt habe, danke ich Joachim Gripp und Michael Karstens.

Ohne die unendlich hilfsbereiten und stets um eine schnelle und technisch saubere(!) Lösung bemühten Mitarbeiter der Elektronik- und Feinmechanikwerkstatt sowie der Haustechnik, Klaus Warns, Uwe Eggers, Klaus-Dieter Will, Frank Laasch, Olaf Wendt, Frank Herzog, Timo Görgens und Andreas Sievers wäre diese Arbeit niemals möglich gewesen. Vielen Dank für jeden Klönschnack und für alles Gelötete, Gebohrte, Gefräste, Gedrehte, Gesägte, Geschweißte, Gepresste, Geklebte, und was ihr sonst noch alles könnt!

Meinem Bachelorstudenten Niklas Helle danke ich für seine großartige Mitarbeit bei den Messungen am Cyclohexanon-Molekül. Meinem Praktikanten Jonas Kus danke ich ebenfalls für seine Mitarbeit und vor allem für die Entscheidung, meine Nachfolge am Massenspektrometrie-Experiment anzutreten. Ich wünsche Dir viel Erfolg!

Falk Renth danke ich sehr für seine Bemühungen um das PL-Inversionsprogramm und die vielen netten Gespräche über Themen fern der Wissenschaft. Harald Studzinski danke ich (unbekannterweise) für den Aufbau des Massenspektrometrie-Experiments und die ausführliche Dokumentation in seiner Dissertation. Matthieu Sala und

Dassia Egorova danke ich für die zahlreichen und äußerst lehrreichen Diskussionen über theoretische Chemie und Quantendynamik-Simulationen. Bernd Hartke, Tim Raeker und Julian Müller danke ich sehr für die Durchführung des Quantenchemie-Crashkurses. Die Berechnungen des Pentafluorbenzol-Moleküls hätte ich ohne ihre Hilfe nicht durchführen können.

Den bereits genannten Julia, Katharina, Mayra, Niklas, Jonas und Falk sowie vielen weiteren langjährigen Mitstreitern in der Arbeitsgruppe, speziell Ron Siewertsen, Hauke Nicken, Thomas Michalak, Alexander Thrun, Uta Corinna Stange, Hendrik Böhnke, Mats Bohnsack, Joss Wiese, Mark Dittner, Joscha Kleber, Nancy Faßheber, Inga Piller, Meike Becker und Johannes Dammeier, danke ich für die große Kollegialität in allen Situationen, die angenehme und sehr freundschaftliche Arbeitsatmosphäre, die netten Gespräche, die abwechslungsreichen Pausen, die Mensagänge, die Dönergänge, die schönen Stunden auf Dienstreisen, den Spaß während des Institutsumzugs, all den Quatsch, und überhaupt.

Auch allen oben nicht namentlich erwähnten Gruppenmitgliedern, sowie der aktuellen Besetzung, von denen Dennis Bank, Jonas Kus, Rebecca Marschan, Sebastian Megow, Elisabeth Moshake, Hendrik Rapp, Sebastian Schatz, Carsten Schröder, Rebecca Stellmacher und Shuangqing Wang noch nicht genannt wurden, danke ich für die schöne gemeinsam verbrachte Zeit.

Unseren Sekretärinnen Frau von der Heydt und Tanja Sharif gebührt großer Dank dafür, das Rückgrat der Arbeitsgruppe zu bilden, die Maschine am Laufen zu halten und aus dem Hintergrund mit unsichtbarer Hand alle Fäden zusammenzuführen.

Abschließend gilt mein größter Dank meiner Familie. Bei meinen lieben Eltern bedanke ich mich dafür, niemals meine Studienwahl und den nicht ganz geradlinigen Studienverlauf mit Wohnortwechseln und anderen Überraschungen in Frage gestellt zu haben, sowie für den bedingungslosen ideellen und finanziellen Rückhalt! Bei Dir, liebe Tina, bedanke ich mich für Dein Verständnis und Deine unendliche Geduld mit mir und meiner Arbeit. Vielen Dank, dass Du für mich da bist! Bei Jelte und Immo bedanke ich mich, dass sie dafür sorgen, dass jegliche Sorge und Frust automatisch an der Wohnungstür zurückbleiben.

A P P E N D I C E S

A LabView Measurement Software

The LabView software controlling the time-of-flight mass spectrometry experiment has been adapted from H. Studzinski (Dissertation, Universität Kiel, 2007) and was in large part rewritten during the work on this Thesis. The LabView software controlling the photoelectron imaging experiment was written from scratch. Additionally, several supplementary data evaluation programs for both experiments were written. The function, interface and output of all programs is explained in the following.

A.1 Time-Of-Flight Mass Spectrometry

The user interface of the LabView time-of-flight mass spectrometry control software is shown in Figure A.1. Several controls and indicators are featured on the main panel:

- The *current delay stage position* in femtoseconds and quickly accessible controls to *move the delay state to a specific position*, or *move relative to the current position* in fixed steps of $\pm$1000 fs, $\pm$500 fs and $\pm$100 fs.
- General status information on the currently running measurement like the *current* and *total number of delay steps*, the numeric value of the last acquired data point and the time when the measurement is finished as well as the time left until then.
- The graphs show the transient ion yield of the running measurement, the last acquired time-of-flight spectrum, and the pressure in the detector vacuum chamber if the corresponding cold-cathode gauge is switched on.
- Some parameters controlling the measurement are set on the main panel, such as the *number of sweeps* (number of individual time-of-flight spectra to average for one data point), the *integration window* over which the averaged time-of-flight spectrum is integrated, or if no window should be used. A running measurement can be *aborted* at any time.
- After a completed measurement, the maximum of the transient ion yield dataset is determined, and the corresponding delay stage position is stored as *tmax*. A button allows the user to quickly move the stage to that position.

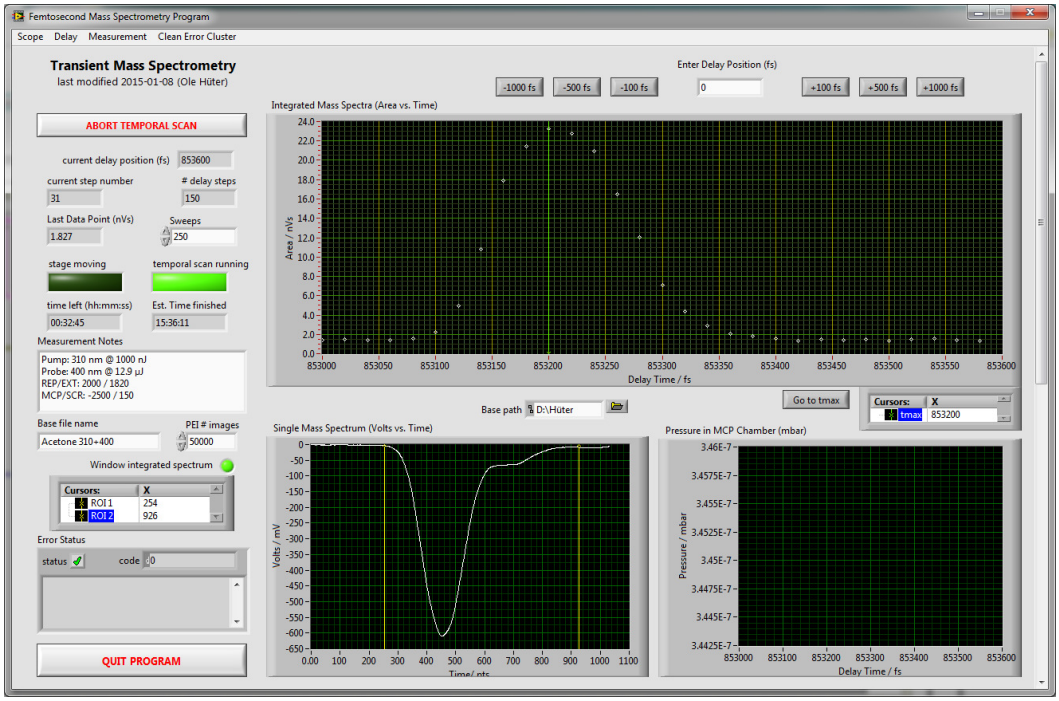

Figure A.1. User interface of the LabView time-of-flight mass spectrometry control software.

- *Notes on the measurement* can be entered in a free-text field that are saved with the acquired data. The measurements are saved in an automatically generated folder structure in the form "*<base path>/<YYYY–MM–DD>/<running number>/<base file name>_<content descriptor>*".

Several program functions are triggered by their corresponding entries in the run-time menu, which is depicted in Figure A.2.

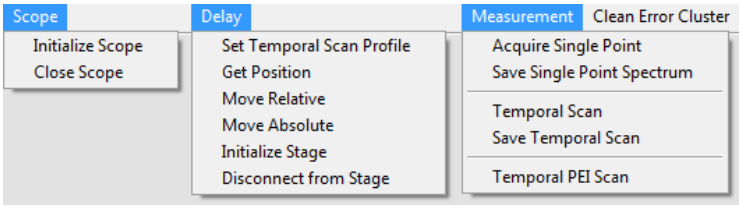

Figure A.2. Run-time menu of the time-of-flight mass spectrometry control software.

If neccessary, the connections to the oscilloscope and the delay stage controller can be initialized and closed, respectively. The temporal scan profile (i. e. the delay steps) can be configured, which will be described below; and measurements can be started and saved. The *acquire single point* command records a time-of-flight mass spectrum at the current delay stage position. The temporal scan command initialized a transient measurement with the defined delay steps. The *temporal PEI scan* command initializes a series of photoelectron imaging measurements, also at the defined delay

steps. The *number of images* that should be acquired at each step is configured on the main panel. While the mass spectrometry measurements have to be saved manually by the respective commands, the photoelectron imaging measurements are saved automatically after each step in the folder structure described above due to their large data size.

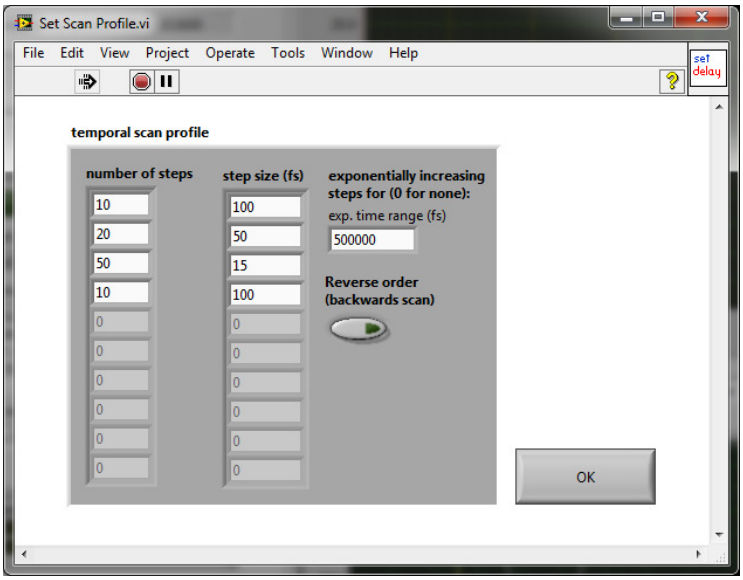

Figure A.3. Configuration dialog for the temporal scan profile.

The temporal scan profile is configured in the dialog shown in Figure A.3. An arbitrary number of *linear delay steps* in terms of number and temporal step width can be set. Afterwards, *steps of exponentially increasing width* in the entered time range are taken. The width of the first exponential step is based on the last linear step width. The *reverse order* button allows the user to take a measurement with negative step width, i. e. in the opposite delay stage movement direction.

When saving a completed transient time-of-flight ion yield measurement, three files are created on the disk: *i)* "*<base file name>_data.dat*", a one-dimensional dataset containing the ion yield data points and corresponding delay times that were displayed in the integrated mass spectra graph, *ii)* "*<base file name>_mass_spectra.dat*", a two-dimensional dataset containing a successive list of all acquired, averaged time-of-flight mass spectra, and *iii)* "*<base file name>_notes.txt*", a text file containing all (digitally) available information about the measurement. An example output of the notes text file is printed below:

```
Begin: 30.01.2015 10:18:42
End: 30.01.2015 11:33:42
Scope settings: 10 ns/div, 250 sweeps
Peak Integration: 174 – 824 pts

Start position: 251 001 fs
20x 50 fs
1500x 20 fs

Number of delay steps: 1 520
tmax: 252 703 fs

Notes:
Pump: 265 nm @ 850 nJ
Probe: 400 nm @ 4.5 µJ
REP/EXT: 2 000 / 1 820 V
MCP/SCR: −2 500 / 0 V
```

```
DG645 Settings:
A = T0 + 0.000 650 000 000 s
B = A + 0.000 500 000 000 s
C = T0 + 0.000 500 000 000 s
D = C + 0.001 000 000 000 s
E = T0 + 0.000 950 000 000 s
F = E + 0.000 500 000 000 s
G = T0 + 0.000 999 450 000 s
H = G + 0.000 000 500 000 s
```

It contains date and time of the measurement, the control program settings, the manually entered notes, and the configuration of the delay generator.

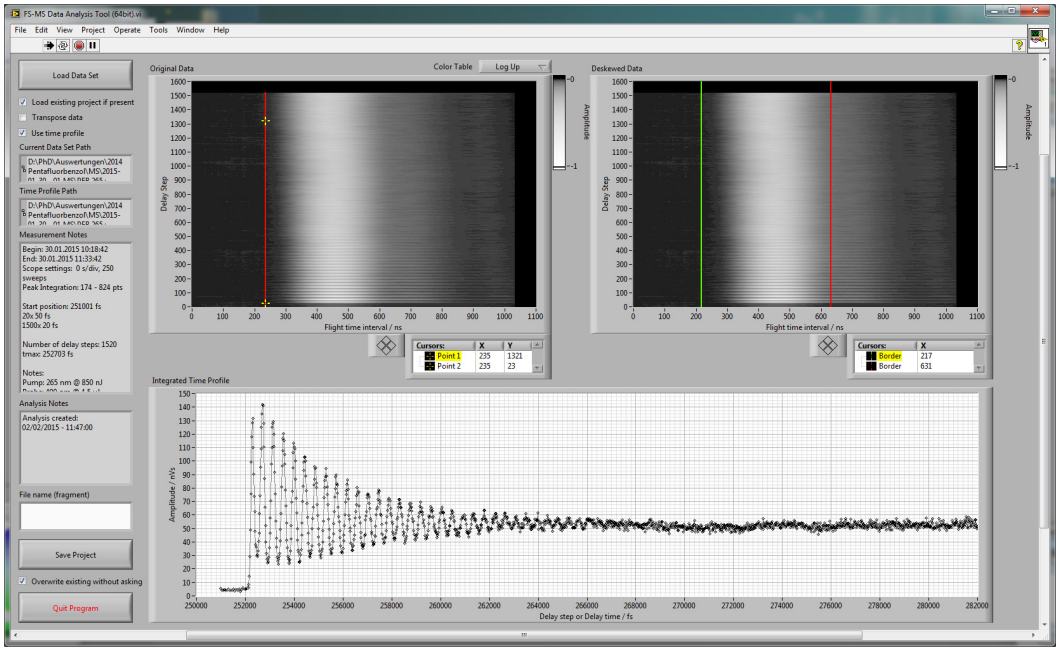

Figure A.4. Data analysis tool to evaluate the measured time-of-flight mass spectra.

The software for the further evaluation of the acquired two-dimensional, transient time-of-flight mass spectrometry datasets is shown in Figure A.4. After loading the dataset, it is displayed in the top left graph. In case the time-of-flight mass signal has shifted during the measurement, a linear correction can be applied by dragging and skewing the red line. Such a shift is an indicator for an experimental instability (mostly when the pulsed valve is not completely warmed up or was incorrectly adjusted) and should therefore not occur; none of the datasets used in this Thesis needed to be corrected in this way.

The (possibly corrected) dataset is shown in the top right graph, where the cursor pair is used to set the integration window. The resulting integrated transient ion yield is displayed in the bottom graph. It is saved together with the cursor positions, which are restored automatically upon reloading an already evaluated dataset. An additional appendix for the filename can be chosen manually, which is useful when more than one time-of-flight mass peak is present in the dataset.

A.2 Photoelectron Imaging Software

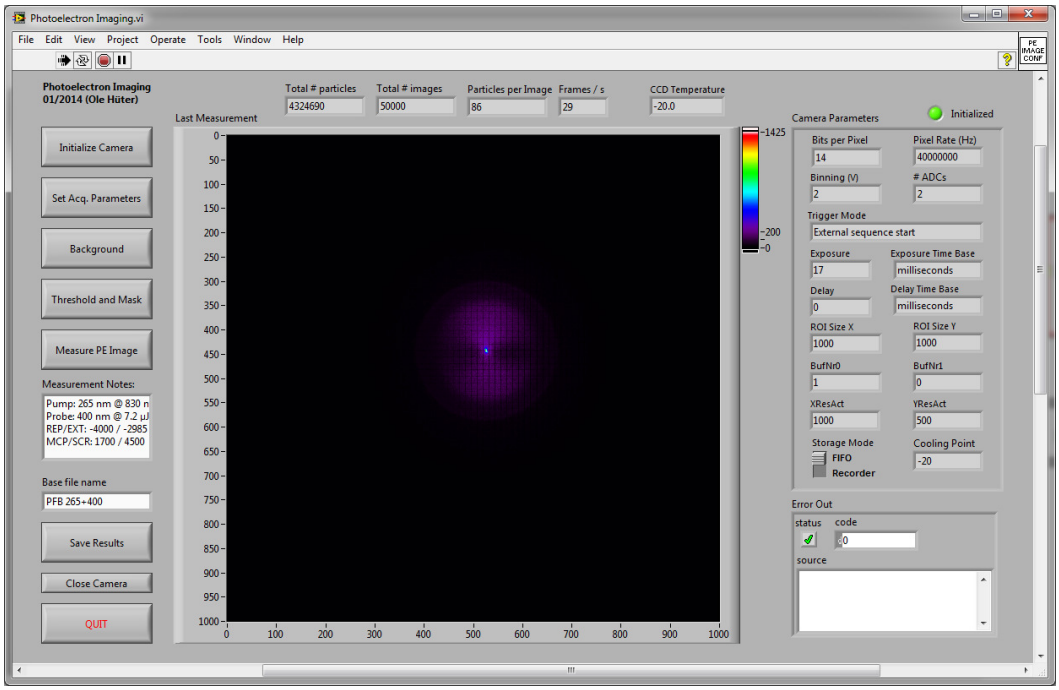

Figure A.5. User interface of the LabView photoelectron imaging spectroscopy control software.

The user interface of the LabView photoelectron imaging spectroscopy control software is shown in Figure A.5. The view of the main panel is divided into a three column layout:

- In the left column, buttons leading to configuration dialogs and the actual measurement dialog are located. Their respective purpose is explained in the following text. Measurement notes and a base file name can be set as well, similar to the mass spectrometry control program.
- In the middle column, the results of the last measurement are shown.
- In the right column, the currently set acquisition parameters of the camera are displayed.

In regular daily operation, the buttons on the left are used in their order from top to bottom to set the correct acquisition parameters. Subsequently, if only a single photoelectron image is to be recorded, the *measure PE image* function is used, and the measurement can be saved manually after completion. Otherwise a temporal scan can be initiated from the time-of-flight mass spectrometry control program, which has to be running simultaneously.

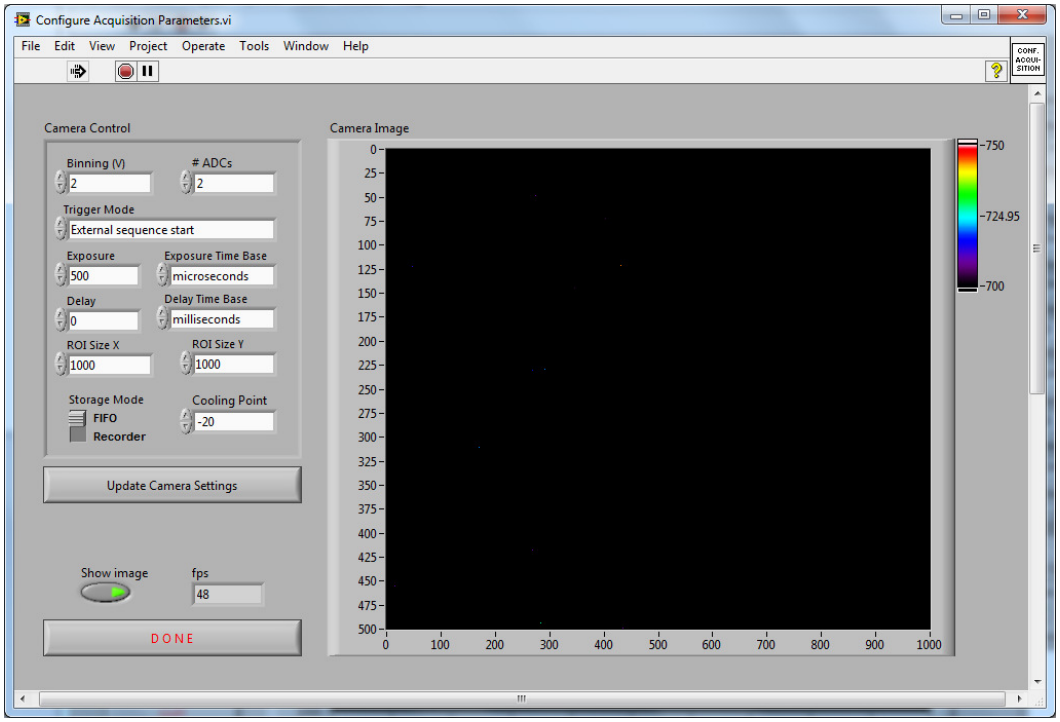

Figure A.6. Configuration dialog of the camera acquisition settings.

In the acquisition parameters configuration dialog pictured in Figure A.6, the camera driver settings can be changed and their immediate impact on the recorded images and the frame rate can be observed. Most of the settings, such as the *vertical binning*, the size of the *region of interest* and the *number of used analog-to-digital conververs* have been explained in the experimental part in Chapter 2. The *trigger and storage mode* settings are usually not to be changed. The Peltier element cooling the CCD sensor can achieve a temperature difference of $\Delta T = -50$ °C with respect to the ambient temperature. Therefore, values smaller than –20 °C for the *cooling point* setting are not useful.

The *exposure time* must be carefully considered. A setting of 500 µs is reasonable when only the electrons generated by the interaction with one single laser pulse are to be captured. In this case, the hardware-limited maximum frame rate of 50 s^{-1} is achieved; but due to the 200 Hz repetition rate of the pulsed valve, 75% of the molecular beam pulses are left unused. In some of the measurements performed during the work on this Thesis, an exposure time of 17 ms was chosen. This setting lowers the frame rate to 29 s^{-1}, but captures the electrons from four laser pulse interactions. The effective "electron detection rate" in electrons per second is therefore increased more than twofold. As the MCPs were switched off during the time between laser shots, no detectable additional noise was introduced to the recorded images.

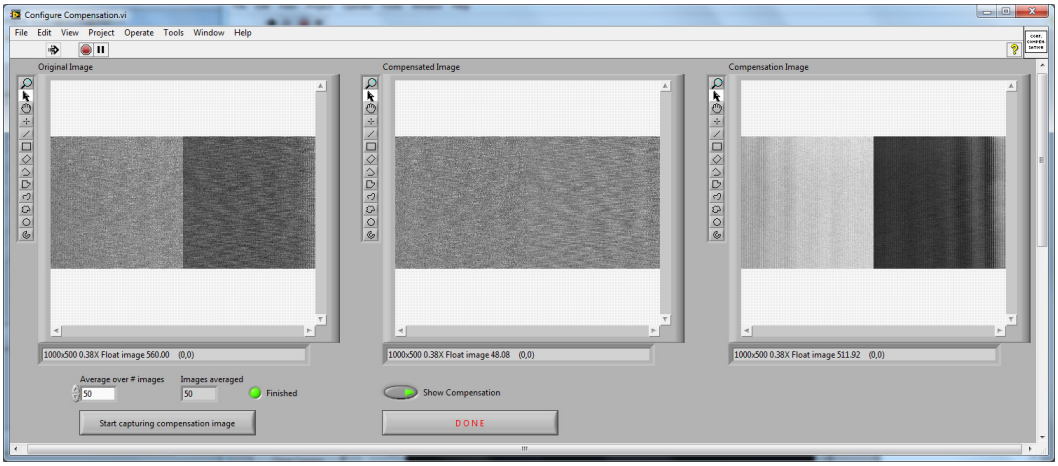

Figure A.7. Acquisition dialog for the background to be subtracted from each single image.

In the dialog shown in Figure A.7, a background image is recorded that is subsequently subtracted from every single image (frame) acquired by the camera. This was neccessary as the photoelectron images were always recorded using the two analog-to-digital converters, which are independent from each other and not a "matched pair" regarding to their electrical characteristics. In the left image displayed in Figure A.7, a raw camera image recorded in darkness can be seen. The two halves of the image, corresponding to the separate digitization regions, can clearly be distinguished by the different electrical noise level of the ADCs. This effect has to be compensated for in order to have a uniform detection sensitivity over the whole imaged area.

There are two ways to achieve this compensation: Either two different thresholding ranges (see Chapter 2) for each image half are applied, or a noise-background image is subtracted from each acquired frame. Here, the second way turned out to be computationally much cheaper. The dark noise was recorded, averaged over typically 50 images and stored. The images compensated in this way display an even noise background over their whole area, as can be seen in the middle image of Figure A.7.

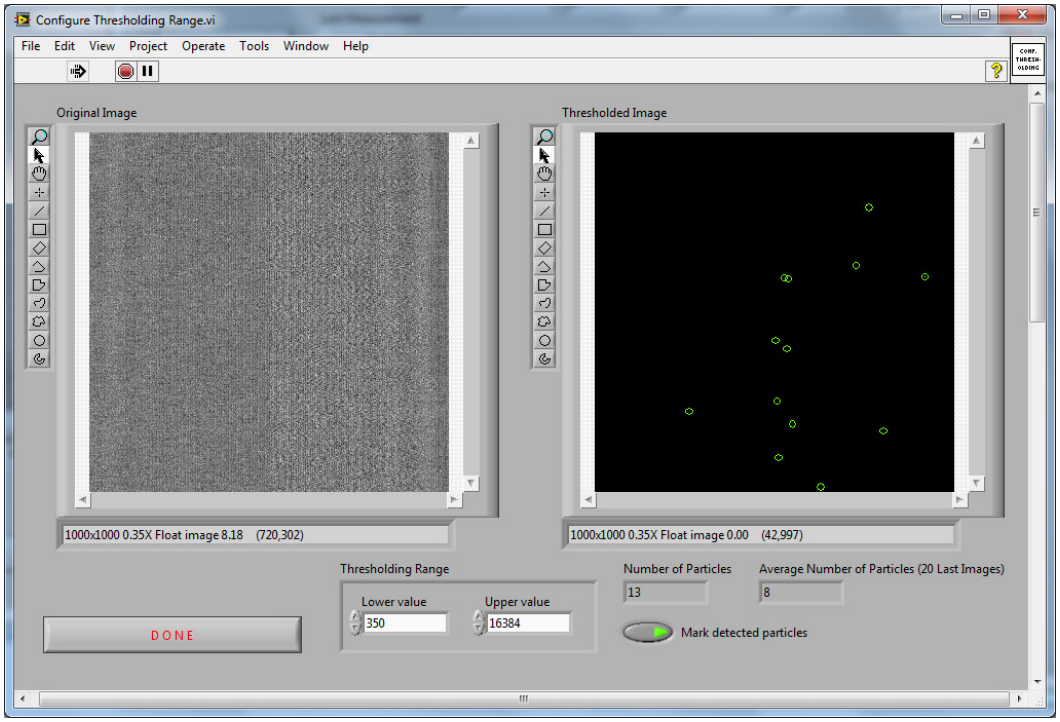

Figure A.8. Configuration dialog for the thresholding range values.

In preparation for the particle detection, the acquired image is thresholded, which means that all pixel values of the image outside of a specified *thresholding range* are set to zero. The configuration dialog for this range is shown in Figure A.8. In our case, an upper bound for the thresholding range was unneccessary and therefore set to the maximum pixel value of a 14-bit image (16 384). The lower bound was adjusted to avoid the "false positive" detection of noise peaks, which typically was achieved with values of 350. If a certain region of the image should be excluded from the particle detection, the drawing tools of the left image display can be used to select an arbitrary geometric shape.

Subsequently, the particle detection algorithm was applied to the image. The thresholded image is displayed on the right side of the dialog shown in Fig. A.8, where the detected particles are marked with green circles for better visibility. The number of particles and its average value over the last 20 acquired images are indicated below.

This configuration dialog was also employed to adjust the femtosecond laser pulse intensities that no electrons from single–color ionization were generated.

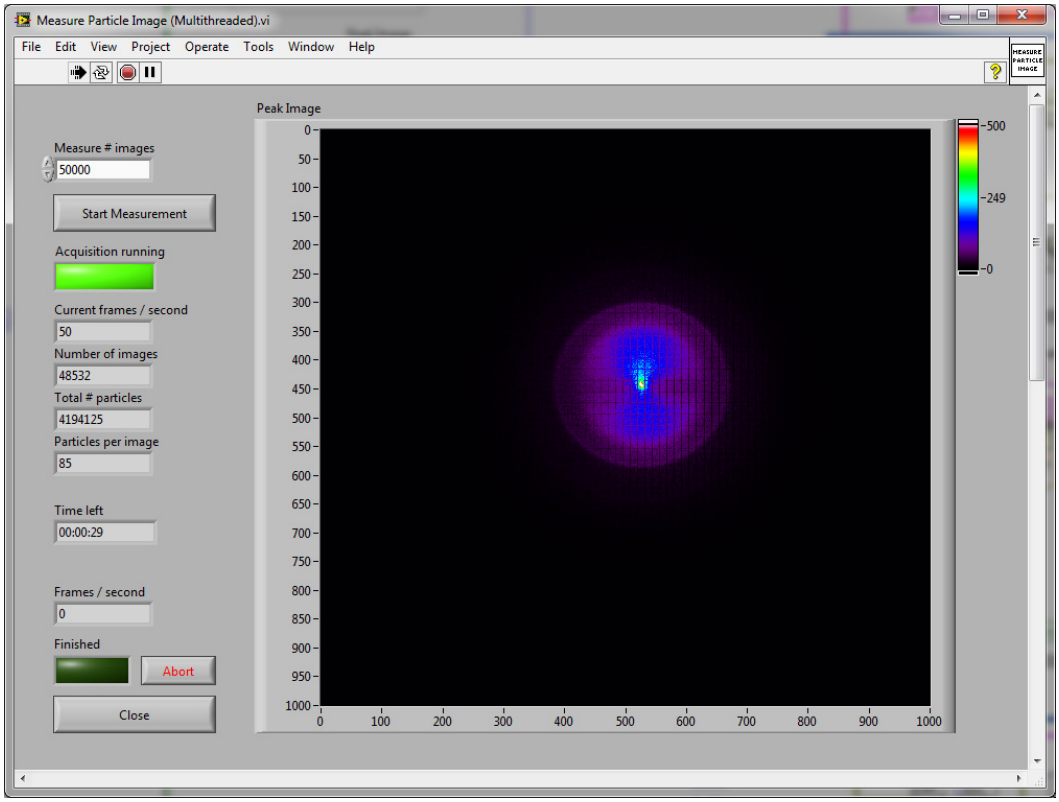

Figure A.9. Photoelectron image measurement window.

After all configuration steps have been completed, a photoelectron image can be acquired using the measurement window shown in Figure A.9. The number of single images that should be acquired has to be specified on the top left. The image display is continuously updated during the measurement process. Additional information on the running measurement are displayed on the left, such as the image acquisition rate, the number of acquired images, the number of detected particles and the average number of particles per image. The time until the measurement is finished is displayed below these indicators. A running measurement can be aborted at any time. After completion, the window can be closed, and the results are displayed in the main window of the control program.

When a measurement is saved, several files are created in the same automatically generated folder structure of the form "*<base path>/<YYYY–MM–DD>/<running number>*" as in the time-of-flight mass spectrometry program. The file names generated are "*<base file name> tmax* $\pm$ *<delay stage position relative to tmax> fs_<descriptor>/*". The photoelectron image is saved as two-dimensional numerical matrix data with the ending "*image.asc*". For quick reference, a version converted to the PNG graphics format is saved in "*image.png*". A tab-separated list of (x, y)–coordinates of all detected particles is saved, compressed to ZIP, in a file ending with

"*peaks.zip*". Furthermore, a text file containing all (digitally) available information about the measurement is saved with the filename ending "*notes.txt*". An example output of the notes text file is printed below:

```
Fr, 30. Jan 2015 13:17:27
Total particles: 4 324 690
Total images: 50 000
Particles per image: 86
Frames per second: 29

Center X: 443
Center Y: 526

Start position: 252 295 fs
2x 415 fs
1x 1 305 fs
1x 1 740 fs
1x 1 720 fs
2x 1 730 fs

Number of delay steps: 7
tmax: 252 295 fs
Stage position: 252 710 fs

Pump: 310 nm @ 830 nJ
Probe: 400 nm @ 7.2 µJ

REP/EXT: −4 000 / −2 985 V
MCP/SCR: 1 700 / 4 500 V
```

```
DG645:
A = T0 + 0.000 650 000 000 s
B = A + 0.000 500 000 000 s
C = T0 + 0.000 500 000 000 s
D = C + 0.001 000 000 000 s
E = T0 + 0.000 950 000 000 s
F = E + 0.000 500 000 000 s
G = T0 + 0.000 999 450 000 s
H = G + 0.000 000 500 000 s

Camera parameters:
ADCs: 2
Exposure: 17 milliseconds
Delay: 0 milliseconds
Binning (vertical): 2
X Res: 1 000 px
Y Res: 500 px
ROI X: 1 000 px
ROI Y: 1 000 px
Cooling Point: −20 °C
Storage Mode: FIFO
Trigger mode: External sequence start
Bits per pixel: 14
Pixel Rate: 40 000 000 Hz
```

Most of the listed information have been discussed in this or the last section. The image center x and y coordinates were automatically determined with the algorithm of Bordas (see Chapter 2).

Image Processing Software

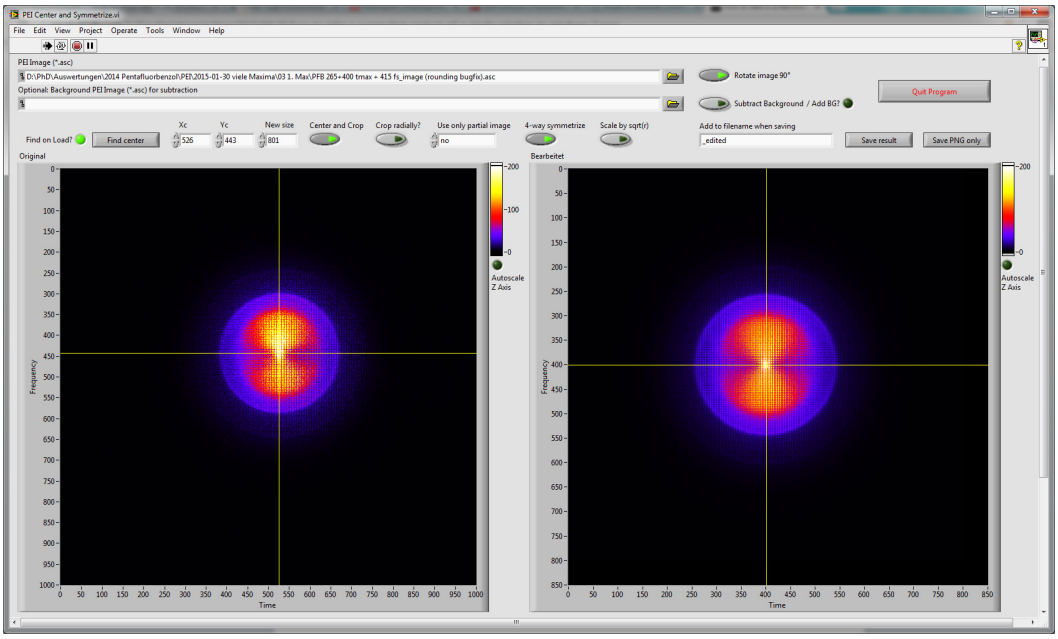

Figure A.10. Photoelectron image evaluation software to find the center of the distribution, average the four quadrants of the resized and centered image and save the result.

The program displayed in Figure A.10 was written for further processing the recorded photoelectron images. The program allows the user to add or subtract two photoelectron images, a function which may be useful, for example, when a constant photoelectron background can not be avoided during the measurement and is recorded separately. As the center of the photoelectron distribution does usually not correspond to the center of the recorded image, it can be determined using a center-of-mass algorithm, which is then refined with the algorithm of Bordas as described in Chapter 2. The image is centered and resized (cropped, not rescaled) as requested by the user. Optionally, only one half or a quarter of the image can be used. As the four quadrants of the photoelectron image are theoretically identical due to the axial symmetry, they can be averaged if desired.

The photoelectron image can then be saved to a new file as two-dimensional matrix data, whereby the chosen parameters and the determined image center coordinates are saved into a separate file for documentation. The photoelectron image file can directly be read and processed by the pBasex image inversion program.

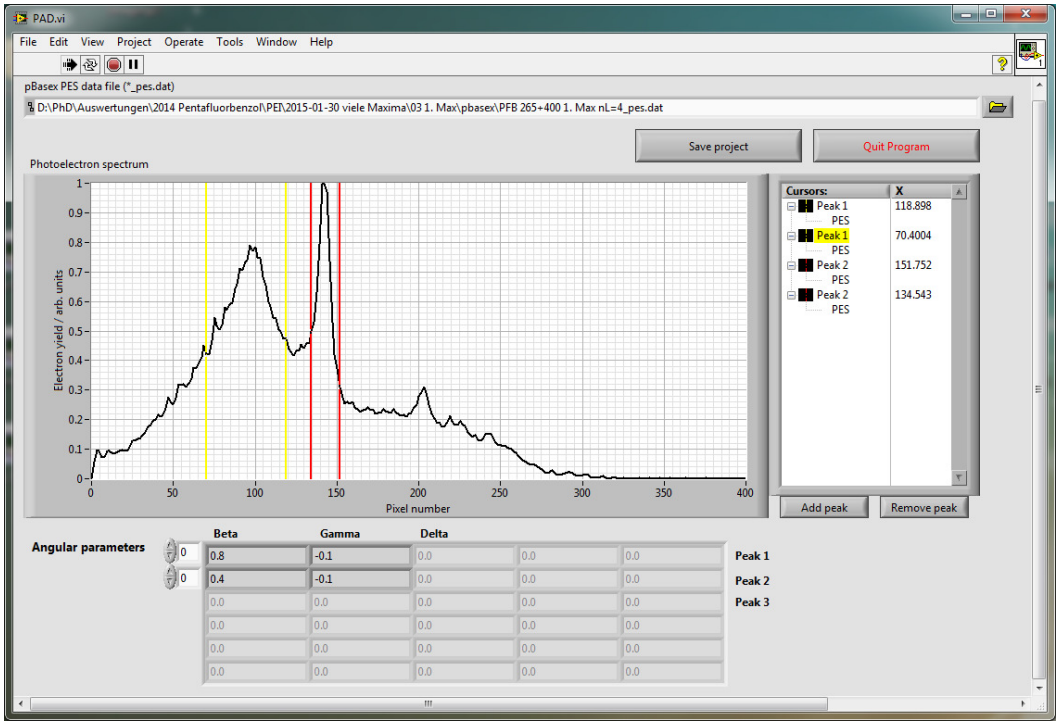

Figure A.11. Photoelectron imaging processing software to calculate the anisotropy parameters of the photoelectron angular distribution of selected bands.

The pBasex image inversion program outputs three files: the inverted photoelectron image, the photoelectron spectrum in terms of the pixel radius and the anisotropy parameters, also in terms of the pixel radius. The documentation of pBasex states, that "*to extract the angular parameters for a given photoelectron band with a finite width, the parameter values have to be weighted by the intensity of the PES*".

To perform this task with an intuitive user interface, the program shown in Figure A.11 was written. It allows the user to load a photoelectron spectrum and add an arbitrary number of cursor pairs (the colored lines in the graph) to select the desired photoelectron bands. The calculated anisotropy parameters are displayed below the graph. The results and the cursor positions are saved to separate files. When loading an already evaluated spectrum, the cursors and their respective positions are automatically restored.

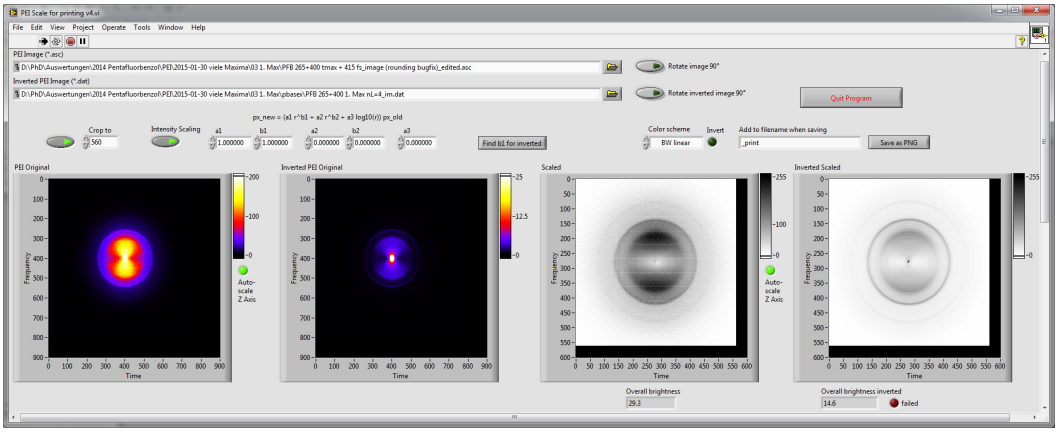

Figure A.12. Photoelectron imaging processing software to scale the photoelectron image with arbitrary, radially symmetric polynomial terms to enhance the visual clarity and save the image with a selected color scheme in the PNG file format.

In all programs presented so far, the photoelectron images were displayed for evaluation purposes by the experimentalist. When the images are to be presented in a projection or a printed medium, one usually wants to adjust several issues:

- On a computer screen, the dark and colorful color scheme used so far works quite well. In projections or on paper, a grayscale color scheme works much better in terms of visibility.
- The size of the displayed image should align with the chosen scale of the photoelectron spectra.
- Low-intensity spectral features in the middle and outer perimeter of the image are hardly visible in the original images. Scaling the image radially with a polynomial r^x with $0.5 \leq x \leq 1$ enhances the visual contrast in these regions to a great extend.
- In the photoelectron image inversion process, noise is concentrated towards the center of the image (see the pBasex theory in Chapter 2). Therefore, when converted to grayscale without further adjustments, the inverted image has a large black spot in the center and no discernable structure in the remaining area. Scaling the inverted image with the polynomial $r^{x'}$ with an appropriate x', usually larger than x, solves this problem.

For this purpose, the program shown in Figure A.12 was written. It allows the user to load the original and inverted photoelectron images, and to choose the new image size and the value of the scaling exponent x. The result is shown in the third graph from the left side. The program then calculates the visual luminosity of the scaled image, and a simple algorithm is executed that was devised to find x' such that the luminosity of the inverted image is $1/2$ of the luminosity of the original image. Both

scaled images are then saved in the PNG graphics format, and all chosen parameters in a separate text file.

The reason for the factor $1/2$ as optimization goal is that the luminosity of the original is a measure for the total number of electrons emitted in the full solid angle of 4π. The inverted image is a two-dimensional slice through the center of the original three-dimensional photoelectron distribution, and is therefore composed of electrons from only 2π solid angle. While this physically motivates the factor $1/2$ for the luminosity, the scaling with the polynomial $r^{x'}$ is an arbitrary choice that is only justified by the appealing visual result: when displayed next to each other, the images "just look right".

B Original and Inverted Photoelectron Images

In this Chapter, all photoelectron images from which photoelectron spectra were shown in this Thesis are pictured. The corresponding meridional slices through the original three-dimensional distributions obtained with the pBasex program are shown next to them. All images were inverted using even Legendre polynomials up to fourth order ($N_L = 4$), unless otherwise noted. All photoelectron images are normalized to 1, and for the radial scaling factor r^x, the exponent $x = 1$ was chosen.

B.1 Acetone

Excitation Wavelength λ_{pump} = 320 nm

Δt = 0.045 ps

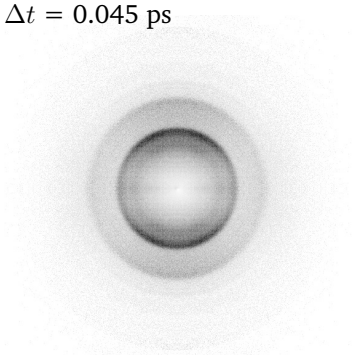

$902\,752$ e$^-$

inverted, N_{L} = 4

Δt = 0.095 ps

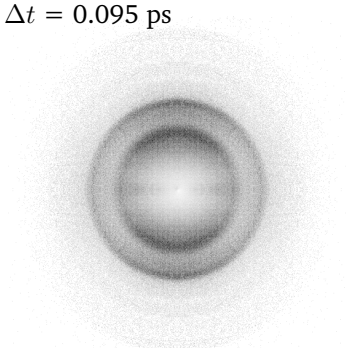

$681\,150$ e$^-$

inverted, N_{L} = 4

Δt = 0.195 ps

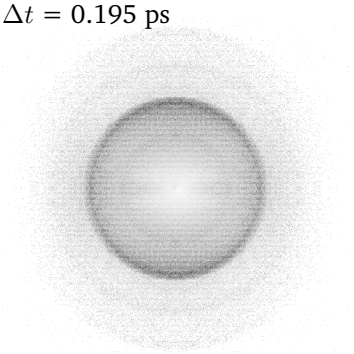

326 120 e^-

inverted, N_L = 4

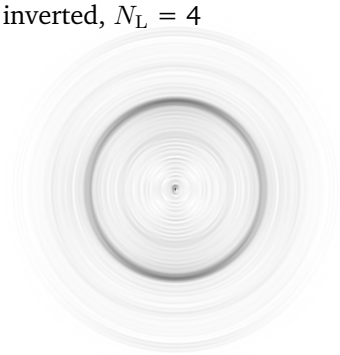

Excitation Wavelength λ_{pump} = 315 nm

Δt = 0.020 ps

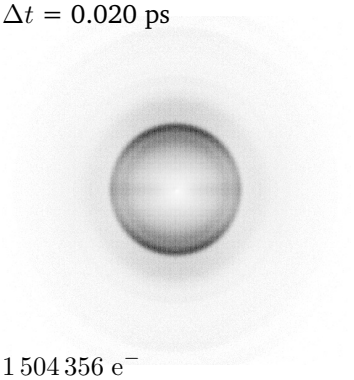

1 504 356 e^-

inverted, N_L = 4

Δt = 0.150 ps

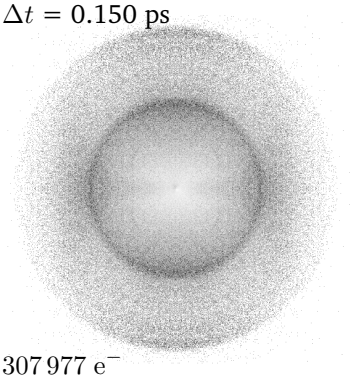

307 977 e^-

inverted, N_L = 4

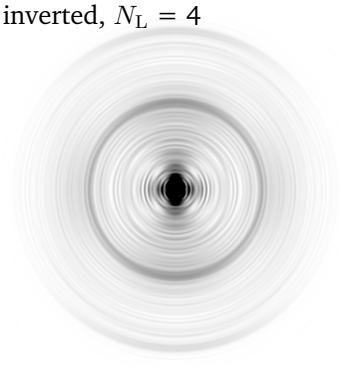

Excitation Wavelength λ_{pump} = 310 nm

Δt = 0.010 ps

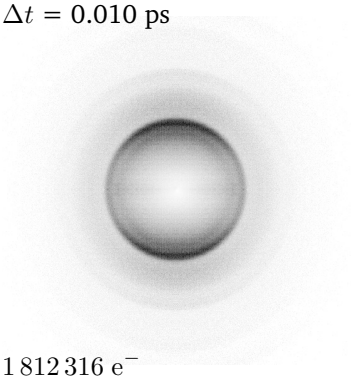

1 812 316 e^-

inverted, N_L = 4

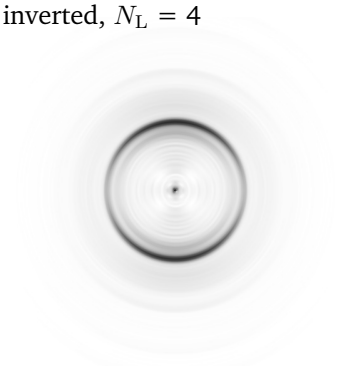

$\Delta t = 0.060$ ps

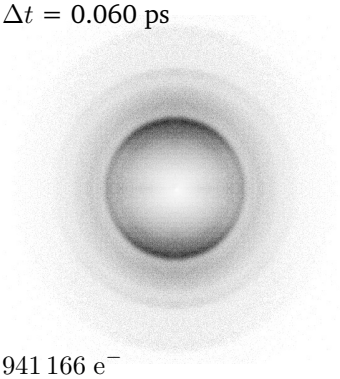

941 166 e^-

inverted, $N_L = 4$

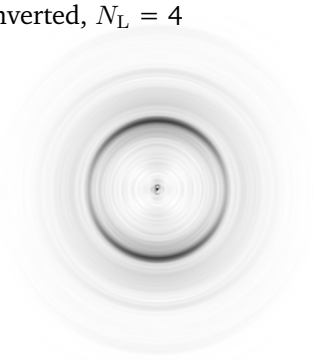

$\Delta t = 0.160$ ps

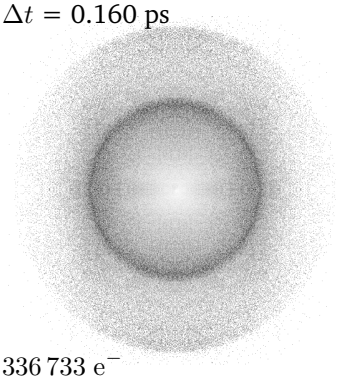

336 733 e^-

inverted, $N_L = 4$

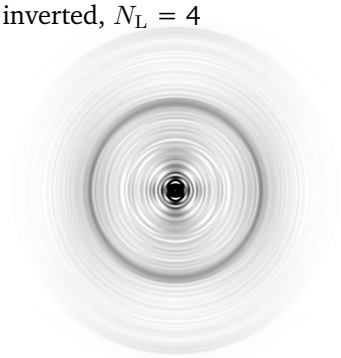

Excitation Wavelength λ_{pump} = 306 nm

$\Delta t = 0.035$ ps

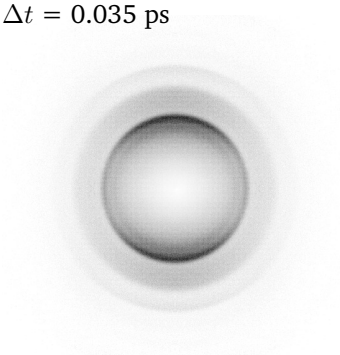

2 499 548 e^-

inverted, $N_L = 4$

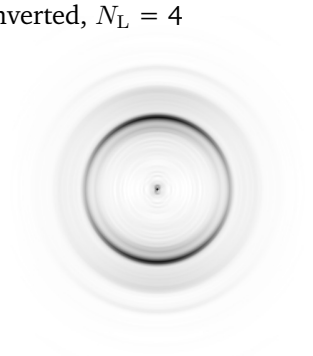

$\Delta t = 0.085$ ps

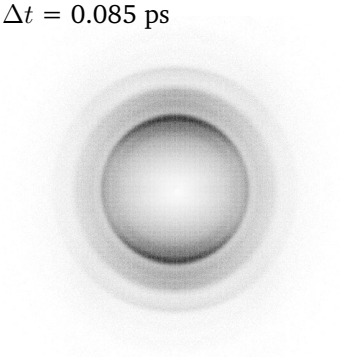

1 778 392 e^-

inverted, $N_L = 4$

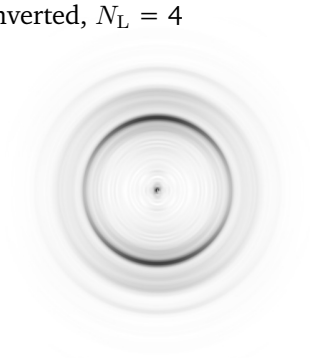

Δt = 0.135 ps

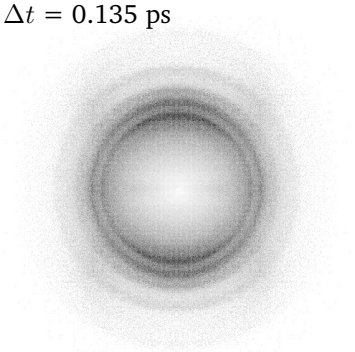

739 627 e^-

inverted, N_L = 4

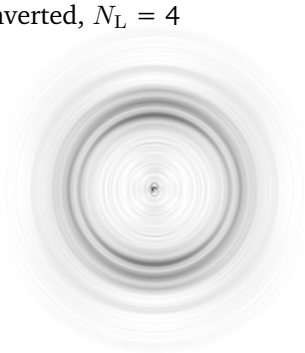

Δt = 0.185 ps

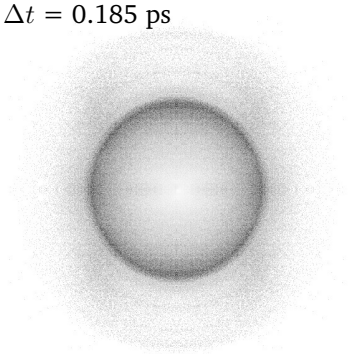

460 502 e^-

inverted, N_L = 4

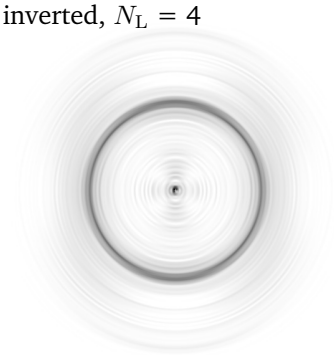

Excitation Wavelength λ_{pump} = 302 nm

Δt = 0.025 ps

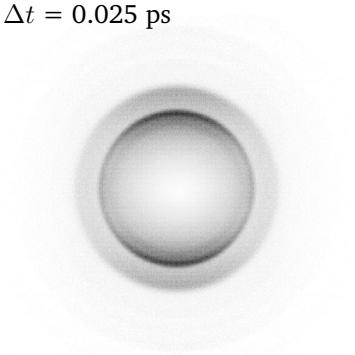

1 660 842 e^-

inverted, N_L = 4

Δt = 0.075 ps

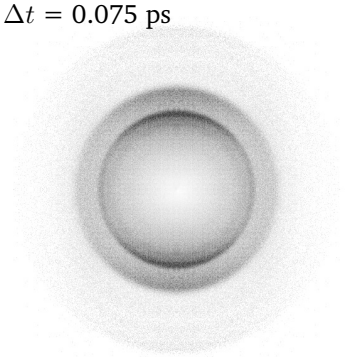

730 057 e^-

inverted, N_L = 4

Excitation Wavelength λ_{pump} = 296 nm

Δt = 0.015 ps

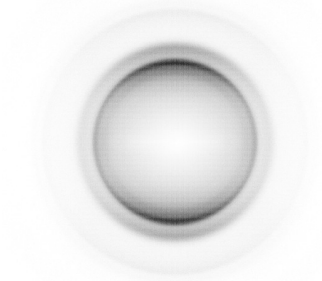

7 325 357 e^-

inverted, $N_{\mathrm{L}} = 4$

Δt = 0.065 ps

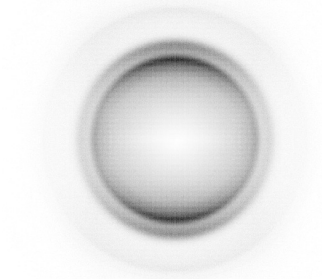

4 165 909 e^-

inverted, $N_{\mathrm{L}} = 4$

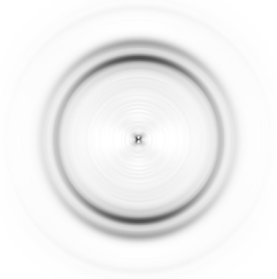

Δt = 0.115 ps

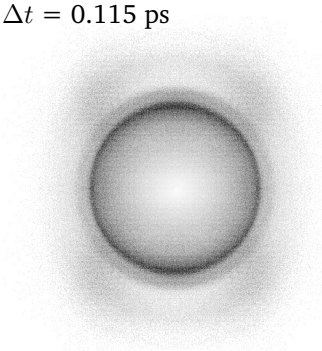

890 961 e^-

inverted, $N_{\mathrm{L}} = 4$

Δt = 0.165 ps

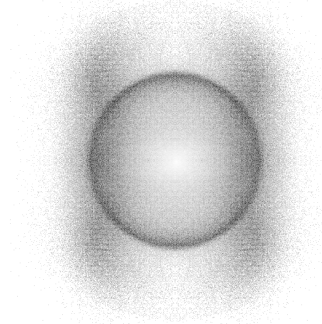

472 308 e^-

inverted, $N_{\mathrm{L}} = 4$

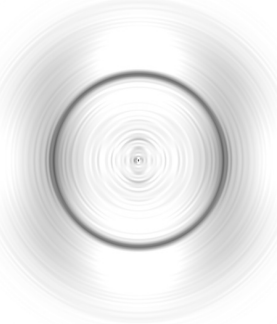

Excitation Wavelength λ_{pump} = 288 nm

Δt = 0.020 ps

inverted, $N_{\mathrm{L}} = 4$

$2\,776\,152\ \mathrm{e}^{-}$

Δt = 0.080 ps

inverted, $N_{\mathrm{L}} = 4$

$2\,070\,262\ \mathrm{e}^{-}$

Δt = 0.140 ps

inverted, $N_{\mathrm{L}} = 4$

$532\,073\ \mathrm{e}^{-}$

Excitation Wavelength λ_{pump} = 275 nm

Δt = 0.015 ps

inverted, $N_{\mathrm{L}} = 4$

$1\,734\,879\ \mathrm{e}^{-}$

$\Delta t = 0.065$ ps

inverted, $N_\mathrm{L} = 4$

$1\,284\,528\ \mathrm{e}^-$

$\Delta t = 0.115$ ps

inverted, $N_\mathrm{L} = 4$

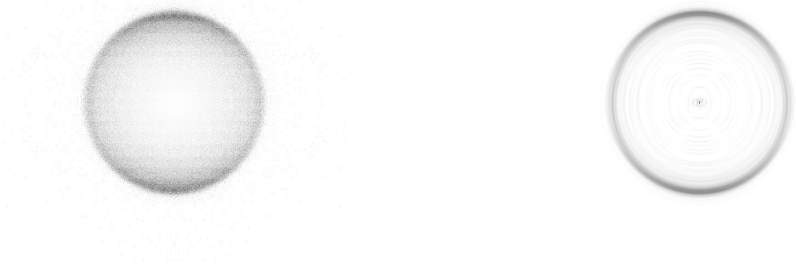

$195\,172\ \mathrm{e}^-$

Excitation Wavelength λ_pump = 265 nm

$\Delta t = 0.015$ ps

inverted, $N_\mathrm{L} = 4$

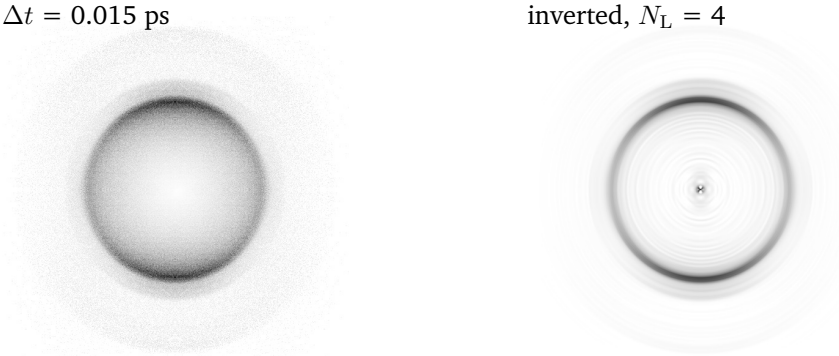

$713\,143\ \mathrm{e}^-$

$\Delta t = 0.065$ ps

inverted, $N_\mathrm{L} = 4$

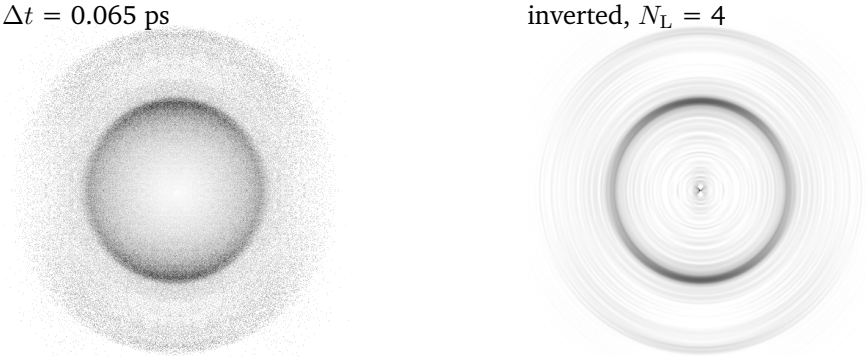

$278\,715\ \mathrm{e}^-$

Δt = 0.115 ps

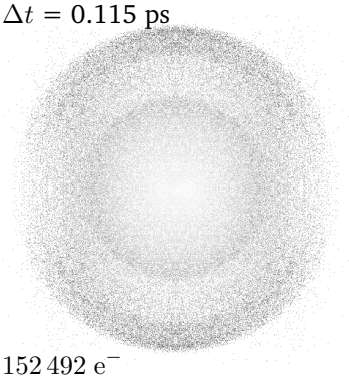

152 492 e^-

inverted, N_L = 4

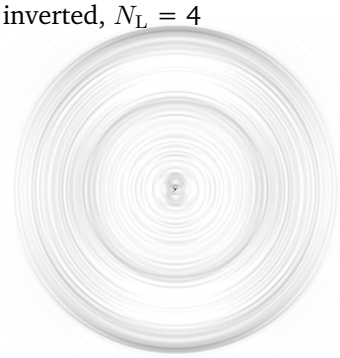

Excitation Wavelength λ_{pump} = 250 nm

Δt = 0.010 ps

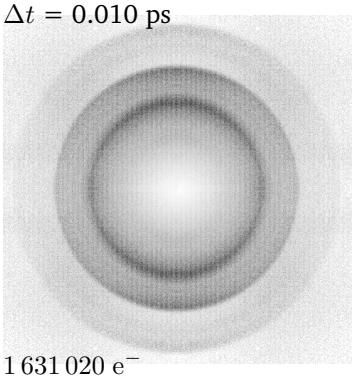

1 631 020 e^-

inverted, N_L = 4

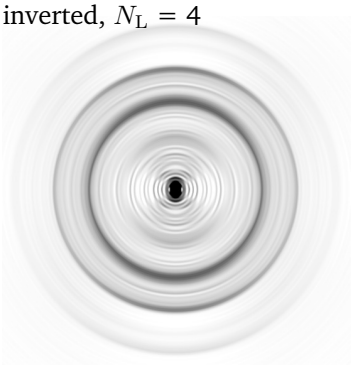

Δt = 0.085 ps

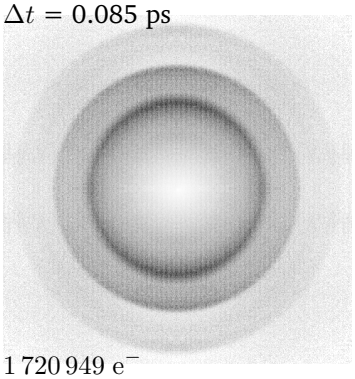

1 720 949 e^-

inverted, N_L = 4

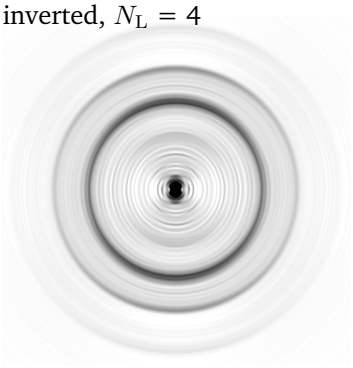

Δt = 0.160 ps

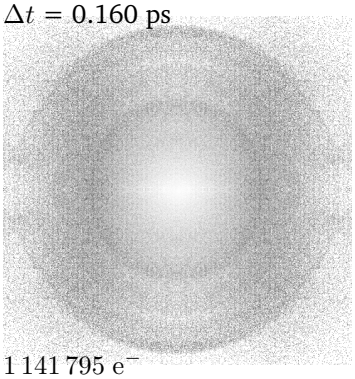

1 141 795 e^-

inverted, N_L = 4

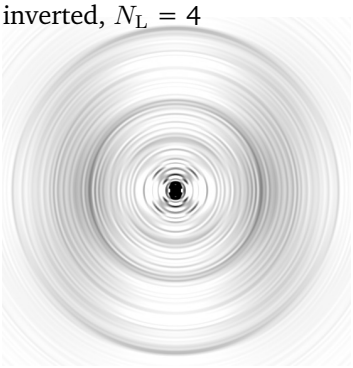

B.2 Cyclohexanone

Excitation Wavelength λ_{pump} = 315 nm

Δt = 0.020 ps

inverted, $N_{\mathrm{L}} = 4$

$243\,447\ \mathrm{e}^{-}$

Δt = 0.070 ps

inverted, $N_{\mathrm{L}} = 4$

$154\,133\ \mathrm{e}^{-}$

Δt = 0.120 ps

inverted, $N_{\mathrm{L}} = 4$

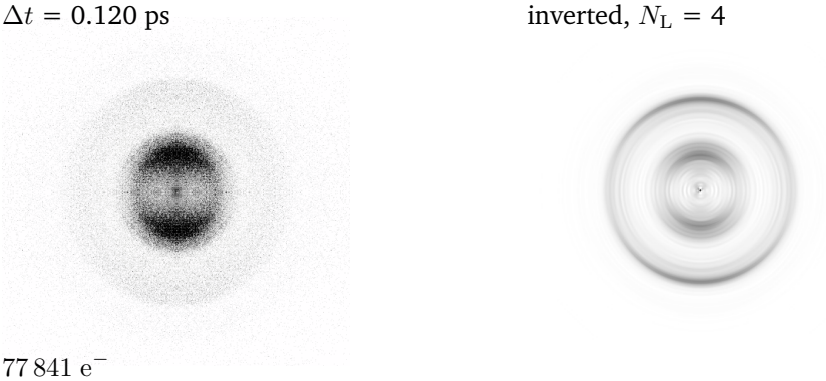

$77\,841\ \mathrm{e}^{-}$

Δt = 0.170 ps

inverted, $N_{\mathrm{L}} = 4$

$68\,058\ \mathrm{e}^{-}$

Δt = 0.220 ps

inverted, N_{L} = 4

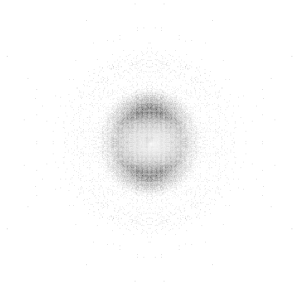

68 314 e^-

Excitation Wavelength λ_{pump} = 300 nm

Δt = 0.025 ps

inverted, N_{L} = 4

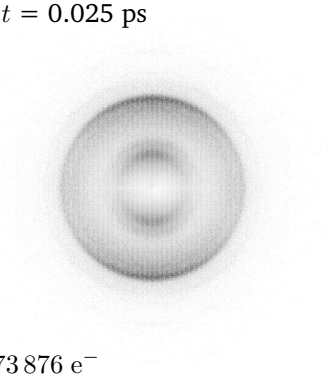

573 876 e^-

Δt = 0.075 ps

inverted, N_{L} = 4

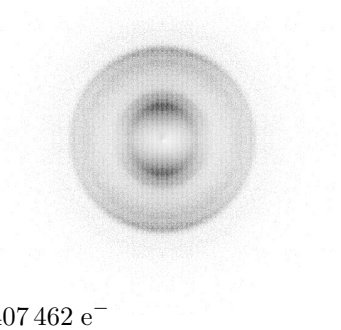

407 462 e^-

Δt = 0.125 ps

inverted, N_{L} = 4

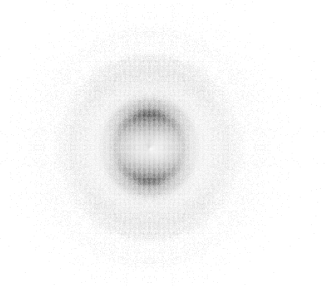

261 556 e^-

Δt = 0.175 ps

inverted, $N_{\mathrm{L}} = 4$

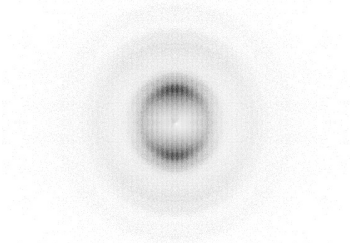

227 184 e^{-}

Δt = 0.225 ps

inverted, $N_{\mathrm{L}} = 4$

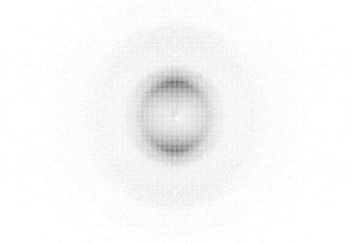

241 268 e^{-}

Excitation Wavelength λ_{pump} = 280 nm

Δt = 0.015 ps

inverted, $N_{\mathrm{L}} = 4$

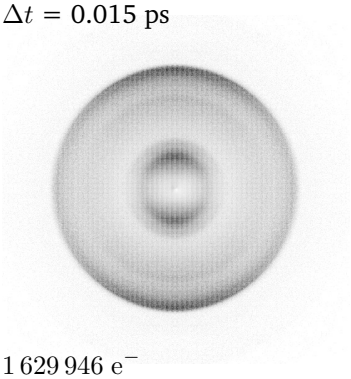

1 629 946 e^{-}

Δt = 0.090 ps

inverted, $N_{\mathrm{L}} = 4$

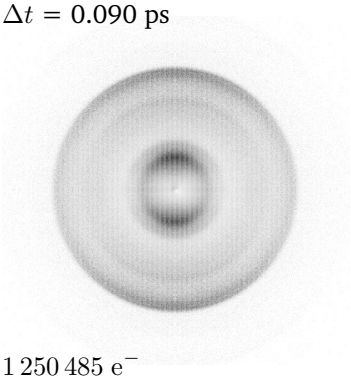

1 250 485 e^{-}

Δt = 0.165 ps

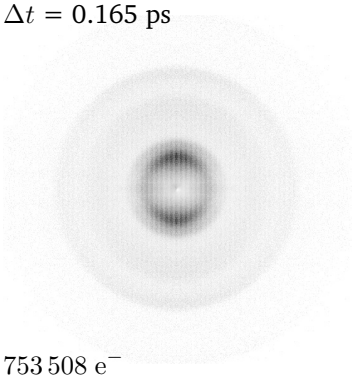

753 508 e^-

inverted, N_L = 4

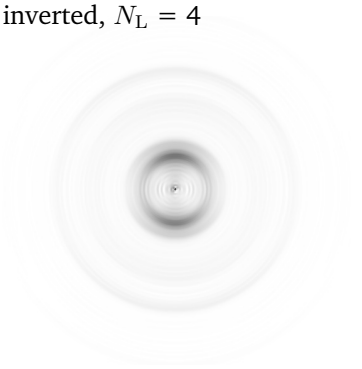

Δt = 0.240 ps

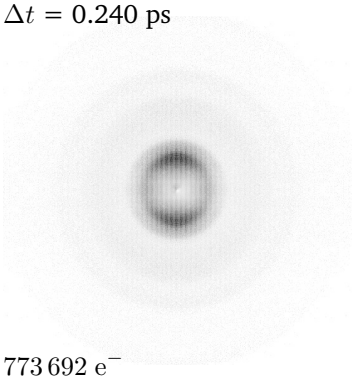

773 692 e^-

inverted, N_L = 4

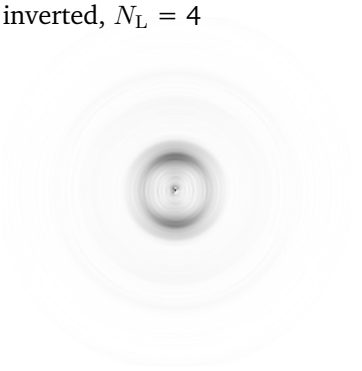

Excitation Wavelength λ_{pump} = 260 nm

Δt = 0.015 ps

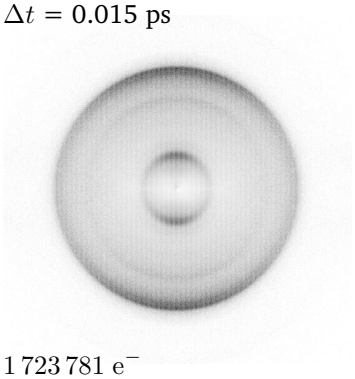

1 723 781 e^-

inverted, N_L = 4

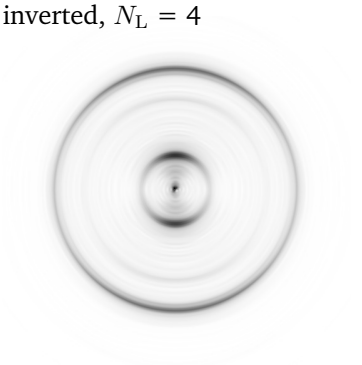

Δt = 0.065 ps

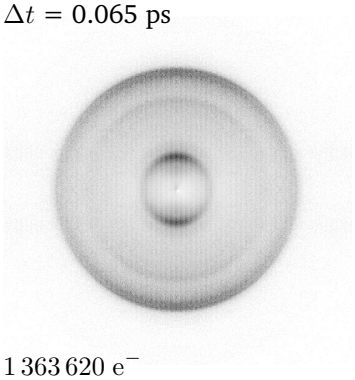

1 363 620 e^-

inverted, N_L = 4

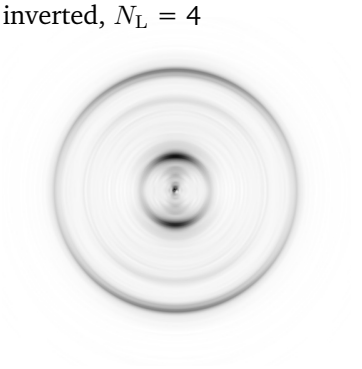

Δt = 0.115 ps

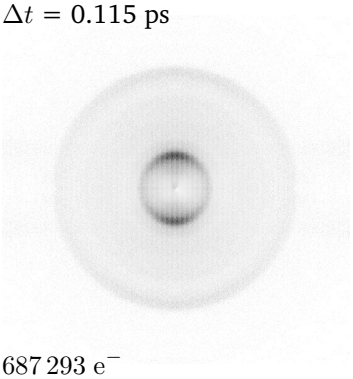

687 293 e^-

inverted, N_L = 4

Δt = 0.165 ps

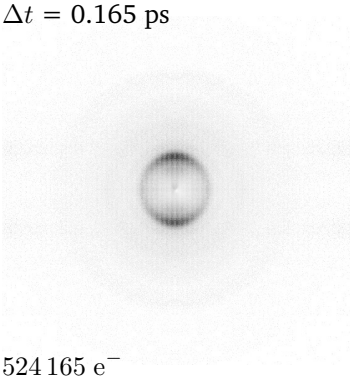

524 165 e^-

inverted, N_L = 4

Δt = 1.165 ps

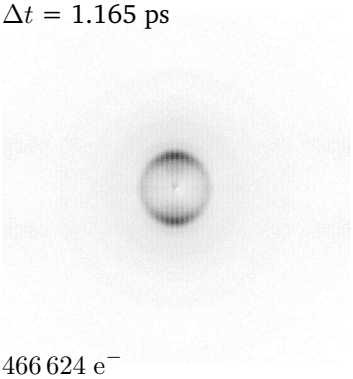

466 624 e^-

inverted, N_L = 4

B.3 Pentafluorobenzene

Maxima–Only Measurement Series, λ_{pump} = 265 nm

Δt = 0.05 ps

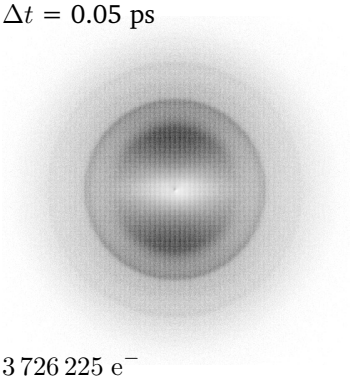

3 726 225 e^-

inverted, N_L = 4

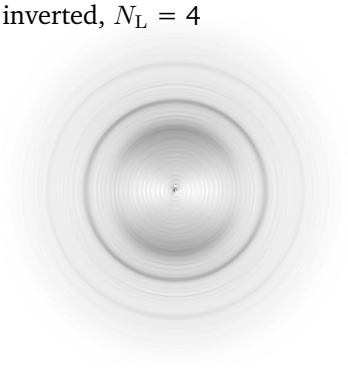

Δt = 0.455 ps

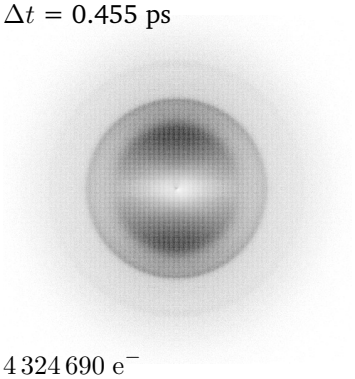

4 324 690 e^-

inverted, N_L = 4

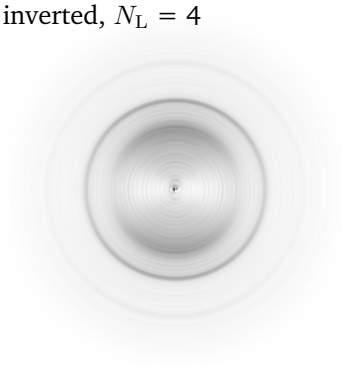

Δt = 0.880 ps

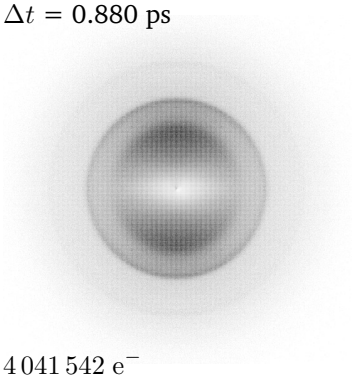

4 041 542 e^-

inverted, N_L = 4

Δt = 2.185 ps

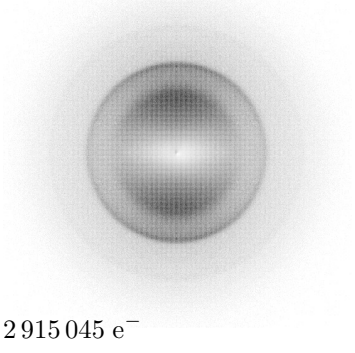

2 915 045 e^-

inverted, N_L = 4

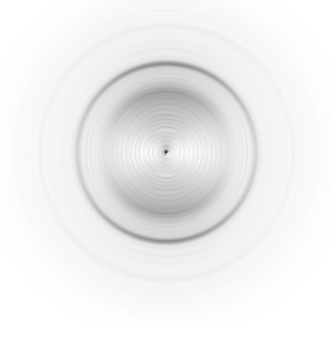

Δt = 3.925 ps

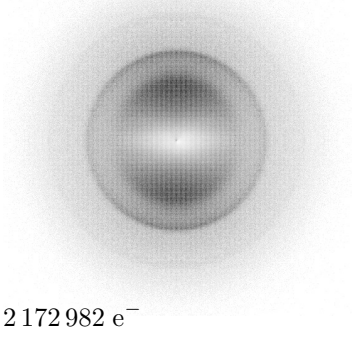

2 172 982 e^-

inverted, N_L = 4

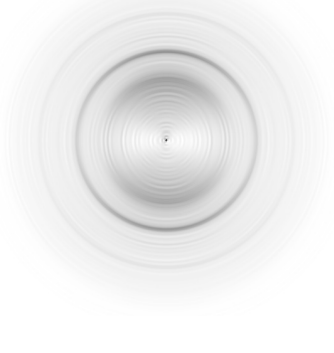

Δt = 5.645 ps

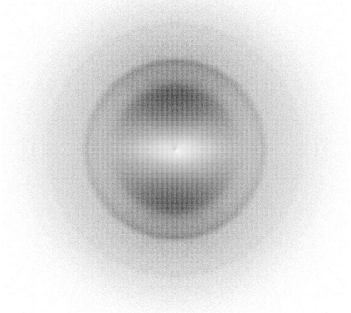

1 882 588 e^-

inverted, N_L = 4

Δt = 7.375 ps

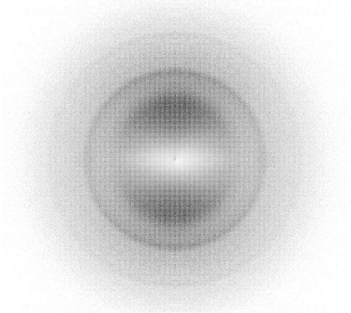

1 662 446 e^-

inverted, N_L = 4

Scan of the First Maximum, λ_{pump} = 265 nm

Δt = 0.235 ps

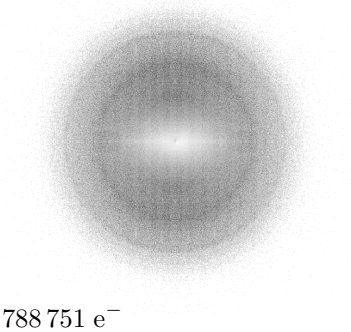

788 751 e^-

inverted, N_L = 4

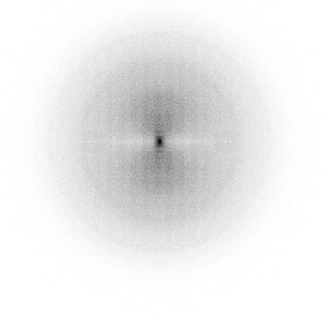

Δt = 0.290 ps

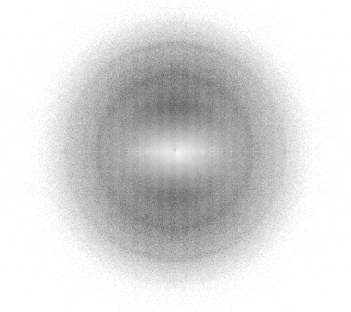

1 189 450 e^-

inverted, N_L = 4

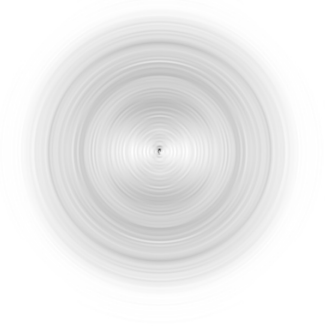

Δt = 0.345 ps

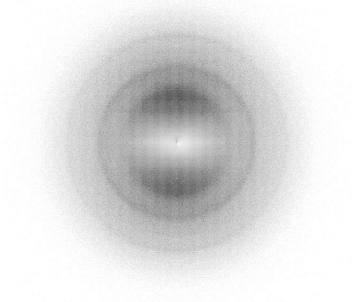

2 162 826 e^-

inverted, N_L = 4

Δt = 0.400 ps

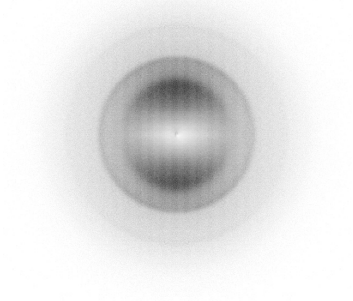

3 735 089 e^-

inverted, N_L = 4

Δt = 0.455 ps

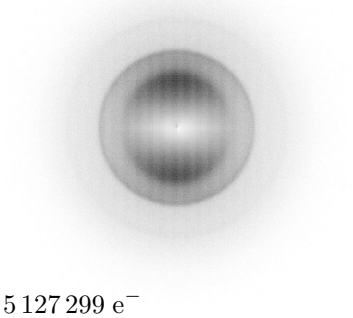

5 127 299 e^-

inverted, N_L = 4

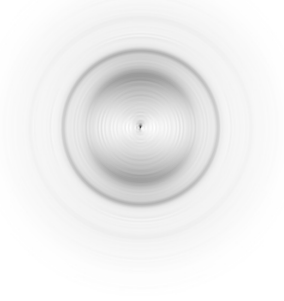

Δt = 0.510 ps

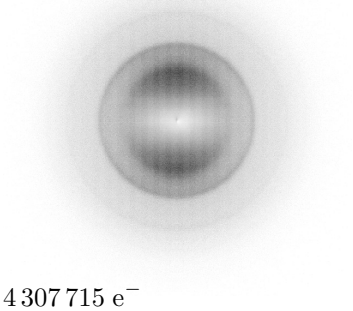

4 307 715 e^-

inverted, N_L = 4

Δt = 0.565 ps

inverted, $N_{\mathrm{L}} = 4$

2 364 360 e^{-}

Δt = 0.620 ps

inverted, $N_{\mathrm{L}} = 4$

1 447 606 e^{-}

Δt = 0.675 ps

inverted, $N_{\mathrm{L}} = 4$

1 187 802 e^{-}

B.4 Xenon

Single-color, multi-photon above-threshold ionization with $\lambda_{\mathrm{pump}} = 402$ nm

inverted, $N_{\mathrm{L}} = 6$

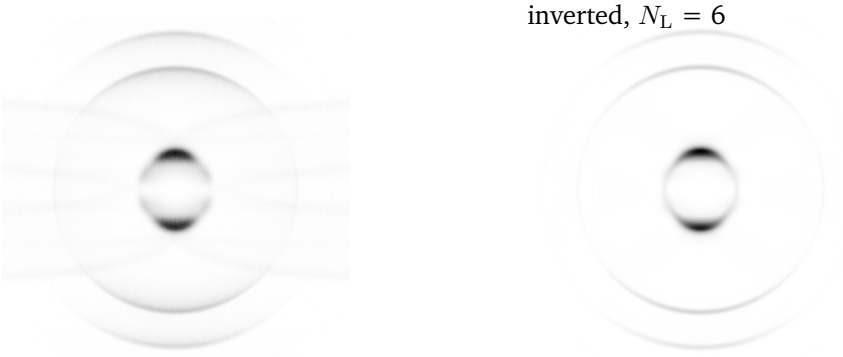

4 187 688 e^{-}

List of Figures

List of Tables

If I had more time, I would have written a shorter thesis.
– loosely based on Blaise Pascal